# The physical and chemical conditions of molecular clouds on large scales

Dissertation

zur

Erlangung des Doktorgrades (*Dr. rer. nat.*)

der

Mathematisch–Naturwissenschaftlichen Fakultät

der

Rheinischen Friedrich–Wilhelms–Universität Bonn

vorgelegt von

Nina BRINKMANN

aus

Bielefeld, Deutschland

Bonn 2020

Angefertigt mit Genehmigung der Mathematisch-Naturwissenschaftlichen Fakultät der Rheinischen Friedrich–Wilhelms–Universität Bonn

**RHEINISCHE FRIEDRICH–WILHELMS–UNIVERSITÄT BONN**

# *Abstract*

by Nina Brinkmann

for the degree of

*Doctor rerum naturalium*

Observations of molecular emission lines in the radio and (sub)millimetre wavelength regime provide insights into the interiors of molecular clouds which are inaccessible by other forms of radiation. Examining the physical and chemical conditions within these centres of star formation furthers our understanding of young stellar objects in the earlier stages of stellar evolution and their interplay with the interstellar medium. Technological advancements are now allowing observations of molecules in distant galaxies, but our ability to interpret these data are limited by our knowledge of exactly how and where molecular emission lines originate within our own galaxy. Until recent years, observational biases caused by pre-selection of either certain positions in a molecular cloud or a few molecular lines only allowed very selective studies.

This thesis describes the acquisition and analysis of the first spectroscopically unbiased data set of the northern part of the prominent Orion A molecular cloud in the 1.3 mm atmospheric window. Orion A is a uniquely suited target as it offers a large range of environments but can also be spatially resolved due to its close proximity. The data were obtained with the PI230 receiver at the APEX telescope, which increased the simultaneous frequency coverage in the 1.3 mm window by a factor of eight. The observations cover an area of around $0.8 \times 3.8$ pc with a resolution of 0.06 pc ($\sim 1.2 \times 10^4$ AU). We examine how 29 molecular species (55 isotopologues in total) emit from environments with a variety of conditions. We thereby aim to not only advance our understanding of the source itself, but the scope of our study allows placing it into the context of the general interstellar medium of the Milky Way and of extragalactic systems.

We develop templates of distinct regions and contrast their respective emission profiles. This highlights common features but also unique characteristics that enable differentiation. We explore the reliability of commonly used line ratios as a tool to infer physical parameters like temperature or UV irradiation, examine correlations between different molecular species and isotopologues, and calculate line luminosities.

We further report on the surprising first detection of larger scale $CF^+$ emission in a variety of environments. This molecule is expected to form under quite specific conditions and previous detections focused on regions meeting those requirements. We confirm its presence throughout Orion A with additional higher frequency observations obtained with the LASMA receiver at APEX and aim to explain its widespread and fairly uniform distribution.

Our data set also enables us to examine the nature of the so-called 'radical region' within Orion A and to determine whether or not it is a distinct entity characterised by unusual molecular abundances. Prior investigations of this region were not conclusive and their

respective observational biases precluded a definite assessment.

Apart from these scientific questions, we also report on the PI230 receiver's performance during its commissioning phase and describe and evaluate its characteristics, e.g. changing main beam efficiencies, spurious features, and sideband rejection.

*To my mother*

# List of publications

**Publication related to the PhD thesis 'The physical and chemical conditions of molecular clouds on large scales' by Nina Brinkmann**

**An imaging line survey of OMC-1 to OMC-3. Averaged spectra of template regions**
Brinkmann, N.; Wyrowski, F.; Kauffmann, J.; Colombo, D.; Menten, K. M.; Tang, X. D.; Güsten, R., A&A, 636, A39
DOI: 10.1051/0004-6361/201936885

**Other publications with contributions from Nina Brinkmann**

First author

**The bound fraction of young star clusters**
Brinkmann, N.; Banerjee, S.; Motwani, B.; Kroupa, P., A&A, 600, A49
DOI: 10.1051/0004-6361/201629312

Co-author

**Kinetic temperature of massive star-forming molecular clumps measured with formaldehyde. III. The Orion molecular cloud 1**
Tang, X. D.; Henkel, C.; Menten, K. M.; Wyrowski, F.; **Brinkmann, N.**; Zheng, X. W.; Gong, Y.; Lin, Y. X.; Esimbek, J.; Zhou, J. J.; Yuan, Y.; Li, D. L.; He, Y. X., A&A, 609, A16
DOI: 10.1051/0004-6361/201731849

**LEGO II: A 3 mm molecular line study covering 100 pc of one of the most actively star-forming portions within the Milky Way Disc**
A.T. Barnes; J. Kauffmann; F. Bigiel; **N. Brinkmann**; D. Colombo; A.E Guzman; W.J. Kim; L. Szücs; V. Wakelam; S. Aalto; T. Albertsson; N.J. Evans; S.C.O. Glover; P.F. Goldsmith; C. Kramer; K. Menten; Y. Nishimura; S. Viti; Y. Watanabe; A. Weiss; M. Wienen; H. Wiesemeyer; F. Wyrowski, MNRAS 497, 1972-2001
DOI: 10.1093/mnras/staa1814

# Contents

# List of Figures

# List of Tables

# Nomenclature

## Frequently used symbols

| | |
|---|---|
| $A_{ij}$ | Einstein coefficient |
| $\alpha_{2000}$ | Right ascension |
| $c$ | Speed of light |
| $\delta_{2000}$ | Declination |
| $E$ | Energy |
| $\eta_{mb}$ | Main beam efficiency |
| $f$ | Filling factor |
| $g$ | Statistical weight |
| $G$ | Gravitational constant |
| $h$ | Planck's constant |
| $J$ | Orbital angular momentum |
| $k_B$ | Boltzmann's constant |
| $\lambda$ | Wavelength |
| $L$ | Luminosity |
| $\mu$ | Reduced mass |
| $M$ | Mass |
| $\nu$ | Frequency |
| $n$ | Numerical density |
| $N$ | Column density |
| $r$ | Distance |
| $\sigma$ | RMS noise (or surface accuracy, or collisional cross section) |
| $\tau$ | Optical depth |
| $t$ | Time |
| $T$ | Temperature |
| $\theta$ | Beam size |
| $v$ | Velocity |

# Numerical constants

arcminute $(1')$ $= 60'' = \frac{1}{60}° = \frac{1}{10800}$ rad

$\pi$ $= 3.14156$

# Physical constants

Speed of light $c = 299\,792\,458 \,\mathrm{m\,s^{-1}} \approx 173 \,\mathrm{AU\,day^{-1}}$

Gravitational constant $G = 6.67430(15) \times 10^{-11} \,\mathrm{m^3\,kg^{-1}\,s^{-2}} = 4.30091(25) \times 10^{-3} \,\mathrm{pc\,M_\odot^{-1}\,km^2\,s^{-2}}$

Planck's constant $h = 6.62607015 \times 10^{-34} \,\mathrm{J}$

Boltzmann's constant $k_\mathrm{B} = 1.380649 \times 10^{-23} \,\mathrm{J\,K^{-1}}$

Electronvolt $(1 \,\mathrm{eV})$ $= 1.602176634 \times 10^{-19} \,\mathrm{J}$

# Astronomical constants

Astronomical unit $(1 \,\mathrm{AU})$ $= 1.495978707 \times 10^{11} \,\mathrm{m}$

Parcec $(1 \,\mathrm{pc})$ $= 3.0857 \times 10^{16} \,\mathrm{m} \approx 2.1 \times 10^5 \,\mathrm{AU}$

Solar mass $(1 \,\mathrm{M_\odot})$ $= 1.98847 \times 10^{30} \,\mathrm{kg}$

Solar luminosity $(1 \,\mathrm{L_\odot})$ $= 3.828 \times 10^{26} \,\mathrm{W}$

# Introduction

## 1.1   The interstellar medium

The space between stars is not empty, but filled with gas, dust, and radiation - the interstellar medium (ISM)[1]. Around 74% of its (baryonic) mass consists of hydrogen, $\sim 25\%$ of helium, and $\lesssim 2\%$ of heavier elements. In astronomical contexts, the latter are referred to as 'metals'. The relative abundances by numbers of some elements are listed in Table 1.1, showing that oxygen, carbon, and nitrogen are the dominant metals. The ISM is not uniformly distributed but rather concentrated in clouds of varying sizes and vastly different parameter ranges, with temperatures between 10 K and $> 10^6$ K and densities from $10^{-4}$ cm$^{-3}$ to $10^8$ cm$^{-3}$ (van Dishoeck 2014, see also Section 1.1.1). Exploring the formation and evolution of these structures is a crucial step in the understanding of star and ultimately planet formation.

**Table 1.1:** Top ten most abundant elements in the ISM, sorted in decreasing order of quantity relative to the number of hydrogen nuclei. Table adapted from van Dishoeck 2014.

| element | abundance | element | abundance |
|---------|-----------|---------|-----------|
| H  | 1                    | Mg | $4.0 \times 10^{-5}$ |
| He | 0.085                | Si | $3.2 \times 10^{-5}$ |
| O  | $4.6 \times 10^{-4}$ | Fe | $3.2 \times 10^{-5}$ |
| C  | $2.7 \times 10^{-4}$ | S  | $1.3 \times 10^{-5}$ |
| N  | $6.8 \times 10^{-5}$ | Al | $2.8 \times 10^{-6}$ |

**Notes.** Heavier elements may not be in the gas phase but bound to the surface of dust grains.

The interplay between the ISM and stars is complex. Stars are formed in the coldest and densest parts of the ISM, molecular clouds, where molecules but also dust and ices are detected (van Dishoeck 2014). Stars in turn enrich the ISM with heavy elements and dust, especially during the later stages of their evolution. Thus the composition of the ISM is altered with time and subsequent generations of stars have a slightly different chemical composition. As shown in Fig. 1.1, both low- and high-mass stars contribute to this change, but their respective feedback processes are different. Evolved low-mass stars ($< 8$ M$_\odot$) eventually start to lose substantial amounts of their outer atmosphere, ejecting some of the produced heavier elements but also dust. High-mass stars ($> 8$ M$_\odot$) end their lives in supernova explosions, where not only the outer layers but also the

---

[1]Magnetic fields are also part of the ISM, constituting a pressure source. Observationally, one can determine the strength of the line-of-sight magnetic field component using the Zeeman effect, and the projected direction (not the strength however) in the plane of the sky through polarised emission of dust grains, which are aligned along the field. Exact measurements are complex and not part of this thesis.

heaviest elements synthesized deep inside the stellar core are ejected into the surrounding ISM. Thus matter continuously cycles through the ISM, its presence in molecular clouds marking both the end and the beginning of a stellar life. With their distinguished position within the cycle, molecular clouds will also be the focus of this thesis.

**Table 1.2:** Typical properties of the different phases of the ISM, adapted from Klessen & Glover (2016) and references therein. Data for the H II region and Hot Core are supplemented from Hollenbach & Tielens (1999) and Tielens (2005), p. 2 and 376.

| phase | density [cm$^{-3}$] | temperature [T] |
|---|---|---|
| coronal gas | $\sim 10^{-2}$ | $\sim 10^6$ |
| intercloud gas | $0.2 - 0.5$ | $\sim 8000$ |
| H II region | $10^3 - 10^4$ (compact region, $\sim 0.5$ pc) $\sim 10$ (diffuse nebula, $\sim 10$ pc) | $10^4$ |
| diffuse cloud | $20 - 50$ | $50 - 100$ |
| molecular cloud | $> 10^2$ | $10 - 20$ |
| hot core | $> 10^6$ | $> 100$ |

### 1.1.1  Phases of the ISM

The main different classes of clouds and their typical density and temperature ranges are depicted in Fig. 1.2, while a summary of some parameters is given in Table 1.2. As described in e.g. Yamamoto (2017), some of these clouds align along a line of constant pressure, indicating that they are in equilibrium. Deviations from this trend are found for H II regions, molecular clouds, and hot cores. All three are closely related to star formation: the H II region is an effect of strong radiation and stellar winds from high-mass stars (see also Section 1.4.1), molecular clouds are the sites of star formation, and hot cores with their rich chemistry can develop in the direct vicinity of young stars. In this thesis, we will mainly examine molecular clouds as a whole (see Section 1.3 for a more detailed introduction), but as they are so closely connected, H II regions and hot cores will also be important and are will be discussed in the context of our data analysis.

### 1.1.2  Interstellar dust and ices

With a mass ratio of $\frac{M_{\mathrm{dust}}}{M_{\mathrm{gas}}} \approx 0.01$, solid grains constitute only a small percentage of the interstellar medium, but their influence is substantial. They shield molecular gas from dissociating interstellar radiation, provide a surface for chemical reactions (including $H_2$ and complex molecules), and remove a significant fraction of heavy elements from the gas phase.

Dust grains in molecular clouds are composed of amorphous silicates and carbonaceous compounds with typical sizes of around 0.1 $\mu$m (van Dishoeck 2014). They are observable through their far-infrared (FIR) thermal emission, which is a consequence of the dust's ability to absorb energetic ultraviolet (UV) radiation from stars and converting it into heat. Observing this FIR emission at
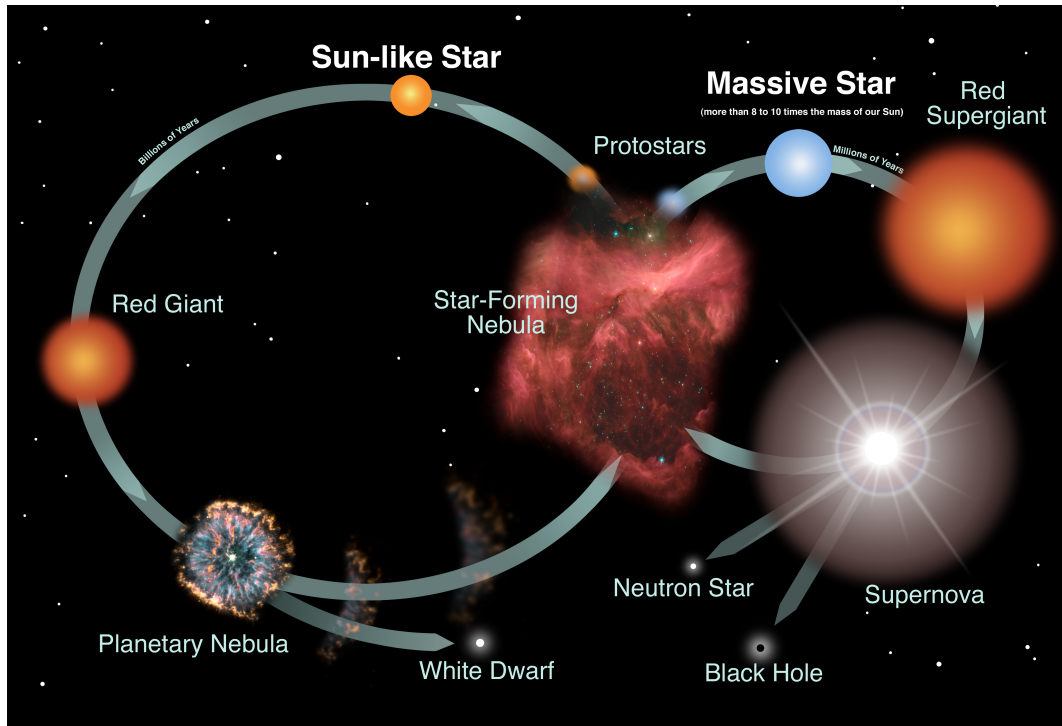
**Figure 1.1:** Simplified life cycle of low- and high-mass stars. Both are formed in dense cores of molecular clouds ('Star-Forming Nebula'), but their different masses result in very distinct evolutions. A low-mass ('sun-like') star is stable for several Billion years while fusing hydrogen to helium. When this nuclear fuel is exhausted, the star increases in size (becoming a 'Red Giant') and loses part of its mass. A 'planetary nebula' is formed when the remaining central star ('White Dwarf'), now very hot and emitting energetic UV radiation, excites the previously shed material. This processed material will eventually return to a molecular cloud and form the next generation of stars. A massive star has a significantly shorter lifetime ($\approx$ 10 Million years) before exploding as a supernova, ejecting the majority of its mass into its environment. The remaining central object can be a neutron star or a black hole, depending on the initial stellar mass. Credit: NASA and the Night Sky Network.

different wavelengths (e.g. with the *Herschel Space Observatory*) enables us to determine properties of the dust. Temperatures and inferred gas column densities (see Kauffmann et al. (2008) for the relation between dust emission and gas column densities and masses) will be used in this thesis to characterise the molecular cloud Orion A and its distinct subregions (see Chapter 3). Converting UV radiation into less energetic FIR emission is also the aforementioned shielding effect, whereby bonds within molecules can be maintained instead of being broken by interaction with high-energy photons.

Dust grains lock up substantial amounts of the available carbon and oxygen ($\sim 70\%$ and $\sim 30\%$, respectively) and almost all of Si, Mg, and Fe (van Dishoeck 2014), thus preventing these materials from participating in gas phase reactions (until they may be vaporized at high temperatures $>$ 1200 K). At low temperatures in dense cores, grains may also be covered in ices, mainly $H_2O$ (see also Section 1.2.2). Depending on the evolutionary stage of star formation, other ices can be generated (see Fig. 1.3): through subsequent hydrogenation and the freeze-out of CO from the gas phase at high densities, molecules like $CH_3OH$ can form, which can be further processed with the energetic input from a young protostar. At higher temperatures ($>$ 100 K), the molecules are released into the gas phase and become observable through their characteristic emission lines.
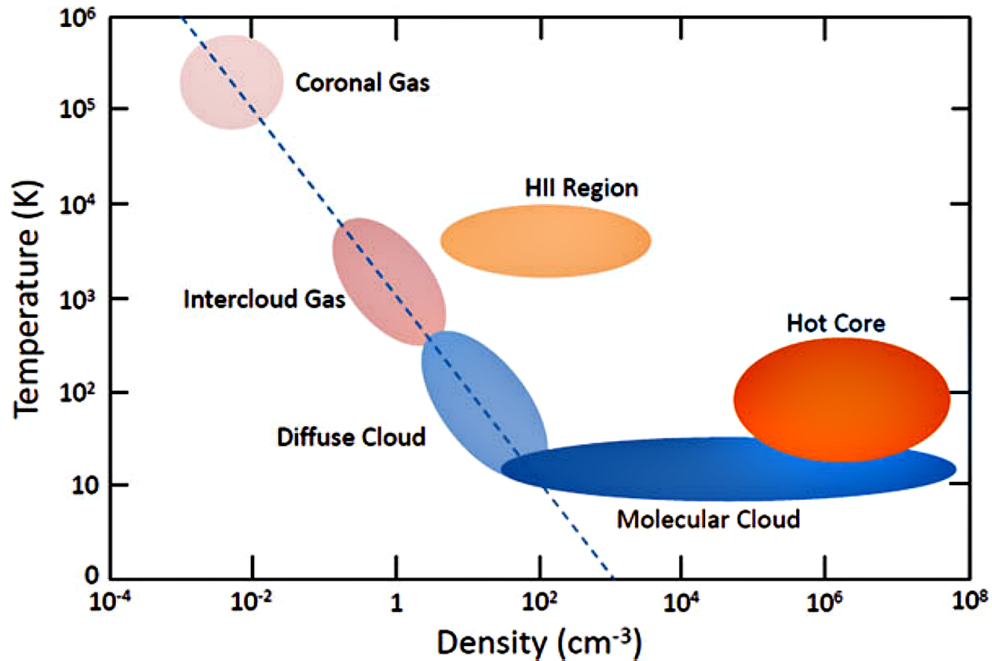
**Figure 1.2:** Phases of the ISM with typical temperature and density ranges. Credit: Yamamoto 2017, p. 4.

## 1.2 Chemical processes

Due to the extreme conditions in the ISM, especially the very low densities, the relevance of different chemical processes differs strongly from Earths'. Only two-body processes are important and reactive species like ions or radicals can survive for a long time. Bonds between species can be formed, destroyed and rearranged both in the gas phase and on grain surfaces. Deciding which processes are dominant for a given molecule depends on the abundance of the involved species but also critically on temperature and available energy sources (e.g. photons or cosmic rays, see e.g. Tielens 2005, chapter 4). Most reactions are endothermic and thus suspended at the typically low temperature levels in molecular clouds, including reactions between the abundant $H_2$ and neutral species. A summary of basic reaction types and their rate coefficients is given in Table 1.3. The highest rate coefficients are typically associated with ion reactions, as their electric charge enhances the probability to attract a reaction partner.

### 1.2.1 Gas phase chemical reactions

Most of the reactions in Table 1.3 occur in the gas phase, their general importance indicated by their respective typical rate coefficient. Owing to the low densities, even in dense molecular clouds, three-body processes are negligible (see low reaction rates of 'collisional association' and 'collisional dissociation') and only contribute to the chemistry in e.g. the inner midplanes of protoplanetary disks (van Dishoeck 2014). They will therefore not be discussed here.

Between the (remaining) bond forming processes, '**associative detachment**' is the fastest, but requires the presence of anions. These have only been recently detected (McCarthy et al. 2006) and are largely absent in the ISM. The reaction is thus limited, but it was important in the early universe for the formation of $H_2$. The other gas phase process '**radiative association**' is intrinsically slow (and difficult to examine in laboratory settings on Earth), as the timescales for photon emission
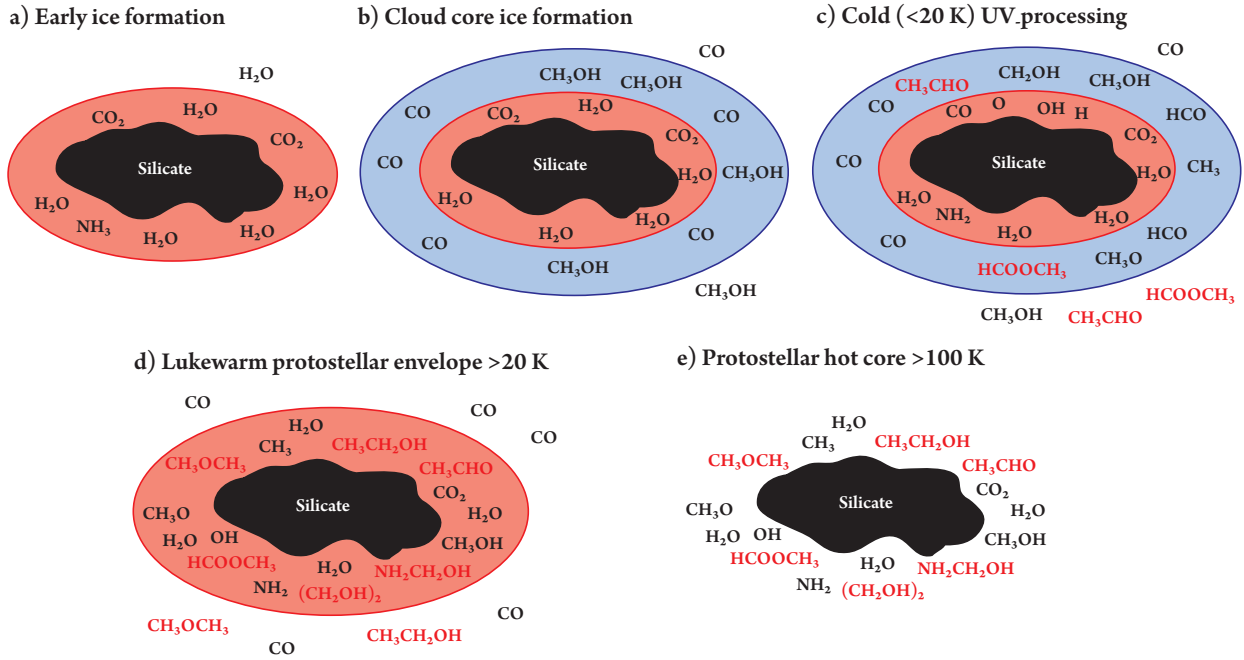
**Figure 1.3:** Evolution of dust and ices and the formation of complex organic molecules. (a) Hydrogenation of e.g. C produces simple molecules like $CH_4$. (b) At high densities, CO freezes out from the gas phase onto the grain, being subsequently hydrogenated into $CH_3OH$. (c) Energy provided by UV radiation enables further reactions into more complex molecules like $HCOOCH_3$. (d) Rising temperatures closer to the young protostar cause sublimation of the outer ice layers, releasing species into the gas phase and facilitating their observation through characteristic line emission. (e) At high temperatures ($> 100$ K), all ices desorb thermally and become observable. The graphic is taken from van Dishoeck (2014), originally published in Öberg et al. (2010).

are several orders of magnitude slower than collision timescales, $\tau_{rad} \simeq 10^{-7}$ s vs. $\tau_{col} \simeq 10^{-13}$ s (Tielens 2005, p. 95). This means that the process is not efficient, as the product might not be able to stabilise from its excited state fast enough and dissociates again. Enhanced efficiencies are found for specific species or large molecules (see also van Dishoeck 2014).

Molecular ions capture electrons to form smaller neutrals during '**dissociative recombination**', which is efficient at low temperatures ($10-30$ K). A primarily formed neutral in an excited electronic state dissociates (Tielens 2005, p. 96f.), while larger molecules may be able to transfer excess energy into vibrational modes, before radiating it away. Energetic photons enabling '**photodissociation**' are supplied by the interstellar radiation field (ISRF[2]) and (indirectly) by cosmic rays[3]. On smaller scales, the immediate vicinity of young high-mass stars is an environment characterised by high intensity UV radiation (see also Section 1.4.1) dominating physical and chemical processes, coining the term 'photodissociation region' or 'photon-dominated region' (PDR). ISRF photons with energies $> 13.6$ eV are absorbed by atomic hydrogen in the diffuse ISM, such that only lower energy FUV photons are present inside clouds. As bonding energies typically range from 5 to 10 eV (Tielens 2005, p. 86), the remaining photons carry enough energy to dissociate molecules. Additionally, dust

---

[2] $\sim 10^8$ photons cm $s^{-1}$, averaged value for the photons produced by the stars in the solar neighbourhood (see van Dishoeck (2014) and references therein, e.g. Draine (1978)).

[3] High energy ($\geq 100$ MeV) nuclei, mainly relativistic protons, originating from supernovae or produced by sputtered interstellar grains (Tielens 2005, p. 15f.).

**Table 1.3:** Basic types of reaction processes and their respective rate coefficients in the ISM. Table adapted from van Dishoeck 2014 and complemented with information from Tielens 2005, p. 86.

| process | | rate coefficient | unit |
|---|---|---|---|
| **bond formation** | | | |
| radiative association | $X + Y \rightarrow XY + h\nu$ | $10^{-17}$ to $10^{-14}$ | $\mathrm{cm^3 s^{-1}}$ |
| grain surface formation | $X + Y : g \rightarrow XY + g$ | $\sim 10^{-17}$ | $\mathrm{cm^3 s^{-1}}$ |
| associative detachment | $X^- + Y \rightarrow XY + e$ | $\sim 10^{-9}$ | $\mathrm{cm^3 s^{-1}}$ |
| collisional association | $X + Y + M \rightarrow XY + M$ | $\sim 10^{-32}$ | $\mathrm{cm^6 s^{-1}}$ |
| **bond destruction** | | | |
| photodissociation | $XY + h\nu \rightarrow X + Y$ | $10^{-10}$ to $10^{-8}$ | $\mathrm{s^{-1}}$ |
| dissociative recombination | $XY^+ + e \rightarrow X + Y$ | $10^{-7}$ to $10^{-6}$ | $\mathrm{cm^3 s^{-1}}$ |
| collisional dissociation | $XY + M \rightarrow X + Y + M$ | $\sim 10^{-26}$ | $\mathrm{cm^6 s^{-1}}$ |
| **bond rearrangement** | | | |
| ion-molecule exchange | $X^+ + YZ \rightarrow XY^+ + Z$ | $10^{-9}$ to $10^{-8}$ | $\mathrm{cm^3 s^{-1}}$ |
| charge transfer | $X^+ + YZ \rightarrow X + YZ^+$ | $10^{-9}$ | $\mathrm{cm^3 s^{-1}}$ |
| neutral-neutral | $X + YZ \rightarrow XY + Z$ | $10^{-11}$ to $10^{-9}$ | $\mathrm{cm^3 s^{-1}}$ |

**Notes.** The Notation ':g' implies that the respective element is located on the grain surface instead of the gas phase.

attenuates the UV radiation inside molecular clouds through absorption and scattering, such that the residual radiation is a function of the depth into the cloud and dust properties like composition, size, and shape. For the most abundant species like $H_2$ and CO (van Dishoeck 2014; Visser et al. 2009) self-shielding also becomes important, by which the dissociating radiation is absorbed in the outer layers, protecting the molecules deeper in the cloud. But even deep inside clouds where the ISRF is nearly fully shielded, a small level of UV radiation is maintained by cosmic rays. Thus, photodissociation is possible in a lot of environments but its efficiency is strongly variable.

If the ISM is even weakly ionised, '**ion-molecule exchange**' can be very efficient down to temperatures of 10 K for exothermic reactions (e.g. Herbst & Klemperer 1973), especially if the involved neutral reaction partner has a permanent dipole moment, as activation barriers may be overcome by the mutual attraction (Tielens 2005, p. 92). But even without a permanent dipole, the ion may induce a dipole in the neutral reaction partner, making the process important for interstellar chemistry. As the number of ions determines the number of possible reactions, ion-molecule exchange is ultimately determined by photoionisation and cosmic rays. The exact reaction rates for '**charge transfer**' processes depend on the involved reaction partners. For two involved atoms, the reaction $O + H^+ \rightarrow O^+ + H$ has a large rate coefficient (Tielens 2005, p. 93f) and is chemically important, as it opens up further reaction paths between oxygen and other species. Reactions with molecules involved may also be efficient, as there is a large number of available electronic states. For most '**neutral-neutral**' reactions activation barriers of $\geq 1000$ K are not uncommon, such that they cannot occur in the diffuse ISM or molecular clouds (Tielens 2005, p. 89ff). The exception being radical-radical or radical-stable molecule reactions (see Shematovich 2012

and references therein, e.g. Smith et al. 2004), which are only a factor $\sim 5$ slower than ion-molecule reactions, even at low temperatures (van Dishoeck 2014).

### 1.2.2 Grain-surface chemistry

Grain surfaces are extremely important for the chemistry in cold environments, as they not only increase the chance of accreted species meeting, but can also absorb excess energy from the reaction products, thus stabilising them before they evaporate into the gas phase. $H_2$, the dominant species in molecular clouds, is effectively produced mostly on grains (e.g. Shematovich 2012 and reference therein, Vidali et al. 2007).

The efficiency of reactions depends on several factors (see Tielens 2005, p. 102ff and Fig. 1.4): the probability of accretion (depending e.g. on the individual species, gas velocity and grain temperature), the mobility on the potentially rough surface by thermal diffusion or the quantum-mechanical tunnel effect, the chance of the chemical reaction occurring (e.g. overcoming reaction barriers), and lastly evaporation from the surface (ultimately dependent on grain temperature). The hydrogena-
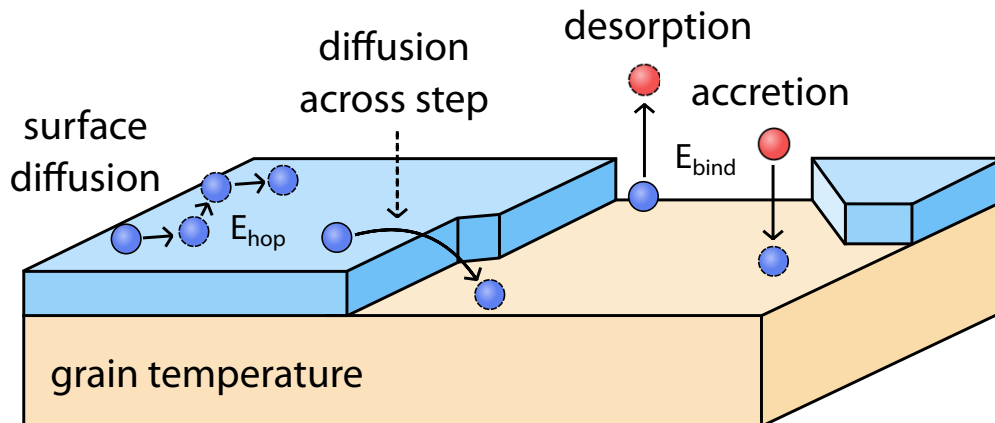


**Figure 1.4:** Steps and energies involved in grain-surface processes: the accretion of educts, their diffusion on the (rough) surface, the reaction (not depicted) and the desorption of the reaction product. The illustration is taken from van Dishoeck 2014, p. 24.

tion of atoms and molecules is possible because hydrogen is abundant and, owing to its lightness, very mobile on the grain surface even at very low temperatures. With oxygen being one of the more abundant metals (Tab. 1.1), the reaction chain

$$O + H \rightarrow OH + H \rightarrow H_2O \tag{1.1}$$

causes the dominance of $H_2O$ ices on grains. The formation of $CH_3OH$, an important first step towards higher molecular complexity, is similarly achieved through the saturation of CO with hydrogen:

$$CO + H \rightarrow HCO + H \rightarrow H_2CO + H \rightarrow H_3CO + H \rightarrow CH_3OH \tag{1.2}$$
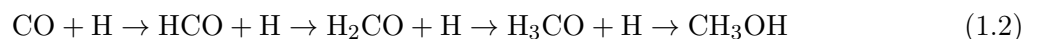
The production of $CH_3OH$ in the gas phase, via dissociative recombination of $CH_3OH_2^+$, is inefficient (Shematovich 2012 and references therein, e.g. Wirström et al. 2011). With $CH_3OH$ mainly formed on grains, its observation offers an opportunity to trace properties of molecular gas. For $CH_3OH$ to become observable at all, it has to be in the gas phase and thus be released from the surface, which can happen at high temperatures or as a consequence of shocks. We can thus use $CH_3OH$ emission to identify these environments in molecular clouds (see also Chapter 3).

## 1.3 Molecular clouds

With some of the very basic characteristics of molecular clouds already mentioned previously, we want to expand on the information in the following sections. Molecular clouds, more specifically the Giant Molecular Cloud (GMC) Orion A will be the focus of this thesis and we want to give an overview of the conditions within GMCs and how we as observers can determine physical and chemical features.

The total mass of the ISM in the Milky Way is estimated to be around $10^{10}$ M$_\odot$ (Ballesteros-Paredes et al. 2020 and references therein, e.g. Girichidis et al. 2020). Molecular gas accounts for roughly 30% of that (see also Evans 1999 and references therein, e.g. Combes 1991), which is around two orders of magnitude smaller than the total stellar mass of $\sim 1.8 \times 10^{11}$ M$_\odot$ (Tielens 2005, p. 19). Understanding more about molecular clouds and under what conditions stars form is crucial for the comprehension of large scale galaxy evolution. As seen in Fig. 1.5, the molecular gas mass is not evenly distributed throughout our Galaxy. Starting at the centre of the Milky Way, the distribution peaks in the so-called Central Molecular Zone (CMZ), located in the central few hundred parsec around the Galactic centre (Ballesteros-Paredes et al. 2020 and reference therein, Molinari et al. 2011), then falls off between 0.5 and 3 kpc, before peaking again in the Molecular Ring ($4 - 8$ kpc). There is a decline beyond the Molecular Ring, but molecular gas is still detected towards large Galactic radii (for reference, the Sun is located at a distance of around 8 kpc from the Galactic centre).

Most of the molecular material was thought to be contained in GMCs with $M > 10^4$ M$_\odot$ (Evans 1999; Blitz & Williams 1999). However, more recent observational studies of CO and CS emission in the Milky Way (Roman-Duval et al. 2016) find that only around 14% of the molecular gas mass is actually associated with known molecular cloud complexes, while the majority resides within a more diffuse component.

Another strongly debated topic concerns the lifetime of GMCs (Ballesteros-Paredes et al. 2020 and references therein), reflecting the difficulties in measuring this parameter: one view considers GMCs to be largely stable, long-lived objects (see e.g. McKee & Holliman 1999; McKee & Ostriker 2007; Evans 1999 and references therein). Observationally, cloud lifetimes of $\sim 100$ Myr have been inferred from GMCs in between spiral arms of galaxies (see e.g. Scoville & Wilson 2004). Contrary to this, it has been argued that GMCs are more transient, short-lived objects with lifetimes $\sim 10$ Myr (see e.g. Dobbs et al. 2011). This is consistent with the observation that molecular clouds are typically associated with stars younger than 3 Myr in the Solar neighbourhood, and that throughout the Milky Way in general, stars with ages $\sim 10$ Myr seem to not be associated with molecular clouds (Hartmann 2001 and references therein).

Based on studies of extragalactic GMCs in nine galaxies, Chevance et al. (2020) suggest a picture in which these two theories may be consolidated. The authors find that GMC lifetimes depend on galactic molecular gas surface density and broadly fall into one of two categories: governed by galactic processes for large surface densities ($\geq 8$ M$_\odot$ pc$^{-2}$), or determined by local processes for small surface densities ($\leq 8$ M$_\odot$ pc$^{-2}$). The respective GMC lifetimes are then those of galactic dynamical timescales (interplay between e.g. gravitational infall of the mid-plane ISM and shear, several 10 Myr), or cloud-scale dynamical timescales (free-fall or crossing time, few Myr). Chevance et al. (2020) find average GMC lifetimes of $10 - 30$ Myr across their galaxy sample, but note significant variations within and between galaxies (see e.g. their Table B1 for measured GMC lifetimes for the nine galaxies and different radial bins).
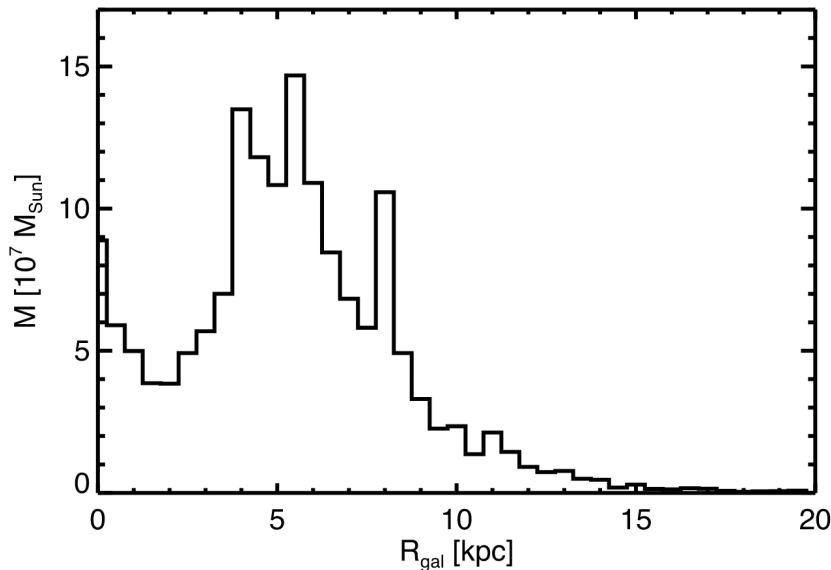
**Figure 1.5:** Molecular mass as a function of galactocentric distance. Taken from Miville-Deschênes et al. 2017 (part of their Fig. 9)

### 1.3.1 Structure and star formation

The mass within a molecular cloud itself is not homogeneously distributed, but distinctly hierarchical (Blitz & Williams 1999; Pokhrel et al. 2018, see also Fig. 1.6): lower density material surrounds higher density clumps, which in turn engulf even higher density cores. While the size of a typical molecular cloud is of the order $\gtrsim 10$ pc, the dense cores at $\lesssim 0.1$ pc are compact (André et al. 2010). The majority of the available material will not be converted into stars (e.g. Lada & Lada 2003), as star formation occurs in these densest cores only, where typically not a single star, but a star cluster forms. This is quantified through the star-formation efficiency $\varepsilon_{\mathrm{SFE}}$,

$$\varepsilon_{\mathrm{SFE}} = \frac{M_{\mathrm{stars}}}{M_{\mathrm{stars}} + M_{\mathrm{gas}}} \quad , \tag{1.3}$$

whose values are typically of the order of a few percent for a cloud as a whole, e.g. $2-3\%$ for Orion A (Megeath et al. 2016), while values around $\sim 30\%$ are suggested for cores from observational studies (Lada & Lada 2003; André et al. 2010).

Whether clouds are long-lived and thus pressure supported on larger scales, or rather transient objects, material must in any case contract on small scales to form the observed clumps and cores. The exact mechanisms are still not fully understood, especially the roles of magnetic fields and turbulence (see e.g. Lequeux 2005, chapter 4). One simplified way to describe the stability of a cloud is to consider its *Jeans Mass* (see e.g. Lequeux 2005, p. 324f; Stahler & Palla 2005, p. 249f)

$$M_{\mathrm{Jeans}} = 1.0 \mathrm{M}_{\odot} \left( \frac{T}{10 \text{ K}} \right)^{1.5} \left( \frac{n_{\mathrm{H}_2}}{10^4 \text{ cm}^{-3}} \right)^{-0.5} \quad , \tag{1.4}$$

which is the largest gravitationally stable mass for a given temperature and density. If a cloud is too cold or too dense, thermal pressure cannot balance out the gravitational attraction and collapse occurs. Typical dense cores are found to be close to the edge of gravitational instability, while those with internal stars have crossed it (Stahler & Palla 2005, p. 249f). Initial instabilities may be caused by e.g. shock waves from nearby supernovae explosions, compressing the gas such that it locally crosses the Jeans limit, triggering star formation along its way.

**Figure 1.6:** Hierarchical structure of molecular clouds. The illustration is taken from Pokhrel et al. (2018).
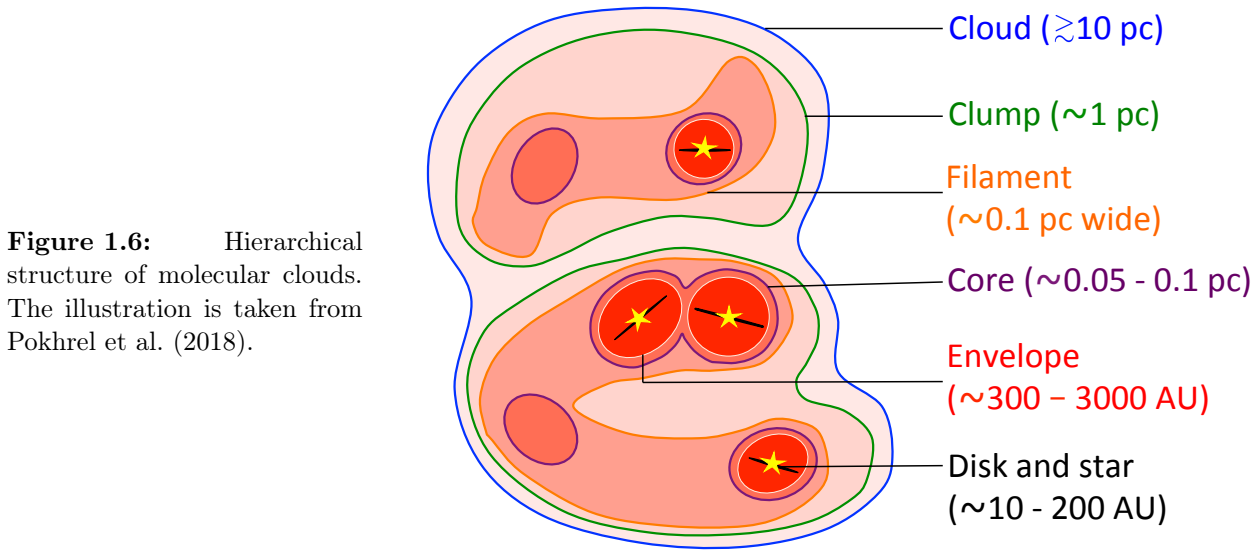
In the earliest stages of star formation, the gas is collapsing from the inside out (e.g. van Dishoeck 2014), building the young protostar in the centre (Class 0). This protostar continues to grow and accrete material from the forming envelope (Class I), generating bipolar outflows in the process. The envelope is gradually dispersed on timescales $\sim 10^6$ years (Class II), revealing a pre-main-sequence star surrounded by a protoplanetary disc (Class III) which may eventually form planets. Once nuclear fusion of hydrogen starts, the stars enters the stable main-sequence phase.

### 1.3.2  Observations of gas and dust

Transitions from one energetic state to another are always connected with the transfer of energy. If an atom or molecule is excited into a higher energy level, it will eventually fall back onto the ground state and emit the excess energy in the process. This emission is what we observe and what gives us information about the emitting species (as emission frequencies are characteristic) and the available energy in the species' environment. Low temperatures and thus the lack of available energy in molecular clouds distinctly limit the excitation possibilities.

The frequency regimes for different kinds of excitations are illustrated in Fig. 1.7. **Electronic transitions**, meaning the excitation of an electron into a higher energy level and the subsequent de-excitation back into the ground state, need energies of a few eV (or $\sim 10^4$ K). The associated photons are usually in the UV or visible frequency spectrum. As a consequence, atoms are difficult to observe in molecular clouds, as they can hardly be excited. In contrast to atomic species, molecules have additional excitation modes available: vibration and rotation. Bonds between the atoms in a molecule can bend or stretch in **vibrational** and **torsional transitions**, or the molecule can rotate around an axis in **rotational transitions**. Vibrations need energies $\sim 0.1$ eV or $\sim 10^3$ K, associated with IR emission. But in the cold environment of molecular clouds, only rotational transitions can be significantly excited. Their energies are the lowest ($\sim 0.001 - 0.01$ eV or $\sim 10 - 500$ K) and the transitions lie in the radio regime. In order to observe the interior of molecular clouds, one must therefore resort to radio frequencies. Even if some of the higher energy transitions were to be locally
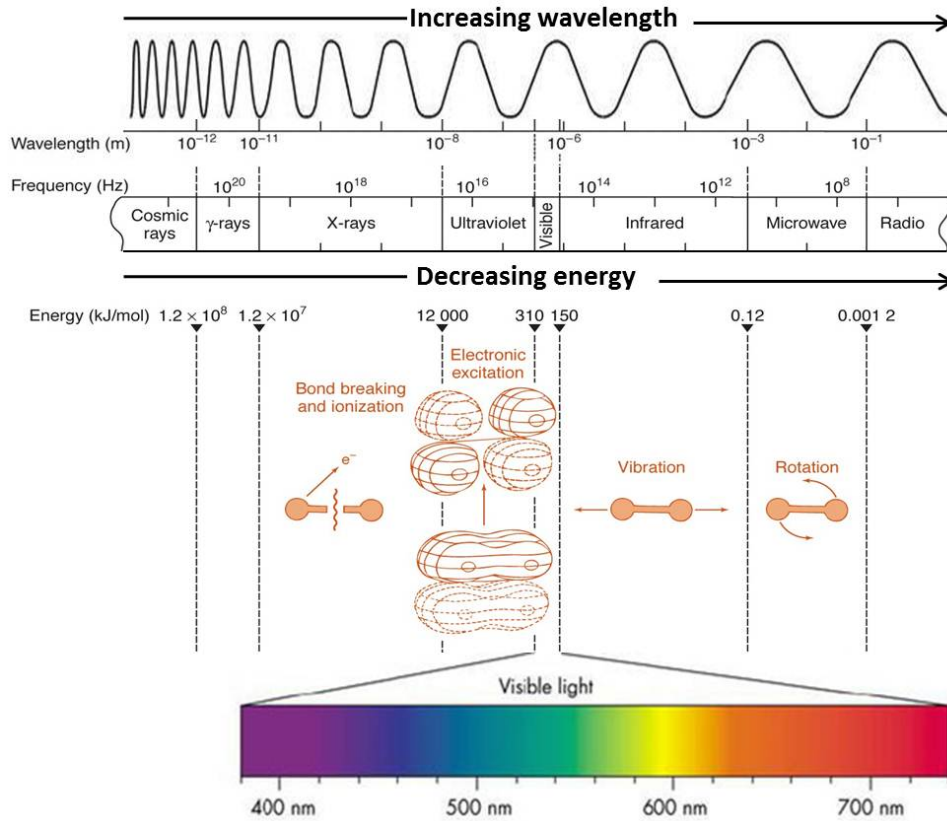
**Figure 1.7:** Excitation processes and associated frequencies. Rotational transitions require the least amount of energy and their photons lie in the radio regime. Vibrations, electronic transitions and ionisation are more energy-intensive and not excited inside molecular clouds. Credit: Virtual Labs

excited (e.g. close to a prestellar object), their emission would be heavily attenuated by dust.

As dust particles are not single molecules but solids, they do not emit at particular frequencies only but are a source of continuum emission. The characteristics of this emission are determined by dust properties (material, shape, and size) and temperature and may be described by modified black-body radiation (e.g. Dent et al. 1998). At high densities $\sim 3 \times 10^4$ cm$^{-3}$ (e.g. Galli et al. 2002) dust and gas temperatures are expected to be coupled. This can be used to infer e.g. gas temperatures from dust observations for high density regions.

### 1.3.3   Molecular line emission

As the main transitions observed for species in molecular clouds are rotational, this Section will concentrate on this process. A more thorough discussion of emission processes can be found in e.g. Tielens 2005, chapter 2. Molecules are excited by collisions with other particles in the gas or radiation (nearby stars, ISRF, cosmic rays). In the cold, shielded regions inside clouds, collisional encounters with $H_2$ dominate. In the case of simple diatomic molecules like CO, the energies $E$ of different rotational states with quantum numbers $J$ are described by

$$E_J = \frac{h^2}{8\pi^2 \mu r^2} J(J+1) \quad , \tag{1.5}$$

with the reduced mass $\mu = \frac{m_1 m_2}{m_1 + m_2}$ determined by the masses $m_1$ and $m_2$ of the constituting atoms, their distance $r$ and the Planck constant $h$. Dipole rotational transitions $\Delta J = \pm 1$ are only possible for species with a permanent dipole and neighbouring lines in the spectrum are spaced with distance

$$E_{J+1} - E_J = \frac{h^2}{4\pi^2 \mu r^2}\,(J+1) \quad \text{or} \quad \nu = \frac{hJ}{4\pi^2 \mu r^2} \quad , \quad J = 1, 2, 3, \dots \quad . \tag{1.6}$$

If the upper-level rotational energy $E_{J+1}$ is significantly higher then the available energy $kT$, only few molecules will be excited and the emission will be weak. For CO, the transition into the first excited state $J = 1$ is efficiently possible at $T \approx 5$ K, and the de-excitation back into the ground state $J = 0$ produces a photon with a frequency of $\sim 115.27$ GHz. For comparison, the minimal rotational energy for $H_2$ (which has no permanent dipole due to its symmetry, so $J = 2 \to 0$ is the lowest energy transition) is equivalent to $\approx 500$ K, far above the typical temperatures $T \lesssim 20$ K in molecular clouds. The transition energies for larger molecules are more complex to calculate than for diatomic species, as there are more states a molecule can be excited into, depending on e.g. the geometry/symmetry of their constituents' arrangement (see e.g. Tielens 2005, p. 40ff). Molecules with more atoms generally have more lines in a given frequency interval.

The population of the different energy levels may be illustrated for the simplified case of a system with just two levels: a lower energy $E_l$ and an upper energy $E_u$. Excitation and de-excitation are equal in equilibrium, and the ratio of the level populations is (see e.g. Tielens 2005, p. 46)

$$\frac{n_u}{n_l} = \frac{g_u}{g_l}\,\exp\left(-\frac{E_u - E_l}{k_B T}\right)\,\left(1 + \frac{n_{crit}}{n}\right)^{-1} \quad . \tag{1.7}$$

Degeneracy of the levels is accounted for with the statistical weights $g$ and the critical density

$$n_{crit} \simeq \frac{A_{ul}}{\sigma v} \tag{1.8}$$

is a measure of the dominant process. De-excitation from $E_u$ to $E_l$ can happen through the emission of a photon, but also by collisions with other molecules (mainly $H_2$). The probability of spontaneously emitting a photon is described by the Einstein coefficient $A_{ul}$, the chance for collision is a function of collisional cross-section $\sigma$ and gas velocity $v$ (e.g. Heiner et al. 2015).

If $n_{crit} << n$, collisions with $H_2$ determine the level populations and Eqn. 1.7 approaches the level populations given by the Boltzmann distribution

$$\frac{n_u}{n_l} \approx \frac{g_u}{g_l}\,\exp\left(-\frac{E_u - E_l}{k_B T}\right) \tag{1.9}$$

at the kinetic temperature $T_{kin}$ of the $H_2$ gas. The system is in local thermodynamic equilibrium (LTE). For the $J = 1 \to 0$ transition of CO (with $A_{10} = 7.20 \times 10^{-8}$ s$^{-1}$) [4], and typical molecular cloud temperatures, $n_{crit} \sim 10^2 - 10^3$ cm$^{-3}$. In the same environment, other molecules may have higher critical densities due to higher dipole moments and corresponding $A_{ul}$ values (e.g. HCN with $A_{10} = 2.43 \times 10^{-5}$ s$^{-1}$). These molecules may be used to trace higher density regions within molecular clouds. For $n_{crit} > n$, the level populations are not set by collisions, but rather determined through interactions with the background radiation field and

$$\frac{n_u}{n_l} \approx \frac{g_u}{g_l}\,\exp\left(-\frac{E_u - E_l}{k_B T}\right)\,\left(\frac{n_{crit}}{n}\right)^{-1} \quad \propto n \quad . \tag{1.10}$$

In this *subthermal* case, the excitation thus becomes density dependant and the excitation temperature $T_{ex}$ of the species is not equal to $T_{kin}$. LTE conditions do not apply and $T_{ex} < T_{kin}$.

---

[4]`https://spec.jpl.nasa.gov/`

### 1.3.4 Diagnostic tools

The main constituents of molecular clouds, molecular hydrogen and helium, are hardly observable due to their high excitation energies combined with the low temperatures and attenuated UV radiation inside clouds. All methods to determine masses and other physical properties thus rely on other molecular species or dust emission, and total masses are inferred from abundance ratios. While ancillary data based on dust measurements will be used in Chapter 3, the interpretation of molecular line emission will be the main tool for this project. We will thus focus on the diagnostic potential of the latter in this section.

The most abundant molecule after $H_2$ is CO (short for its main form $^{12}C^{16}O$), and it is also the most commonly used tracer of molecular gas (e.g. Evans 1999). In contrast to $H_2$, CO has a permanent dipole moment and low critical density. The low-$J$ transitions can thus be easily excited, resulting in bright CO emission even in cold environments. In regions of higher density however,the emission can become optically thick, meaning that CO does not trace all of the molecular material but only the outer layers of a cloud. To probe deeper layers, rarer CO isotopologues like $^{13}CO$, $C^{18}O$ or $C^{17}O$ may be used. Assuming a constant conversion factor between CO line intensity and $H_2$ column density allows the calculation of the total gas mass from CO observations (Bolatto et al. 2013). While the line strength (or the total amount of radiation measured) gives an estimate of the mass, the line position and shape indicate motion: if the centre of the line is blue (red) shifted in regard to the frequency at rest, the source moves towards (away) from Earth. Additionally, several mechanisms (e.g. rotation, temperature, turbulence) can increase the line width or influence the line shape (from infall or outflow motions).

Depending on the observed species and their different critical densities (see Section 1.3.3), other parts of the cloud become accessible. It is important to note however that not only the physical conditions determine if a molecule emits or not, the chemical environment is equally relevant. For example, $HCO^+$ and $N_2H^+$ have similar critical densities ($n_{\mathrm{crit}}^{HCO^+} = 6.8 \times 10^4$ cm$^{-3}$ vs. $n_{\mathrm{crit}}^{N_2H^+} = 6.1 \times 10^4$ cm$^{-3}$ for the $J \to 1 - 0$ transition at $T = 10$ K, see Shirley (2015)), but they trace very different environments. $N_2H^+$ is destroyed in reactions with CO and is thus only abundant in cold regions where CO is frozen onto grains. $HCO^+$ emission does not have this restriction and is a lot more extended.

### 1.3.5 Radiative transfer

Before the radiation of molecular transitions reaches the telescopes on Earth, it propagates through the ISM and may interact with atoms, molecules, free electrons, photons, and dust along the way. These interactions alter the original emission and need to be accounted for. Ignoring scattering events, consider a beam of radiation with intensity $I_\nu$ (at frequency $\nu$) passing through a medium along the path length $s$ (see e.g. Draine 2011, p. 64 ff for a comprehensive derivation of the following formulae). Along an infinitesimal small part $ds$ of the path, the change in intensity can be described as

$$dI_\nu = \underbrace{-I_\nu \kappa_\nu ds}_{\text{absorption}} + \underbrace{j_\nu ds}_{\text{emission}} \quad . \tag{1.11}$$

The attenuation of $dI_\nu$ is represented by the absorption coefficient $\kappa_\nu$, while the increase of $dI_\nu$ is described by the emissivity $j_\nu$. It is important to note that both absorption and emission are frequency dependent, meaning that the same medium may be completely opaque for some frequencies (e.g. visible light), but transparent for others (radio regime). By defining the optical depth $\tau_\nu$

through $d\tau_\nu = \kappa_\nu ds$, one can rewrite Eqn. 1.11 as

$$dI_\nu \; + \; I_\nu d\tau_\nu \;\; = \;\; \frac{j_\nu}{\kappa_\nu} d\tau_\nu \quad , \tag{1.12}$$

for which a general solution is

$$I_\nu(\tau_\nu) \;\; = \;\; \underbrace{I_\nu(0)\exp(-\tau_\nu)}_{\substack{\text{attenuated background} \\ \text{intensity}}} + \underbrace{\int_0^{\tau_\nu} \exp\left(-\left(\tau_\nu - \tau'\right)\right)\frac{j_\nu}{\kappa_\nu}d\tau'}_{\substack{\text{attenuated emission integrated} \\ \text{over the traversed path}}} \quad . \tag{1.13}$$

Assuming that the intensity of the radiation travelling through the medium is uniform ($\frac{dI_\nu}{d\tau_\nu} = 0$) and that it can be described by the Planck function (black body in thermal equilibrium, $I_\nu = B_\nu(T_{\text{ex}})$), and that the medium is comprised of molecules (discrete energy states) in LTE (level population described by a single temperature $T_{\text{ex}}$), one can simplify the solution (Eqn. 1.13) to

$$\begin{aligned} I_\nu(\tau_\nu) \;\; &= \;\; I_\nu(0)\exp(-\tau_\nu) + \int_0^{\tau_\nu} \exp\left(-\left(\tau_\nu - \tau'\right)\right)B_\nu(T_{\text{ex}})\,d\tau' \\ &= \;\; I_\nu(0)\exp(-\tau_\nu) + B_\nu(T_{\text{ex}})\left(1 - \exp(-\tau_\nu)\right) \quad \text{for } T_{ex} = constant. \end{aligned} \tag{1.14}$$

If we further assume that the background emission $I_\nu(0)$ can be approximated by black body radiation at the background temperature $T_{\text{bg}}$, we obtain

$$I_\nu(\tau_\nu) \;\; = \;\; B_\nu(T_{\text{bg}})\exp(-\tau_\nu) \; + \; B_\nu(T_{\text{ex}})\left(1 - \exp(-\tau_\nu)\right) \quad . \tag{1.15}$$

As observations usually aim to characterise the emission of the source itself without background contributions, an 'off' or 'reference' position is observed as well. This reference is selected to contain only background radiation. The two observations are then subtracted, such that only the source intensity remains:

$$\begin{aligned} I_{\nu,\text{source}}(\tau_\nu) \;\; &= \;\; I_\nu(\tau_\nu) \; - \; I_\nu(0) \\ &= \;\; B_\nu(T_{\text{bg}})\exp(-\tau_\nu) + B_\nu(T_{\text{ex}})\left(1 - \exp(-\tau_\nu)\right) - B_\nu(T_{\text{bg}}) \\ &= \;\; \left[B_\nu(T_{\text{ex}}) - B_\nu(T_{\text{bg}})\right]\left(1 - \exp(-\tau_\nu)\right) \quad . \end{aligned} \tag{1.16}$$

With the definitions of brightness temperature $T_{\text{B}}$ and Planck function, and the Rayleigh-Jeans law (see e.g. Draine 2011, Eqn. 7.5 and 7.6) for the radio regime, we obtain for the observed brightness temperature of the source

$$\begin{aligned} T_{\text{B}}(\nu) \;\; &\approx \;\; \frac{c^2}{2k_{\text{B}}\nu^2}\, I_{\nu,\text{source}}(\tau_\nu) \\ &= \;\; \frac{c^2}{2k_{\text{B}}\nu^2}\, \left[B_\nu(T_{\text{ex}}) - B_\nu(T_{\text{bg}})\right]\left(1 - \exp(-\tau_\nu)\right) \\ &= \;\; \frac{c^2}{2k_{\text{B}}\nu^2}\, \left[\frac{2h\nu^3}{c^2}\left(\frac{1}{\exp\left(\frac{h\nu}{k_{\text{B}}T_{\text{ex}}}\right) - 1} - \frac{1}{\exp\left(\frac{h\nu}{k_{\text{B}}T_{\text{bg}}}\right) - 1}\right)\right]\left(1 - \exp(-\tau_\nu)\right) \\ &= \;\; \left[J_\nu(T_{\text{ex}}) - J_\nu(T_{\text{bg}})\right]\left(1 - \exp(-\tau_\nu)\right) \quad , \\ &\text{with } J_\nu(T) \;\; = \;\; \frac{h\nu}{k_{\text{B}}}\left[\exp\left(\frac{h\nu}{k_{\text{B}}T}\right) - 1\right]^{-1} \quad . \end{aligned} \tag{1.17}$$

This expression of the radiative transfer equation will be used in Chapter 5 to infer excitation temperatures and opacities (optical depths) from observed line intensities.

## 1.4   Source: Orion A

The Orion Molecular Cloud complex at a distance of $414 \pm 7$ pc (Menten et al. 2007), one of thousands of GMCs in the Milky Way (Stahler & Palla 2005, p. 2), is an active star forming region around $\gtrsim 70$ pc in size. It contains thousands of low- and high-mass stars subdivided into several subgroups and clusters with stellar ages between $< 2$ Myr and $\sim 12$ Myr (Bally 2008). The two GMCs Orion A and Orion B are part of the complex, together with emission nebulae, reflection nebulae and H II regions (see Fig. 1.8). The observations for this thesis cover the northern part of Orion A, on which we will thus focus for the subsequent sections. The molecular emission of Orion B is discussed in Pety et al. (2017) and companion papers.

The molecular clouds themselves possess a clumpy structure and have historically been divided into subregions, as seen in Fig. 1.9 showing $HCO^+$ line emission of Orion A. The bright OMC-1 in the South, and the comparatively dim OMC-2 and OMC-3 north of it. While OMC-1 contains high-mass star formation and is strongly influenced by UV radiation (harbouring e.g. an H II region, a photon-dominated region (PDR), molecular outflows, and a hot core), OMC-2 and OMC-3 are more quiescent. They do form numerous stars, but most of them are of low mass, still embedded in their envelopes. The energies are mainly driven by outflows of these young sources, whereas feedback from the H II region constitutes an important additional energy source in OMC-1 (Berné et al. 2014).

### 1.4.1   OMC-1

Thousands of mostly low-mass stars formed in the so-called integral-shaped filament in the northern part of Orion A (Bally 2008 and references therein, Bally et al. 1987; Johnstone & Bally 1999), $\sim 2000$ of them concentrated around the massive 'Trapezium' cluster located in OMC-1, named after the arrangement of its four brightest members. The most luminous of them is $\theta^1$ Orionis C (HD 37022), a binary system of a rare massive blue O7-type star with a close companion (Sota et al. 2011). With a system mass $\gtrsim 40$ $M_\odot$ and temperatures of $3.6 \times 10^4$ K and $\sim 2.8 \times 10^4$ K respectively (Patience et al. 2008), $\theta^1$ Orionis C is the primary source of ionising photons and responsible for the illumination of the Orion Nebula. From Earths' perspective, the Trapezium is located at the front of the molecular cloud it formed in, the strong stellar winds and radiation from its massive stars continuously pushing away remaining material (see also Fig. 1.10). The optical visibility of the cluster is caused by this increasing exposure, as there is only little molecular gas and dust to absorb or scatter photons. As a secondary effect, the compression of molecular material may induce further star formation in the future ('sweep-up, compress, trigger' Bally 2008). Besides the Trapezium cluster, there are currently two other main sites of star formation: BN/KL and Orion South. BN/KL ('BN' Becklin & Neugebauer 1967, 'KL' Kleinmann & Low 1967) is the more luminous source ($\sim 10^5$ $L_\odot$) and not exposed like the Trapezium cluster, but lies $\sim 0.2$ pc inside the molecular cloud, causing it to be only visible in X-ray, infrared and radio emission (O'Dell et al. 2008). It is the brightest infrared source in the Orion Nebula and contains a rich chemistry of molecular species. The less luminous ($\sim 10^4$ $L_\odot$) Orion South region is likely located just a few hundredths of a pc behind the ionisation front created by the Trapezium cluster (O'Dell et al. 2008), its material gradually eroding from the radiation. The substructure of all three star forming regions is complex and comprised of several components with differing densities, temperatures, velocities, and spatial extensions (O'Dell et al. 2008; Tahani et al. 2016).

Optical
Credit: John Gauvreau

Optical + Hα filter
Credit: Rogelio Bernal Andreo

Barnards Loop

Horsehead Nebula

Orion Nebula

NH$_3$ emission (orange) observed with the GBT, infrared
radiation from NASA's WISE telescope (blue)

Credit: R. Friesen, Dunlap Institute / J. Pineda, MPIP /
GBO / AUI / NSF / NASA
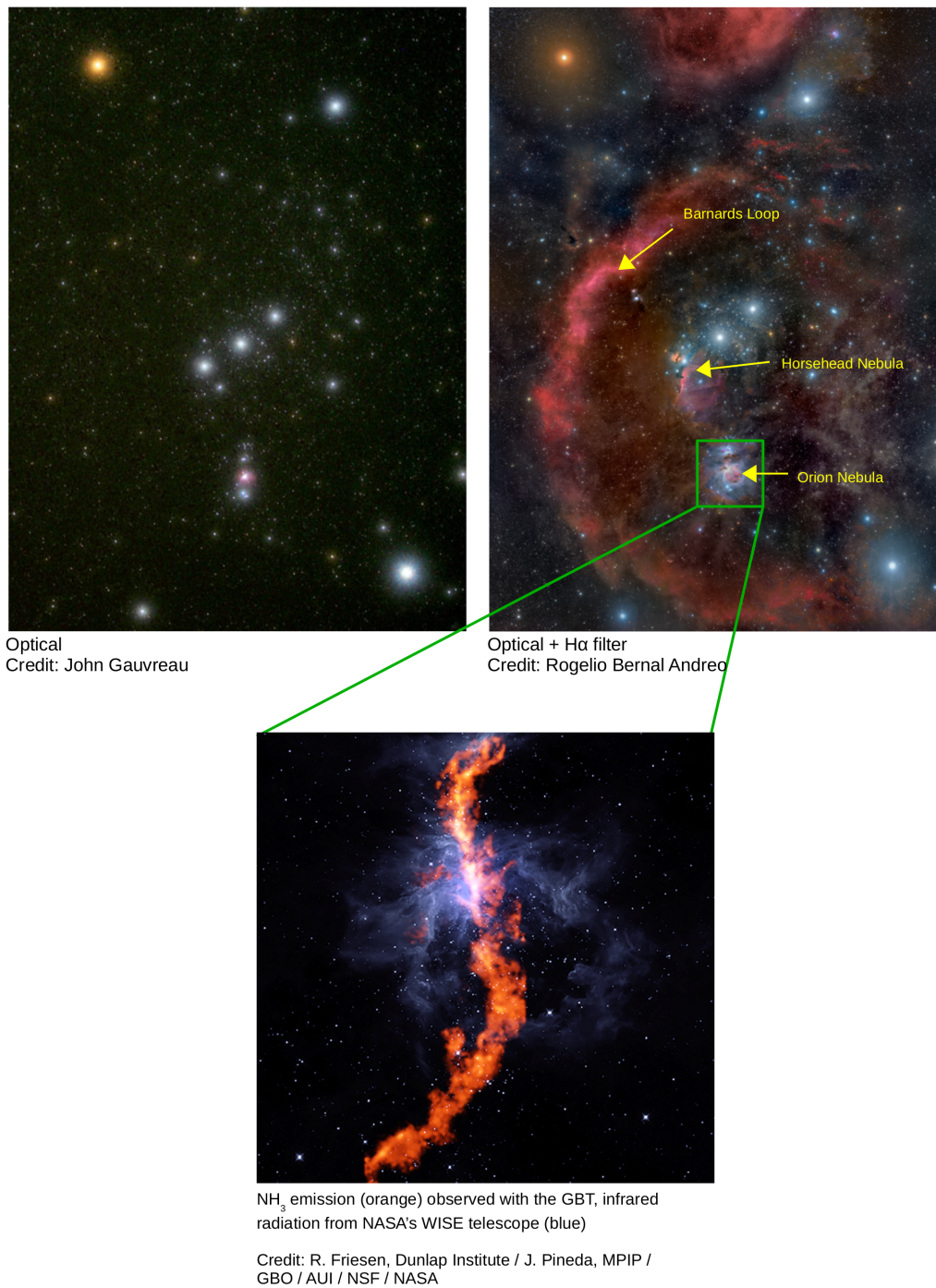
**Figure 1.8:** Constellation of Orion as seen in optical light (*top left*), and with an added H$_\alpha$ filter to enhance radiation from hydrogen at $\sim 656$ nm (*top right*). In the first image, only the Orion Nebula can be seen as a fuzzy reddish speck besides different stars. The visible hydrogen emission in the second image emphasises that the space between these stars is not empty, but filled with gas spanning large distances to form continuous clouds. Very prominent is the arc of Barnard's Loop, but also the Horsehead (belonging to Orion B) and the Orion Nebula (belonging to Orion A). The bottom false colour image shows a zoom on the Orion Nebula and its direct environment in emission of dust (blue) and ammonia (orange). The shape of the high density gas traced by ammonia emission is reminiscent of an integral shape $\int$ and gives this structure its name.
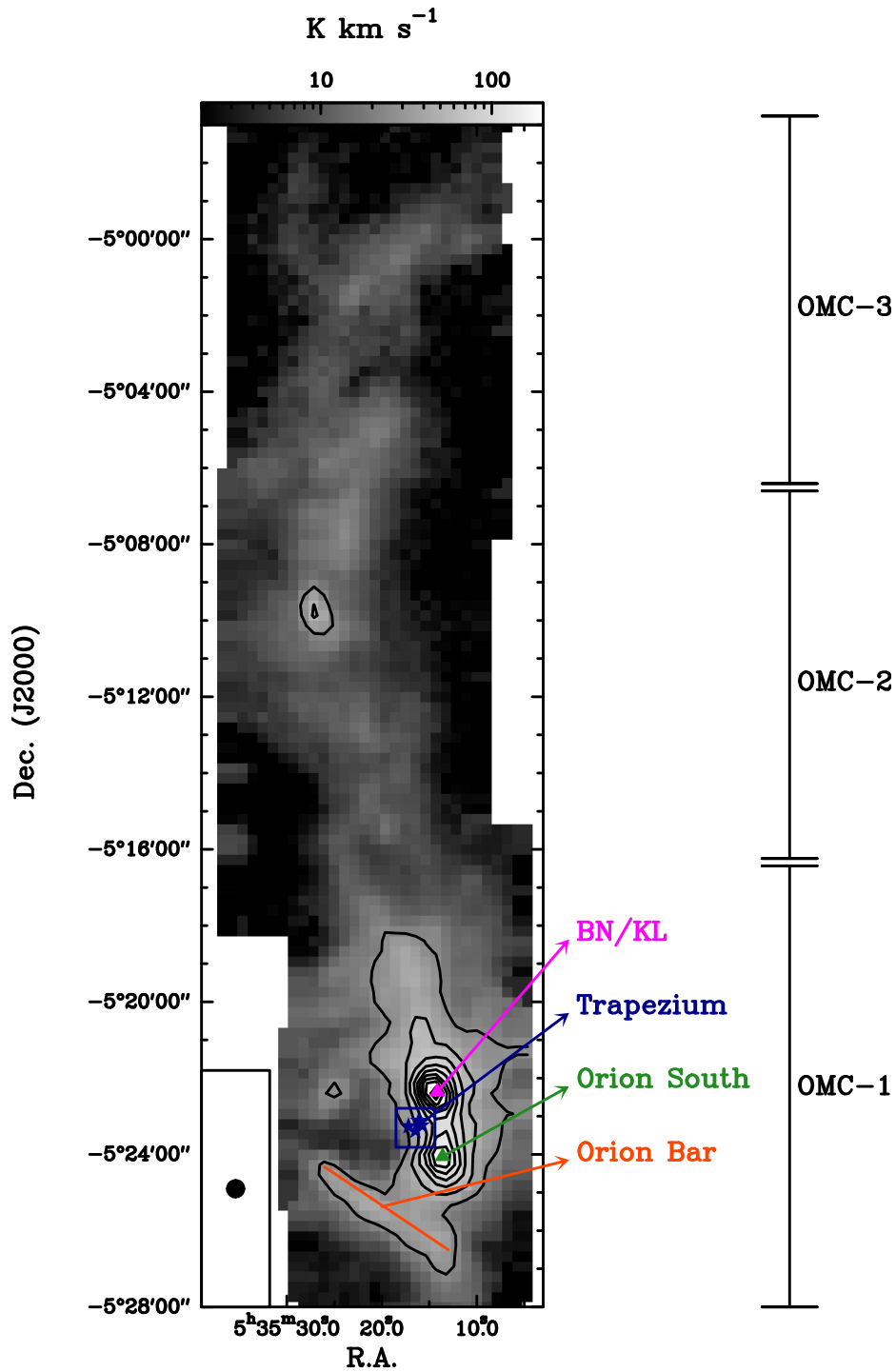
**Figure 1.9:** Integrated [5, 15] km s$^{-1}$ intensity map of HCO$^+$ emission from the northern part of Orion A, obtained with our PI230 data. The historically established subregions OMC-1, OMC-2 and OMC-3 are marked on the sides. The positions of the star forming regions BN/KL, 'Trapezium', Orion South and the PDR Orion Bar are highlighted in colours and will be further discussed in Section 1.4.1. The 'Trapezium' cluster is not obscured by the molecular cloud but is located in front of it. Its bight stars emit the majority of their energy in UV radiation (10 − 400 nm), such that the cluster is not visible in the depicted mm-emission.

### Explosive outflow

There is evidence that the BN/KL region experienced a violent energetic event $\sim 500 - 1000$ years ago, which is the source of a major explosive outflow (Pagani et al. 2019 and references therein). This event may have been triggered by a catastrophic gravitational encounter between stars in BN/KL (see also e.g. O'Dell et al. 2008 and references therein), during which the stars were ejected. The kinetic energy of these runaway stars is comparable to the observed energy of the outflow (Kwan & Scoville 1976; Gómez et al. 2005), evidence of a link between the two events. Observationally, the outflow manifests itself in the broad line wings seen in the emission of species like CO or HCN, which may span $\sim 200$ km s$^{-1}$, compared to $< 10$ km s$^{-1}$ for most of the molecular cloud.

### H II region

The massive system $\theta^1$ Orionis C is the main ionising source of the region and has significant impact on its surrounding material. The spectral class O7 of its main component means that the hot star with $3.6 \times 10^4$ K emits most of its radiation in the UV regime. Photons with energies $> 13.6$ eV can ionise neutral hydrogen (H I $\rightarrow$ H II), such that the environment of the star is composed mainly of H II and free electrons. In the case of Orion, this region is around 0.5 pc in size (Tielens 2005, p. 2). Species like oxygen, nitrogen or other trace elements may also be ionised, the spatial extent of their ionised layer larger than that of hydrogen (see also Fig. 1.10). The recombination of an ion with a free electron gives rise to bright recombination lines, which may lie in the visible or radio frequency regime. In case the particles do not recombine, their encounters create free-free emission in the radio regime. Dust, emitting absorbed UV radiation back in IR, constitutes another source of radiation.
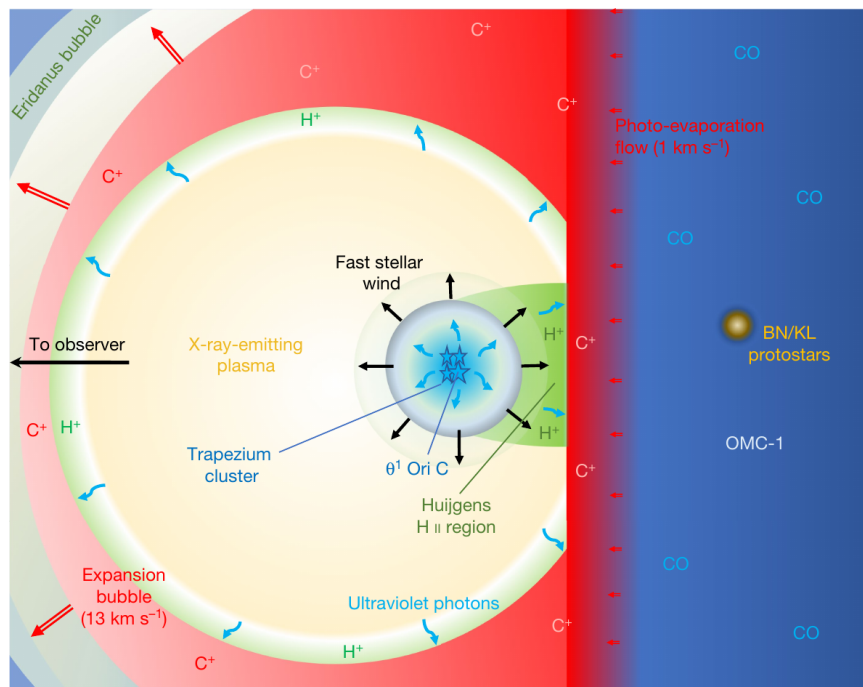


**Figure 1.10:** Sketch of the Trapezium cluster (with the massive star $\theta^1$ Orionis C) and its direct environment, illustrating the general geometry of the region: the cluster being at the outer edge of the dense molecular cloud, expanding towards the observer. Credit: Pabst et al. 2019.

**Photon-dominated regions: the Orion Bar**

The intensity of the photons in an H II region decreases with the distance to the ionisation source, as more and more are absorbed along the way. At one point the probability of H II to recombine into H I will be larger than the opposing ionising reaction, such that atomic and molecular hydrogen become more abundant again. The transition layer from ionised to atomic/molecular hydrogen is called a photon-dominated region (PDR). Photons with energies $< 13.6$ eV, which cannot be absorbed by hydrogen, can still ionise species with lower ionisation energies like carbon or molecules (Tielens 2005, p. 5, 317). Physical and chemical processes are thus still dominated by the energetic input from $\theta^1$ Orionis C, but hydrogen is neutral. The geometry of the H II region in Orion causes its associated PDR to be seen nearly edge-on for an observer from Earth, giving it a bar-like shape. As one thus sees emission 'added up' along the line-of-sight, the Orion Bar appears as a bright object in both line and dust emission.

### 1.4.2 OMC-2 and OMC-3

The environment of OMC-2/3 is very different from OMC-1, as there is no high-mass star formation but $> 300$ lower-mass Class 0/Class I protostars (Chini et al. 1997; Lis et al. 1998; Johnstone & Bally 1999; Furlan et al. 2016), several Class II and Class III pre-main sequence stars and a number of brown dwarfs (Peterson & Megeath 2008). As reviewed in Peterson & Megeath (2008), it is not clear whether or not the stars in OMC-2/3 and OMC-1 are part of the same cluster, of which the 'Trapezium' marks the centre. While Hillenbrand & Hartmann (1998) argue for a total cluster radius of 2.06 pc (partially including OMC-2), Carpenter (2000) proposes 3.86 pc (fully including OMC-2/3). It is also unclear if the differing $J$-band magnitudes between the sources in OMC-2 and those of OMC-3 (higher vs. lower) are caused by different stellar masses or if they are a consequence of different stellar ages (Peterson & Megeath 2008 and references therein).
Stars in both regions drive outflows which are observable through their optical, infrared and millimetre emission.

## 1.5 Aims and outline of this dissertation project

Molecular clouds harbour all star formation. Understanding the physical and chemical conditions within them is a prerequisite to a deeper comprehension of the earliest stages of star and planet formation. The gradual enrichment of the ISM with heavier elements and more complex molecules will influence subsequent generations of stars, their planetary systems and their host galaxy as a whole.

Until recently, all observations of molecular clouds were biased in that they were restricted in either frequency or spatial coverage. These constraints, due to instrumentation limits, have been overcome with new wide bandwidth receivers. This new generation of instruments has not only a large frequency coverage but is also sensitive enough to map large sources on reasonable timescales. Our selected source Orion A is the closest region of low- to high-mass star formation, presenting a unique laboratory for investigations of physical and chemical conditions over a large range of environments. However, a full description of molecular clouds demands the examination of large numbers, both in the Milky Way and other galaxies. The interpretation of such observations from distant objects is challenging, as different environments cannot be spatially resolved and their signatures may be diluted by larger scale emission. For extragalactic observations, the resolution is

currently at best $\sim 10$ pc, well above the dimensions of individual star forming clumps and cores.

This thesis aims to help with the interpretation of other observations but also wants to give more insights into the conditions within Orion A itself. After giving an overview of the observations and data reduction in Chapter 2, the following Chapter 3 will report our results on the larger scale emission in Orion A. By dividing the source into distinct regions based on e.g. column density or temperature, we examine the resulting spectra and create 'templates' of these environments. These templates may aid with interpretations of distant objects, as we can gauge what characteristic emission features persist on large scales, and what features may be strongly diluted. The next chapters will focus on specific aspects of Orion A. Chapter 4 reports on the emission of $CF^+$ and how its unexpected detection in some regions may be explained. Chapter 5 centres on a particular region in OMC-1 and tries to answer if it is indeed a distinct entity, or just part of the general molecular material with no special characteristics. The conclusions will be presented in Chapter 6, together with a perspective on future projects.

# Observations, calibration and data reduction



**Figure 2.1:** The APEX telescope on Llano de Chajnantor. Image taken from www.apex-telescope.org .

All observations for this thesis were conducted with the APEX 12 m telescope (Güsten et al. 2006) depicted in Fig. 2.1, located at an altitude of 5105 m on Llano de Chajnantor in Chile. Data were primarily taken with the PI230 receiver operating in the 1.3 mm atmospheric window, which forms the basis for the analyses in Chapter 3 and 4. For Chapters 4 and 5, we supplement the 1.3 mm data with higher frequency observations using LASMA in the 0.8 mm window. A short description of observations and data reduction will be given in the respective chapters. Here we want to give an overview over all observations and explain the calibration and data reduction process in more detail. As the PI230 data used for this project was in large parts obtained during the early commissioning phase of the receiver, it needed more extensive corrections. Section 2.2 summarizes the observations, Section 2.3.1 explains the efficiency corrections, Sections 2.3.2 and 2.3.4 describe the encountered defects and Section 2.4 illustrates the data reduction process accounting for all these elements.

## 2.1 APEX and the new PI230 receiver

The PI230 receiver employs eight FFTS backends, each providing 4 GHz of bandwidth for a total coverage of 32 GHz with an IF range of $4 - 12$ GHz (see Klein et al. (2012) for details on the previous FFTS generation). LSB and USB (lower and upper sideband) are separated and recorded using 2SB mixers. The splitting into polarisations and a 0.2 GHz overlap between two backends per sideband result in an actual frequency coverage of $2 \times 7.8$ GHz. An example of a spectrum is given Fig. 2.2. The high number of frequency channels (65536 per backend) facilitates a frequency resolution of 61 kHz or corresponding velocity resolution of $0.07 - 0.09$ km s$^{-1}$.

### System and receiver temperatures

Data for our maps were taken between October 2015 and November 2018. The mean and median system temperature averaged over all these observations are $T_{\mathrm{sys}}^{\mathrm{mean}} \approx 266$ K and $T_{\mathrm{sys}}^{\mathrm{median}} \approx 239$ K
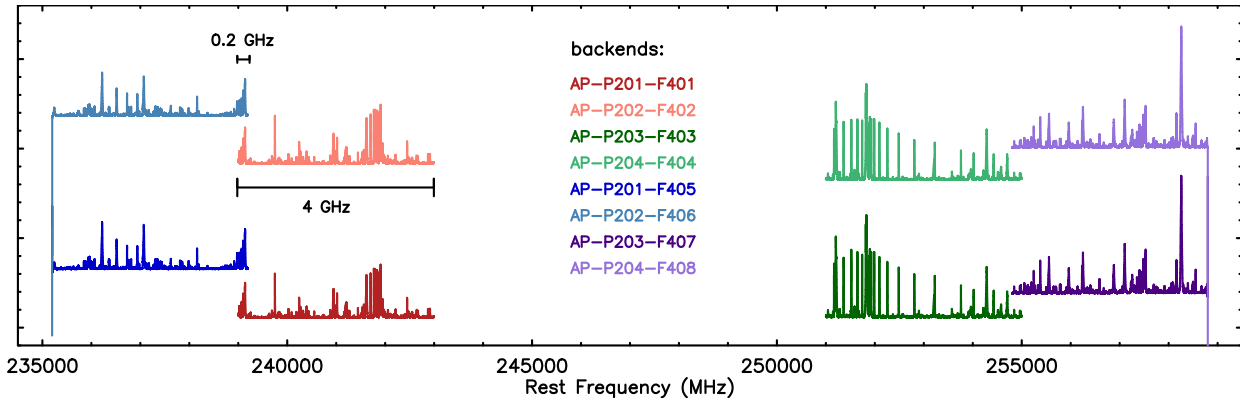
**Figure 2.2:** Example of a single observation taken with PI230, using the frequency set-up 241 GHz LSB observed in November 2018: The coloured spectra each belong to one of the eight backends. The receiver accounts for different polarisation (hence the double coverage of the frequencies) and offers $2 \times 7.8$ GHz in total, owed to the 0.2 GHz overlap between neighbouring backends. Numerous spectral lines are clearly visible and the only obvious defects are the high intensity spikes at the outer edges of the spectrum.

respectively. The spread is quite large however, with a minimal value of $\approx 125$ K and maximum value of $\approx 597$ K. The median value for all backends and frequency settings is shown in Fig. 2.3, including the minimal and maximum recorded value. The main influence on $T_{\text{sys}}$ is typically the water vapour in the atmosphere but can also be increased in case of hardware issues. High values of $T_{\text{sys}}$ are in our case likely associated with temporary misalignments and/or degradation of the subreflector in the first observing period and again in mid 2017. For the Uranus pointings of these times, we find that the beam width appears different in azimuth and elevation (see Fig. 2.4), marking it as distorted (elliptical), which is an effect of optical misalignments. The telescope may thus have picked up radiation not only from the sky, but also from its direct environment. This additional (warm) component is interpreted by the software as coming from high amounts of water in the atmosphere, from which the atmospheric opacity is retrieved[1]. This calculated high opacity is then producing high system temperatures.

The mean and median receiver temperatures over all observations are $T_{\text{rec}}^{\text{mean}} \approx 81$ K and $T_{\text{rec}}^{\text{median}} \approx 78$ K, respectively. The associated histogram (Fig. 2.5) shows some high temperature outliers, but an overall Gaussian distribution. The outliers are a consequence of some high intensity artifacts (see also Section 2.3.2) seen in spectra from earlier observations. By default, 4% of the channels are cut off at the very edge of each band to avoid including the spikes seen in Fig. 2.2. $T_{\text{rec}}$ for a given spectrum is calculated by averaging the individual $T_{\text{rec}}$ of the remaining 92% of channels. If there are enough extreme artifacts further towards the middle of the band, this averaged value may be significantly influenced by them.

During the course of three years, hardware changes to both instrumentation and the telescope dish itself improved the performance of the PI230 significantly. After being identified as the main source of the encountered artifacts, faulty FFTS backend units were exchanged, distinctly improving later observations and preventing very high system and receiver temperatures from occurring again. APEX was undergoing major refurbishment during the shutdown phase between the end of 2017 and early 2018. A new subreflector was installed and the main dish equipped with new panels. Comparison data obtained with this new set-up validates the older observations for this project

---

[1]APEX Calibration and Data Reduction Manual, p. 9 :
http://www.apex-telescope.org/documents/public/APEX-MPI-MAN-0012.pdf
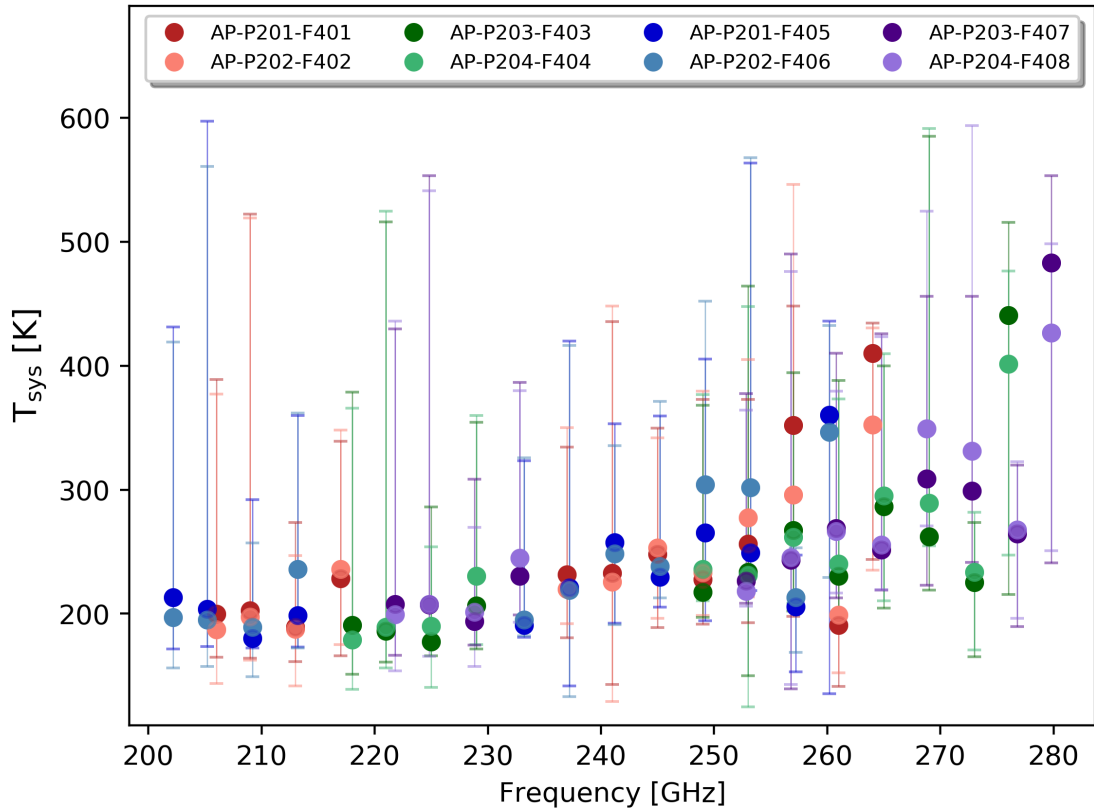
**Figure 2.3:** $T_{\mathrm{sys}}$ as a function of frequency. The data points refer to the median value for every backend in every frequency set-up (same colour code as Fig. 2.2), while the bars indicate the respective extrema.

within the assumed uncertainties (see also Chapter 3).

## 2.2 Observations

For all three receivers, the vast majority of data for this project consists of *on-the-fly* maps. In this observation mode, the telescope continuously moves across the sky, tracing along grid lines of the source region. In short time intervals $t_{\mathrm{dump}}$, the data is read out (or 'dumped'). The speed of the telescope, the distance between grid lines and $t_{\mathrm{dump}}$ depend on the needed integration time (determined by the intensity of the source) and the observed frequency. For the PI230 maps, we used $t_{\mathrm{dump}} = 0.3$ s for every $8''$ step of the maps, while LASMA data employed $t_{\mathrm{dump}} = 0.2$ s and $5''$ steps. The smaller steps for the higher frequency observations account for the smaller beam sizes. For each receiver, several frequency set-ups were needed to obtain the coverage of the respective atmospheric window.

In addition to the maps, pointed observations for selected sources were added with both PI230 and LASMA (see Chapter 4), as well as planet observations used for efficiency calibrations (Section 2.3.1). Exact observation scripts are found in the respective project folders (M-096.F-0021-2015, M-098.F-0007-2016, and M-099.F-9509A-2017).
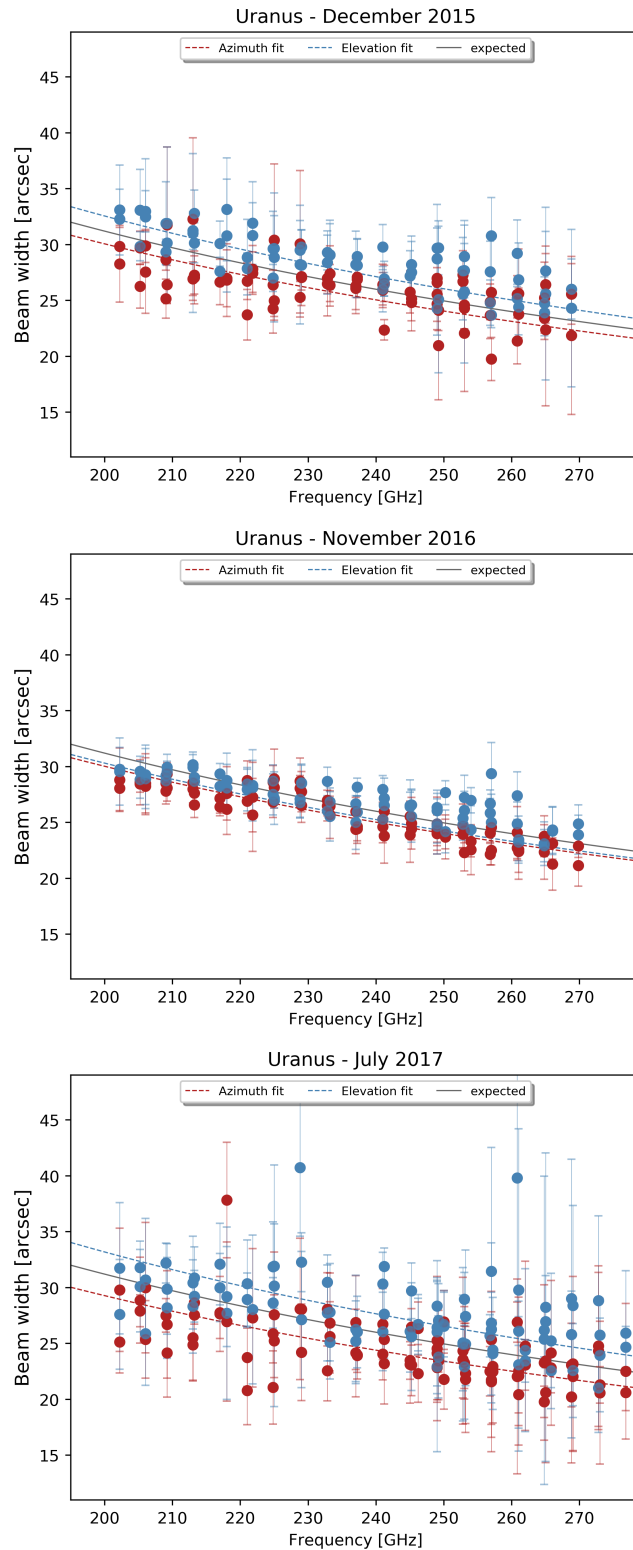
**Figure 2.4:** Beam widths from Uranus pointings in 2015, 2016 and 2017. A notable difference between azimuth and elevation is found in 2015 and 2017, hinting that the beam may have been elliptical, not spherical. The varying errorbars are a consequence of inferior signal-to-noise ratios in the 2015 and 2017 data compared to 2016.
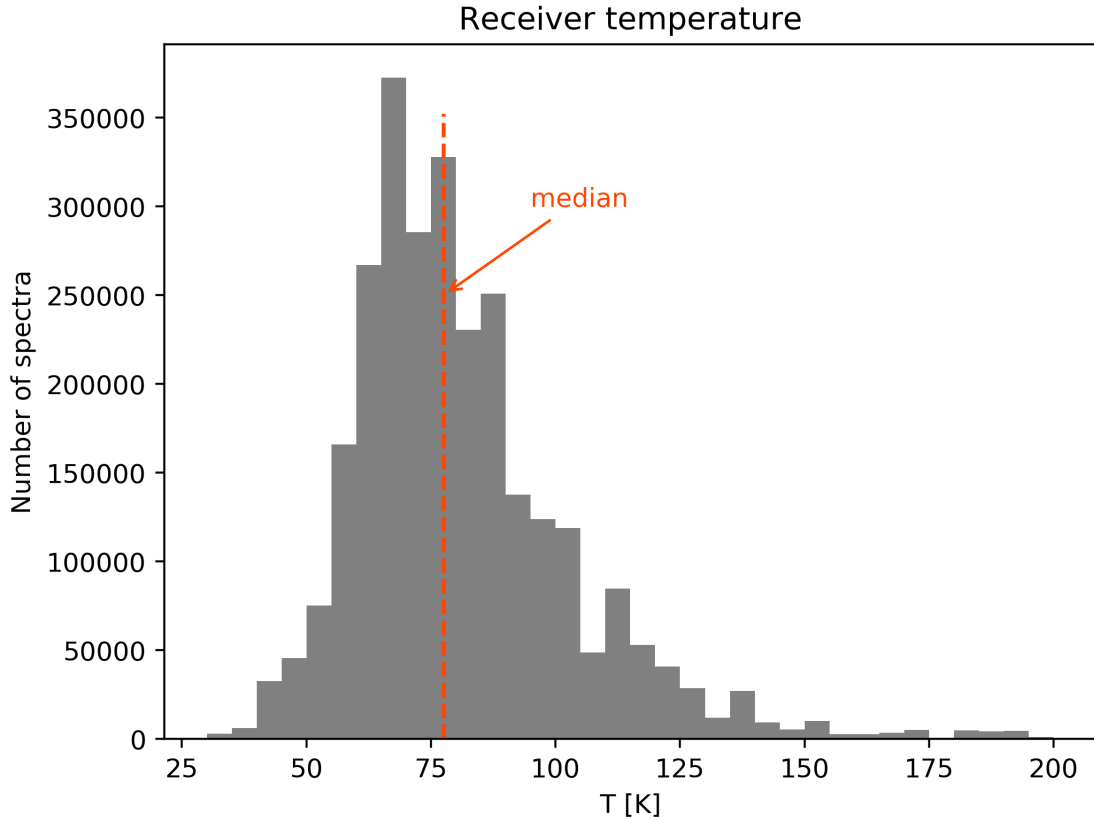
**Figure 2.5:** Histogram of $T_{rec}$ over all observations ($\sim 2.8 \times 10^6$ spectra).

## 2.3 PI230 corrections

The PI230 data were taken over a time span of more than three years. As changes to the hardware of PI230 continued during that time span, defects like spurious lines or artifacts arose and disappeared. Some changes (especially concerning the subreflector) also affected the main beam efficiencies. For each observing period, defects needed to be identified and corrections for the changing efficiencies applied. This ensures that the observed line intensities are consistent with each other, such that the final data set is homogeneous. The pure integration time on source, without any overheads, was around 37 h in total, in which $\sim 2.8$ million individual spectra were taken.

### 2.3.1 Main beam efficiencies

Continuum observations of planets offer an opportunity to obtain beam efficiencies, as the emission of a planet is usually stable and well described. In contrast to line observations on point sources (e.g. the CO line of a suitable star), continuum observations enable us to get the beam efficiencies over the whole frequency range, giving a better impression of the receiver performance.

We used Uranus and Jupiter to calibrate our data, both of which can provide slightly different insights: Uranus is smaller than the typical beam size ($\lesssim 4''$ vs. $22'' - 31''$), while Jupiter fills the beam ($\gtrsim 30''$). One might thus prefer to use Uranus derived efficiencies for compact and Jupiter data for extended sources. The observed peak intensities of the planet were compared to theoretical

values from the ASTRO[2] software package. In accordance with procedures at APEX, only the azimuth value was used. Together with the forward efficiency (taken as a fixed value of 0.95), this yields the main beam efficiency $\eta_{\mathrm{mb}}$ as a function of frequency. This relationship is described by the *Ruze* formula:

$$\eta_{\mathrm{mb}} = \eta_{\mathrm{mb}}^0 \exp\left(-\left(\frac{4\pi\sigma}{\mathrm{c}/\nu}\right)^2\right),\tag{2.1}$$

where $\sigma$ denotes the surface accuracy of the dish and $\nu$ the frequency. The Ruze formula is fitted to our planet observations as exemplarily shown in Fig. 2.6, yielding $\eta_{\mathrm{mb}}^0$. The exact value of the surface accuracy $\sigma$ has only a marginal impact for the 1.3 mm window, its value of 30 $\mu$m determined with holography measurements (not done in this thesis, the value was supplied). The observational data of our source is then corrected with the values of $\eta_{\mathrm{mb}}^0$ and $\sigma$, such that each frequency is corrected individually. The Uranus observations and data analysis were completely part of our project, while some of the Jupiter data was supplemented by others. Some results were also supplied by APEX staff (especially for 2018). The $\eta_{\mathrm{mb}}^0$ values for all observing periods are listed in Table 2.1. As our source is mainly characterised by extended emission, we decided to employ the Jupiter derived efficiencies.

**Table 2.1:** Main beam efficiencies for the different observing periods obtained from Uranus and Jupiter continuum pointings. All maps for this project were finished in November 2018. Between May and December 2019, additional pointed observations (see Chapter 4) were conducted.

| observing period | Uranus $\eta_{\mathrm{mb}}^0$ | Jupiter $\eta_{\mathrm{mb}}^0$ |
|---|---|---|
| 2015 - June 2016 | 0.53 | $0.62 - 0.66$ |
| July 2016 - End of 2016 | 0.77 | 0.73 |
| early 2017 (February - April/May) | - | 0.74 |
| end of June/July 2017 | 0.67 | 0.66 |
| May 2018 - July 2018 | - | 0.73 |
| November 2018 | - | 0.75 |
| May - August 2019 | - | 0.78 |

### 2.3.2 Removing spurious features

Data was affected by spikes, artifacts, and spurious lines to various degrees in the different observing periods. Early data needed the most corrections, while resolved hardware issues considerably improved later data. Whereas single channel spikes are not problematic, the multi-channel artifacts and spurious lines were more challenging to identify and remove. The artifacts presented themselves as defects with characteristic shapes but varying amplitude (a typical pattern of artifacts is shown in Fig. 2.7). For a given backend and observation period, they often appeared in the same channels, depending only weakly on the observed frequency. They showed continuous behaviour

---

[2]http://www.iram.fr/IRAMFR/GILDAS
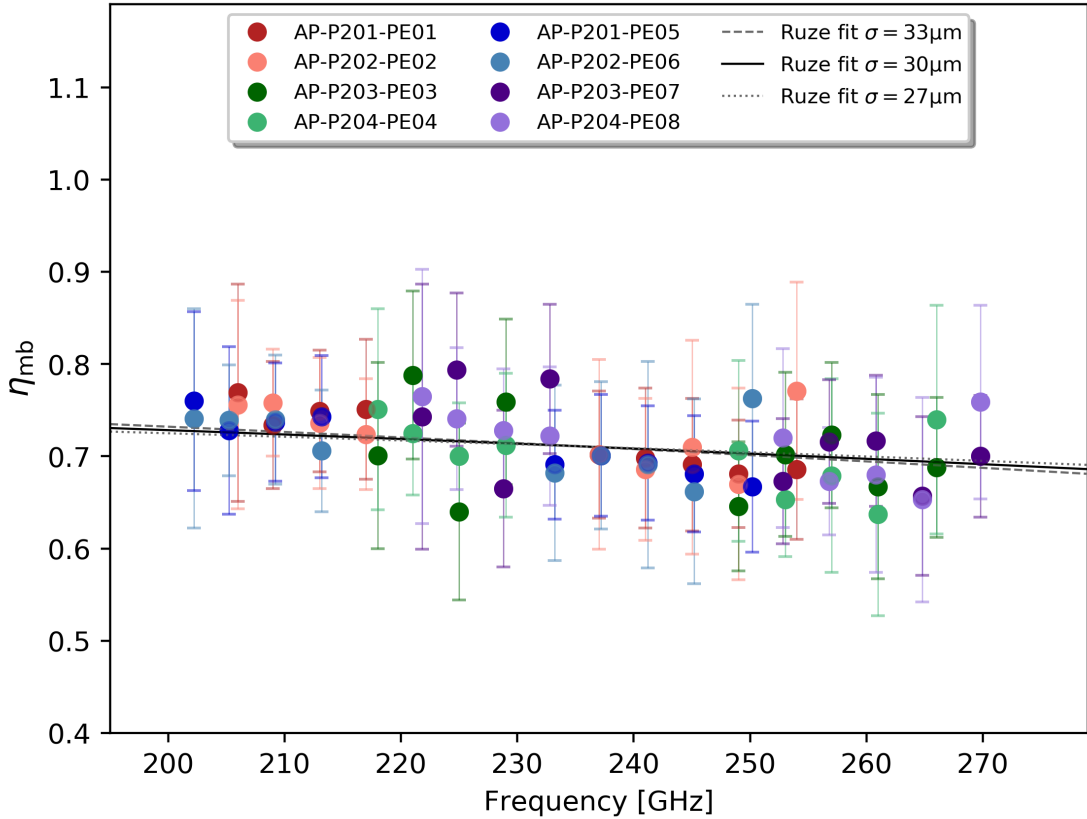
**Figure 2.6:** Main beam efficiency as a function of frequency for Uranus data from November 2016. The different colours again mark the different backends of the PI230 receiver, while the lines show fits for varying values of the telescopes surface accuracy $\sigma$. The marginal difference between the three fits shows that the value of $\sigma$ is not of great importance in the 1.3 mm window. Over the observed frequency range, $\eta_{\mathrm{mb}}$ varies roughly between $68 - 73\%$.

towards their edges and were therefore much harder to distinguish from unaffected channels in the spectrum. Sometimes the artifacts would overlap with actual spectral lines and alter their shape. Artifacts with small amplitude were only visible when the noise level was reduced due to the averaging of several spectra. To remove the artifacts, we checked multiple spectra for each backend and each frequency setting for the different observing periods separately, identified the affected channels manually and blanked them. This was the most time consuming part in this thesis and demanded several iterations before the defects could be reliably removed without taking away too many unaffected channels.

The spurious lines had several origins: Some easily identified lines from the image band and several lines originating from the local oscillator. Additionally, a few lines with no straightforward explanation were present. To identify and remove these lines, we did a first assignment of all observed lines to molecular transitions from the JPL[3] (Pickett et al. 1998) and CDMS[4] (Endres et al. 2016) molecular spectroscopy data bases using the WEEDS (Maret et al. 2011) extension of GILDAS. If a line could not be identified, we checked if it was present in all relevant backends and frequency settings. The respective channels in the originating backends were blanked if the line

---

[3]http://www.spec.jpl.nasa.gov/
[4]http://www.astro.uni-koeln.de/cdms/

only appeared in some instances.

### 2.3.3 Sideband rejection

Although hardware filters are employed to reject unwanted signals from the other sideband, strong lines may still leave spurious features. The quality of the sideband rejection was assessed by examining the five typically strongest lines (CO, $^{13}$CO, CS, HCN and HCO$^+$) and their imprints in the image band. A line may be covered in different frequency set-ups and the sideband rejection was calculated for all of these. This examination was done with our data before any intensity corrections and especially before gridding (see also Fig. 2.9), hence the peak temperatures between frequency set-ups may differ. As we averaged over the different polarisations in our later analysis, we also did so for the values compiled in Table 2.2. A sideband rejection of around $-20$ dB is achieved on average.

**Table 2.2:** Sideband rejection of five luminous lines, based on spectra averaged over all project observations from 2015 to 2018 and smoothed to a resultion of 0.4 km s$^{-1}$. Refer to Fig. 2.2 for the backend names.

| line | covered with set-up(s) | signal backends | $T_{\mathrm{peak}}$ [K] | rms [K] | image backends | $T_{\mathrm{peak}}$ [K] | rms [K] | sideband re-rejection [dB] |
|---|---|---|---|---|---|---|---|---|
| CO | 217 GHz LSB | 403/404 | 29.538 | 0.160 | 401/402 | 0.208 | 0.006 | $-(21.52^{+0.14}_{-0.14})$ |
| $^{13}$CO | 206 GHz LSB | 407/408 | 9.025 | 0.011 | 405/406 | 0.088 | 0.004 | $-(20.10^{+0.22}_{-0.21})$ |
| | 209 GHz LSB | 403/404 | 9.325 | 0.011 | 401/402 | 0.092 | 0.005 | $-(20.08^{+0.25}_{-0.23})$ |
| CS | 245 GHz LSB | 401/402 | 1.728 | 0.029 | 403/404 | 0.030 | 0.005 | $-(17.59^{+0.79}_{-0.69})$ |
| | 249 GHz LSB | 405/406 | 1.724 | 0.033 | 407/408 | 0.041 | 0.004 | $-(16.20^{+0.51}_{-0.47})$ |
| HCN | 249 GHz LSB | 407/408 | 2.080 | 0.052 | 405/406 | 0.004 | 0.004 | $< -23.70$ [(*)] |
| | 253 GHz LSB | 403/404 | 1.619 | 0.038 | 401/402 | 0.019 | 0.005 | $-(19.37^{+1.44}_{-1.12})$ |
| | 264 GHz LSB | 401/402 | 1.395 | 0.034 | 403/404 | 0.034 | 0.005 | $-(16.16^{+0.87}_{-0.76})$ |
| HCO$^+$ | 253 GHz LSB | 407/408 | 2.337 | 0.032 | 405/406 | 0.040 | 0.005 | $-(17.71^{+0.77}_{-0.67})$ |
| | 257 GHz LSB | 403/404 | 2.757 | 0.044 | 401/402 | 0.026 | 0.007 | $-(20.28^{+1.37}_{-1.07})$ |

**Notes.** [(*)] No image line detected, the value is based on the rms noise levels.

As the number of signal and image lines is limited, a breakdown of the differences between backend groups is not conclusive. That said, inferior rejections seem to be associated with images in the upper side band (backend groups 403/404 and 407/408). When considering all eight backends separately and not averaging over the different polarisations (e.g. comparing backend 401 with 402), we encountered differences of 2.5 to 9.0 dB.

Assuming an average rejection of $-20$ dB (or an image line with 1% intensity of the signal line) and knowing the rms noise levels of our data products, we can estimate what lines could produce spurious features: to produce a $5\sigma$ feature in a spectrum with e.g. an rms noise level of 20 mK, one needs a signal line of 10 K. In our data, these intensities are typically only achieved for a very
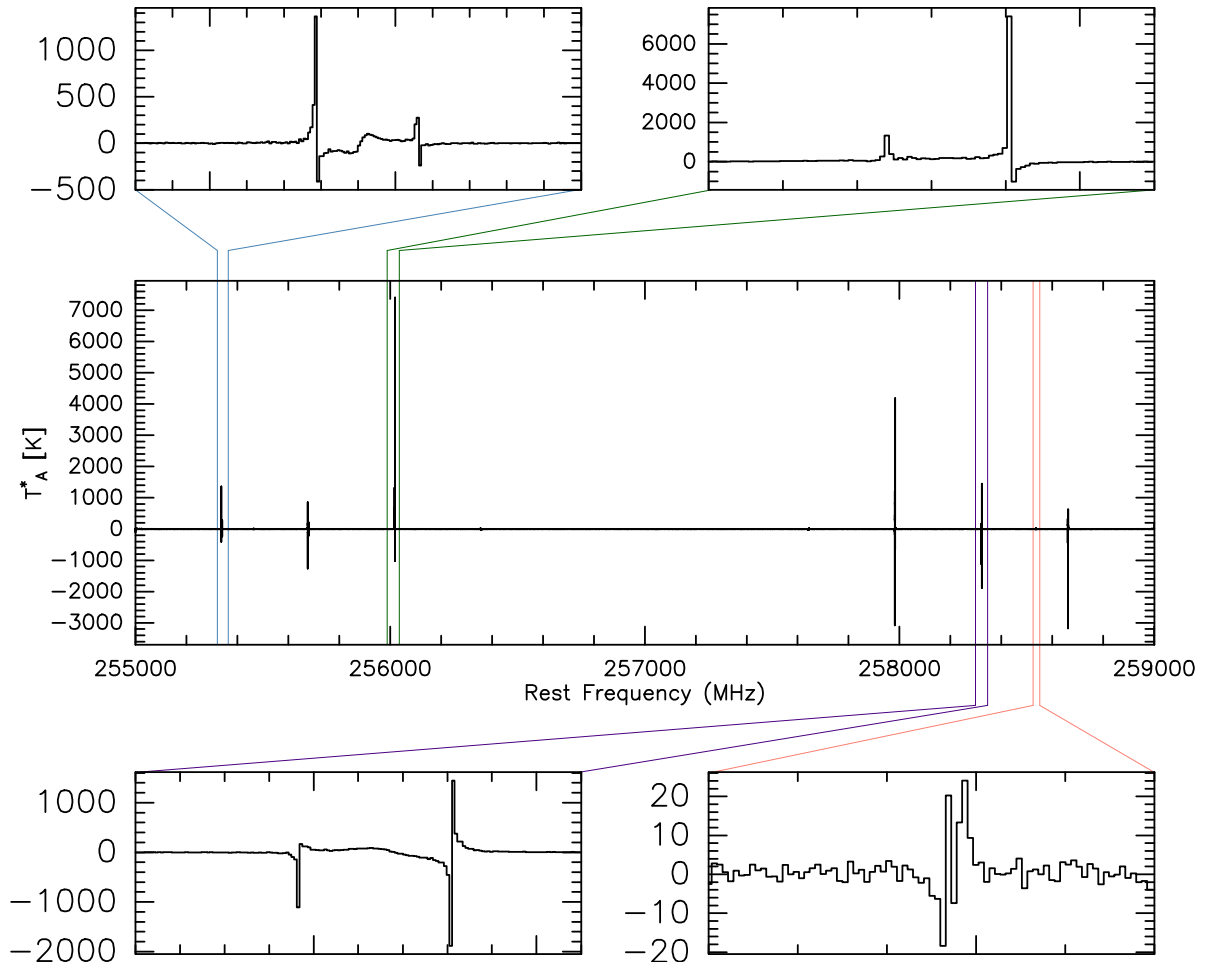
**Figure 2.7:** Typical pattern and shapes of artifacts, here from backend AP-P201-F401 in the frequency set-up 257 GHz LSB from November 18th 2016. Six high intensity spikes dominate the spectrum, with peak temperatures around three orders of magnitude above actual lines from the observed source. They are spaced in regular intervals and form two main groups. Their shapes are similar (see zoom ins) and hard to pick up in automated procedures, as their flanks can be quite smooth. Additionally, we find other such groups on smaller temperature scales (see lower right zoom in). The only way to reliably identify these features and their actual extent is to manually inspect a representative number of spectra, preferably from positions with little line emission.

limited number of lines.

Deviations from this overall good sideband rejection, including larger differences between polarisations, are seen in data collected in 2019 for our pointed observations discussed in Chapter 4. In individual cases, we encountered sideband rejections of only $-8$ dB[5] to $-10$ dB[6]. As we only examine specific transitions for these 2019 observations and the sources are not line rich, our analysis is not compromised and no further examination was performed.

### 2.3.4   Baselines
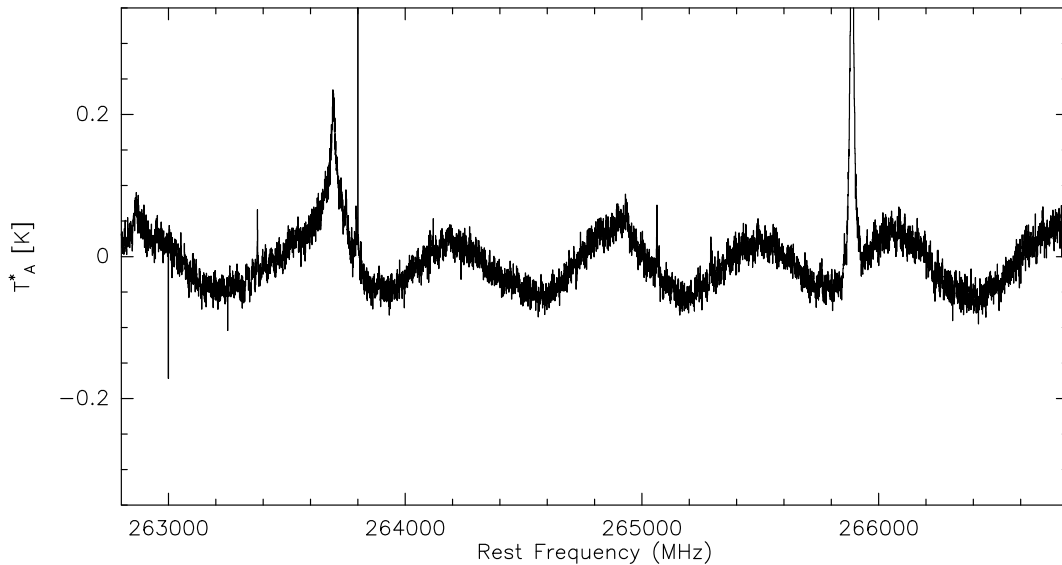


**Figure 2.8:** Early observations sometimes showed sinusoidal baselines. Depending on their amplitude, they were often noticeable when averaging over a larger number of spectra. The depicted spectrum is averaged over all observations with backend AP-P204-F408 in set-up 249 GHz LSB from October 16th 2015

Especially in data obtained during early observations, some spectra showed sinusoidal baseline shapes, as exemplarily shown in Fig. 2.8. The option of subtracting a corresponding sinusoidal proved unsatisfactory for larger quantities of spectra like in maps, as the subtracted sinusoid was very sensitive to given input parameters and could not be used on successive spectra. A high-order polynomial was therefore used instead. This could both compensate the sinusoidal baseline and handle fairly flat baselines at the same time.

## 2.4   Data reduction

As the PI230 data was obtained over a longer period of time, we need to correct data from different observing periods individually, before combining them for further processing. Some defects like artifacts and spikes were not only dependent on backend and frequency, but likewise on observing period (possibly correlated with hardware changes to the receiver). To account for all these characteristics, each backend is treated separately for each of the frequency set-ups (8 backends $\times$ 12

---

[5]Observations of the source HOPS 96 on the 27th of July 2019: An $H_2CO$ line at $\sim 225.698$ GHz with a peak temperature of around 1.35 K produces an image line of 0.2 K in backend 405.

[6]Source FIR4 on the 23th of May 2019, the same $H_2CO$ line and likewise affecting backend 405.

frequency set-ups = 96 elements). An overview of the procedure is given in the flowchart in Fig. 2.9. Once the data is corrected and processed like this, we can easily extract both maps and spectra, which in turn form the basis for further analyses.
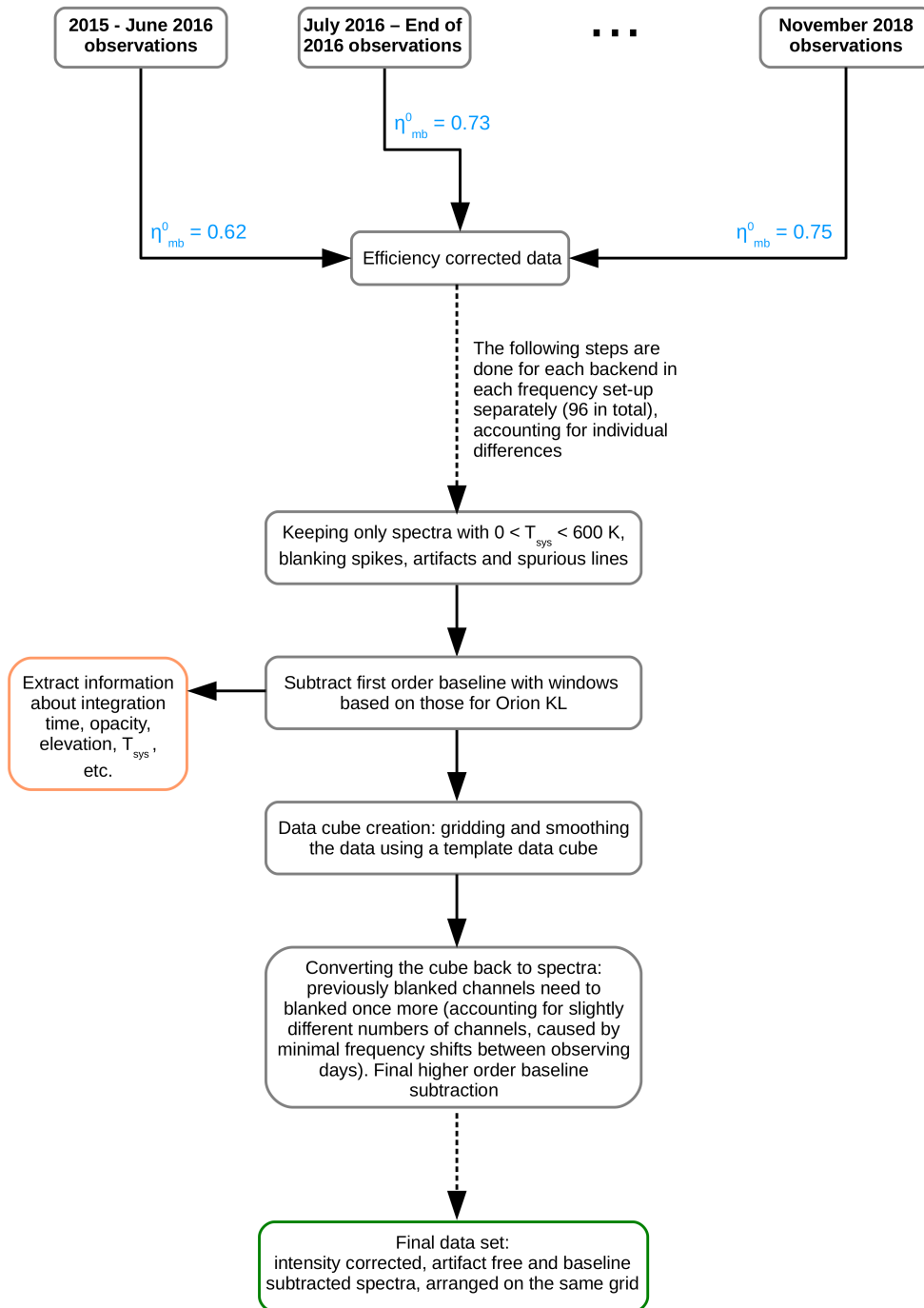
**Figure 2.9:** Process of data reduction for the PI230 receiver: data from different observing periods was corrected with individual main beam efficiencies. For each backend and frequency set-up, low quality spectra were rejected and defects removed for the remaining. Then a first order baseline with windows based on the line dense region Orion KL was subtracted. As a lot of meta data is lost in the following gridding process, relevant information is first extracted from each spectrum. After gridding, the cube is converted back to single spectra and previously blanked channels may need to be blanked again (due to how the GILDAS software handles blanking values during the gridding process, and slight frequency shifts between observations). After following this procedure for the 96 backend/frequency set-up combinations, we have the final data set with which we will work.

# An imaging line survey of OMC-1 to OMC-3

We used the PI230 data set described in the previous Chapter to analyse the emission of distinct regions within the northern part of Orion A over the whole 1.3 mm window and identified dominant molecular cooling lines and characteristic emission features. This not only furthers our understanding of the molecular cloud itself, but may also be used for the interpretation of distant, spatially unresolved sources, including extragalactic objects.

This chapter was originally published as a paper titled 'An imaging line survey of OMC-1 to OMC-3 – Averaged spectra of template regions' in *Astronomy & Astrophsics* (Brinkmann et al. 2020)[1]. Layout changes were made to adapt to the different print formats. The following sections are copied from the accepted paper after language editorial, as submitted to the publisher on March 15th 2020.

## 3.1 Introduction

The northern part of the Orion A molecular cloud is one of the most prominent regions of current low- to intermediate-mass star formation, whose close proximity of just $\sim 400$ pc (Menten et al. 2007; Kounkel 2017) enables us to spatially resolve its physically and chemically different regions. Continuum maps show substructures which divide Orion A into morphologically different regions: the bright OMC-1 in the south, with a group of filaments radiating away from its central region (O'Dell et al. 2008 and references therein, e.g. Wiseman & Ho 1998), and the less prominent OMC-2/3 in the north.

OMC-1 hosts star formation and is heavily influenced by intense UV radiation from the young massive Trapezium stars. In addition to the Trapezium, Orion BN/KL (hereafter KL) and Orion South are sites of recent of star formation (O'Dell et al. 2008). Their positions are indicated in Fig. 3.2. OMC-1 also includes an archetypical photon-dominated region (PDR), the Orion Bar, outflows, and the eponymous hot core (e.g. Masson et al. 1984) containing a rich chemistry of complex molecules, but also more quiescent gas around it. OMC-2 and OMC-3, located northwards of OMC-1, appear to be a continuation of the gas in OMC-1, apart from a shift in velocity (e.g. O'Dell et al. 2008; Peterson & Megeath 2008). A large number of pre-stellar Class 0 and Class I objects following the filamentary structure have been discovered through submillimetre observations (e.g. Chini et al. 1997; Johnstone & Bally 1999; Lis et al. 1998), in addition to a number of brown dwarfs (Peterson et al. 2008). In contrast to OMC-1, there are no massive O/B stars, resulting in very different conditions with outflows driven by young embedded stars (Peterson & Megeath 2008 and references therein, e.g. Yu et al. 1997), but without strong UV radiation.

Investigating the characteristics of these distinct regions helps us to understand how low- to high-mass star formation influences the surrounding material and vice versa. Previous line surveys

---

[1]Brinkmann, A&A, 636, A39, 2020, reproduced with permission ©ESO

could be biased in that they have often been focused on a single or few positions (e.g. Sutton et al. 1985; Blake et al. 1987; Tercero et al. 2010, 2011; Esplugues et al. 2013; Johnstone et al. 2003), or spatially extended regions were mapped in selected molecular lines only (e.g. Ungerechts et al. 1997), missing out on information a complete frequency coverage offers.

New opportunities arise with sensitive, wide-bandwidth receivers which combine an extensive frequency coverage with a mapping speed sufficient for large fields of view. This enables us now to obtain a comprehensive and unbiased picture of a molecular cloud. It facilitates the deduction of a variety of physical and chemical conditions using several molecular tracers. These possibilities start being utilised in lower frequency regimes (Pety et al. 2017 and companion papers, e.g. Gratier et al. 2017; Bron et al. 2018 focusing on Orion B or the LEGO project started with Kauffmann et al. 2017). Our data set described in Section 3.2 deals with higher energies, and is thus sensitive to higher critical densities and constitutes a useful complement to these observations.

This will help us to better understand the conditions (e.g. column density, temperature, strength of UV illumination) under which different molecules are excited, and in particular identify those molecules predominantly present in very specific environments (e.g. $N_2H^+$ in dense cores; see also Pety et al. 2017). This information is crucial for understanding emission of more distant molecular clouds, including extragalactic sources.

Although CO emission is dominant in the 1.3 mm window, its share of the total intensity (and thus cooling) changes for distinct regions (see also Goldsmith 2001). Comparing the influence of different molecular species to the cooling in Orion A under various conditions will help us to develop templates. These can be used to 'reproduce' spectra of other clouds when regions with different physical and chemical conditions are not resolved.

## 3.2   Observations and data reduction

### 3.2.1   Observations

All observations were carried out with the Atacama Pathfinder Experiment (APEX) 12 m submillimetre telescope (Güsten et al. 2006) using the PI230 receiver operating in the 1.3 mm atmospheric window. We covered the area of OMC-1 to OMC-3 from 200.2 to 281.8 GHz with data collected over several observing periods from October 2015 to November 2018.

The PI230 receiver offers 32 GHz bandwidth per tuning, apportioned into two sidebands and two polarisations, with the two polarisation mixers co-aligned on sky. Eight Fourier Transform Spectrometer (FFTS4G) backends each provide 65536 channels for 4 GHz. An overlap of 0.2 GHz between two backends results in 7.8 GHz coverage for each sideband and polarisation per tuning. The sideband rejection is $\approx 20$ dB. The width of the telescope beam changes from around $22''$ to $31''$ over the 1.3 mm window.

The overall spatial coverage of around $400'' \times 1900''$, corresponding to roughly $0.8 \times 3.8$ pc at the distance of the Orion Nebula Cluster, was achieved with on-the-fly maps scanned in the x- and y-directions in steps of $8''$ with a dump time of 0.3 seconds. The reference position was $\alpha_{2000} = 5^{\mathrm{h}}31^{\mathrm{m}}14.5^{\mathrm{s}}$, $\delta_{2000} = -5°52'29.0''$. The frequency coverage was obtained with 12 overlapping frequency set-ups as shown in Fig. 3.1. The mean and median system temperatures in main-beam brightness temperature scale ($T_{\mathrm{mb}}$) determined over all observations are $T_{\mathrm{sys}}^{\mathrm{mean}} \approx 266$ K and $T_{\mathrm{sys}}^{\mathrm{median}} \approx 239$ K, respectively. Mean and median receiver temperatures were $T_{\mathrm{rec}}^{\mathrm{mean}} \approx 81$ K and $T_{\mathrm{rec}}^{\mathrm{median}} \approx 78$ K, respectively.
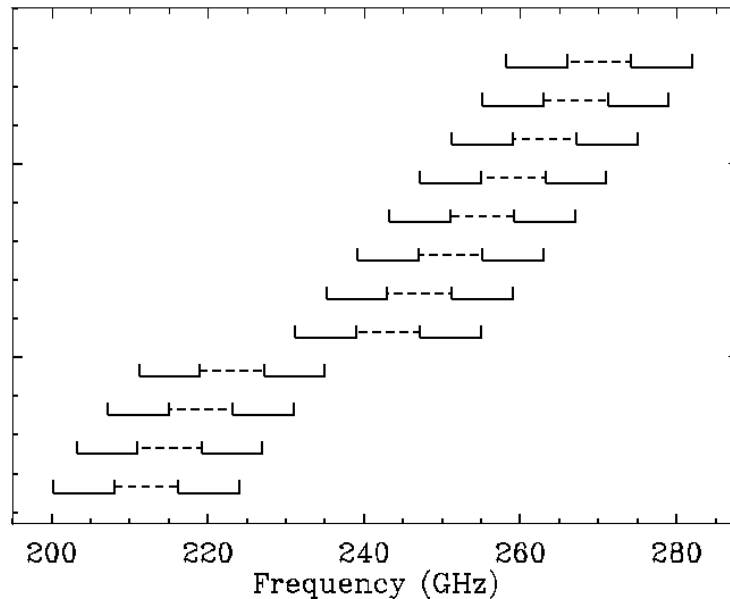
**Figure 3.1:** Twelve overlapping frequency set-ups were used to cover the 1.3 mm window, each providing $2 \times 7.8$ GHz bandwidth.

### 3.2.2 Calibration and data reduction

All data reduction was done with the GILDAS[2] software package. This included analysis of spectra and maps of the lines' intensity distribution. In the first processing step the data were calibrated and correction factors for the beam efficiencies applied separately for each observing period. These correction factors were obtained from Jupiter continuum pointings at different frequencies. The observed peak temperature of the planet was compared to the expected value calculated by the GILDAS ASTRO module, yielding the main beam efficiency. These main beam efficiencies were then fitted by the Ruze formula, facilitating a frequency dependent correction for every observing period, summarised in Table 3.1. The exact value of the surface accuracy of the dish has only a marginal impact on the data observed in the 1.3 mm window, however. The main beam efficiency varies by $\lesssim 5$ % over the observed frequency range. The spectra are also converted from corrected antenna temperature, $T_{\mathrm{A}}^{*}$, to $T_{\mathrm{mb}}$ units in this step, which is thus the temperature scale used in this paper.

A substantial amount of data was collected during the commissioning phase of the PI230 receiver, entailing larger uncertainties. However, parts of the maps have been observed repeatedly in different observing periods such that efficiency corrected spectra could be compared and the earlier data validated, suggesting our calibration uncertainty to be around 30% overall.

In the next processing step we removed spikes, artefacts, and spurious lines that only appeared during the early commissioning of the receiver/backend system and affect parts of the data. Furthermore, spectra with $T_{\mathrm{sys}} \geq 600$ K were rejected. While single channel spikes are readily identified by simple scripts, the artefacts needed to be manually identified and blanked as they showed continuous behaviour towards their edges, making it more challenging to discriminate between them and unaffected channels. A larger number of spectra were checked for each backend and each frequency

---
[2]http://www.iram.fr/IRAMFR/GILDAS

**Table 3.1:** Main beam efficiencies ($\eta_{\mathrm{mb}}^0$) and surface accuracy ($\sigma$) used to correct the data from different observing periods

| Observing period | $\eta_{\mathrm{mb}}^0$ | $\sigma \; [\mu\mathrm{m}]$ |
|---|---|---|
| October 2015 - December 2015 | 0.62 | 30 |
| July 2016 - November 2016 | 0.73 | 30 |
| April 2017 | 0.74 | 30 |
| July 2017 | 0.66 | 30 |
| May 2018 - July 2018 | 0.73 | 15 |
| November 2018 | 0.75 | 13 |

setting for the different observing days.

To identify and remove spurious lines, we did a first assignment of all observed lines to molecular transitions from the JPL[3] (Pickett et al. 1998) and CDMS[4] (Endres et al. 2016) molecular spectroscopy databases using the WEEDS (Maret et al. 2011) extension for GILDAS. If a line could not be identified, we checked if it was present in all relevant backends and frequency settings. The respective channels in the originating backends were blanked if the line only appeared in some instances.

### 3.2.3   Final data set

In the following processing step, a first-order baseline was subtracted from each spectrum. The boundaries of the line windows were based on the Orion KL spectrum, where we expect the broadest lines and strongest overlap between them. To simplify the analysis and speed up both imaging and the extraction of spectra, we assembled all data for each backend and each frequency set-up and gridded it using the same template cube with a smoothed beam size of $32''$. This results in 96 data cubes (8 backends $\times$ 12 frequency set-ups), each containing around 3000 spectra and each of which with 65536 channels (corresponding to a resolution of $0.07 - 0.09 \; \mathrm{kms}^{-1}$ or 61 kHz). These spectra are intensity corrected, (mostly) artefact-free, baseline subtracted, and arranged on the same grid, and form the basis for all further analyses.

The 1.3 mm window gives us access to a variety of molecular species and transitions. In this paper we want to concentrate on 29 species (55 isotopologues), which are listed in Table 3.2. We can work with our data set both in terms of imaging and spectral analysis. An example of the differing spatial extensions of typical molecular tracers is given in the integrated intensity maps of Fig. 3.2. The maps are resampled to a resolution of 0.4 km s$^{-1}$, resulting in a typical rms noise of around 0.5 K. However, not all species contained in our data set can be mapped as for an individual image pixel their intensity may be too low. Those molecules (like CF$^+$) are detectable when we average over larger areas. These averaged spectra will be further described in Sections 3.3.2 and 3.3.3.

---

[3]http://spec.jpl.nasa.gov/
[4]http://www.astro.uni-koeln.de/cdms/

**Table 3.2:** All considered species and isotopologues.

| species | isotopologues |
|---|---|
| CO | CO , $^{13}$CO , $C^{18}O$ , $C^{17}O$ , $^{13}C^{18}O$ |
| $c - C_3H_2$ | $c - C_3H_2$ |
| $C_2H$ | $C_2H$ , $C_2D$ |
| $CF^+$ | $CF^+$ |
| $CH_3CCH$ | $CH_3CCH$ |
| $CH_3CN$ | $CH_3CN$ |
| $CH_3OH$ | $CH_3OH$ |
| CN | CN, $^{13}CN$ |
| CS | CS, $^{13}CS$ , $C^{34}S$ , $C^{33}S$ |
| HCCCN | HCCCN |
| HCN | HCN, DCN, $H^{13}CN$ , $HC^{15}N$ |
| HCO | HCO |
| $HCO^+$ | $HCO^+$ , $DCO^+$ , $H^{13}CO^+$ , $HC^{18}O^+$ , $HC^{17}O^+$ |
| $HCS^+$ | $HCS^+$ |
| HDO | HDO |
| $H_2CCO$ | $H_2CCO$ |
| $H_2CO$ | $H_2CO$ , HDCO , $H_2^{13}CO$ |
| $H_2CS$ | $H_2CS$ , HDCS , $H_2C^{34}S$ |
| $H_2S$ | $H_2S$ |
| HNC | HNC, DNC, $HN^{13}C$ |
| HNCO | HNCO |
| $N_2H^+$ | $N_2H^+$ , $N_2D^+$ |
| NO | NO |
| NS | NS |
| OCS | OCS |
| SiO | SiO, $^{29}SiO$ , $^{30}SiO$ |
| SO | SO, $^{34}SO$ |
| $SO^+$ | $SO^+$ |
| $SO_2$ | $SO_2$ |

**Notes.** Summary of the species and isotopologues used for our analysis. A List of all transitions is found in Sect. A.1

## 3.3   Analysis

The final data set offers a starting point for varied analyses. In this paper, we want to concentrate on the cooling by different molecular species depending on their environment, focusing on an observational point of view.

### 3.3.1   Ancillary data

Attributing column density, temperature, or the strength of UV irradiation to different parts of Orion A is done with the help of ancillary data. Dust column density[5] and temperature based on *Herschel* data are from Guzmán et al. (2015), while C65$\alpha$ emission data (here used to define the dense PDR region) are from Wyrowski et al. (1997). Dust and gas temperature are expected to be coupled for densities $\sim 3 \times 10^4$ cm$^{-3}$ (Galli et al. 2002), and Guzmán et al. (2015) found that for the examined MALT90 clumps (Jackson et al. 2013; Foster et al. 2013, 2011) under 22 K ammonia and dust temperatures agree within $\pm 3$ K, while the uncertainties become larger with increasing temperature. We will mainly use the temperature map to differentiate between colder ($< 25$ K) and warmer ($\geq 25$ K) regions. Maps of gas kinetic temperatures based on NH$_3$ (Orion A) and H$_2$CO (OMC-1 only) observations can be found in Friesen et al. (2017) and Tang et al. (2018), respectively. As the utilised molecular lines require higher column densities to be excited, these maps do not cover all of the ambient material within our maps. Hence we decided on the use of dust-derived temperatures. Reproductions of the column density and dust temperature maps (reprojected using our template data cube) are shown in Fig. 3.3.

### 3.3.2   Regions and masks

Masks were used to define regions meeting certain conditions (e.g. column density or temperature ranges). These masks were mostly based on dust column density and temperature maps, but in some cases also selected around chosen coordinates. To this end, the maps were reprojected using the same template cube as for the gridding of our observational data, such that combinations of masks (e.g. high column density concurrent with low temperature) were possible. See Table 3.3 for a summary of the selected regions and their basic properties. For a better visual idea of the spatial extension of these regions, images of the masks are included in the Appendix (Fig. B.1).

Our choice of masks aims to assess the effects of temperature and column density, for example. For the reasons described in Section 3.3.3, KL and Orion South are excluded in some masks, despite matching the column density or temperature criteria. We have masks with only one condition ('high column density' vs. 'low column density', 'high temperature without KL and Orion South' vs. 'low temperature'), but also more restrictive masks, which also define other parameters ('high column density, low temperature' vs. 'low column density, low temperature' vs. 'low column density, high temperature' vs. 'high column density, high temperature without KL and Orion South'). The masks 'high column density' and 'high column density without KL and Orion South' intend to show how the spatially quite compact emission of KL and Orion South influences the larger scale emission. Additionally, UV irradiation is considered in the masks 'H II' and 'dense PDR'. Choosing this 'dense PDR' traced by radio recombination lines, instead of a more 'diffuse PDR' traced by C II (Pabst et al. 2019), has the advantage of the edge-on view in Orion. This means we will only probe the actual PDR and are not affected by projection effects. Earlier papers (Turner &

---

[5]Converted from g cm$^{-2}$ to cm$^{-2}$ under the simplifying assumption that all mass comes from H$_2$, 1g $\approx 2.134 \times 10^{23}$ molecules.

Thaddeus 1977) pointed out that the 'radical region' may be a chemically distinct environment within OMC-1, although subsequent observations were not conclusive (Greaves & White 1992). We decided to include this region in our analysis, hoping that our unbiased data set might advance its characterisation. Column density and temperature values listed in Table 3.3 for the 'radical region' are thus not its defining features. Lastly, using no mask at all ('all averaged') and employing the results from the other regions, we can evaluate which features or regions dominate on the largest considered scale and which might disappear, indicating that those latter regions may be hard to identify in other, spatially unresolved sources.

The exact values we chose for the column density and temperature thresholds ($N = 3.6 \times 10^{22}$ cm$^{-2}$ , $T = 25$ K) are somewhat arbitrary. We selected them such that they divide Orion A broadly into the denser parts of the filament ($N \geq 3.6 \times 10^{22}$ cm$^{-2}$) and the ambient material ($N < 3.6 \times 10^{22}$ cm$^{-2}$), and distinguish between the historically established regions OMC-1 ($T > 25$ K) and OMC-2/3 ($T < 25$ K). Based on these basic distinctions, combinations of masks are added and complemented by the 'H II', 'dense PDR' and 'radical region' masks.

Our masks are thus not devised to divide Orion A into strictly disjointed regions, but to explore the emission of template regions meeting physical or chemical conditions. A listing of all overlaps between the selected regions is given in Table A.3.
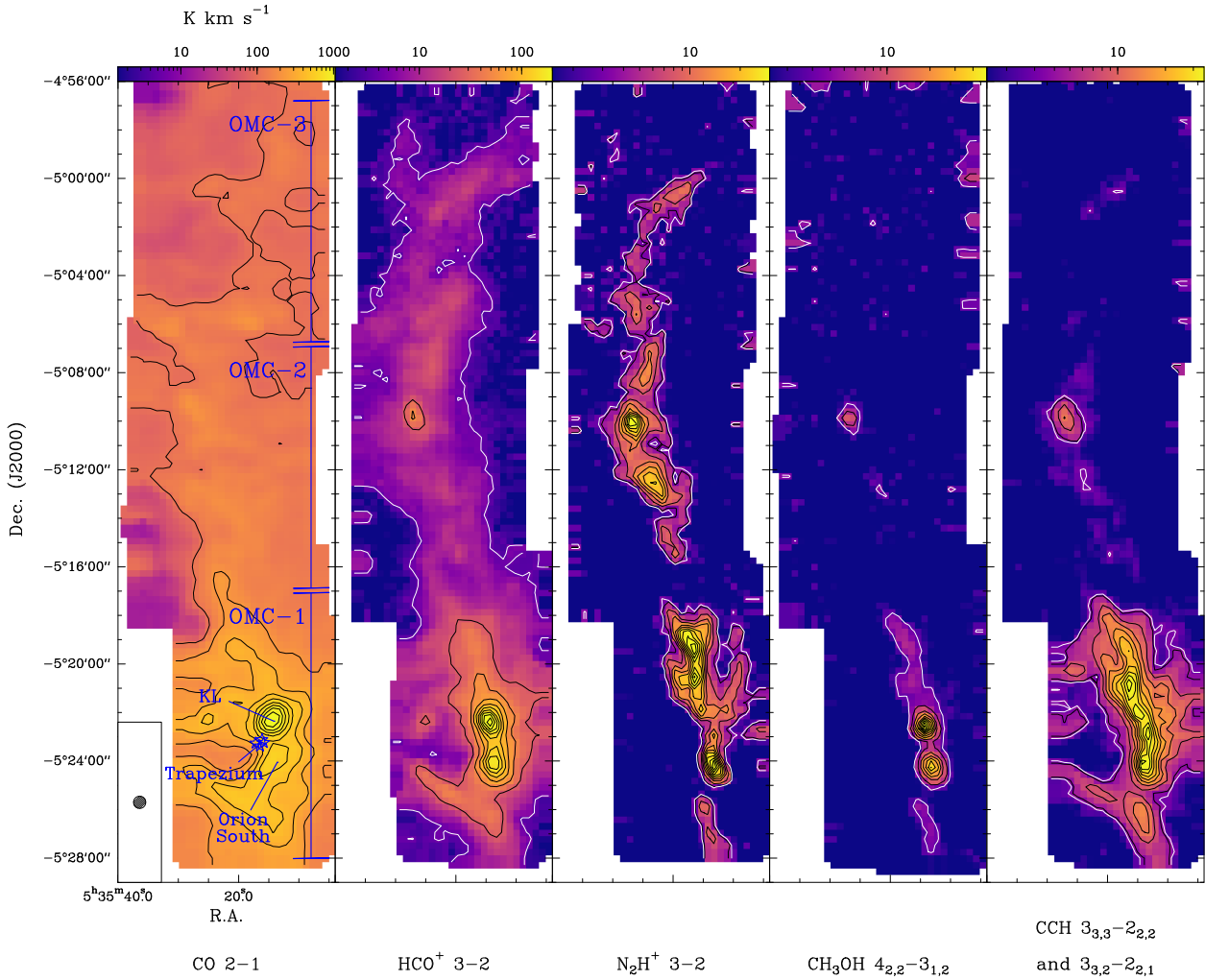
**Figure 3.2:** Selected integrated intensity [5,15] km s$^{-1}$ maps. Black contours run from 10% to 90% of the maximum value in steps of 10%, while the white contour shows the 3 $\sigma$ level. The maps highlight some of the molecules typically used as tracers: CO for the bulk of molecular gas, HCO$^+$ as an indicator of high density, N$_2$H$^+$ for cold dense gas, CH$_3$OH for shocked material, and C$_2$H associated with UV irradiation. The velocity range used for the maps does not encompass the whole line width (which differs strongly, especially comparing OMC-1 to OMC-3), but covers all central velocities.
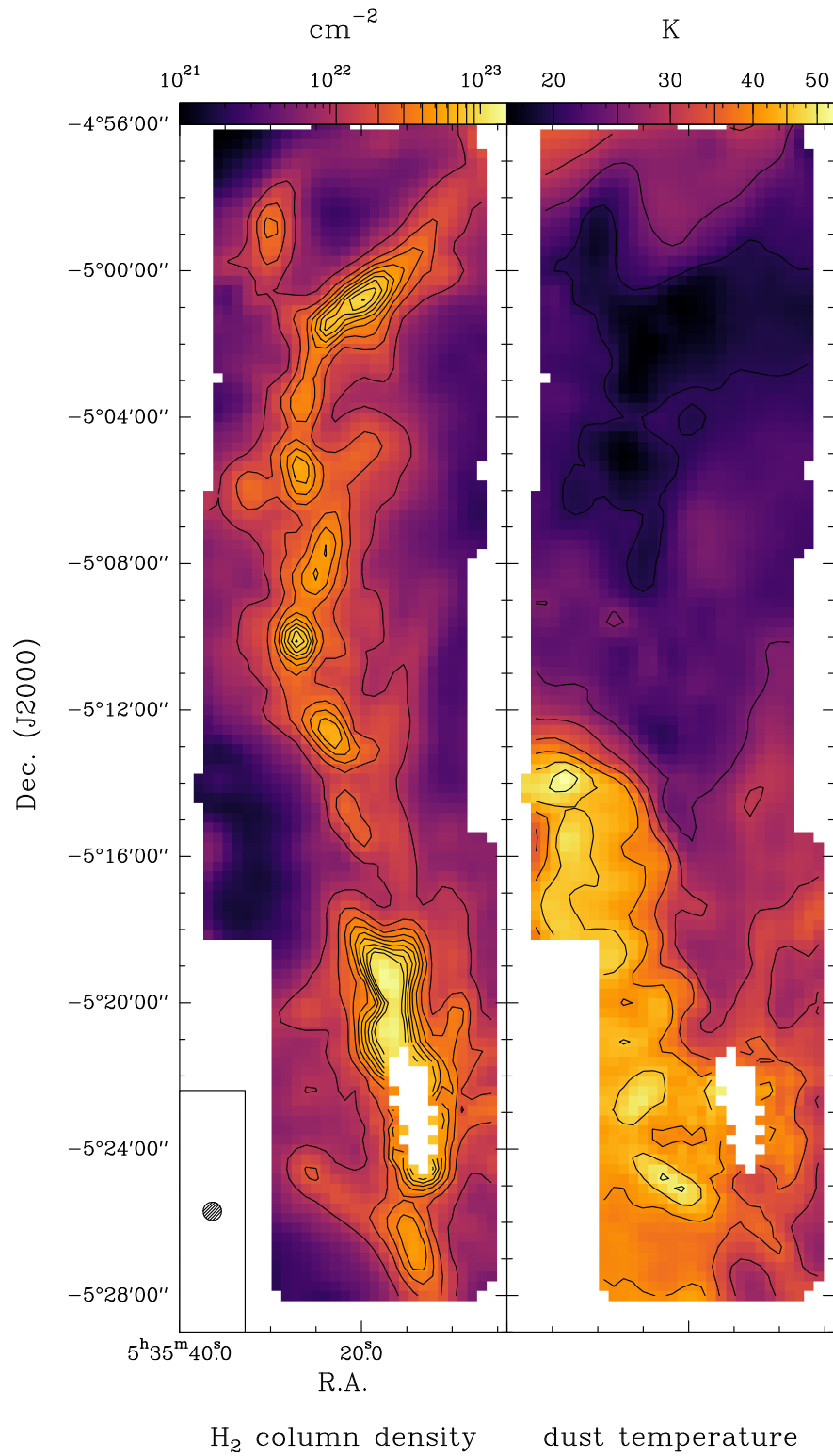
**Figure 3.3:** Dust derived column density and temperature map, modified (reprojected and cropped, the column density unit converted) from Guzmán et al. (2015). The area around KL and Orion South is saturated and blanked.
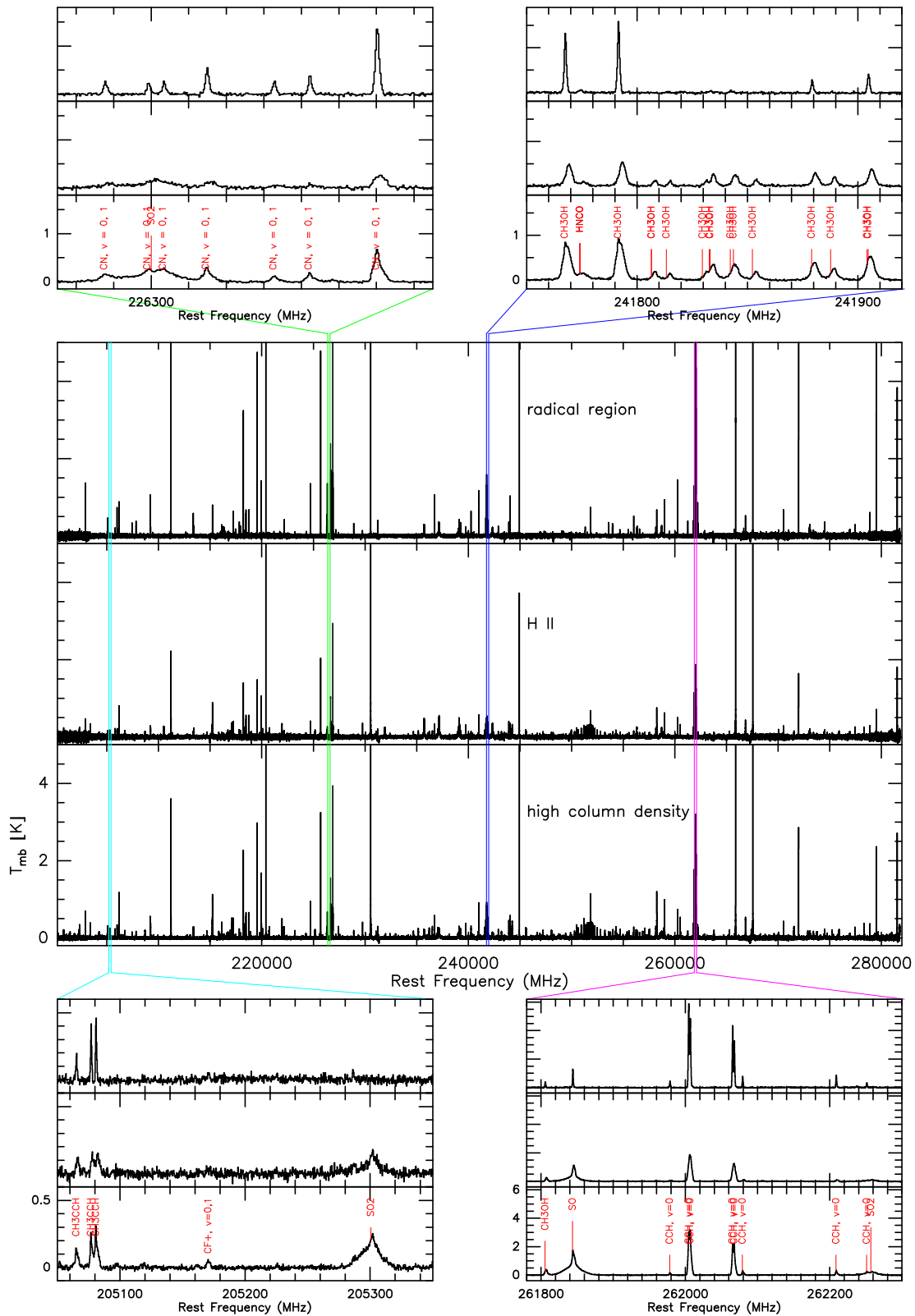
**Figure 3.4:** Spectra obtained from different masks as described in Sections 3.3.2 and 3.3.3. The restriction of the y-axis to 5 K for the middle panel is done to make the weaker lines visible (the CO line has a peak temperature of roughly 57 K), while the zoomed-in boxes illustrate some of the molecular variety.

**Table 3.3:** Selected regions and their fundamental properties.

| region | explicit mask | approx. size [arcmin$^2$] | column density range [cm$^{-2}$] | median column density [cm$^{-2}$] | temperature range [K] | median temperature [K] | label[†] |
|---|---|---|---|---|---|---|---|
| all averaged | no mask | 210.0 | $9.3 \times 10^{20}$ $-$ $> 1.4 \times 10^{23}$ [*] | $1.0 \times 10^{22}$ [*] | 17 - 53 [*] | 25 [*] | 1 |
| high column density | $N \geq 3.6 \times 10^{22}$ cm$^{-2}$ | 23.3 | $3.6 \times 10^{22}$ $-$ $> 1.4 \times 10^{23}$ [*] | $4.9 \times 10^{22}$ [*] | 17 - 51 [*] | 27 [*] | 2 |
| high column density without KL and Orion South | $N \geq 3.6 \times 10^{22}$ cm$^{-2}$ | 21.5 | $3.6 \times 10^{22}$ $-$ $1.4 \times 10^{23}$ | $4.9 \times 10^{22}$ | 17 - 51 | 27 | 3 |
| high column density, low temperature | $N \geq 3.6 \times 10^{22}$ cm$^{-2}$ $T < 25$ K | 9.2 | $3.6 \times 10^{22}$ $-$ $9.3 \times 10^{22}$ | $4.7 \times 10^{22}$ | 17 - $< 25$ | 19 | 4 |
| high column density, high temperature, without KL and Orion South | $N \geq 3.6 \times 10^{22}$ cm$^{-2}$ $25 < T < 55$ K | 11.5 | $3.6 \times 10^{22}$ $-$ $1.4 \times 10^{23}$ | $5.5 \times 10^{22}$ | 26 - 51 | 32 | 5 |
| low column density | $N < 3.6 \times 10^{22}$ cm$^{-2}$ | 186.7 | $9.3 \times 10^{20}$ $-$ $< 3.6 \times 10^{22}$ | $9.0 \times 10^{21}$ | 17 - 53 | 25 | 6 |
| low temperature | $T < 25$ K | 102.1 | $2.1 \times 10^{21}$ $-$ $9.3 \times 10^{22}$ | $1.2 \times 10^{22}$ | 17 - $< 25$ | 21 | 7 |
| low column density, low temperature | $N < 3.6 \times 10^{22}$ cm$^{-2}$ $T < 25$ K | 92.9 | $2.1 \times 10^{21}$ $-$ $< 3.6 \times 10^{22}$ | $1.1 \times 10^{22}$ | 17 - $< 25$ | 22 | 8 |
| low column density, high temperature | $N < 3.6 \times 10^{22}$ cm$^{-2}$ $25 < T < 55$ K | 93.7 | $9.3 \times 10^{20}$ $-$ $< 3.6 \times 10^{22}$ | $7.5 \times 10^{21}$ | 25 - 53 | 34 | 9 |
| high temperature, without KL and Orion South | $25 < T < 55$ K | 105.2 | $9.3 \times 10^{20}$ $-$ $1.4 \times 10^{23}$ | $8.5 \times 10^{21}$ | 25 - 53 | 33 | 10 |
| H II | high H31$\alpha$ emission [**] | 6.4 | $7.9 \times 10^{21}$ $-$ $6.7 \times 10^{22}$ [*] | $1.7 \times 10^{22}$ [*] | 36 - 51 [*] | 42 | 11 |
| radical region [***] | $130'' \times 130''$ around $\alpha_{2000} = 5^h 35^m 16.51^s$ $\delta_{2000} = -5°19'33.0''$ | 5.1 | $1.8 \times 10^{22}$ $-$ $1.4 \times 10^{23}$ | $5.8 \times 10^{22}$ | 27 - 38 | 30 | 12 |
| dense PDR | $N < 3.6 \times 10^{22}$ cm$^{-2}$ high C65$\alpha$ emission [****] | 4.7 | $8.8 \times 10^{21}$ $-$ $3.5 \times 10^{22}$ | $1.8 \times 10^{22}$ | 37 - 51 | 44 | 13 |

**Notes.** (†) To be used as an identifier in later plots. (*) The area around Orion KL and Orion South is saturated, thus the given maximum column density, maximum temperature, and median values are actually lower limits. (**) Mask based on an integrated [-20, 15] km s$^{-1}$ intensity image of the H31$\alpha$ emission at 210501.788 MHz, where pixels with an integrated intensity over $\approx 3.1$ K km s$^{-1}$ were selected. (***) Coordinates based on Greaves & White (1992). (****) Mask based on an integrated intensity image of the C65$\alpha$ emission at 23415.9609 MHz from Wyrowski et al. (1997), where pixels with an integrated intensity over 4 K km s$^{-1}$ were selected.

### 3.3.3   Obtaining total intensities

The total intensity of different molecular species for the different regions was determined in three steps. Firstly, the spectrum of the region was extracted from our data cubes using the masks described in section 3.3.2. All spectra within a mask were combined into a single spectrum, the 'regional spectrum' or average. The idea is that local effects should average out in this step when the area is large, while common characteristic features will add up. Smoothing along the frequency axis to a resolution of around 305 kHz was done to improve the signal-to-noise ratio. Three of these averaged spectra are shown as examples in Fig. 3.4.

In the second step, the spectral lines listed in Table A.1 were considered in Gaussian fits. Line-of-sight velocities do not vary significantly within the mapped area, from $\sim 9$ km s$^{-1}$ for most of OMC-1 (especially when excluding KL and Orion South with slightly lower velocities) and increasing to $\sim 12$ km s$^{-1}$ towards OMC-3. Different velocity components thus overlap in a spectrum. The list of lines is based on the spectrum obtained with the high column density mask (which includes Orion KL and Orion South), where we expect the greatest number of lines. Omitted are complex molecules with the exception of CH$_3$OH, CH$_3$CN, and CH$_3$CCH. The lines of CH$_3$OCH$_3$ or CH$_3$OCHO, for example, are numerous but weak and their contribution to the overall emission as typical hot core molecules should be negligible on larger scales. The main goal is to capture most of the line emission, which in some cases means that not each individual transition is fitted. The automated fitting is more robust when strongly overlapping lines are not fitted separately, but covered in a single Gaussian fit. This favouring of robustness was abandoned when the overlapping lines belonged to different species. In that case, the lines were fitted separately. Overlap between lines becomes an issue whenever KL and Orion South are involved, hence the decision to only include them in two larger regions, as automated fitting is not feasible otherwise.

In the third and final step all lines above $5\sigma$ with reasonable widths and velocity were considered to be real detections and the area of their fit added to the total intensity of their respective species.

Noise levels vary within a single spectrum depending on frequency, and between different spectra due to the varied spatial extension of the regions. This influences the possibility to detect very weak lines and will be addressed further in Fig. B.2.

## 3.4   Results

The averaged total intensity for each species and region is listed in Table 3.4, together with the detection limit for each region. Owing to space constraints, the formal fit errors are listed separately in Table A.2, but they usually amount to $2-6\%$ for all species and regions. Due to the overall low noise levels and the high number of free parameters, the fit errors for a single line are very small. The actual uncertainties are thus dominated by the calibration uncertainties discussed in Section 3.2.2.

The high column density region has the highest averaged total intensity with $\sim 1360$ K km s$^{-1}$. Removing just the region around KL and Orion South has a significant impact on the overall emission and reduces the averaged total intensity by 48%, although the removed area represents only 8% of the high column density region. The regions 'high column density, high temperature, without KL and Orion South' and 'H II' have comparable averaged total intensities ($\sim 954$ K km s$^{-1}$ and $\sim 925$ K km s$^{-1}$), which are a factor of $\sim 3$ above average ($\sim 319$ K km s$^{-1}$). The averaged total CO intensity is also similar for these two regions, their differences lying in the species with less emission. The 'dense PDR' and 'radical' regions both emit a factor of $\sim 2$ above average, but

their share of CO emission differs by around 20%, indicating that their emission profiles (meaning the breakdown of the total emission into contributions from different species) are distinct from each other. The 'high temperature without KL and Orion South' region is most similar to the 'averaged' region not only in terms of total intensity, but also regarding the most prominent species. The remaining regions, including 'high column density, low temperature', emit below average.

For easier comparison, hereafter the data is presented in three complementing ways, each highlighting different aspects. Figure 3.5 shows the visualisation for the different species with the example of our average data (where no mask was used). The normalised intensity of all species in descending order is shown in Fig. 3.5a with a logarithmic plot, down to 0.1% of the CO intensity. This order of species is used in the corresponding total intensity plots for all other regions (see Fig. B.2). For the comparison of regions, this representation of the data helps to make shifts in the influence of species more apparent. The pie charts (Fig. 3.5b and Fig. B.4) visualise the percentage of the total intensity originating from different species, with shares under 2% summed under 'other'. Plots in this form are more conducive from an observational point of view, as they highlight the most dominant and accessible species.

The third visualisation (Fig.B.3) concentrates more on a comparison between species. The plot again shows the percentaged share of each molecule, while the colour bar helps to highlight in which region each species has its largest or smallest share and which species are overall stronger or weaker emitters.

Of the 55 species considered in our analysis, 15 are seen to contribute over 2% each of the total intensity for at least one region. Members of these 15 species account for around 88% to 94% of line emission in the 1.3 mm window in all cases (or 5.6% to 53% when excluding CO and its isotopologues). In addition to CO and $^{13}$CO, only HCO$^+$ and H$_2$CO are prominent in every region, each contributing between 3% and 6% in all cases.

In terms of averaged total intensity, there is a factor of $\sim 8$ between the lowest ('low column density, low temperature') and highest ('high column density') regions. The high column density region has the lowest share of CO and the highest diversity of species noticeably involved in cooling. SO$_2$, with a share of 11.4% being the most important coolant after CO in the high column density region, is no longer relevant when KL and Orion South are removed (its share drops to around 1%; see also Fig. B.4a, B.4b and Fig. B.2a, B.2b). SO and CH$_3$OH show similar trends. In the high column density region, their total intensities exceed that of the typically strong emitters HCN, HCO$^+$, and H$_2$CO, while they lose importance without KL and Orion South.

The regions 'high column density, low temperature' and 'high column density, high temperature, without KL and Orion South' are parts of 'high column density without KL and Orion South' (see also Fig. B.1), coinciding with OMC-2/OMC-3 and OMC-1, respectively. Both in terms of averaged total intensity and as suggested by the pie charts and detailed normalised intensities (Fig. B.4b, B.4c, B.4d and Fig. B.2b, B.2c, B.2d), OMC-1 dominates the emission. Higher N$_2$H$^+$ emission, indicative of OMC-2/OMC-3, is not seen in the 'high column density without KL and Orion South' region, which is instead very similar to OMC-1 alone.

The regions 'low column density', 'low temperature', 'low column density, low temperature' and 'low column density, high temperature' are similar in the sense of high CO shares (60% to 67% for CO, 15% to 21% for $^{13}$CO) and only two to four species over 2% (Fig. B.4e, B.4f, B.4g, and B.4h). Their averaged total intensities are similar and below average. Their distinctions lie in the lower intensity species (Fig. B.2e, B.2f, B.2g, and B.2h).

The regions 'high temperature, without KL and Orion South' and 'dense PDR' are similar to each other and—with the the exception of SO emission and slightly different CO shares—to the

'averaged' region (Fig. B.4i, B.4l, 3.5b). The averaged total intensity is noticeably higher in the 'dense PDR' region than in the two others. The differences between regions lie again in the fainter species (Fig. B.2i, B.2l, 3.5a).

The 'H II' region is the only other region, in addition to 'high column density', with relevant $SO_2$ emission and also has higher shares of $CH_3OH$ and SO, which is the dominant coolant after CO and $^{13}CO$. The 'radical region' has the highest shares of $C_2H$ and CN and is the only other region besides 'high column density, low temperature' (dense part of OMC-2/OMC-3) with notable shares of $N_2H^+$.

### 3.4.1   Approximating the emission of KL and Orion South

While automated fitting procedures are problematic for high column density and high temperature environments with heavily overlapping lines, we can approximate the emission around KL and Orion South from our existing regions. With the known pixel sizes of 'high column density' and 'high column density without KL and Orion South' we can gauge the emission of the region and compute its average. The result is not as robust as the others, as more lines are expected for some species which are not accounted for in our routine (especially for $SO_2$, SO, and $CH_3OH$), and omitted complex organic molecules like $CH_3OCH_3$ presumably have non-negligible impact here. However, the overall results, as presented in Table 3.5 and Fig. B.5, are in general agreement with Schilke et al. (1997) for the 325 to 360 GHz frequency regime. The dominant species are in both cases $SO_2$, followed by CO, SO, $CH_3OH$, and HCN.

### 3.4.2   Correlations and line ratios on large scales

In the following analysis of correlations and line ratios, the integrated intensity for a given species always refers to the sum of all of its considered transitions in the 1.3 mm window listed in Table A.1. For some species (CO, $^{13}CO$, $C^{18}O$, $HCO^+$, $H^{13}CO^+$, HCN, HNC, $N_2H^+$, and CS) this involves only one transition, but includes several for others ($C_2H$, CN, $CH_3OH$, $H_2CO$, and SO). For the discussion of line ratios, we use simplified quantum numbers for species with one transition, and mark those species with multiple transitions with the letter $\Sigma$. Not all energy levels, for example of $CH_3OH$, will be populated in all regions, but its integrated intensity still carries meaning as a measure of the cooling in the examined frequency range. Furthermore, neighbouring transitions from complex species like $CH_3OH$ will strongly overlap in the broad lines from extragalactic sources, thus also inherently limiting the transferability of results concerning single or a few transitions only.

Correlations between species do not only point to similarities in their physical and chemical behaviour, but also reduce the number of necessary transitions for gauging the conditions in a molecular cloud. If the emission of two species correlates strongly it is possible, for example, to limit the frequency coverage to one species and save observation time. We limit our analysis to 14 species that are typically used as tracers.

All emission correlates to the first order with column density (see also Fig. 3.6), which will thus influence the correlation between species. To reduce this effect in our analysis of the 13 regional spectra, we divided the total intensity for each species and region by the respective median column density for the region (see Table 3.3). This is not as good as a pixel-by-pixel normalisation, but it is more feasible, especially for SO with its numerous partially overlapping lines. Furthermore, the number of data points is small (13 regions), meaning we do not have enough statistical data for a truly reliable correlation coefficient. However, we mainly hope to distinguish between species with strong correlation and those without correlation. Linear correlations were measured with the

**Table 3.4:** Averaged total intensities $\int T_{\mathrm{mb}}dv$ [K km s$^{-1}$] for all regions and species. The detection limit is based on the median line width for each region and assumes a $5\sigma_{\mathrm{median}}$ feature. Real detections below this limit may occur, for example when $\sigma_{\mathrm{local}} < \sigma_{\mathrm{median}}$ or when the line is narrow.

| species | all averaged | high column density | high column density without KL and Orion South | high column density, low temperature | high column density, high temperature, without KL and Orion South | low column density | low temperature | low column density, low temperature | low column density, high temperature | high temperature without KL and Orion South | H II | radical region | dense PDR |
|---|---|---|---|---|---|---|---|---|---|---|---|---|---|
| CO | 174.21 | 393.21 | 303.48 | 137.13 | 405.67 | 146.64 | 112.19 | 110.06 | 187.64 | 209.34 | 431.08 | 279.67 | 391.86 |
| $^{13}$CO | 45.19 | 90.51 | 81.37 | 46.54 | 103.78 | 39.91 | 38.91 | 38.10 | 41.71 | 48.31 | 69.57 | 81.02 | 71.17 |
| C$^{18}$O | 5.61 | 12.82 | 11.22 | 9.00 | 12.78 | 4.83 | 6.19 | 5.86 | 3.79 | 4.58 | 6.41 | 10.19 | 4.74 |
| C$^{17}$O | 1.89 | 4.13 | 3.82 | 3.19 | 3.98 | 1.62 | 2.16 | 2.03 | 1.19 | 1.50 | 2.12 | 3.46 | 1.73 |
| $^{13}$C$^{18}$O | - | 0.15 | 0.14 | 0.14 | 0.15 | - | 0.11 | - | - | - | - | 0.16 | - |
| c-C$_3$H$_2$ | 0.34 | 3.27 | 2.71 | 0.36 | 4.09 | - | - | - | 0.38 | 1.02 | 1.41 | 3.10 | 3.83 |
| C$_2$H | 6.96 | 30.33 | 25.48 | 7.01 | 37.11 | 3.96 | 2.11 | 1.65 | 6.19 | 9.72 | 18.66 | 35.05 | 13.82 |
| C$_2$D | - | 0.77 | 0.70 | 0.36 | 0.86 | - | - | - | - | - | - | 0.78 | - |
| CF$^+$ | 0.13 | 0.25 | 0.21 | - | 0.21 | 0.12 | 0.11 | - | - | - | - | - | - |
| CH$_3$CCH | 0.35 | 10.06 | 5.14 | 0.52 | 8.18 | - | - | - | - | 0.36 | 3.74 | 5.74 | - |
| CH$_3$CN | - | 30.02 | 1.20 | - | 1.25 | - | - | - | - | 1.36 | 1.73 | - | - |
| CH$_3$OH | 4.87 | 87.74 | 17.96 | 4.05 | 25.79 | 0.73 | 0.58 | 0.43 | 0.85 | 1.90 | 40.63 | 17.96 | 0.92 |
| CN | 9.26 | 36.02 | 26.50 | 9.33 | 38.77 | 5.62 | 3.29 | 2.05 | 4.76 | 8.38 | 29.60 | 35.05 | 17.98 |
| $^{13}$CN | - | 0.37 | 0.32 | - | 0.48 | - | - | - | - | - | - | 0.32 | - |
| CS | 4.86 | 29.57 | 18.69 | 3.27 | 27.50 | 2.03 | 1.09 | 0.96 | 3.05 | 5.88 | 18.63 | 16.48 | 8.96 |
| $^{13}$CS | 0.23 | 2.47 | 1.33 | - | 2.01 | - | - | - | - | - | 1.80 | 0.97 | 0.58 |
| C$^{34}$S | 0.50 | 3.32 | 2.17 | - | 3.23 | - | - | - | 0.27 | 0.56 | 2.25 | 1.75 | 0.93 |
| C$^{33}$S | - | 0.84 | 0.44 | - | 0.74 | - | - | - | - | - | 0.58 | 0.38 | 0.28 |
| HC$_3$N | - | 17.21 | 2.28 | - | 3.23 | - | - | - | - | - | 6.57 | 0.84 | 0.27 |
| HCN | 12.46 | 70.94 | 36.67 | 9.37 | 49.07 | 4.38 | 3.02 | 2.32 | 6.45 | 11.62 | 50.43 | 26.35 | 21.14 |
| DCN | 0.34 | 2.51 | 1.51 | 0.35 | 1.96 | - | - | - | - | 0.33 | 1.69 | 1.09 | 0.34 |
| H$^{13}$CN | 0.74 | 7.43 | 2.24 | 0.25 | 2.73 | - | - | - | 0.19 | 0.53 | 2.47 | 1.61 | 0.70 |
| HC$^{15}$N | - | 2.42 | 0.56 | - | 0.77 | - | - | - | - | - | 0.97 | 0.30 | - |
| HCO | - | 0.13 | 0.15 | - | 0.54 | - | - | - | - | - | - | 0.25 | 0.43 |
| HCO$^+$ | 13.22 | 61.37 | 39.97 | 14.92 | 52.21 | 7.29 | 6.39 | 5.59 | 9.42 | 14.78 | 50.30 | 29.17 | 27.65 |
| DCO$^+$ | 0.12 | 1.06 | 0.81 | 0.97 | 0.64 | 0.07 | 0.22 | 0.15 | - | - | - | 0.48 | - |
| H$^{13}$CO$^+$ | 0.64 | 3.31 | 2.55 | 1.27 | 3.09 | 0.15 | 0.36 | 0.27 | 0.30 | 0.62 | 2.11 | 2.30 | 0.44 |
| HC$^{18}$O$^+$ | - | 0.30 | 0.21 | - | 0.28 | - | - | - | - | - | 0.24 | 0.23 | - |
| HC$^{17}$O$^+$ | - | - | - | - | - | - | - | - | - | - | - | - | - |
| HCS$^+$ | 0.13 | 1.88 | 1.44 | - | 2.15 | - | - | - | - | - | 0.37 | 1.21 | 1.60 |
| HDO | - | 0.59 | - | - | - | - | - | - | - | - | - | - | - |
| H$_2$CCO | - | 0.81 | - | - | - | - | - | - | - | - | - | 0.16 | - |
| H$_2$CO | 12.10 | 64.62 | 41.28 | 17.95 | 53.55 | 6.15 | 5.75 | 4.42 | 7.75 | 12.51 | 40.88 | 36.38 | 21.44 |
| HDCO | - | 2.09 | 0.35 | 0.18 | 0.95 | - | - | - | - | - | 0.37 | 0.61 | - |
| H$_2^{13}$CO | - | 2.34 | 0.39 | 0.15 | 1.04 | - | - | - | - | - | 0.71 | 0.29 | - |
| H$_2$CS | 1.54 | 18.10 | 10.15 | - | 16.35 | - | - | - | 0.32 | 2.15 | 10.07 | 10.97 | 0.27 |
| HDCS | - | - | - | - | 0.30 | - | - | - | - | - | - | 0.26 | - |
| H$_2$C$^{34}$S | - | - | - | - | - | - | - | - | - | - | - | - | - |
| H$_2$S | - | 2.30 | - | - | 0.49 | - | - | - | - | - | - | - | - |
| HNC | 2.86 | 14.37 | 10.25 | 5.53 | 12.94 | 1.56 | 1.70 | 1.31 | 1.74 | 2.97 | 7.51 | 10.66 | 3.71 |
| DNC | 0.08 | 0.63 | 0.50 | 0.53 | 0.56 | - | 0.11 | - | - | - | - | 0.52 | - |
| HN$^{13}$C | - | 0.58 | 0.47 | 0.22 | 0.64 | - | 0.06 | - | - | - | 0.27 | 0.58 | - |
| HNCO | - | 2.44 | - | - | 0.49 | - | - | - | - | - | - | - | - |
| N$_2$H$^+$ | 2.40 | 11.14 | 10.67 | 9.75 | 11.40 | 1.28 | 2.37 | 1.62 | 0.84 | 2.05 | 2.67 | 13.39 | - |
| N$_2$D$^+$ | - | 0.19 | 0.20 | 0.44 | - | - | - | - | - | - | - | - | - |
| NO | 0.10 | 2.23 | 1.01 | 0.44 | 1.24 | 0.08 | 0.25 | 0.24 | - | - | 1.07 | - | - |
| NS | - | 2.26 | 1.66 | - | 2.63 | - | - | - | - | - | - | 2.66 | - |
| OCS | - | 5.05 | - | - | - | - | - | - | - | - | 1.20 | - | - |
| SiO | 2.94 | 27.77 | 5.83 | - | 7.30 | - | - | - | - | - | 13.93 | - | - |
| $^{29}$SiO | - | 1.64 | - | - | - | - | - | - | - | - | - | - | - |
| $^{30}$SiO | - | - | - | - | - | - | - | - | - | - | - | - | - |
| SO | 11.81 | 129.66 | 32.39 | 2.91 | 42.62 | 0.97 | 0.98 | 0.77 | 1.61 | 4.28 | 65.82 | 8.00 | 9.64 |
| $^{34}$SO | - | 12.05 | - | - | 0.85 | - | - | - | - | - | 1.16 | 0.09 | - |
| SO$^+$ | - | - | - | - | 0.59 | - | - | - | - | - | - | 0.13 | 0.36 |
| SO$_2$ | 2.65 | 155.03 | 4.15 | - | 6.57 | - | - | - | - | - | 35.27 | - | - |
| sum : | $\sim$ 319 | $\sim$ 1360 | $\sim$ 711 | $\sim$ 286 | $\sim$ 954 | $\sim$ 227 | $\sim$ 188 | $\sim$ 178 | $\sim$ 279 | $\sim$ 345 | $\sim$ 925 | $\sim$ 641 | $\sim$ 603 |
| approx. detection limit [K km s$^{-1}$] : | 0.17 | 0.29 | 0.22 | 0.16 | 0.20 | 0.15 | 0.11 | 0.10 | 0.19 | 0.16 | 0.38 | 0.14 | 0.27 |
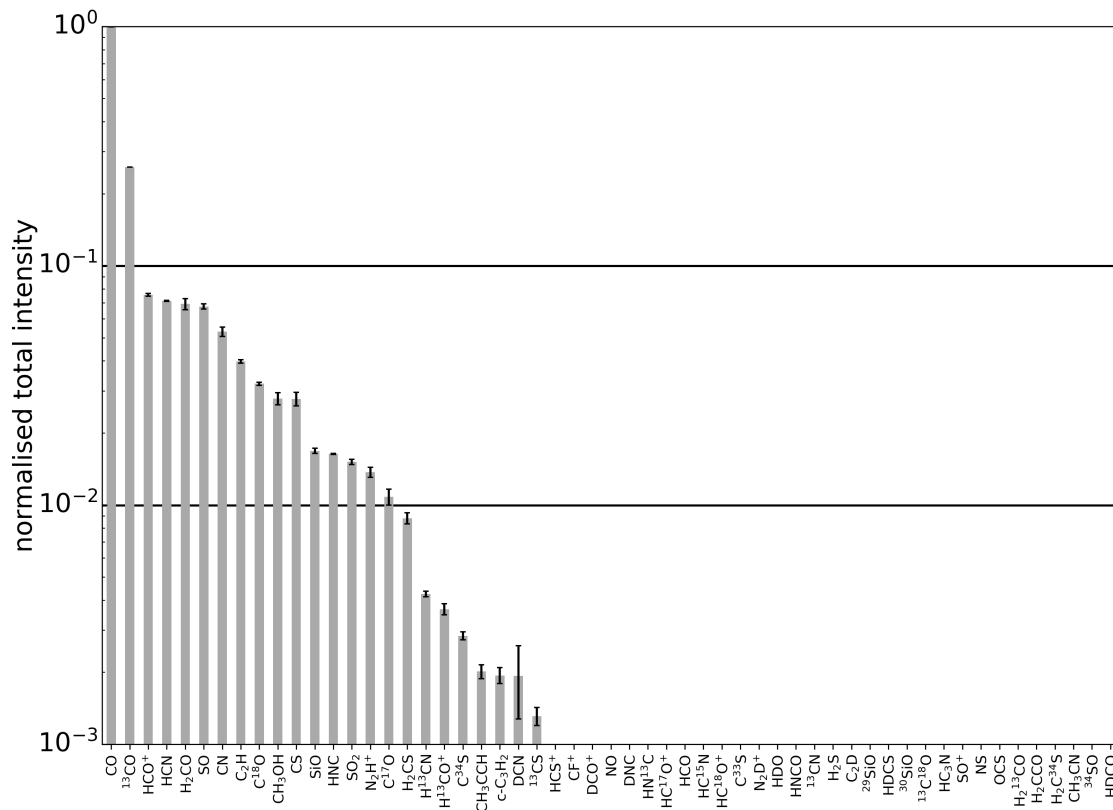
**(a)** all averaged normalised total intensities
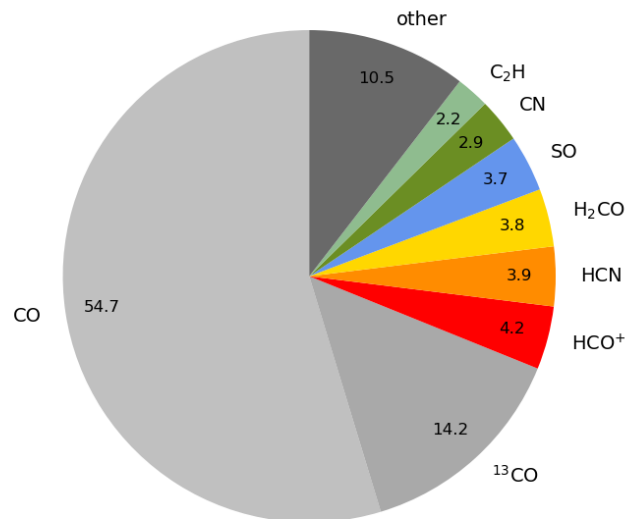


**(b)** all averaged pie chart

**Figure 3.5:** Normalised total intensity and pie chart for our averaged data. The order of species in the normalised plot is also used for every other region (see Fig. B.2). The pie chart gives the percentage of the total intensity originating from different species. Shares under 2% are summed under 'other'.

**Table 3.5:** Approximated averaged total intensities from the region around KL and Orion South

| species | $\int T_{\mathrm{mb}}dv$ [K km s$^{-1}$] | species | $\int T_{\mathrm{mb}}dv$ [K km s$^{-1}$] |
|---|---|---|---|
| CO | 1464.9 | HCS$^+$ | 7.0 |
| $^{13}$CO | 199.6 | HDO | 7.7 |
| C$^{18}$O | 31.9 | H$_2$CCO | 10.4 |
| C$^{17}$O | 7.8 | H$_2$CO | 343.3 |
| $^{13}$C$^{18}$O | 0.3 | HDCO | 22.9 |
| c-C$_3$H$_2$ | 9.9 | H$_2^{13}$CO | 25.6 |
| C$_2$H | 88.2 | H$_2$CS | 113.1 |
| C$_2$D | 1.5 | HDCS | - |
| CF$^+$ | 0.7 | H$_2$C$^{34}$S | - |
| CH$_3$CCH | 68.9 | H$_2$S | 29.8 |
| CH$_3$CN | 374.2 | HNC | 63.6 |
| CH$_3$OH | 921.1 | DNC | 2.1 |
| CN | 149.8 | HN$^{13}$C | 2.0 |
| $^{13}$CN | 1.0 | HNCO | 31.6 |
| CS | 159.4 | N$_2$H$^+$ | 16.7 |
| $^{13}$CS | 16.1 | N$_2$D$^+$ | 0.1 |
| C$^{34}$S | 17.0 | NO | 16.7 |
| C$^{33}$S | 5.7 | NS | 9.3 |
| HC$_3$N | 195.5 | OCS | 65.3 |
| HCN | 480.3 | SiO | 289.8 |
| DCN | 14.5 | $^{29}$SiO | 21.2 |
| H$^{13}$CN | 69.5 | $^{30}$SiO | - |
| HC$^{15}$N | 24.6 | SO | 1291.6 |
| HCO | - | $^{34}$SO | 156.0 |
| HCO$^+$ | 317.0 | SO$^+$ | - |
| DCO$^+$ | 4.1 | SO$_2$ | 1957.2 |
| H$^{13}$CO$^+$ | 12.4 | | |
| HC$^{18}$O$^+$ | 1.4 | | |
| HC$^{17}$O$^+$ | - | | |
| | | total | 9120.2 |
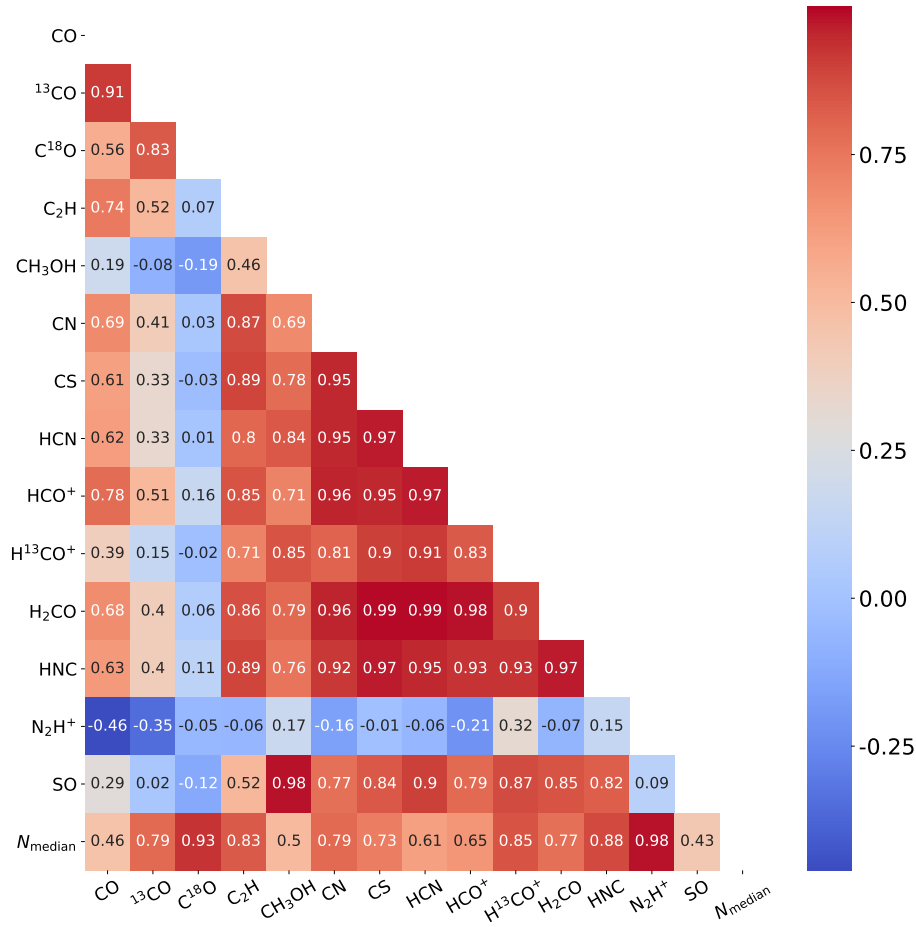
**Figure 3.6:** Pearson product-moment correlation coefficients between prevalent species (normalised with the median column density) and between prevalent species and the median column density.

Pearson correlation coefficient[6] and are shown in Fig. 3.6, while selected plots are presented in Figs. B.6 and B.7. Using our averaged (and therefore unresolved) regional data adds uncertainty for the interpretation compared to a pixel-by-pixel analysis (e.g. the discussed column density value, which is only an approximation for the whole region). On the other hand, our averaged data enables us to include species like SO and $CH_3OH$ even in low column density and low-temperature environments.

### 3.4.2.1 Correlations and tracers

We expect chemical effects to influence correlation, and also different optical depths of the species. We do not correct for the latter, as our aim is to stay as close to the data an observer might receive from an unresolved source, where the assumptions needed to correct for optical depth may add additional uncertainty.

Strong correlations ($\gtrsim 0.90$) are found between the typical high-density tracers HCN, $HCO^+$, $H_2CO$, HNC, CS, but also CN. There is generally little spread between the data points in the correlation plots, for example between $H_2CO$ and $HCO^+$ (Fig. B.6a) or $H_2CO$ and HCN (Fig. B.6b), but the 'H II' region with its high integrated intensities (after normalisation) constitutes a

---

[6]Calculated using scipy.stats.pearsonr from the SciPy library (Jones et al. 2001-2019) in Python.

more isolated data point.

To a lesser degree, correlations are also found between $H^{13}CO^+$ and the other high-density tracers (Fig. B.6c). However, the integrated intensity of the former is often an order of magnitude smaller than for the latter, making its observation more challenging.

Not only is CN correlated with $C_2H$, which is often associated with UV irradiation (Nagy et al. 2015 and references therein), but it is also correlated with high-density tracers (e.g. Fig. B.6d,B.6e). Another strong correlation is found between the shock tracers (e.g. Bachiller & Pérez Gutiérrez 1997, Sakai et al. 2012, Nagy et al. 2015 and references therein, e.g. Wakelam et al. 2004) SO and $CH_3OH$ (Fig. B.6f).

For the evaluation of correlations between species and column density in this case we have to factor in that the intensities are not normalised (with the median column density). Hence, it is possible to see two species correlating strongly with column density, but not with each other after normalisation (see $C^{18}O$ and $N_2H^+$). Of all the considered species, $N_2H^+$ shows the strongest correlation with the median column density (Fig. B.7a), the outlier being the non-detection ($< 5\sigma$) in the 'dense PDR' region, where $N_2H^+$ is most likely expected to be destroyed. We also see a strong correlation between $C^{18}O$ and the median column density (Fig. B.7b), but the data points show a wider spread. When considering slope (and intercept) of the linear fit between species and median column density, we see that $N_2H^+$ reacts more sensitively to changes in column density. From the more luminous high-density tracers, HNC may correlate the most with the median column density, in agreement with Pety et al. (2017).

CO and its isotopologues do not show clear correlations with other species (but they do with each other). This may be explained to some degree by optical depth effects, meaning that CO mainly traces the surface of the cloud, while other species probe deeper layers. Especially for $C^{18}O$, which is unlikely to be optically thick, depletion may be an important factor. High-density tracers generally profit from higher (volume) densities, while $C^{18}O$ may freeze out in these environments if the temperatures are low (as the chance to collide with and stick to dust grains is increased). $N_2H^+$ only correlates with the median column density.

### 3.4.2.2   Line ratios

A related important diagnostic, especially for extragalactic observations, but also for molecular clouds in the Milky Way, are line or integrated intensity ratios. They are more reliable tracers of physical or chemical conditions than lines from a single species as calibration errors can cancel out for ratios, depending on the observation technique. These ratios can also be examined with our data.

We will examine some integrated intensity ratios which have also been discussed in Pety et al. (2017), Gratier et al. (2017), or Bron et al. (2018), among others, in the 3 mm window. The considered transitions are thus different, but general trends (e.g. HCN/HNC value increasing with temperature) may still be seen with our data. Selected integrated intensity ratios are compiled in Fig. 3.8.

Our sample supports the notion from Pety et al. (2017) that the CN/HCN ratio is not a reliable tracer of UV illuminated gas. As the photodissociation of HCN produces CN, one might expect the highest ratio in the 'dense PDR' region of our data ($CN(\Sigma)/HCN(3-2) \approx 0.9$). Instead we find it in the 'low column density' and 'radical region' environments (both $\approx 1.3$). The lowest ratio is found for the 'high column density' region ($\approx 0.5$). The $CN(1-0)/HCO^+(1-0)$ ratio, discussed in Bron et al. (2018), is suggested to help distinguish UV-illuminated gas from shielded gas, with higher

values associated with higher illumination. We find the lowest value $(CN(2-1)/HCO^+(3-2) \approx 0.4)$ for our 'low column density, low temperature' region, the highest $(\approx 1.2)$ in the 'radical region', not with the expected 'dense PDR' $(\approx 0.7)$. So at least on our examined large scales and without correction for optical depth, using this ratio in the 1.3 mm window to trace UV illumination seems difficult too.

The ratio HCN/HNC should increase with temperature (Pety et al. 2017 and references therein, e.g. Graninger et al. 2014) due to HNC reacting with H to form HCN at temperatures $\gtrsim$ 30 K. Indeed we find the three lowest values $(HCN(3-2)/HNC(3-2) = 1.7-1.8)$ for our regions associated with the lowest median temperatures, while the highest two values of $5.7 - 6.7$ coincide with the highest temperatures, found in our case in the 'H ii' and 'dense PDR' regions. Larger deviations from this trend are found for the 'radical region', for example (see also Fig. B.7c).

In their PCA of Orion B data in the 3 mm window, Gratier et al. (2017) found that a higher $N_2H^+(J = 1 - 0, F1 = 2 - 1, F = 3 - 2,)/ CH_3OH(J = 2 - 1, K = 0 - 0, A^+)$ ratio possibly highlights the chemistry of the densest cores. This cannot be meaningfully examined for the 1.3 mm window with our spatially unresolved data, and we do not see a correlation with column density. While the emission of both species is higher in regions of enhanced column density in our data, their ratio is not. The highest ratios are not found in the regions encompassing the dense filament, but instead in the 'low temperature' and 'low column density, low temperature' regions $(N_2H^+(3 - 2)/CH_3OH(\Sigma) \approx 3.8 - 4.1)$, while the spectra from the high column density regions have notably lower values $(\approx 0.1$ for the 'high column density', $\approx 2.4$ for the 'high column density, low temperature', and $\approx 0.4$ for the 'high column density, high temperature, without KL and Orion South' region). However, we see a potential correlation of $N_2H^+(3-2)/CH_3OH(\Sigma)$ with temperature (Fig. B.7d).

### 3.4.2.3 Line luminosities

For the interpretation of emission from unresolved and/or extragalactic sources, information on line luminosities [K km s$^{-1}$pc$^2$] is important. Regions with low overall emission may still contribute considerably to the emission of some species if these regions are spatially extended. Conversely, strong but compact emission may be diluted on larger scales. Figure 3.7 lists the total luminosity (sum over all considered species in the 1.3 mm window) and the values for selected species for all our examined regions, including the approximations for KL and Orion South (see also Section 3.4.1).

Despite its overall lower emission, the extended 'low column density' region is the source of $\sim 75\%$ of the CO, $^{13}$CO, and C$^{18}$O emission, while $\sim 25\%$ can be allotted to the 'high column density' region. For the high-density tracers HCO$^+$ and HNC, but also N$_2$H$^+$, the allocation between low and high column density is around 50%/50%. For HCN and CS it is less of an even split between the two column density regimes and $\sim 65\%$ originate from the high column density region.

A lot of the emission from the high column density region can be attributed to the environment of KL and Orion South: with a size of $< 1\%$ of the total examined area, it emits $\sim 20\%$ of the HCO$^+$ and HNC, and $\sim 30\%$ of HCN and CS. When considering all emission in the 1.3 mm window, KL and Orion South are the source of roughly 25%.

| | total | CO | $^{13}$CO | C$^{18}$O | CS | HCN | HCO$^+$ | HNC | N$_2$H$^+$ |
|---|---|---|---|---|---|---|---|---|---|
| all averaged (100%) | 970.06 (100%) | 530.57 (100%) | 137.62 (100%) | 17.09 (100%) | 14.79 (100%) | 37.93 (100%) | 40.27 (100%) | 8.70 (100%) | 7.30 (100%) |
| high column density (11%) | 459.65 (47.4%) | 132.87 (25.0%) | 30.58 (22.2%) | 4.33 (25.4%) | 9.99 (67.5%) | 23.97 (63.2%) | 20.74 (51.5%) | 4.85 (55.8%) | 3.76 (51.6%) |
| high column density without KL and Orion South (10%) | 221.56 (22.8%) | 94.63 (17.8%) | 25.37 (18.4%) | 3.50 (20.5%) | 5.83 (39.4%) | 11.43 (30.1%) | 12.46 (30.9%) | 3.20 (36.7%) | 3.33 (45.6%) |
| high column density, low temperature (4%) | 38.18 (3.9%) | 18.30 (3.4%) | 6.21 (4.5%) | 1.20 (7.0%) | 0.44 (3.0%) | 1.25 (3.3%) | 1.99 (4.9%) | 0.74 (8.5%) | 1.30 (17.8%) |
| high column density, high temperature, without KL and Orion South (6%) | 159.07 (16.4%) | 67.66 (12.8%) | 17.31 (12.6%) | 2.13 (12.5%) | 4.59 (31.0%) | 8.18 (21.6%) | 8.71 (21.6%) | 2.16 (24.8%) | 1.90 (26.1%) |
| low column density (89%) | 615.62 (63.5%) | 397.06 (74.8%) | 108.05 (78.5%) | 13.08 (76.6%) | 5.50 (37.2%) | 11.85 (31.2%) | 19.73 (49.0%) | 4.23 (48.6%) | 3.46 (47.4%) |
| low temperature (49%) | 278.31 (28.7%) | 166.13 (31.3%) | 57.61 (41.9%) | 9.16 (53.6%) | 1.62 (11.0%) | 4.47 (11.8%) | 9.46 (23.5%) | 2.52 (28.9%) | 3.51 (48.1%) |
| low column density, low temperature (44%) | 239.61 (24.7%) | 148.29 (27.9%) | 51.34 (37.3%) | 7.90 (46.2%) | 1.29 (8.7%) | 3.13 (8.2%) | 7.54 (18.7%) | 1.76 (20.2%) | 2.18 (29.9%) |
| low column density, high temperature (45%) | 378.41 (39.0%) | 254.99 (48.1%) | 56.69 (41.2%) | 5.16 (30.2%) | 4.15 (28.0%) | 8.77 (23.1%) | 12.80 (31.8%) | 2.36 (27.1%) | 1.14 (15.7%) |
| high temperature, without KL and Orion South (50%) | 526.52 (54.3%) | 319.39 (60.2%) | 73.70 (53.6%) | 6.99 (40.9%) | 8.97 (60.6%) | 17.72 (46.7%) | 22.55 (56.0%) | 4.53 (52.0%) | 3.12 (42.8%) |
| H II (3%) | 85.87 (8.9%) | 40.01 (7.5%) | 6.46 (4.7%) | 0.59 (3.5%) | 1.73 (11.7%) | 4.68 (12.3%) | 4.67 (11.6%) | 0.70 (8.0%) | 0.25 (3.4%) |
| radical region (2%) | 47.41 (4.9%) | 20.69 (3.9%) | 5.99 (4.4%) | 0.75 (4.4%) | 1.22 (8.2%) | 1.95 (5.1%) | 2.16 (5.4%) | 0.79 (9.1%) | 0.99 (13.6%) |
| dense PDR (2%) | 41.11 (4.2%) | 26.71 (5.0%) | 4.85 (3.5%) | 0.32 (1.9%) | 0.61 (4.1%) | 1.44 (3.8%) | 1.88 (4.7%) | 0.25 (2.9%) | |
| KL and Orion South$^*$ (1%) | 238.08 (24.5%) | 38.24 (7.2%) | 5.21 (3.8%) | 0.83 (4.9%) | 4.16 (28.1%) | 12.54 (33.1%) | 8.28 (20.6%) | 1.66 (19.1%) | 0.44 (6.0%) |

**Figure 3.7:** Total line luminosity (first column) and absolute and relative line luminosities [K km s$^{-1}$pc$^2$] for selected species in the different regions. A region's relative size is given in the brackets beside its name. Regions are generally not disjointed, but overlap to varying degrees. Additionally, rounding uncertainties for both intensities and region sizes accumulate and slightly different detection limits apply for each region. Hence the percentages do not add up to 100% and should be considered as estimates. $^{(*)}$ Approximated as described in Section 3.4.1.

| | $^{12}$CO/$^{13}$CO | $^{12}$CO/C$^{18}$O | $^{13}$CO/C$^{18}$O | HCN/H$^{13}$CN | HCO$^+$/H$^{13}$CO$^+$ | HNC/HN$^{13}$C | CN/HCN | CN/HCO$^+$ | HCN/HNC | HCN/HCO$^+$ | HCN/CO | HCO$^+$/CO | HNC/CO |
|---|---|---|---|---|---|---|---|---|---|---|---|---|---|
| all averaged | 3.86 | 31.05 | 8.05 | 16.79 | 20.63 | >19.17 | 0.74 | 0.70 | 4.36 | 0.94 | 0.07 | 0.08 | 0.02 |
| high column density | 4.34 | 30.66 | 7.06 | 9.55 | 18.57 | 24.60 | 0.51 | 0.59 | 4.94 | 1.16 | 0.18 | 0.16 | 0.04 |
| high column density without KL and Orion South | 3.73 | 27.04 | 7.25 | 16.39 | 15.70 | 21.90 | 0.72 | 0.66 | 3.58 | 0.92 | 0.12 | 0.13 | 0.03 |
| high column density, low temperature | 2.95 | 15.24 | 5.17 | 36.90 | 11.74 | 25.38 | 1.00 | 0.63 | 1.69 | 0.63 | 0.07 | 0.11 | 0.04 |
| high column density, high temperature, without KL and Orion South | 3.91 | 31.75 | 8.12 | 17.95 | 16.89 | 20.25 | 0.79 | 0.74 | 3.79 | 0.94 | 0.12 | 0.13 | 0.03 |
| low column density | 3.67 | 30.35 | 8.26 | >34.00 | 49.90 | >11.98 | 1.28 | 0.77 | 2.80 | 0.60 | 0.03 | 0.05 | 0.01 |
| low temperature | 2.88 | 18.14 | 6.29 | >33.67 | 17.55 | 30.38 | 1.09 | 0.51 | 1.78 | 0.47 | 0.03 | 0.06 | 0.02 |
| low column density, low temperature | 2.89 | 18.78 | 6.50 | >27.26 | 20.57 | >17.05 | 0.88 | 0.37 | 1.78 | 0.41 | 0.02 | 0.05 | 0.01 |
| low column density, high temperature | 4.50 | 49.46 | 10.99 | 34.32 | 30.98 | >13.32 | 0.74 | 0.51 | 3.72 | 0.69 | 0.03 | 0.05 | 0.01 |
| high temperature, without KL and Orion South | 4.33 | 45.72 | 10.55 | 22.04 | 23.81 | >23.42 | 0.72 | 0.57 | 3.92 | 0.79 | 0.06 | 0.07 | 0.01 |
| H II | 6.20 | 67.29 | 10.86 | 20.39 | 23.79 | 28.21 | 0.59 | 0.59 | 6.72 | 1.00 | 0.12 | 0.12 | 0.02 |
| radical region | 3.45 | 27.46 | 7.95 | 16.39 | 12.67 | 18.35 | 1.33 | 1.20 | 2.47 | 0.90 | 0.09 | 0.10 | 0.04 |
| dense PDR | 5.51 | 82.74 | 15.03 | 30.20 | 62.55 | >17.21 | 0.85 | 0.65 | 5.70 | 0.76 | 0.05 | 0.07 | 0.01 |

**Figure 3.8:** Integrated intensity ratios of selected species for the different regions. Lower limits are based on a hypothetical line with the median line width for the respective region and a peak intensity of five times the local noise level. Assuming an uncertainty of 30% for the intensities, all ratios have an uncertainty of $\sim 42\%$. The maximum and minimum value of the colour bar are not defined globally, but for every ratio (column) individually.

## 3.5   Discussion

By averaging over the area, we highlight the individual emission profile of the regional spectra, including lower intensity species, while ignoring their actual spatial extent (which here mainly influences the respective noise level). This approach might help to characterise sources for which the spatial resolution is not good enough to differentiate between distinct regions. It is also a different approach compared to the analysis of the Orion B data set (Pety et al. 2017; Gratier et al. 2017; Bron et al. 2018) in the 3 mm window, where the focus is more on selected, typically more luminous transitions, not necessarily on a complete inventory of species. We discuss our findings further in this section and compare them with results from other authors.

We find that temperature has a significant impact on the total intensities of our selected regions; considering column density alone is not sufficient. This is illustrated most obviously in the cases of the 'high column density, low temperature' and 'H II' regions. The former has higher column densities but low overall emission, while the latter has lower median column density but a factor of $\approx 2.6$ higher total intensity (total intensity summed over all considered species). We mostly consider temperatures and column densities, but it also seems instructive to keep the main feedback processes in different regions in mind. While the column densities in OMC-2/3 are similar to values found in parts of OMC-1, the energy input in the former is mainly driven by outflows from low-mass protostars, while in the latter it is shared between outflows and feedback from the H II region, as discussed in Berné et al. (2014) and inferred from CO and $^{13}$CO $2-1$ emission. The kinetic energy in KL was found to be dominated by feedback of massive protostars (outflows, jets, explosive motion). In contrast, the Bar exhibits very little outflow activity; its kinetic energy is mainly caused by the expanding H II region.

We find very similar total CO intensities for the 'high column density' and 'dense PDR' regions ($\sim 393$ K km s$^{-1}$ and $\sim 392$ K km s$^{-1}$), but their total intensities summed over all species vary by more than 50% ($\sim 1360$ K km s$^{-1}$ and $\sim 603$ K km s$^{-1}$). While the different column densities and temperatures in the two regions still result in similar CO intensities, other species react very differently and are much more enhanced in the 'high column density' region. This might again be partly due to opacity effects and CO only tracing the outer layers.

The median column densities for the 'dense PDR' and 'H II' regions are about a factor of 3 lower than for 'high column density' and 'high column density, high temperature without KL and Orion South', but their median temperatures are the highest for all considered regions. This might explain their high emission despite overall lower column densities.

### 3.5.1   Correlations

For the further examined most luminous species, strong correlations are typically found between high-density tracers, excluding N$_2$H$^+$. This may be related to the optical depth effects mentioned before, but also to the influence of temperature, as shown in the case of the warm 'dense PDR' region, where N$_2$H$^+$ does not emit over $5\sigma$ despite enhanced column densities. N$_2$H$^+$ shows no correlation with any other prevalent species in the 1.3 mm window, but instead with column density. If N$_2$H$^+$ data is not available, HNC might overall be a better tracer of column density than HCN or HCO$^+$, for example. HNC shows similar intensities to N$_2$H$^+$, however, so it should not be a question of observation time. That HCN does not exclusively trace dense gas was also shown in Kauffmann et al. (2017) for the $1-0$ transition in Orion A, where HCN was found to trace lower densities $\sim 10^3$ cm$^{-3}$ in cold sections of the cloud. Additionally, they found that the cold dense gas emits

too little HCN to explain the luminosities observed in extragalactic sources. This is consistent with the below average emission we see for the OMC-2/3 region in our data ('high column density, low temperature').

Different papers discuss additional mechanisms which may excite 'dense gas' tracers. As elaborated in Goldsmith & Kauffmann (2017), electron excitation may be important for high-dipole moment molecules in regions where the fraction of ionised carbon is significant. The low-J transitions of HCN (but also HCO$^+$, CN, and CS) could thus be observed in lower density environments and may not qualify as indicators of high density. Another mechanism could be radiative trapping (Shirley 2015; Pety et al. 2017). It is argued that fundamental lines of HCN, HNC, and HCO$^+$ could be excited in regions well below their critical density as the latter is computed assuming optically thin emission only. Both mechanisms could explain our observations. Particularly in OMC-1, where C$^+$ is abundant (Pabst et al. 2019), the emission of HCN, for example, may originate in part from electron excitation. Additionally, some transitions may have a high optical depth, increasing contributions from photon-trapping. An alternative approach to the detection of low-lying rotational lines is discussed in Liszt & Pety (2016). They discuss the observability of transitions for HCO$^+$, HNC, and CS in regions where the density is far below the critical density. The authors find, in the limit of weak collisional excitation, that there is a column density (not a volume density) that will produce a given output.

We find that the typical UV tracers CN and C$_2$H correlate not only with each other, but also strongly with high-density tracers. This means that tracing UV illumination on large scales could be challenging, as enhanced CN or C$_2$H emission might not necessarily be indicative of higher UV illumination.

### 3.5.2   Emission on larger scales

The stark difference in the emission profile of KL and Orion South (see Section 3.4.1) compared to the other regions was also found for some species in Ungerechts et al. (1997), where the integrated intensity maps of SO or HC$_3$N showed distributions strongly peaked towards KL. While we find that line emission from KL and Orion South has a noticeable impact on spectra averaged over larger scales (compare Fig. B.4a and B.4b, but also appreciate that SiO and SO$_2$ are detectable in the averaged spectrum despite not being detected for the majority of regions), this influence of high column density regions on the averaged spectrum was not seen by Watanabe et al. (2017) for the spectrum of W51 in the 3 mm window. Their spatial coverage of 39 pc $\times$ 39 pc is significantly larger than for our data set, so emission from high-density regions is expected to be smeared out more, such that they find a dominance of the quiescent material over the averaged spectrum.

In their analysis of a line survey of the central parts of the starburst galaxy M82 in the 1.3 mm and 2 mm window, Aladro et al. (2011) found that the physical processes are dominated by PDRs. Arguing that feedback from young OB stars leaves an imprint on molecular composition in the form of an overabundance of CO$^+$, HCO, c-C$_3$H$_2$, and CH$_3$CCH, for example, they find M82 to match these criteria. While we can confirm the high c-C$_3$H$_2$ emission in our dense PDR region, CH$_3$CCH is below the 5$\sigma$ limit there. This is also interesting because their spatial resolution varies between 158 pc and 333 pc, which is 2 to 3 orders of magnitude higher than our averaged spectra, but we observe CH$_3$CCH emission as quite compact and thus strongly diluted on larger scales. The noise levels are comparable in both studies, $\sim 3-8$ mK for M82, around $8-20$ mK median noise for the different regions in our Orion data.

### 3.5.3 Line ratios on larger scales

Line ratios seem to be more ambiguous on large scales, where both $CN(\Sigma)/HCN(3-2)$ and $CN(\Sigma)/HCO^+(3-2)$ do not clearly highlight regions with enhanced UV irradiation. We can confirm a correlation between $HCN(3-2)/HNC(3-2)$ and temperature. On even larger scales, however, as examined by Meier & Turner (2005), among others, for the nuclear region of IC 342 in the 3 mm window ($\sim 50$ pc resolution), the ratio seems to be fairly constant and not related to (kinetic) temperature. Their value of $HCN(1-0)/HNC(1-0) \approx 1-2$ is found in our data set for those regions associated with low temperature (see Fig. B.7c). The considered transitions are different to ours, but both species still have comparable upper energies, such that a comparison seems meaningful.

Extragalactic studies like that of Jiménez-Donaire et al. (2017), where the $1-0$ transitions of HCN, $HCO^+$, HNC, and some of their isotopologues are mapped for six nearby galaxies (a few hundred pc to $\sim 1$ kpc resolution), use spectral stacking to maximise the signal-to-noise ratio for the examined lines. The resulting line ratios of $HCN(1-0)/HCO^+(1-0)$ are higher than seen for our regions ($HCN(1-0)/HCO^+(1-0) = 1.0-1.7$ vs. $HCN(3-2)/HCO^+(3-2) = 0.4-1.2$, see also Fig. 3.8). Instead, our ratio values are comparable to those found by Harada et al. (2018) in the two nuclei of Merger NGC 3256 (likewise examining the $1-0$ transitions, $\sim 300$ pc resolution), although the ratio is critically discussed in this context mainly as a diagnostic for AGN and/or starburst galaxies. Dense gas tracers ($1-0$ transitions) for nine nearby massive spiral galaxies were further examined for the EMPIRE survey (Jiménez-Donaire et al. 2019), a continuation of these authors' 2017 work. Their Table 4 shows the dense gas line ratios averaged over their galaxy sample, separated into the center (inner $30''$, $1-2$ kpc resolution) and the disc. Their values of $\sim 0.018 - 0.034$ for the $HCN(1-0)/CO(1-0)$ ratio are found in our 1.3 mm data for regions associated with low column density and low temperature, while higher column density regions have a higher value (e.g. $HCN(3-2)/CO(2-1) = 0.18$ for the 'high column density' environment). Our $HCO^+/CO$ values are always higher than theirs ($HCO^+(3-2)/CO(2-1) \sim 0.050-0.156$ vs. $HCO^+(1-0)/CO(1-0) \sim 0.014-0.025$), the most similar again associated with lower column density regions. Their values for $HNC(1-0)/CO(1-0)$ ($\sim 0.010-0.014$) can also be found in our data, where we find deviations towards higher values to be associated with higher column density regions (e.g. $HNC(3-2)/CO(2-1) \sim 0.04$ for the 'high column density' environment).

The correlation of $N_2H^+(3-2)/CH_3OH(\Sigma)$ with temperature we found on larger scales might be explained both with the temperature sensitivity of $N_2H^+$ and the association of $CH_3OH$ with shocks. If temperatures rise, more CO can enter the gas phase and subsequently destroy $N_2H^+$, while more $CH_3OH$ evaporates.

## 3.6 Summary

We have conducted an imaging line survey of OMC-1 to OMC-3 from 200.2 to 281.8 GHz and examined the emission of distinct regions. These were selected to represent regimes of low or high column density and differing temperature, but also to cover the influence of UV irradiation. By contrasting their emission with each other, we aim to provide templates for the interpretation of other more distant, spatially unresolved sources. Comparing spectra from these unresolved sources with our different templates might reveal similarities that can help to further characterise the distant object. The transitions of the 29 species (55 isotopologues) listed in Table A.1 were considered for the analysis. The integrated intensity of a given species is considered here to be the sum over all of

their respective transitions. From our analysis we would like to highlight the following results:

1. Line emission from an Orion KL-like source can contribute significantly to spectra averaged over larger regions, both in terms of averaged total intensity and chemical diversity. In terms of line luminosities, KL and Orion South contribute around 25% of all emission in the 1.3 mm window in the area of OMC-1 to OMC-3.

2. Regions like OMC-2/3, with pre-stellar Class 0 and Class I objects and enhanced column density but low temperature, have a much lower total intensity. Their signatures (e.g. high $N_2H^+$ emission coincident with a low $HCN(3-2)/HNC(3-2)$ ratio) would be difficult to pick up in a non-resolved source.

3. While the contribution of CO to the share of the total intensity can vary more strongly in the examined 1.3 mm window, $HCO^+(3-2)$ contributes $\sim 3\% - 6\%$ in all cases (average $\approx 4\%$). This seems to hold true even in the case of the emission around KL and Orion South.

4. The emissions of the high-density tracers HCN, $HCO^+$, $H_2CO$, HNC, CS, but also CN are strongly correlated with each other, but not with $N_2H^+$. Of all the examined species, $N_2H^+$ shows the strongest correlation with column density. If $N_2H^+$ observations are not available, HNC seems to trace the column density most reliably.

5. Around 50% of the line luminosity of $HCO^+$ and HNC in the 1.3 mm window comes from lower column density material, for CS and HCN $\sim 35\%$.

6. The ratios $HCN(3-2)/HNC(3-2)$ and $N_2H^+(3-2)/CH_3OH(\Sigma)$ may be related to temperature.

7. Identifying UV illuminated material on large scales seems to be challenging, as both $CN(\Sigma)/HCN(3-2)$ and $CN(\Sigma)/HCO^+(3-2)$ show ambiguous results.

# Intriguing CF$^+$ emission in Orion A

The following chapter describes the analysis of the CF$^+$ $J = 2 - 1$ and $J = 3 - 2$ emission lines in Orion A. This closer examination was motivated by the discovery that the $J = 2 - 1$ line was detected in almost all of our selected regions (although not always above the $5\,\sigma$ threshold) discussed in the previous Chapter 3. This observation is quite unexpected from a theoretical point of view, in which CF$^+$ emission is suggested to be predominantly enhanced in specific environments. After a brief overview of the literature concerning CF$^+$, we will discuss the detections in our original data set and the additional pointed observations done to confirm our findings. Our result challenges the notion that CF$^+$ can be used as a reliable tracer for C$^+$ layers in PDRs as proposed in Guzmán et al. (2012a).

## 4.1  Theory: formation of CF$^+$

One of the major cooling lines in the ISM is emitted by the C$^+$ ion (or C II). Singly ionised carbon not only constitutes an important reservoir of carbon, but the C II fine structure line is widely used in the Milky Way to e.g. trace PDRs and CO-dark molecular gas[1], and also in external galaxies to measure their star formation rate (Wiesenfeld & Goldsmith 2014 and references therein, e.g. Stacey et al. 2010). At a frequency of around 1.9 THz (or a wavelength of $\sim 158\ \mu$m) however, Earth's atmosphere is opaque and the C$^+$ line therefore not observable from the ground. This is where CF$^+$ may prove to be valuable: due to its chemistry (to be discussed below), it is suggested as a proxy for C$^+$ (mainly in PDRs) that is easily observed because its rotational transitions lie in frequency regimes accessible by ground based telescopes. As a simple diatomic molecule, the frequencies of the low-$J$ transitions of CF$^+$ are well spaced out, starting at around 102 GHz ($J = 1 - 0$), followed by 205 GHz ($J = 2 - 1$), and 307 GHz ($J = 3 - 2$). One may thus still profit from some of the tracing capabilities of C$^+$, while circumventing the need for costly observations with airborne/space based telescopes (Guzmán et al. 2012a).

The chemistry of CF$^+$ is governed by a very limited number of reactions. Its formation occurs in the sequence

$$\mathrm{F} + \mathrm{H_2} \ \rightarrow \ \mathrm{HF} + \mathrm{H} \tag{4.1}$$

$$\mathrm{C^+} + \mathrm{HF} \ \rightarrow \ \mathrm{CF^+} + \mathrm{H} \quad , \tag{4.2}$$
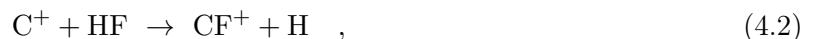
while it is primarily destroyed by dissociative recombination:

$$\mathrm{CF^+} + e^- \ \rightarrow \ \mathrm{C} + \mathrm{F} \quad . \tag{4.3}$$

---

[1]While hydrogen is present mainly in the form of H$_2$ in these regions, carbon is not in its molecular form of CO because of e.g. too low column densities (Pineda et al. 2013). At comparable column densities, the self-shielding of CO is less efficient than that of H$_2$. As a consequence, these regions are neither detected in H I (atomic hydrogen), nor CO emission lines. Without C$^+$, this component of the ISM would thus remain largely unobservable.

This simplicity is owed to some unique characteristics of the fluorine chemistry. Fluorine is the only light atom reacting exothermically with H$_2$ (Neufeld et al. 2005), such that the path of Eqn. 4.1 is readily available even in cold environments. This reaction has been experimentally examined (Dagdigian et al. 2019 and reference therein, Tizniti et al. 2014) and was found to occur down to temperatures < 20 K due to quantum-mechanical tunneling overcoming the initial $\sim$ 800 K activation barrier. As an easily formed and very stable hydride, HF accounts for a significant fraction of interstellar gas phase fluorine (Gerin et al. 2016).

In the presence of C$^+$, HF then reacts to form CF$^+$ (Eqn. 4.2). The rate of this reaction has not been measured experimentally, but successive improvements to theoretical approaches have resulted in better agreement between observations and chemical models (Dagdigian et al. 2019, Denis-Alpizar et al. 2018). The rate of the destructive reaction (Eqn. 4.3) has been inferred from storage ring experiments (Novotny et al. 2005). Photodissociation, as another way to destroy CF$^+$, is thought to be irrelevant in most cases (see e.g. Guzmán et al. (2012a) and their analysis of CF$^+$ in the Horsehead nebula).

Theoretical considerations (Neufeld et al. 2005, 2006) thus concluded that CF$^+$ should be observable in regions where both HF and C$^+$ are present. These conditions are met in PDRs, where there is substantial overlap between the molecular material where HF forms, and the illuminated surface layers of the cloud where C$^+$ is prevalent. Consequently, CF$^+$ emission lines have been observed in the Orion Bar (Neufeld et al. 2006; Nagy et al. 2013) and the Horsehead PDRs (Guzmán et al. 2012a). In absorption, CF$^+$ was detected in the diffuse ISM (Liszt et al. 2014) and extragalactic sources (Muller et al. 2016).

### 4.1.1 Abundance of CF$^+$

Under the assumptions that CF$^+$ is predominantly destroyed via dissociative recombination and the free electron density is everywhere equal to the C$^+$ density, Dagdigian et al. (2019) argue that $N(\mathrm{CF}^+)/N(\mathrm{HF}) = k_\mathrm{F}/k_\mathrm{DR}$, where $k_\mathrm{F}$ and $k_\mathrm{DR}$ are the rate coefficients for the formation and destruction of CF$^+$, respectively[2]. With $k_\mathrm{F}$ from Dagdigian et al. (2019) (for the reaction of the ground $j = \frac{1}{2}$ spin-orbit state) and $k_\mathrm{DR}$ from Novotny et al. (2005), we obtain

$$
\begin{aligned}
N(\mathrm{CF}^+)/N(\mathrm{HF}) &= \frac{4.33 \times 10^{-9} \times \left(\frac{T}{300}\right)^{-0.425} \times \exp\left(-\frac{18.29}{T}\right) \text{ cm}^3 \text{ s}^{-1}}{5.2 \times 10^{-8} \times \left(\frac{T}{300}\right)^{-0.8} \text{ cm}^3 \text{ s}^{-1}} \\
&\approx 0.01 \times \exp\left(\frac{-18.29}{T}\right) \times T^{0.375} \quad ,
\end{aligned}
\tag{4.4}
$$

such that the ratio rises with temperature. For a given temperature, the ratio is constant, regardless of density. This is because, while CF$^+$ does form more efficiently in regions with more C$^+$ (like a PDR), the equally rising number of electrons will also destroy it. With increasing temperature (and larger electron velocities), the chance of CF$^+$ to capture an electron decreases, leading to a larger $N(\mathrm{CF}^+)/N(\mathrm{HF})$ abundance ratio. For, e.g., $T = 20$ K, the abundance ratio is predicted to be $\sim$ 0.012, while it is $\sim$ 0.029 for $T = 50$ K. For our data, this means that to first order we expect more CF$^+$ in warm regions. In absolute numbers, we naturally also expect CF$^+$ to increase with column density if the latter is a consequence of larger volumes and thus longer sightlines, rather than of increasing volume density.

---

[2]The ratio was already discussed in Neufeld et al. (2005), but both rates could only be estimated at the time, as no experimental measurements or results from dedicated computations were available.

However, $k_\mathrm{F}$ has not been measured experimentally and several estimates besides the one used above are published in the literature. Figure 4.1 (modified from Dagdigian et al. (2019), their Fig. 2b) illustrates that these reaction rates differ significantly in the low temperature regimes relevant to molecular clouds. While $k_\mathrm{F}$ from Dagdigian et al. (2019) initially rises with temperature, $k_\mathrm{F}$ from Neufeld & Wolfire (2009) and Wakelam et al. (2012) always decreases. The calculations in Denis-Alpizar et al. (2018) report values for $k_\mathrm{F}$ at temperatures $\geq$ 50 K only. One would need actual measurements of the formation reaction to resolve this contradictory behaviour.
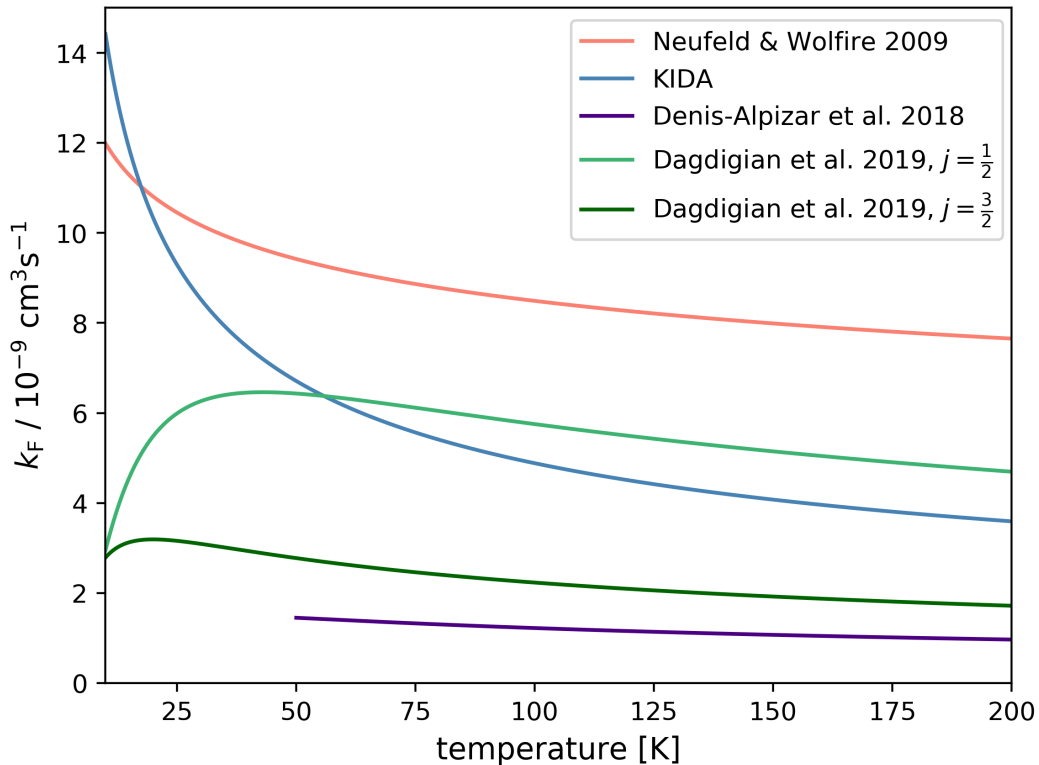


**Figure 4.1:** CF$^+$ formation rate coefficients as a function of temperature used in the literature: Neufeld & Wolfire (2009); Denis-Alpizar et al. (2018); Dagdigian et al. (2019), and the KIDA database (Wakelam et al. 2012, `http://kida.obs.u-bordeaux1.fr`). The plot is modified from Dagdigian et al. (2019).

### 4.1.2 What can we expect for our data?

Based on this theoretical background, the knowledge of previous detections in the Orion Bar, and additional data from C$^+$ observations in Orion A, we can gauge where to anticipate CF$^+$ in our data set. An integrated intensity C$^+$ map of Orion A (Fig. 4.2) was published in early 2019 (Pabst et al. 2019)[3], showing that the emission is strongest in the PDR surrounding the H$_\alpha$ region and is in very general terms concentrated towards OMC-1, with comparatively little emission in OMC-2/3. If the ideas concerning the simple chemistry of CF$^+$ are correct, one would expect most CF$^+$ emission in regions where the depicted C$^+$ emission is strong and overlaps with high density material from the

---

[3]Data products are publicly available via the SOFIA Data Cycle System (`https://dcs.arc.nasa.gov/dataRetrieval/SearchScienceArchiveInfoBasic.jsp`), here specifically the file Cycle4_GR_OT_04_0066_ATielens_Tmb_cube.lmv.

molecular filament, whose contours were added to Fig. 4.2. We see this configuration (at least in projection) in OMC-1. Considering the logarithmic intensity scale in the image, the low intensity of the CF$^+$ line previously detected towards the Orion Bar ($T_{\mathrm{peak}}^{\mathrm{A}} \approx 120 - 150$ mK, Neufeld et al. 2006) and the noise levels in our data, we expect CF$^+$ detections in the PDR and parts of the OMC-1 filament for our averaged regional spectra from Chapter 3. With integrated intensities of C$^+$ lower by a factor of $\sim 10$ and smaller column densities, we do not expect to observe CF$^+$ emission in averaged OMC-2/3 spectra.

Our initial findings are discussed in Section 4.2. Additional pointed observations towards selected positions were conducted at a later date (May to December 2019) and will be presented in Section 4.3.

## 4.2 Previous CF$^+$ detections in averaged spectra

With our coverage of the 1.3 mm window, data for the $J = 2 - 1$ transition at around 205 GHz is available from the imaging line survey described in Chapter 3. As the CF$^+$ line is quite weak, we were unable to map the emission due to noise levels being too high (see also Fig. B.8). But as seen in the previous chapter (see also Table 3.4), the line becomes detectable in spectra averaged over larger areas.

All CF$^+$ lines from our averaged spectra are shown in Fig. 4.3, and the results of single Gaussian fits compiled in Table 4.1[4]. Note that the listed uncertainties for position and width are from the Gaussian fits only and additional uncertainties arise due to the unresolved hyperfine structure of CF$^+$ (Guzmán et al. 2012b). A visual inspection of the spectra, together with the consistency of central velocities and line widths with those of other molecular species, suggests that CF$^+$ may be considered 'detected' in all but two cases, despite line intensities $< 5\sigma$ for most regions. In regions 11 ('H$_\alpha$') and 12 ('radical region'), the noise levels are too high for a confident detection. The CF$^+$ line is indeed brightest in the PDR, but the other regions exhibit emission with very similar intensities. The results of the CF$^+$ line fits (varying by maximally $\sim 60\%$ for both peak temperature and integrated intensity) lie within the same order of magnitude, despite large gradients in C$^+$ emission and differences in column density. On these large scales then, CF$^+$ emission alone does not seem to be a reliable indicator of the presence of a PDR. The fairly uniform appearance, together with our unsuccessful mapping of the line (with an rms noise of around 0.15 K), rather points towards generally extended emission with no strong compact sources.

## 4.3 Additional pointed observations

After the unexpected detections of CF$^+$ in averaged spectra of OMC-2/3, we decided to conduct further pointed observations towards eight selected positions (see Table 4.2), which are highlighted in Fig. 4.2. Selection criteria were enhanced 1300 $\mu m$ emission (MMS and FIR sources, see Chini et al. 1997) and higher C$^{18}$O intensities at positions of known young stellar objects (HOPS sources, see Furlan et al. 2016). With this we intend to probe emission on smaller scales compared to the large scales of the averaged spectra (Section 4.3.1).

For a definitive confirmation that the line is real to begin with and can be attributed to CF$^+$, we additionally observed the 307 GHz ($J = 3 - 2$) transition for three of the eight sources using the

---

[4]Due to rounding uncertainties, the exact fit values for e.g. the peak temperature may differ in the order of a few mK from our analysis in Chapter 3, resulting in slight differences compared to Table 3.4. This has no qualitative impact on the analysis, but as the signal-to-noise ratio is in all cases small to begin with, it can decide whether CF$^+$ is considered 'detected' or not with the strict $5\sigma$ criterion of in the automated procedure used in Chapter 3.
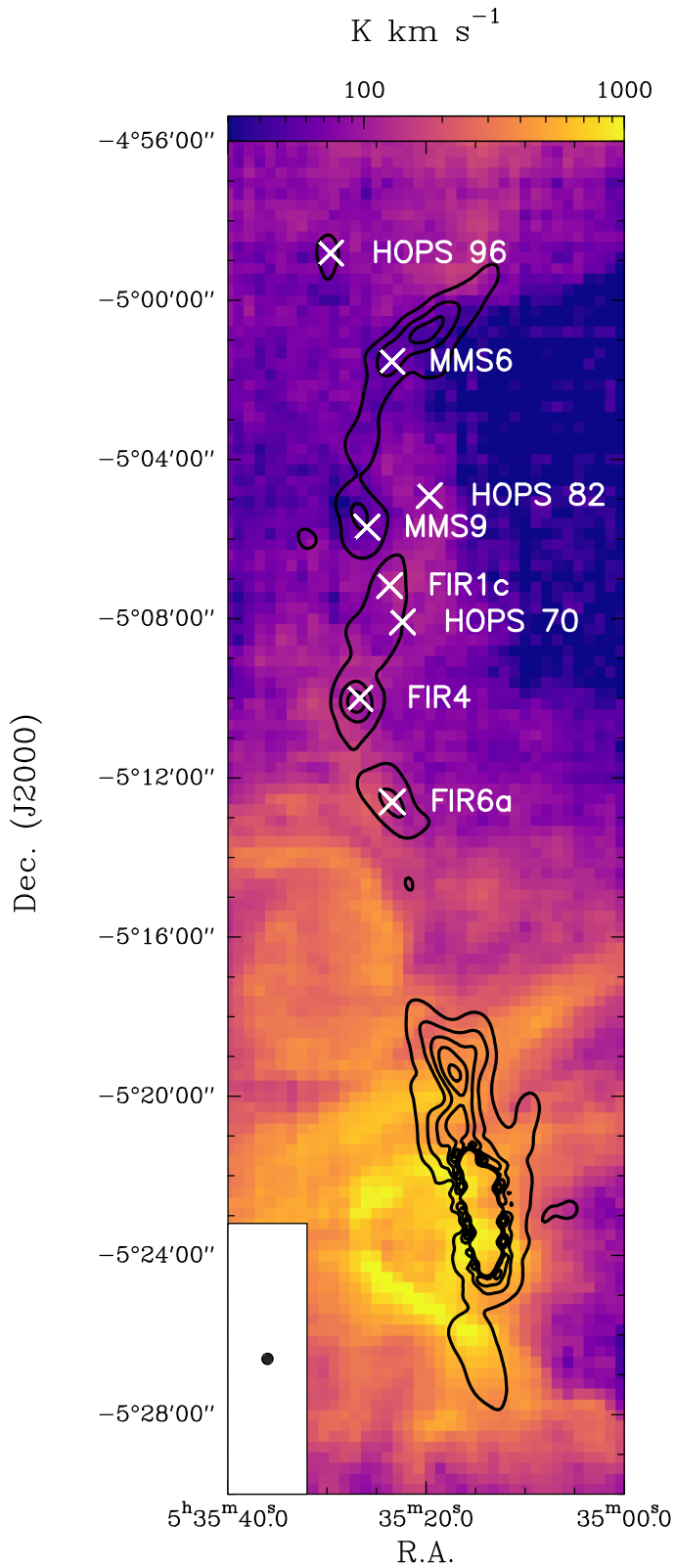
**Figure 4.2:** Integrated intensity [-5, 15] km s$^{-1}$ C II emission in Orion A, part of the larger map published in Pabst et al. (2019). The eight marked positions show our additional pointed observations discussed in Section 4.3, while the contours are from dust inferred H$_2$ column density (Guzmán et al. 2015).

CII at 158 $\mu$m with
H$_2$ column density contours

**Table 4.1:** Results for single Gaussian fits of CF$^+$ in the averaged spectra.

| region | $T_{peak}$ [mK] | area [mK km s$^{-1}$] | $\Delta$area [mK km s$^{-1}$] | position [km s$^{-1}$] | $\Delta$position [km s$^{-1}$] | width [km s$^{-1}$] | $\Delta$width [km s$^{-1}$] | $\sigma$ [mK] | label |
|---|---|---|---|---|---|---|---|---|---|
| all averaged | 35 | 140 | 15 | 10.37 | 0.18 | 3.80 | 0.56 | 7 | 1 |
| high density | 51 | 242 | 22 | 9.47 | 0.20 | 4.45 | 0.44 | 11 | 2 |
| high density without KL and Orion South | 51 | 209 | 19 | 9.75 | 0.17 | 3.86 | 0.38 | 10 | 3 |
| high density, low temperature | 70 | 161 | 24 | 10.56 | 0.16 | 2.14 | 0.36 | 17 | 4 |
| high density, high temperature, without KL and Orion South | 59 | 207 | 23 | 9.25 | 0.18 | 3.27 | 0.47 | 12 | 5 |
| low density | 35 | 125 | 16 | 10.51 | 0.18 | 3.38 | 0.60 | 7 | 6 |
| low temperature | 53 | 116 | 15 | 10.70 | 0.13 | 2.08 | 0.31 | 10 | 7 |
| low density, low temperature | 51 | 112 | 16 | 10.72 | 0.14 | 2.08 | 0.34 | 11 | 8 |
| low density, high temperature | 29 | 155 | 20 | 9.74 | 0.33 | 5.06 | 0.74 | 9 | 9 |
| high temperature without KL and Orion South | 31 | 160 | 19 | 9.66 | 0.28 | 4.81 | 0.63 | 8 | 10 |
| H$_\alpha$ | 38 | 258 | 58 | 9.09 | 0.71 | 6.44 | 1.74 | 22 | 11 |
| radical region | 48 | 128 | 28 | 9.31 | 0.29 | 2.54 | 0.56 | 18 | 12 |
| PDR | 86 | 245 | 38 | 10.10 | 0.20 | 2.69 | 0.51 | 22 | 13 |

seven pixel LASMA receiver (Section 4.3.2). As the beam sizes of PI230 and LASMA are different ($\sim 30''$ vs. $\sim 20''$), we will not be able to reliably infer more information regarding the excitation of CF$^+$, but we will get some insight into its smaller scale distribution, as the seven pixels cover different positions on the sky.

### 4.3.1　Pointed observations: PI230

As with our line imaging survey described in the previous chapter, we used the reference position $\alpha_{2000} = 5^h31^m14.5^s$, $\delta_{2000} = -5°52'29.0''$. The chosen frequency setting covers the frequency ranges of $204.2 - 212.0$ GHz and $220.0 - 227.8$ GHz. Integration times on source varied between $\sim 12$ min for FIR6A and $\sim 64$ min for HOPS 70, but were around $\sim 30$ min for most sources. The different integration times are mostly owed to Orion getting into sun avoidance during the observing period. We used main beam efficiencies of $\eta_{mb}^0 = 0.77$ (May) and $\eta_{mb}^0 = 0.80$ (July and August) with an assumed surface accuracy of $\sigma = 15$ $\mu$m to correct the data.

#### 4.3.1.1　Line contamination

The challenge with the the $J = 2 - 1$ transition at 205170.520 MHz is the overlap with the $J = 11_{1,11,0} - 10_{1,10,0}$ transition of CH$_3$CHO at 205170.686 MHz (Fechtenbaum et al. 2015). As a complex molecule, CH$_3$CHO is expected to have a significant abundance mainly in warm, high density regions and to express quite compact emission. As such, contamination was not found to be an issue in the spectra averaged over larger regions discussed above, where no blending with

**Table 4.2:** Coordinates of the eight observed sources in OMC-2/3.

| source | $\alpha_{\mathrm{J2000}}$ | $\alpha_{\mathrm{J2000}}$ | column density [cm$^{-2}$] | $\int_5^{15} T_{\mathrm{mb}}(\mathrm{C}^+)dv$ [K km s$^{-1}$] | $T_{\mathrm{dust}}$ [K] | $T_{\mathrm{gas}}$ [K] | label |
|---|---|---|---|---|---|---|---|
| FIR6A | 05:35:23.4 | -05:12:36.00 | $5.93 \times 10^{22}$ | 113.5 | 20.15 | 19.42 | a |
| FIR4 | 05:35:26.7 | -05:10:00.00 | $8.39 \times 10^{22}$ | 106.7 | 23.77 | 26.06 | b |
| HOPS 70 | 05:35:22.4 | -05:08:04.92 | $3.57 \times 10^{22}$ | 92.49 | 20.77 | 21.45 | c |
| FIR1C | 05:35:23.7 | -05:07:10.00 | $4.65 \times 10^{22}$ | 109.0 | 19.35 | 18.97 | d |
| MMS9 | 05:35:26.0 | -05:05:42.00 | $5.49 \times 10^{22}$ | 52.80 | 18.13 | 16.73 | e |
| HOPS 82 | 05:35:19.7 | -05:04:54.48 | $2.53 \times 10^{22}$ | 87.46 | 20.35 | 19.94 | f |
| MMS6 | 05:35:23.5 | -05:01:32.00 | $7.28 \times 10^{22}$ | 48.13 | 17.71 | 17.58 | g |
| HOPS 96 | 05:35:29.7 | -04:58:48.72 | $3.18 \times 10^{22}$ | 73.29 | 18.69 | 17.80 | h |

**Notes.** The positions of FIR and MMS objects were taken from Chini et al. (1997) and converted from B1950 to J2000 epochs to match our coordinate system, HOPS sources are discussed in Furlan et al. (2016) and their coordinates taken from the online resources available under `https://irsa.ipac.caltech.edu/data/Herschel/HOPS/overview.html`.

CH$_3$CHO was observed. However, as we selected most of our eight additional sources at position with higher column density, we cannot rule out contamination.

Fortunately, CH$_3$CHO emission occurs in doublets, in which neighbouring lines should have the same line intensity. This property can be used to gauge the amount (or upper limits) of CF$^+$ emission. Our chosen frequency set-up includes five CH$_3$CHO doublets (see Table 4.3), which also have similar level energies overall, meaning that if we detect one doublet, we expect to also detect the other four.

The plot with all doublets (the first of which may have CF$^+$ emission) for the eight sources is shown in Fig. 4.4. With the exception of FIR4, no source displays emission of CH$_3$CHO doublets. This suggests that the lines detected at the CF$^+$ frequency do indeed belong to CF$^+$ only. For FIR4, we can clearly see contamination with CH$_3$CHO. While doublets 2 to 5 are showing very similar intensities, doublet 1 appears asymmetric. To extract the possible CF$^+$ line there, we subtract one of the CH$_3$CHO lines from the other for all doublets (see Fig. 4.5). If there is only one line left after subtraction, the two lines of a doublet have the same intensity. If there is some feature left after subtraction, the lines do not have the same intensity, suggesting the presence of another species. The decision which line is subtracted from the other is in principle arbitrary, but in our case chosen in regard to the intensity of neighbouring lines (outside the shown windows in Fig. 4.5), which can lead to apparent absorption features in the subtracted image. Indeed we find that the lines in doublets 2 to 5 can be subtracted from each other without a remaining feature (within the noise level), while doublet 1 still shows a feature at the CF$^+$ frequency.

**Table 4.3:** All CH$_3$CHO doublets (E$_{up}$ < 100 K, A$_{ij}$ ≥ 1.0e-04) covered with our frequency set-up.

|  | Frequency [MHz] | E$_{up}$ [K] | G$_{up}$ | A$_{ij}$ [s$^{-1}$] | Transition $J_{K_a, K_c, v}$ |
|---|---|---|---|---|---|
| doublet 1 | 205161.898 | 61.5 | 46 | 2.90e-04 | $11_{1,11,1} - 10_{1,10,1}$ |
|  | 205170.686 | 61.5 | 46 | 2.90e-04 | $11_{1,11,0} - 10_{1,10,0}$ |
| doublet 2 | 208228.560 | 60.5 | 46 | 3.05e-04 | $11_{0,11,2} - 10_{0,10,2}$ |
|  | 208267.045 | 60.4 | 46 | 3.05e-04 | $11_{0,11,0} - 10_{0,10,0}$ |
| doublet 3 | 211243.043 | 70.0 | 46 | 3.09e-04 | $11_{2,10,0} - 10_{2,9,0}$ |
|  | 211273.792 | 70.0 | 46 | 3.09e-04 | $11_{2,10,1} - 10_{2,9,1}$ |
| doublet 4 | 223650.093 | 72.3 | 50 | 3.78e-04 | $12_{1,12,1} - 11_{1,11,1}$ |
|  | 223660.603 | 72.2 | 50 | 3.78e-04 | $12_{1,12,0} - 11_{1,11,0}$ |
| doublet 5 | 226551.622 | 71.4 | 50 | 3.94e-04 | $12_{0,12,2} - 11_{0,11,2}$ |
|  | 226592.725 | 71.3 | 50 | 3.94e-04 | $12_{0,12,0} - 11_{0,11,0}$ |
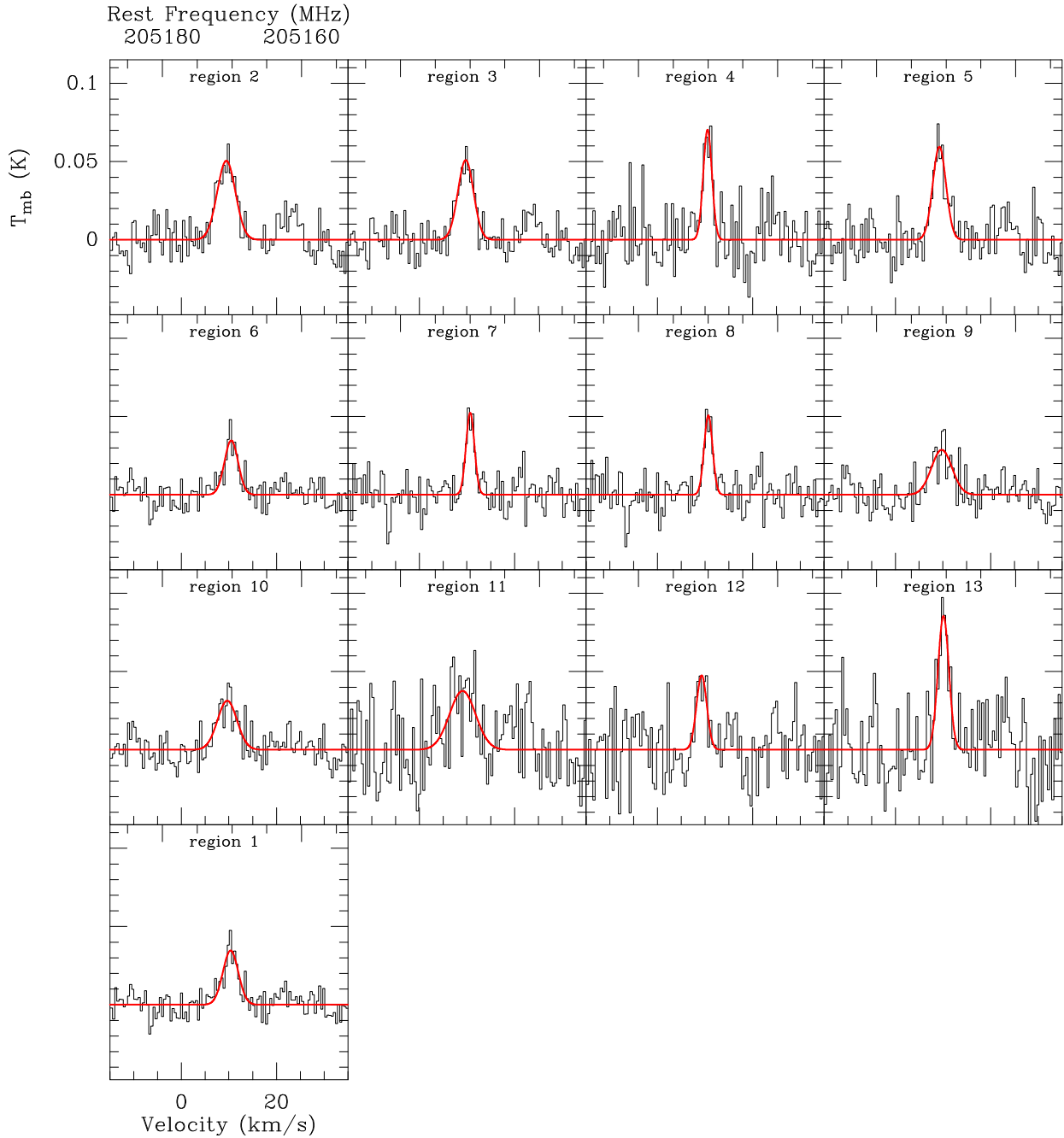
**Figure 4.3:** CF$^+$ line with single Gaussian fit (results in Table 4.1) in the averaged spectra of all regions with identifying labels listed in Table 4.1. For a more direct comparison, the temperature and velocity scales are identical in all images. This highlights the different noise levels of the regions and explains why e.g. the line in region 13 ('PDR') is the strongest in comparison to the others, but considered 'non-detected' in the automated procedure of the previous chapter because of poor signal-to-noise.

**Figure 4.4:** CF$^+$ line and CH$_3$CHO doublets for the pointed observations. The temperature scale is the same for all images. The frequency range is the same within a particular doublet (columns in the image), but varies between different doublets (rows) to always cover both lines (see also Table 4.3 for the respective frequency differences of doublet pairs). Within the noise levels, only FIR4 shows CH$_3$CHO emission. However, all sources show a feature at the CF$^+$ frequency in doublet 1. We aim to extract the CF$^+$ line suggested by the differing line intensities in doublet 1 for FIR4 (see Fig. 4.5).
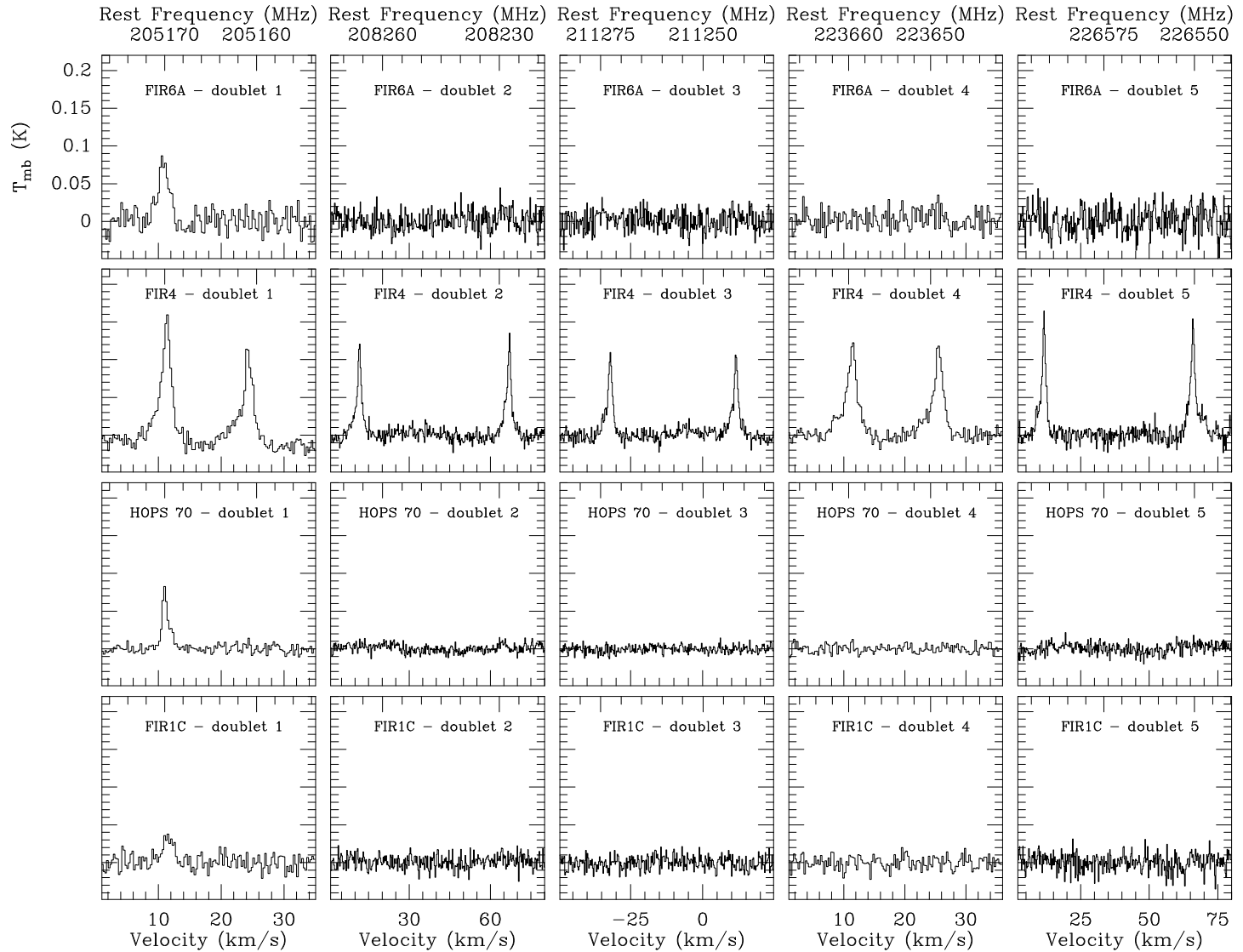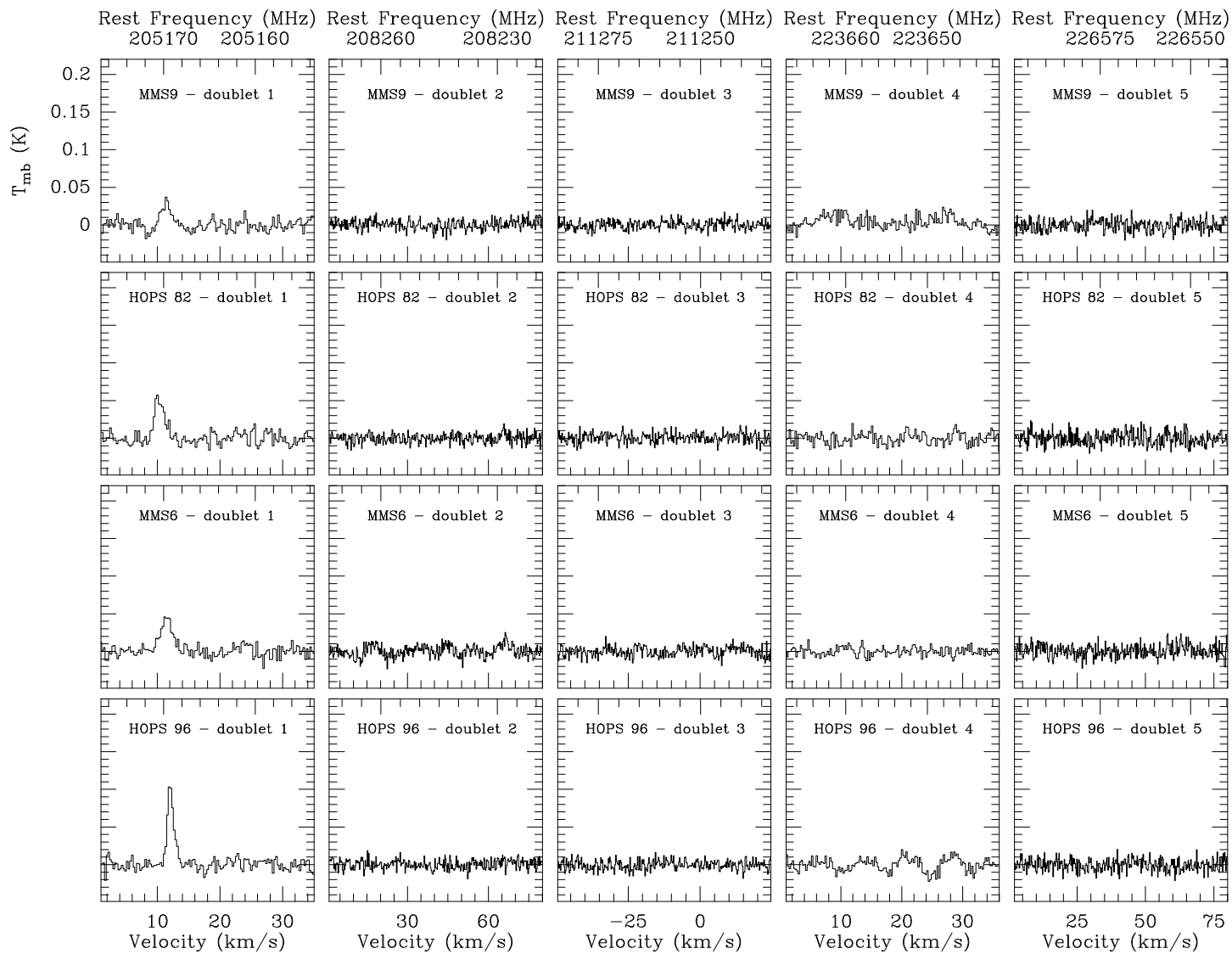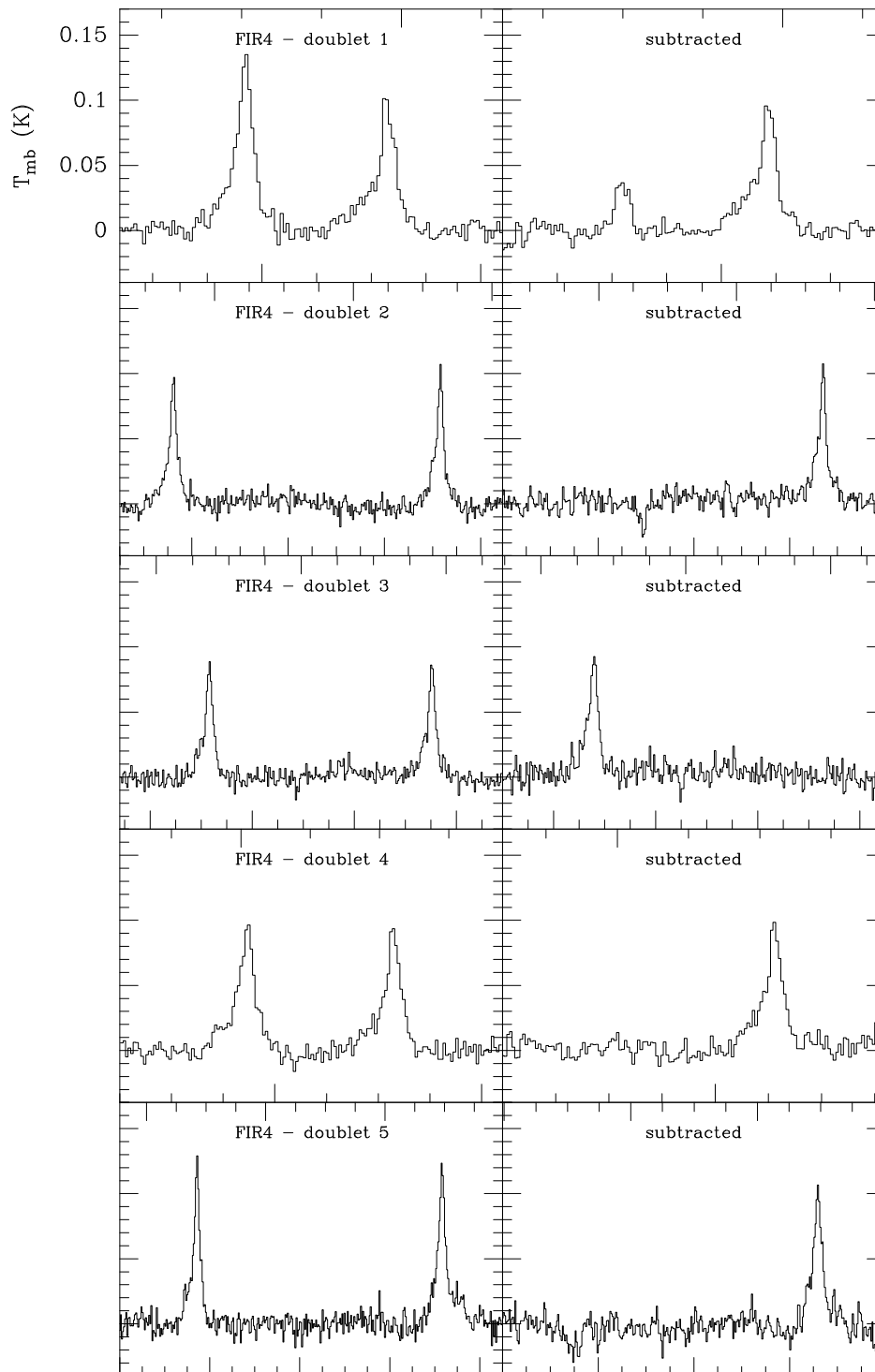
**Figure 4.5:** CH$_3$CHO doublets in FIR4 before and after subtraction of one component. The second line always cancels out in all but the first doublet, where the residual may be identified as the previously blended CF$^+$ line.

#### 4.3.1.2 CF$^+$ detections

The results for Gaussian fits for all CF$^+$ lines are compiled in Table 4.4 (for source FIR4, the residual feature after subtraction of the CH$_3$CHO line was used), showing overall similar peak temperatures, but slightly lower integrated intensities than for the averaged regions. The latter is a consequence of the narrower line widths, which in turn reflect that – in contrast to the large, averaged regions – there are no multiple velocity components for the pointed observations. Consequently, we also used a higher velocity resolution as compared to the averaged spectra (0.2 km s$^{-1}$ instead of 0.4 km s$^{-1}$).

**Table 4.4:** Results for single Gaussian fits of the CF$^+$ $J = 2 - 1$ transition in the pointed observations with PI230.

| region | T$_{peak}$ [mK] | area [mK km s$^{-1}$] | $\Delta$area [mK km s$^{-1}$] | position [km s$^{-1}$] | $\Delta$position [km s$^{-1}$] | width [km s$^{-1}$] | $\Delta$width [km s$^{-1}$] | $\sigma$ [mK] |
|---|---|---|---|---|---|---|---|---|
| FIR6A | 78 | 176 | 16 | 10.84 | 0.10 | 2.13 | 0.23 | 16 |
| FIR4 | 48 | 79 | 6 | 10.96 | 0.06 | 1.54 | 0.13 | 8 |
| HOPS 70 | 71 | 101 | 6 | 11.10 | 0.03 | 1.33 | 0.10 | 6 |
| FIR1C | 34 | 71 | 10 | 11.59 | 0.14 | 1.93 | 0.31 | 11 |
| MMS9 | 31 | 55 | 7 | 11.43 | 0.11 | 1.67 | 0.24 | 8 |
| HOPS 82 | 54 | 103 | 7 | 10.32 | 0.07 | 1.80 | 0.15 | 8 |
| MMS6 | 45 | 103 | 9 | 11.41 | 0.10 | 2.16 | 0.23 | 9 |
| HOPS 96 | 102 | 127 | 6 | 12.11 | 0.03 | 1.17 | 0.06 | 7 |

### 4.3.2 Pointed observations: LASMA

For the higher frequency $J = 3 - 2$ observations with LASMA, we likewise used the reference position $\alpha_{2000} = 5^h31^m14.5^s$, $\delta_{2000} = -5°52'29.0''$, while the frequency setting covered the frequency ranges of $293 - 297$ GHz and $305 - 309$ GHz. Due to time constraints, we only observed three of the eight point sources (FIR6A, HOPS 70, and HOPS 96), which were selected based on their CF$^+$ peak temperature seen in the previously conducted PI230 observations. The seven pixels of the LASMA receiver are arranged in a hexagonal pattern around a central pixel. In the default configuration typically used for mapping (with a derotation angle of 19.1°), this places them at offsets listed in Table 4.5 around the selected coordinates on sky.

We assumed a main beam efficiency of $\eta_{mb} = 0.74$, drawn from the APEX website[5] for December 2019, to correct our data obtained on the 26th and 29th of November, and 2nd of December 2019. Integration times on source varied between $\sim 16$ min for HOPS 70 and $\sim 44$ min for HOPS 96.

#### 4.3.2.1 CF$^+$ detections

At a frequency of $\sim 307$ GHz, we are more sensitive to atmospheric conditions and could not obtain the same noise levels as for the PI230 observations within the available time. However, one may reduce the noise by averaging over all pixels, but will consequently lose information of how

---

[5]http://www.apex-telescope.org/telescope/efficiency/index.php

**Table 4.5:** Pixel offsets for LASMA observations

| pixel | backend LSB | backend USB | offset $\alpha$ [''] | offset $\delta$ [''] |
|-------|-------------|-------------|-------------|-------------|
| 1 | AP-L301-F401 | AP-L308-F402 | +0.1 | 0.0 |
| 2 | AP-L302-F401 | AP-L309-F402 | +31.3 | −27.6 |
| 3 | AP-L303-F401 | AP-L310-F402 | +38.4 | +14.1 |
| 4 | AP-L304-F401 | AP-L311-F402 | +7.1 | +39.5 |
| 5 | AP-L305-F401 | AP-L312-F402 | −32.7 | +24.9 |
| 6 | AP-L306-F401 | AP-L313-F402 | −37.5 | −15.1 |
| 7 | AP-L307-F401 | AP-L314-F402 | −5.6 | −41.3 |

the emission is distributed. As there were issues with pixel 6 at the time of observation, it will be excluded from these averaged spectra. To visualize the observations for our three sources, the images of all seven pixels (arranged to match their offsets) are shown in Figures 4.6, 4.7, and 4.8 together with the respective spectrum averaged over all pixels. Gaussian fit results are listed in Table 4.6, where only lines with detections above $3\,\sigma$ are considered 'detected'. Contamination with other species is not in issue for the $J = 3 - 2$ transition, as neighbouring lines of complex molecules would appear separated with our velocity resolution and have in any event upper energy levels $> 300$ K.

For FIR6A, we have a $\approx 3.0\,\sigma$ detection in the central pixel, but none in the others. The averaged spectrum shows a $\approx 2.7\,\sigma$ feature. This is below our detection criterion, but could be a tentative indication of weak extended emission. Within the inherent uncertainties associated with fits concerning weak detections and the hyperfine structure not being resolved, we see a match between the central velocities and line widths of the $J = 3 - 2$ and $J = 2 - 1$ transitions in the central pixel, confirming the presence of CF$^+$ in the source.

HOPS 70 has no clear detection in the central pixel, but the averaged spectrum shows a $\approx 4.6\,\sigma$ feature at the proper position, and with the proper line width within uncertainties, again supporting the presence of CF$^+$. The $\approx 3.4\,\sigma$ line in pixel 4 appears to be narrower.

In the case of HOPS 96, we benefit from the fact that it previously showed the strongest emission in the $J = 2 - 1$ line and that it got more observation time with LASMA. We hence see detections in four pixels, the strongest in pixel 4 with $\approx 7.6\,\sigma$ and $T_{peak}\sim 106$ mK. The averaged spectrum shows a $\approx 9.1\,\sigma$ line with $T_{peak}\sim 58$ mK. Again, position and line widths agree within the uncertainties with those of the $J = 2 - 1$ transition and corroborate the presence of CF$^+$.

## 4.4 Discussion

The detection of the CF$^+$ $J = 2 - 1$ line in all additional eight point sources supports our previous result of its presence in the averaged spectra. Its correct identification is corroborated by observations of the $J = 3 - 2$ transition. We also used three different frequency settings for the $J = 2 - 1$ line and observed the regions at different times, making an explanation of the line as a spurious
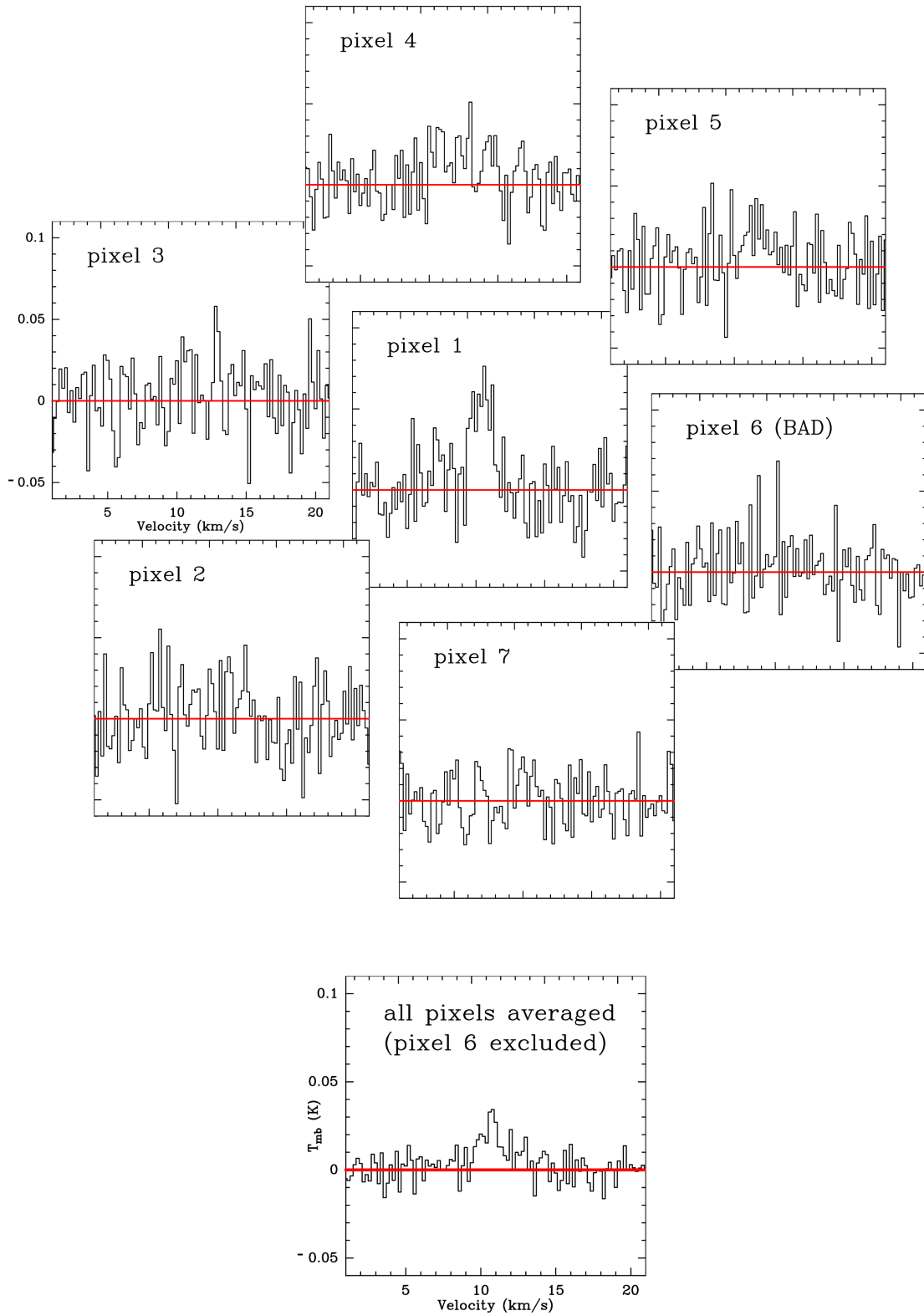
**Figure 4.6:** FIR6A: LASMA observations of the CF$^+$ $J = 3 - 2$ transition. *Top*: Separated into the seven pixels. *Bottom*: Averaged over all pixels to improve the signal-to-noise ratio.
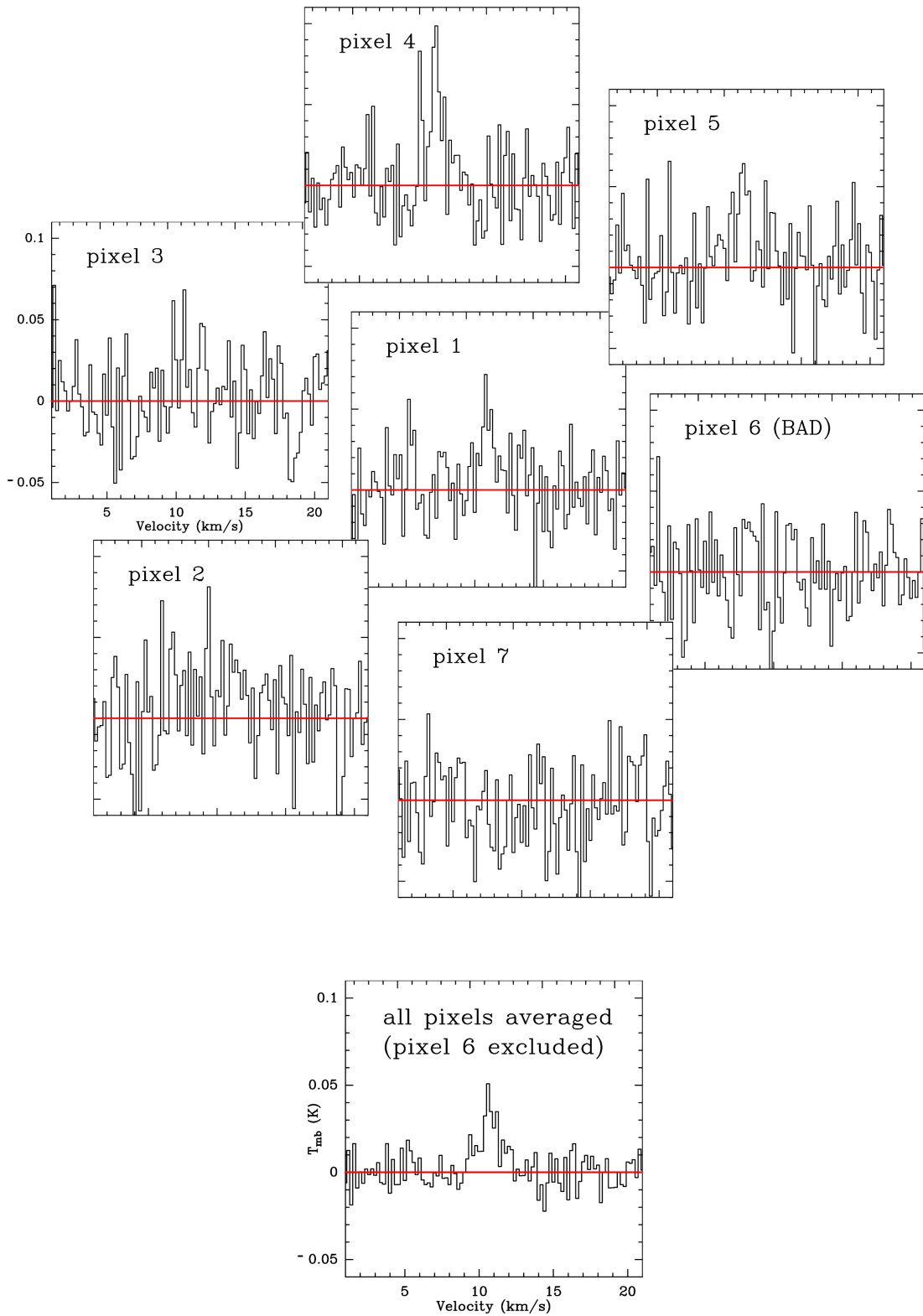
**Figure 4.7:** HOPS 70: LASMA observations of the CF$^+$ $J = 3 - 2$ transition. *Top*: Separated into the seven pixels. *Bottom*: Averaged over all pixels to improve the signal-to-noise ratio.
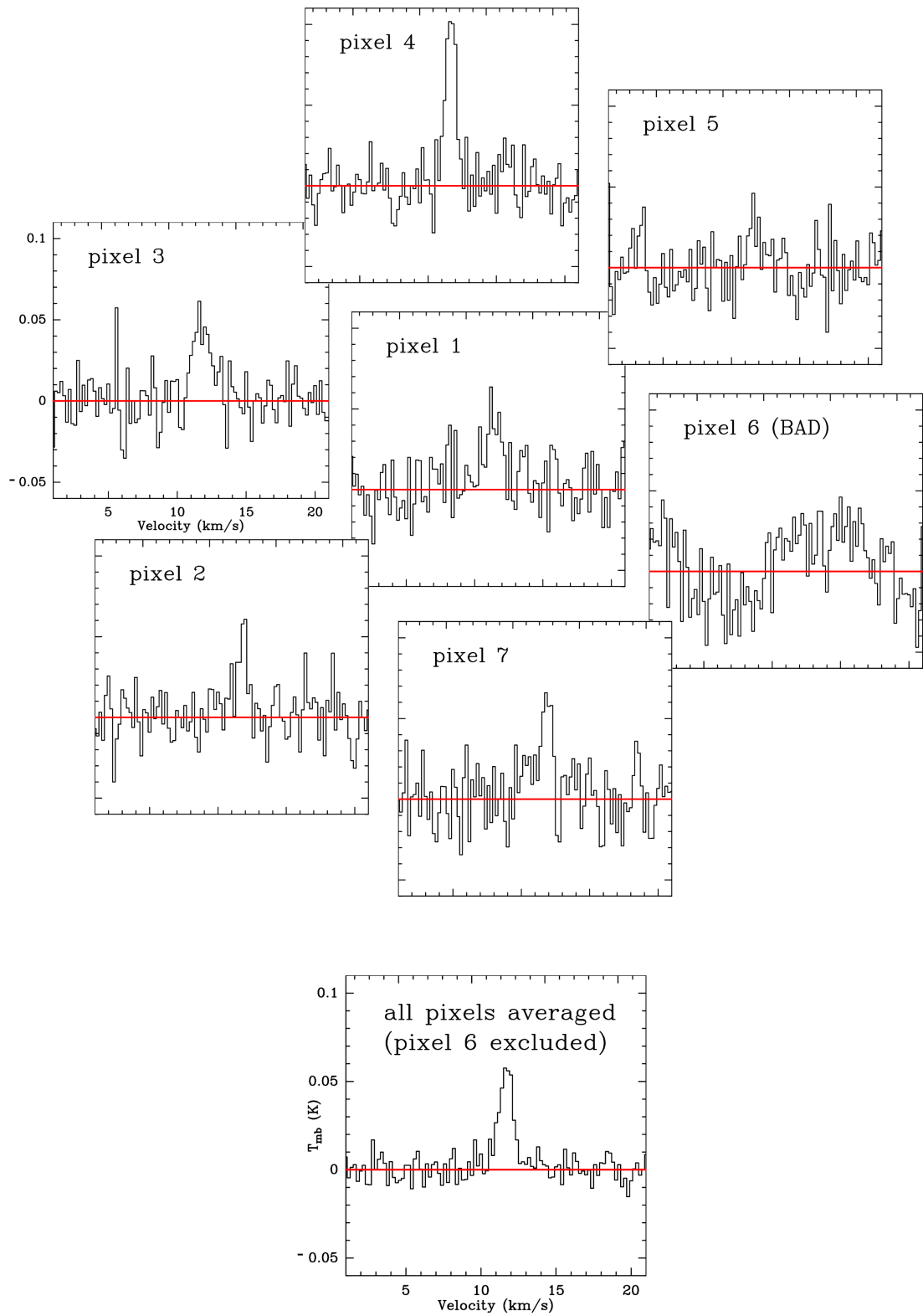
**Figure 4.8:** HOPS 96: LASMA observations of the CF$^+$ $J = 3 - 2$ transition. *Top*: Separated into the seven pixels. *Bottom*: Averaged over all pixels to improve the signal-to-noise ratio.

**Table 4.6:** Results for single Gaussian fits of the CF$^+$ $J = 3 - 2$ transition in the pointed observations with LASMA. Only lines with detections $> 3\,\sigma$ are listed.

| source/ pixel | T$_{peak}$ [mK] | area [mK km s$^{-1}$] | $\Delta$area [mK km s$^{-1}$] | position [km s$^{-1}$] | $\Delta$position [km s$^{-1}$] | width [km s$^{-1}$] | $\Delta$width [km s$^{-1}$] | $\sigma$ [mK] |
|---|---|---|---|---|---|---|---|---|
| FIR6A: | | | | | | | | |
| 1 | 57 | 88 | 14 | 10.46 | 0.13 | 1.46 | 0.23 | 19 |
| 2 | - | - | - | - | - | - | - | 21 |
| 3 | - | - | - | - | - | - | - | 16 |
| 4 | - | - | - | - | - | - | - | 17 |
| 5 | - | - | - | - | - | - | - | 22 |
| 6 | - | - | - | - | - | - | - | 18 |
| 7 | - | - | - | - | - | - | - | 14 |
| averaged | - | - | - | - | - | - | - | 9 |
| HOPS 70: | | | | | | | | |
| 1 | - | - | - | - | - | - | - | 24 |
| 2 | - | - | - | - | - | - | - | 28 |
| 3 | - | - | - | - | - | - | - | 25 |
| 4 | 84 | 82 | 26 | 10.57 | 0.09 | 0.91 | 0.50 | 25 |
| 5 | - | - | - | - | - | - | - | 30 |
| 6 | - | - | - | - | - | - | - | 25 |
| 7 | - | - | - | - | - | - | - | 27 |
| averaged | 35 | 71 | 7 | 10.72 | 0.09 | 1.89 | 0.24 | 8 |
| HOPS 96: | | | | | | | | |
| 1 | 40 | 49 | 12 | 11.39 | 0.14 | 1.16 | 0.31 | 17 |
| 2 | 55 | 54 | 10 | 11.79 | 0.08 | 0.92 | 0.27 | 12 |
| 3 | 52 | 89 | 13 | 11.79 | 0.12 | 1.61 | 0.29 | 15 |
| 4 | 106 | 100 | 9 | 11.65 | 0.04 | 0.89 | 0.09 | 14 |
| 5 | - | - | - | - | - | - | - | 14 |
| 6 | - | - | - | - | - | - | - | 16 |
| 7 | 68 | 61 | 11 | 11.84 | 0.08 | 0.85 | 0.17 | 17 |
| averaged | 58 | 69 | 5 | 11.67 | 0.04 | 1.12 | 0.09 | 6 |

feature unlikely. There is also no strong line in the image band, so contamination from there can be excluded. Possible blending with other lines has been addressed and could be excluded as well in all but one source (FIR4). Despite its low intensity emission, we are thus confident that CF$^+$ is present in all observed sources.

So far the only detection of CF$^+$ emission outside of a PDR was reported in Fechtenbaum et al. (2015) for the high-mass protostar CygX-N63. They discuss different scenarios to explain the existence of the indirectly traced C$^+$ in the absence of an H II region and conclude that accretion and outflow shocks may provide the ionisation to establish a C II region, assuming a favourable geometry of the object. In contrast to CygX-N63 however, we know that there is only comparatively little C II in our eight sources and for some of the regions in our averaged spectra. Therefore we cannot argue for a 'hidden' C II region. We must instead aim to explain the apparent discrepancy between the emission gradient seen in C$^+$ and the fairly uniform emission of CF$^+$. This may be approached in two ways, exploring either possible reasons for enhanced emission in OMC-2/3, or explaining reduced emission in OMC-1. Ultimately it may be a combination of several effects. Starting with source FIR4, for which we have the most data on involved species, we will continue with observations of the CF$^+$ and C$^+$ emission in our pointed sources and averaged regions. Lastly, we want to focus on the special conditions within OMC-1 and how they might affect the formation and destruction of CF$^+$.

### 4.4.1 FIR4

As the only source with additional information on its HF content, FIR4 presents a special case in our analysis. Due to the high frequency of its ground state at $\sim 1.2$ THz, the HF line is difficult to observe and only few data are available. Besides FIR4, the *Herschel* Science Archive[6] (HSA) lists pointed observations towards Orion KL, Orion South and the $CO^+$ peak position in the Orion Bar. The only (small) map was obtained perpendicular to the Bar and is discussed in Kavak et al. (2019). The Orion Bar is the only source in which HF is seen in emission, while detections in absorption are common in the ISM. As we do not have pointed observations towards Orion KL and Orion South deep enough to detect $CF^+$ (and line blending would be a considerable challenge), we will focus on FIR4 [7].

Its $C^+$, $CF^+$, and HF lines are shown in Fig. 4.9 on a common velocity axis. Note that the beam sizes of the three observations are not identical: while $C^+$ and $CF^+$ are both based on beam sizes of roughly $30''$, the HF line was observed with the *Herschel* beam of $\sim 20''$. However, Chini et al. (1997) report a size of around $22'' \times 17''$ for FIR4, such that the source should be approximately covered with the *Herschel* beam. Between the lines, we see variations in central velocities and different components. $C^+$ does not clearly show distinct components at a resolution of $\sim 0.3$ km s$^{-1}$ and is centred around 10 km s$^{-1}$. HF shows roughly the same central velocity and width, but is comprised of several components ($\sim 0.1$ km s$^{-1}$ resolution). In contrast, the central velocity of $CF^+$ is shifted towards higher velocities ($\sim 11$ km s$^{-1}$), in agreement with other molecular lines from the source. The two peaks of $CF^+$ could be different velocity components, as the hyperfine splitting discussed in Guzmán et al. (2012b) is not resolved. Although $C^+$ and HF may originate from the same space (as indicated by their velocities), that overlap only produces $CF^+$ in parts of it. This could be explained by the high critical density $n_{\mathrm{crit}} \approx 8.25 \times 10^4$ cm$^{-3}$ of the $CF^+$ $J = 2 - 1$ line at 10 K[8] (Denis-Alpizar & Rubayo-Soneira 2019). In lower density environments, the line may thus not be collisionally excited. Conversely, the critical density of $C^+$ is around a factor of 15 lower ($\sim 5.5 \times 10^3$ cm$^{-3}$)[9] and absorption features (HF) occur independent of density thresholds.

### 4.4.2 Pointed observations and averaged spectra

The changing relation between $C^+$ and $CF^+$ emission in seen both on large and small scales. In our averaged spectra (Fig. 4.10), regions with comparatively little $C^+$ may still have $CF^+$ emission very similar to regions with higher $C^+$ (see e.g. region 4 vs. regions 5, 'high density, low temperature' vs. 'high density, high temperature, without KL and Orion South'). However, as the density and temperature structures, and with them the situation of HF, of the averaged spectra are complex, a direct comparison between extended regions is difficult. In some of the depicted spectra (e.g. regions 11 and 12), a second velocity component at roughly 2.5 km s$^{-1}$ or 5 km s$^{-1}$, respectively, is clearly seen in $C^+$. These low velocity components are likely associated with Orion's 'veil' (Salas et al. 2019 and references therein, e.g. Abel et al. 2016), which refers to the lower density 'bubble' of atomic and ionised material driven away by the star $\theta^1$ Orionis C (see also Section 1.4.1). Hence

---

[6] http://archives.esac.esa.int/hsa/whsa/

[7] Observation ID 1342217735 in the HSA. Conversion from $T_A^*$ to $T_{\mathrm{mb}}$ was done using a forward effciency $\eta_{\mathrm{f}} = 0.96$. Main beam efficiencies and surface accuracies of $\eta_{\mathrm{mb}}^0 = 0.595$ and $\sigma = 2.068$ $\mu$m were used for the horizontal polarisation, $\eta_{\mathrm{mb}}^0 = 0.595$ and $\sigma = 2.114$ $\mu$m for the vertical polarisation. See also 'The HIFI Beam: Release #1': https://www.cosmos.esa.int/documents/12133/996743/The+HIFI+Beam+-+Release+No1+Release+Note+for+Astronomers

[8] See also supplementary online material from Denis-Alpizar & Rubayo-Soneira (2019) for collisional rates.

[9] Collisional rates taken from the Leiden Atomic and Molecular Database (LAMDA) https://home.strw.leidenuniv.nl/~moldata/ (Schöier et al. 2005).
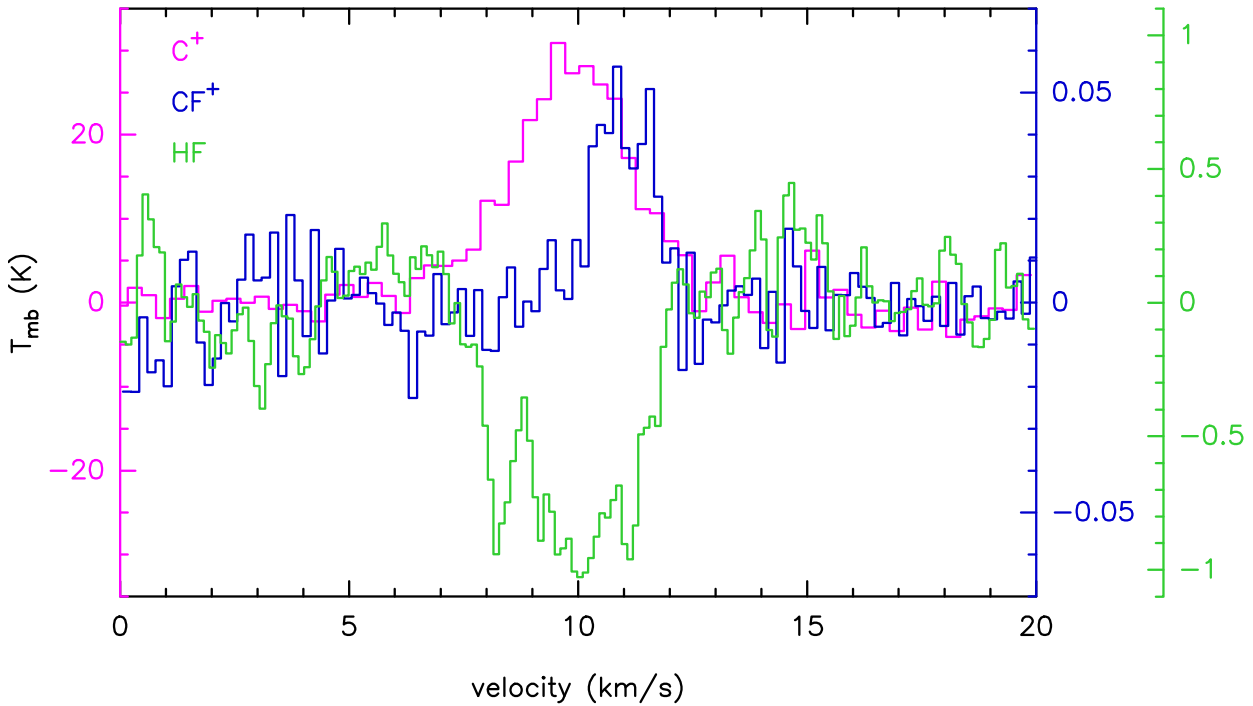
**Figure 4.9:** Emission lines of C$^+$ and CF$^+$, and absorption line of HF for the source FIR4.

these secondary components are only accentuated in averaged spectra enclosing parts of OMC-1 and the 'Trapezium'. With gas mainly atomic and densities of $n_{\mathrm{H}} \sim 10^3$ cm$^{-3}$, one would not expect CF$^+$ to be formed (or excited) in the 'veil'.

It is unclear whether some of the velocity components of C$^+$ in the pointed observations (Fig. 4.11) are also associated with the 'veil', as the distance to $\theta^1$ Orionis C has increased for these sources. But irrespective of its exact origin, C$^+$ will trace some low density material from which we do not expect much molecular emission, let alone CF$^+$. However, in contrast to spectra averaged over extended regions, pointed observations can be compared more easily with each other, as their variations of temperature and density are limited to those across a beam. As listed in Tab. 4.2, the sources vary by a factor of $\sim 3.3$ in density and $\sim 1.6$ in temperature (dust and gas temperatures agree within a few %). Due to their similar temperatures, we expect an overall similar degree of HF freeze out, suggesting that their H$_2$ column densities are a suitable indicator of their HF content (higher H$_2$ column density $\rightarrow$ more HF).

As for the averaged spectra, the actual CF$^+$ emission does not seem to strictly highlight denser regions with more C$^+$ exposure: source HOPS 96 with comparatively low density and moderate C$^+$ emission exhibits notable CF$^+$ emission. On the other hand FIR4, with higher density and temperature (both favourable for more HF in the gas phase) and more C$^+$, shows less CF$^+$ emission.
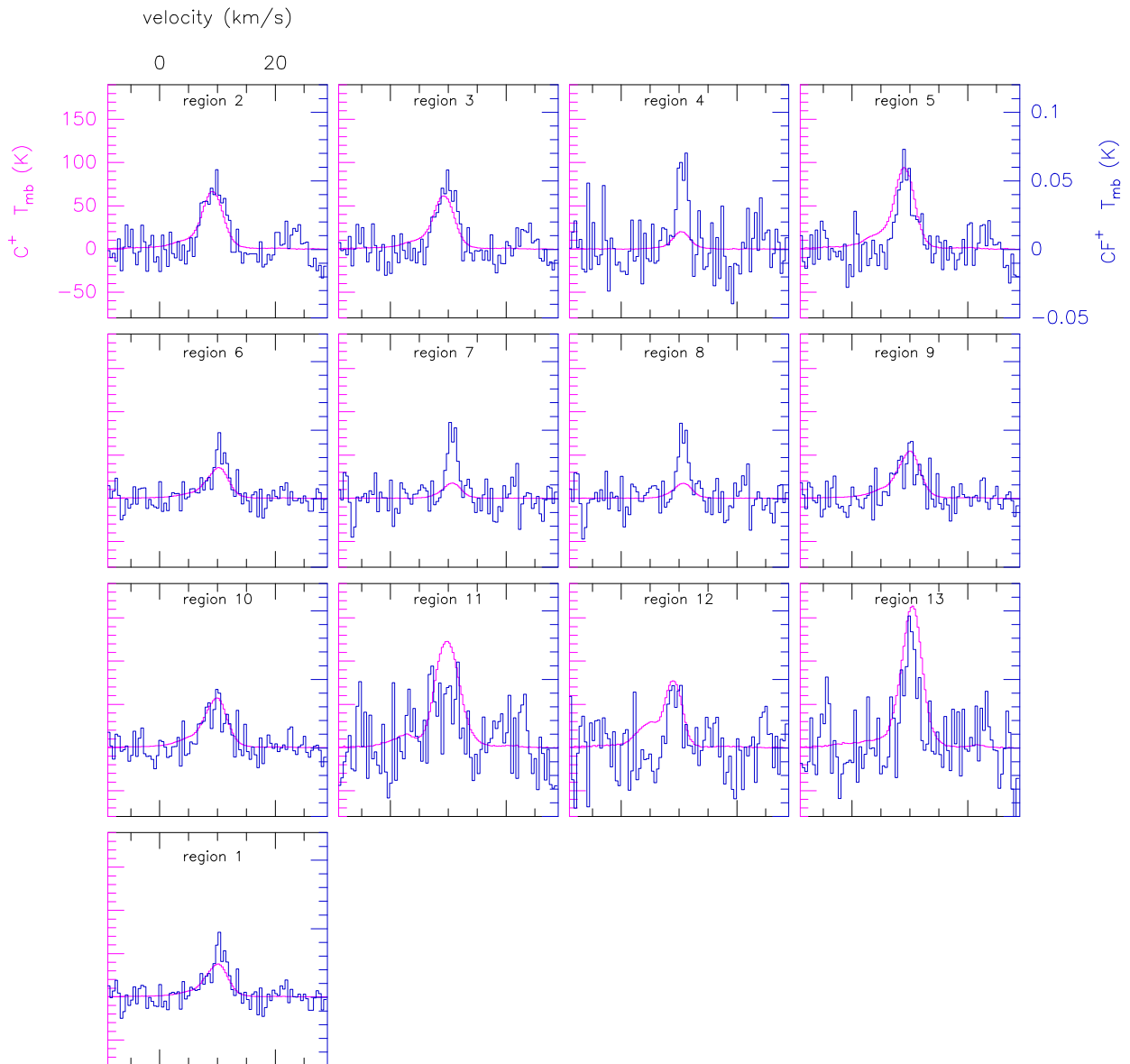
**Figure 4.10:** $C^+$ (magenta) and $CF^+$ (blue) emission in our averaged spectra with number identifiers listed in Table 4.1. With the intensity scales fixed for each species, we can gauge their variation between regions and also see their changing relation.
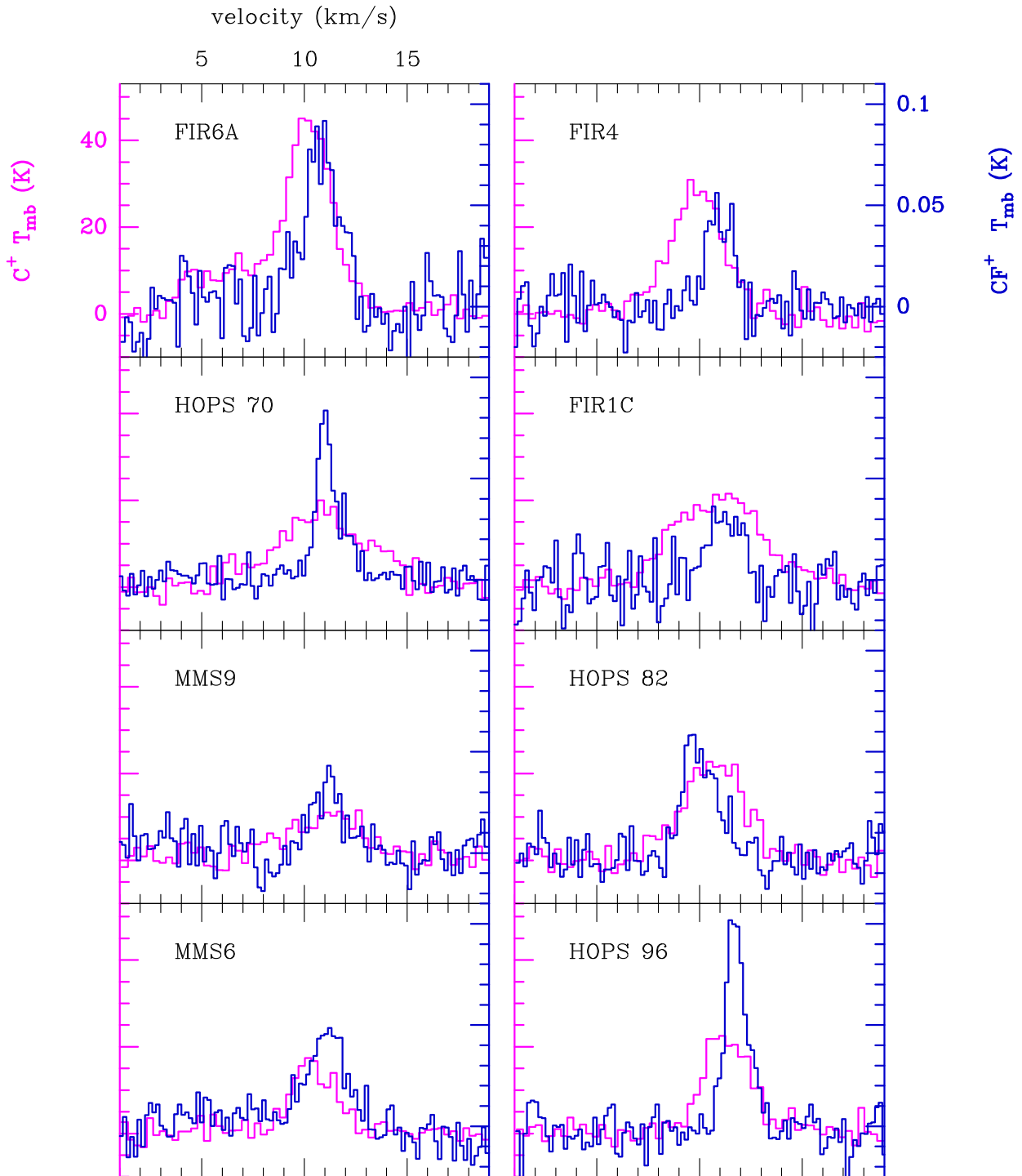
**Figure 4.11:** C$^+$ (magenta) and CF$^+$ (blue) emission for the pointed observations in OMC-2/3. Similar to Fig. 4.10, the intensity scales are fixed for each species to facilitate easier comparisons.

### 4.4.3 Additional considerations for OMC-1

As our observations do not support the idea that $CF^+$ emission is primarily enhanced in PDRs, we want to further examine the special conditions within OMC-1 and how they might affect the formation and destruction paths.

By analysing millimetre carbon recombination lines (mmCRL), far-IR $^{13}C^+$ observations, and models, Cuadrado et al. (2019) argue that the broad line profile of the $^{13}C^+$ line in the Orion Bar suggests that a significant fraction of its emission originates from atomic gas layers ($x_H > x_{H_2}$). As HF is closely linked with molecular gas, the forming reaction (see Eqn. 4.2) is not as effective, because the reactants do not fully occupy the same space.

#### 4.4.3.1 $CF^+$ abundances in strong radiation fields

Abundances of halogen-bearing species in diffuse and dense molecular clouds are predicted through chemical models in Neufeld & Wolfire (2009). The authors' one-sided slab models (applicable to PDRs) cover densities of H nuclei of $n_H = n(H) + 2n(H_2) = 10^3 - 10^7$ cm$^{-3}$ and an incident radiation field of $\chi_{UV} = 10^2 - 10^5$. The models do however not include dissociative recombination as a destruction path. Their results for $CF^+$ can be seen in Fig. 4.12 (a copy of their Fig. 5). With volume densities in the Orion Bar between $n_{H_2} \approx 5 \times 10^5$ cm$^{-3}$ for the interclump material and $(5-20) \times 10^6$ cm$^{-3}$ for the clumps (Leurini et al. 2006), we cover the ranges of $n_H \approx 10^6 - 10^7$ cm$^{-3}$, under the assumption that all hydrogen is molecular. Increasing the radiation field in these dense environments from $\chi_{UV} = 10^2$ to $10^4$ increases the abundance of $CF^+$ by around three orders of magnitude. However, a further increase of the radiation field ($\chi_{UV} = 10^5$) enhances the $CF^+$ abundance only marginally. For our considerations concerning OMC-1, this means that part of the gradient in radiation field strength may not translate to a gradient in $CF^+$ abundance, which rather reaches a 'saturated' value.

#### 4.4.3.2 Destruction paths

That the omission of photodissociation as a destruction path of $CF^+$ might not be adequate for sources with strong UV radiation fields like Orion was already acknowledged in Guzmán et al. (2012a). However, both effects were never formally compared. Using some simplifying assumptions, we want to gauge the impact of both reactions in the Orion Bar PDR.

Recalling that $CF^+$ forms in regions where molecular material (and with it HF) is exposed to $C^+$, we will examine PDR layers meeting these criteria. Tielens et al. (1993) state that the transition from atomic to molecular hydrogen occurs at optical depths $A_V \approx 2$ mag, while $C^+$ recombines to C and begins to form CO at $A_V \approx 4$ mag. This close to the surface, heating occurs through the photoelectric effect on e.g. dust grains, such that temperatures of $\sim 500$ K are common and exceed those measured for the dust alone ($\sim 50$ K). Neufeld & Wolfire (2016) estimate the photodissciation rate of $CF^+$ to be

$$
\begin{aligned}
k_{PD} &= 2.2 \times 10^{-10} \times \chi_{UV} \times E_2 \left(2.1 A_V\right) \text{ cm}^3 \text{ s}^{-1} \\
&= 2.2 \times 10^{-10} \times \chi_{UV} \times \int_1^\infty \frac{\exp\left(-2.1 A_V\right)}{t^2} dt \text{ cm}^3 \text{ s}^{-1}
\end{aligned}
\tag{4.5}
$$

With $\chi_{UV} = 5 \times 10^4$ for the Orion Bar (Tielens & Hollenbach 1985), we obtain

$$
\begin{aligned}
k_{PD} \left(A_V = 2\right) &\approx 2.8 \times 10^{-8} \text{ cm}^3 \text{ s}^{-1} \\
k_{PD} \left(A_V = 4\right) &\approx 2.4 \times 10^{-10} \text{ cm}^3 \text{ s}^{-1}
\end{aligned}
\tag{4.6}
$$
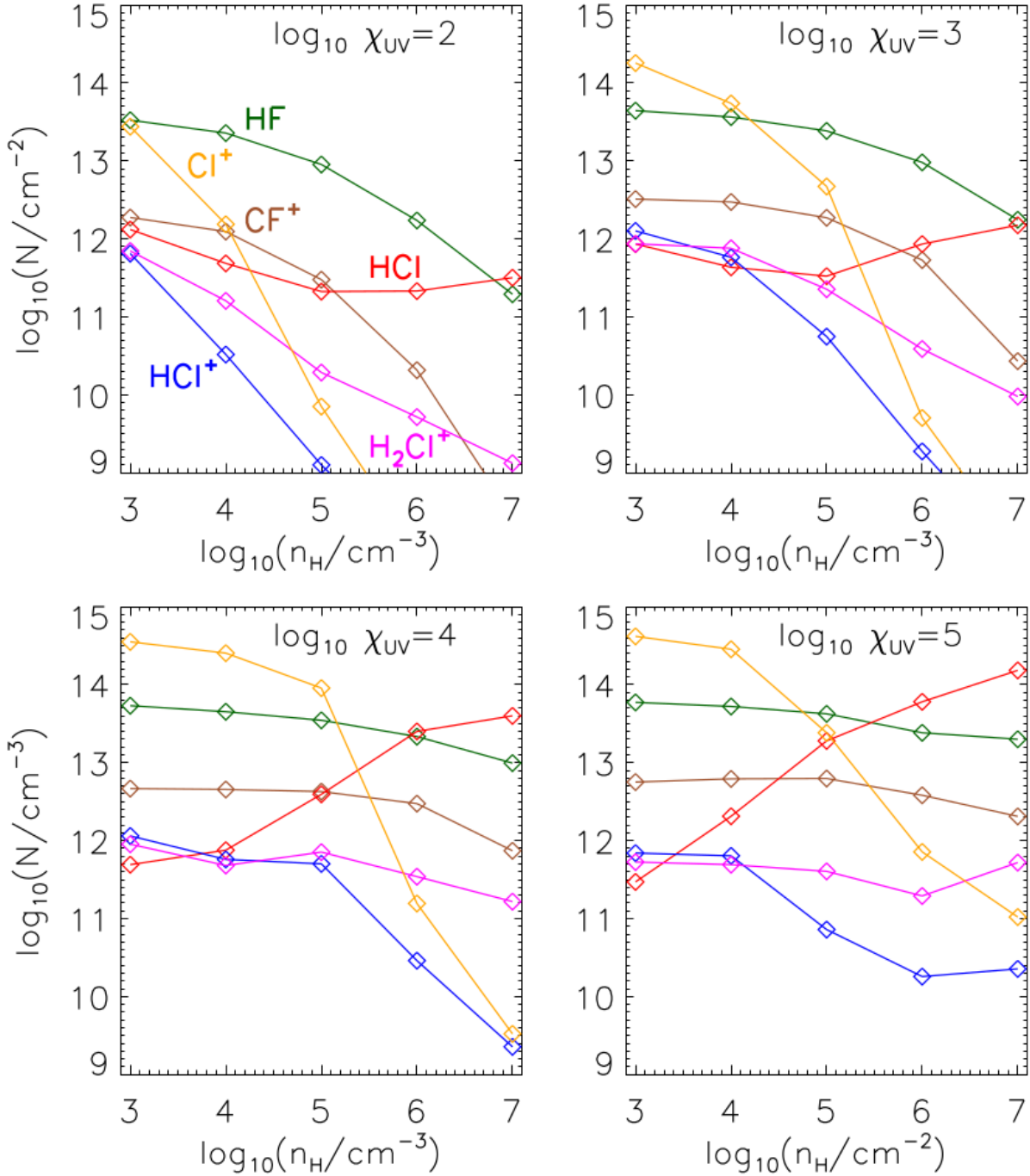
**Figure 4.12:** Computed abundances of halogens for a one-sided slab model as a function of $n_{\rm H}$ for four different radiation fields $\chi_{\rm UV}$. The figure is taken from Neufeld & Wolfire (2009).

for the edges of our considered slab. The temperature dependent dissociative recombination (Novotny et al. 2005) yields

$$k_{\mathrm{DR}} \approx 3.5 \times 10^{-8} \mathrm{~cm^3~s^{-1}} \qquad . \tag{4.7}$$

Close to the surface, photodissociation thus seems to be an equally important destruction mechanism of $CF^+$, while deeper into the cloud – with $A_V$ rising and $T$ decreasing – dissociative recombination dominates. As $k_{\mathrm{PD}}$ is directly proportional to the strength of the radiation field $\chi_{\mathrm{UV}}$, this comparability of $k_{\mathrm{PD}}$ and $k_{\mathrm{DR}}$ found for parts of the Orion Bar is however not transferable to other sources. With e.g. $\chi_{\mathrm{UV}} = 60$ for the Horsehead PDR (Habart et al. 2005), $k_{\mathrm{PD}}$ is at least a factor $\sim 10^3$ smaller than $k_{\mathrm{DR}}$, rendering photodissociation negligible for most practical purposes.

### 4.4.4 Correlations

While a visual inspection of the $C^+$ and $CF^+$ lines in Figs. 4.10 and 4.11 does not suggest a very strong correlation, the two molecules are firmly linked chemically. Hence one expects some degree of correlation. We will try to gauge that degree of correlation and compare it with other molecules which were observed concurrently due to the large receiver bandwidth ($^{13}CO$, $C^{17}O$, and CN). As with the correlation analysis in Section 3.4.2, the limited number of samples (11 regions, and 8 pointed observations with $CF^+$ detections $> 3\,\sigma$) considerably restricts the reliability of any inferred Pearson correlation coefficient. However, broad similarities or differences between molecules may still be shown. We also again normalise the integrated intensities by their respective (median) column density $N_{\mathrm{median}}$ in Fig. 4.13.

Assuming a linear correlation between $CF^+$ and $C^+$, we see a larger deviation from a general trend for region 13 ('PDR'), and smaller deviations for region 7 ('low temperature'), and region 8 ('low density, low temperature'). While the former is characterised by strong $C^+$ emission, the latter two emit below average. The 'overbright' $C^+$ in region 13 may be explained by the before mentioned partial origin of $C^+$ in atomic and ionised layers, which do not belong to the PDR itself, but are seen in projection. This aspect is also interesting for extragalactic observations where $C^+$ emission needs to be corrected for this effect (otherwise, derived star formation rates would be too high). Regions 7 and 8 are located in OMC-2 and OMC-3 (see also Fig. B.1), and are thus farther from the ionising source, resulting in notably less $C^+$ emission. Observationally, temperature effects may also play a role. With upper energy levels differing by more than 75 K ($E_{\mathrm{up}}\left(CF^+, J = 2 - 1\right) \approx 15$ K, $E_{\mathrm{up}}\left(C^+\right) \approx 91$ K), the $CF^+$ line is bright at low temperatures, while $C^+$ will be dimmer.

The very good correlation between $CF^+$ and $^{13}CO$ over all scales agrees with the formation of $CF^+$ in molecular material (Eqn. 4.2). The markedly weaker correlation with $C^{17}O$ on the other hand corroborates that the reaction does not take place in deeply embedded regions, but rather in more exposed cloud layers. A similar degree of correlation is found between $CF^+$ and CN (we choose the CN $2_{0,2,3} - 1_{0,2,3}$ transition for all regions and pointed observations). CN is generally associated with UV irradiation (Nagy et al. 2015 and references therein) and has a high critical density, but has however also been found to be excited in lower density material (Goldsmith & Kauffmann 2017), making a definite interpretation difficult.

The correlation plots between $C^+$ and $^{13}CO$, and $C^+$ and CN are shown in Fig. 4.14. Owed to the strong correlation between $CF^+$ and $^{13}CO$, deviations from a linear relation between $C^+$ and $^{13}CO$ are the same (namely regions 13, 7, and 8). Based on our limited number of samples then, $CF^+$ and $^{13}CO$ carry the same information. However, the radiation field in Orion A is overall enhanced, meaning we do not cover regions of molecular material scarcely exposed to $C^+$ in our
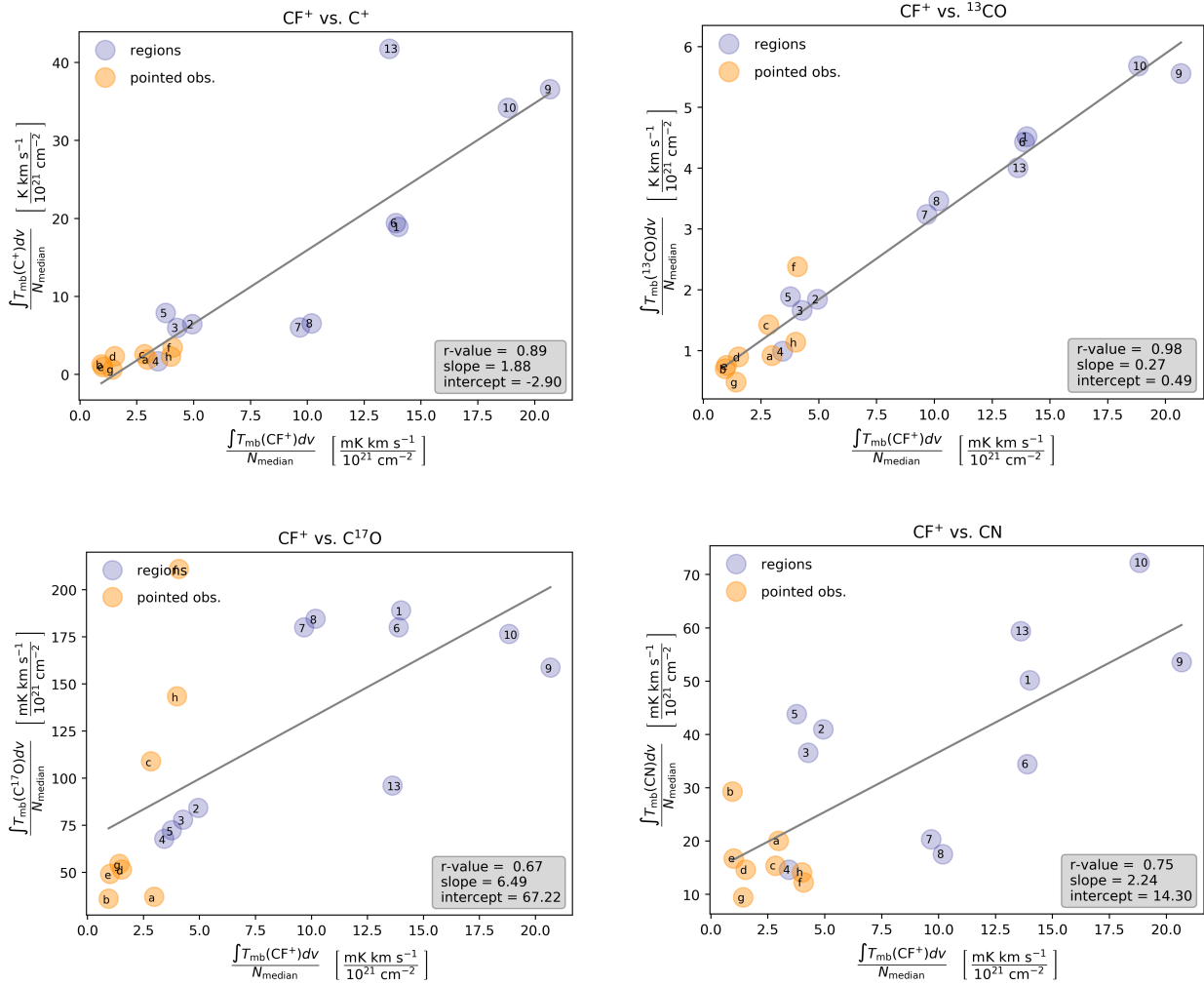
**Figure 4.13:** Correlations between CF$^+$ and C$^+$, and other molecules. Error bars are not plotted to allow for better legibility, but we assume a 30% uncertainty for all intensities. Numbers and letters within the data points refer to the labels of regions and pointed observations listed in Tables 4.1 and 4.2.

data set. These regions with low radiation fields are likely to point out the differences between CF$^+$ and $^{13}$CO and might show different degrees of correlation.

CN also shows correlations with C$^+$, as CN is related to UV irradiation, which is in turn responsible for the ionisation of C. The data points show a broader spread however, and do not distinctly highlight the PDR region as a deviation from a general trend. This could suggest that CN observations may not be helpful to correct extragalactic C$^+$ observations for their share originating in atomic material. The ambiguous relation between CN (or the HCN/CN line ratio) and UV irradiation was also discussed in Section 3.5.3.

## 4.5   Summary

In theory, the relatively simple chemistry related to the formation and destruction of CF$^+$ should make it a good tracer of PDRs. In practice, our observations in Orion A are not straightforward to interpret. It is not immediately clear why the cold and less dense regions of OMC-2/3, less exposed
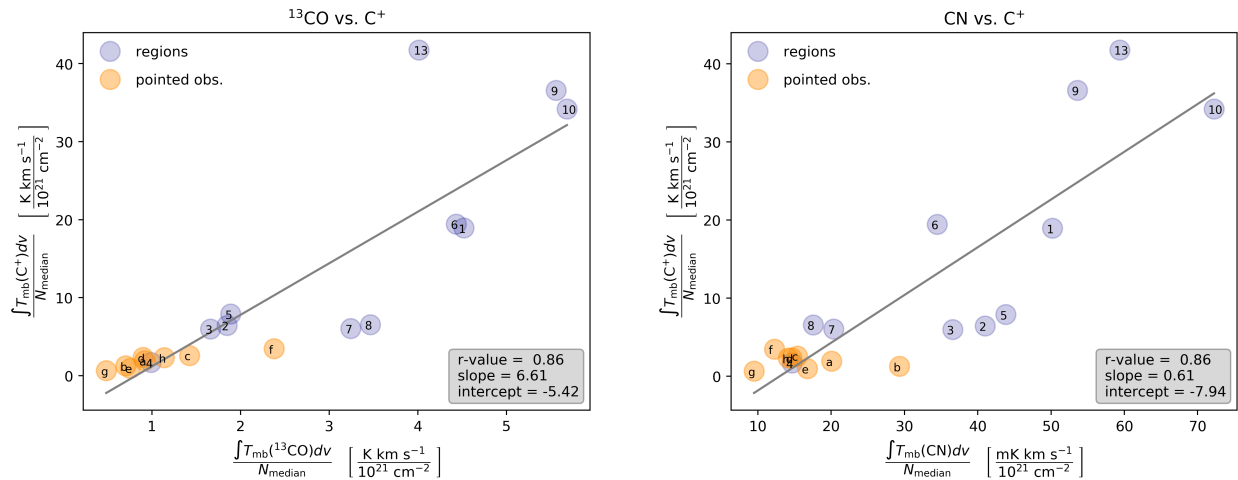
**Figure 4.14:** Correlations between $C^+$ and $^{13}CO$ (*left*), and $C^+$ and CN (*right*). Data point labels are identical to those in Fig. 4.13.

to $C^+$ emission, should show $CF^+$ emission similar to a PDR region. Yet we see fairly uniform $CF^+$ emission on large scales. On smaller scales of around $30''$ (corresponding to $60\,\text{mpc}$ or $1.2 \times 10^4\,\text{AU}$), the relation between $C^+$ and $CF^+$ emission seems complex as well, with unexpectedly high $CF^+$ emission in cold and less dense sources. On the yet smaller scales of the $J = 3 - 2$ transition ($20''$, corresponding to $40\,\text{mpc}$ or $8.3 \times 10^3\,\text{AU}$), the $CF^+$ emission appears heterogeneous between the seven pixels.

A possible explanation for the relative uniformity of $CF^+$ on larger scales despite the strong gradient seen in $C^+$ emission might be in part the spatial separation of the reactants in OMC-1, as $C^+$ also resides in atomic layers where HF is absent. Additionally, a faster destruction of $CF^+$ through photodissociation in surface layers of the PDR is conceivable.

A meaningful analysis and test for theories regarding the chemistry of $CF^+$ will eventually require extended maps of all three species. Due to low line intensities ($CF^+$) or unfavourable transition frequencies (HF and $C^+$), these necessary observations are currently not obtainable. For a thorough discussion of highly UV illuminated regions like OMC-1, photodissociation rates of $CF^+$ will also need to be determined. Additionally, a formation rate of $CF^+$, that is reliable at low temperatures, needs to be determined. Our Orion A data and its seeming conflict with theoretical expectations suggests that using $CF^+$ as a proxy for $C^+$ to detect and highlight PDRs may be problematic when photodissociation is not accounted for. PDRs with strong radiation fields, like the Orion Bar, may exhibit comparatively low $CF^+$ emission.

The strong correlation found between $CF^+$ and $^{13}CO$ on both large and small scales corroborates that $CF^+$ forms in molecular layers which are not too deeply embedded. Differences between $CF^+$ and $^{13}CO$ are expected to occur in molecular material with very little exposure to ionising radiation, but this constellation is not covered in our data.

Observing $CF^+$ in emission is no unambiguous indication of the presence of a PDR, but may rather be a common occurrence in regions with a generally enhanced radiation field. However, having more data on the relation between $CF^+$ and $C^+$ might enable us to correct extragalactic $C^+$ observations for their contribution from atomic material not associated with star formation. $CF^+$ may thus not be a proxy for $C^+$ in PDRs, but a useful tool for a more accurate interpretation.

# Radical region

The Orion 'radical region' was first described in Turner & Thaddeus (1977) as a region within OMC-1 characterised by particularly strong emission from CN, $N_2H^+$ and, to a lesser degree, $HCO^+$. While most species have their maximum intensity around Orion KL, these ions and radicals were found to deviate from this trend, showing their maximum $\sim 3.4'$ north and $\sim 0.4'$ east (see also Ungerechts et al. 1997) from Orion KL instead. This behaviour was subsequently also seen for $C_2H$ (Tucker & Kutner 1978). The question was whether these observations were indicative of actual local abundance enhancements of the molecules, or if there was an alternative explanation. In their earlier analysis, Turner & Gammon (1975) already found the CN abundance to decrease towards KL, but the authors did not state any distinct region as the location of the maximum. Thorough analyses were challenging due to technical limitations of the telescope and receiver performance in these days. The angular resolution was relatively low ($> 60''$) and any calculations relied on several assumptions. Sufficient noise levels for weaker transitions could often only be achieved for pointed observations, not on maps.

Characterising the nature of the radical region was continued with improved data sets in Greaves & White (1992). The authors mapped a $7'$ strip along the OMC-1 ridge in $^{13}CO\ J = 2-1$, $^{13}CS\ J = 5-4$, and CN $N = 2-1$, and complemented their analysis with data from an (unpublished) spectral survey of the radical region. They focused mainly on the estimation of CN abundances, calculated using averaged values across $75''$ squares along the ridge, and found no significant variations. They observed weak CN $N = 2-1$ transitions in the radical region and concluded that previously reported strong CN $N = 1-0$ lines (Turner & Thaddeus 1977) were a result of low excitation temperatures (such that the $N = 2$ has a small population compared to the $N = 1$ level). The authors argued that any anomalous intensity ratios of hyperfine components are caused by selective pumping of specific energy levels. However, for some species, including $HCO^+$, Greaves & White (1992) confirmed an abundance enhancement by around an order of magnitude in the radical region (this analysis is based on the pointed observations however, and the calculations have not been performed for maps). Nonetheless, the authors overall conclude that the radical region is not chemically different to the ridge gas reported on in Blake et al. (1987), but they also acknowledge that an insufficient number of observed lines hindered exact abundance calculations.

Further abundance calculations in OMC-1 were subsequently performed in Ungerechts et al. (1997) with a much more extensive set of integrated intensity maps. This allowed all calculations to be performed within a self contained data set, without relying on previous works for certain regional values. This approach reduces uncertainties produced by, e.g., varying data quality or different beam sizes. The authors report abundances for selected positions including the radical region (referred to as $3'.5N$) and conclude that the abundance of ions is enhanced in the radical region compared to other parts of the cloud. However, only selected positions (not regions) were discussed and again only ground state transitions were covered. Low intensity transitions of e.g. $HN^{13}N$ also required the use of data averaged over several pixels. The abundances for single positions may not permit definitive statements regarding the radical region, as variations may be present across the area.

Our following analysis does not have the same limitations as these previous studies. Due to improved noise levels, we can present maps that allow us to gauge abundance variation across large parts of OMC-1. Where necessary, the PI230 data in the 1.3 mm window are complemented by higher frequency LASMA data, such that we do not have to rely on molecular transitions observed by other projects. Our velocity resolution also allows us to account for the different velocity components present in OMC-1. We thus do not need to estimate excitation temperatures and opacities, but may calculate $T_{\text{ex}}$ and $\tau$ for each species using different isotopologues or their hyperfine structure resolved in our data. The exact methods are explained in Sections 5.1 and 5.2, and the results presented in Section 5.3. A discussion of these results and how they fit within the context of previous studies is given in Section 5.4, before a short summary in Section 5.5.

## 5.1   Determining molecular column densities

Data cubes of the respective main and rare isotopologue, as well as their associated noise maps, form the basis for our analysis. They were obtained from the reduced data set described in Chapter 3 with a common spatial resolution of $32''$. The calculations were performed on voxel basis, meaning that we determined column densities for every velocity channel before summing over them for each pixel. This allowed us to treat different velocity components individually and obtain more accurate results. The additional consideration of noise maps, which assigned uncertainties to each pixel, further improved the reliability of the inferred column densities, as noisy pixels could be excluded more efficiently. An impression of the different noise levels across the mapped area is given in Fig. 5.1. Uniform noise levels were not achieved due to the varying receiver performance during its commissioning phase and because parts of maps have been observed repeatedly. The noise maps were obtained from emission free channels close to the observed lines.

The determination of column densities from observed line intensities and known molecular constants is described in e.g. Mangum & Shirley (2015). The basic idea is that one may obtain the optical depth and excitation temperature of the main isotopologue (e.g. HCN) by solving the radiative transfer equation with the help of its optically thin isotopologue (e.g. H$^{13}$CN). Assuming LTE (see also Section 1.3.3), one can then relate these properties to the population of a specific energy state and expand this result to the total column density by the molecules' respective partition function $Q_{\text{rot}}$, which describes the sum over all rotational energy states at a given temperature.

While CO may reasonably assumed to be optically thick due to its high abundance, the same must not hold true for other species, especially in regions where column densities are lower. Ignoring this and assuming a high optical depth to simplify the equation of radiative transfer would result in systematic overestimates of column densities. We thus calculated our abundances presuming that the rarer isotopologue is optically thin, but made no a priori assumptions regarding the optical depth of the main isotopologue. To ensure reliable results, we only considered detections above $5\sigma$ in each voxel. Abundances were determined in the following five steps:

1. Calculate optical depth $\tau$ using the isotopic ratio:

   In general, the main-beam brightness temperature $T_{\text{B}}$ at frequency $\nu$ is given by the radiative transfer equation (see Section 1.3.5, or e.g. Mangum & Shirley (2015), their equation 27)

$$T_{\text{B}}\left(\nu\right) \;=\; f\,\frac{h\nu}{k_{\text{B}}}\left(\frac{1}{\exp\left(\frac{h\nu}{k_{\text{B}}T_{\text{ex}}}\right)-1}-\frac{1}{\exp\left(\frac{h\nu}{k_{\text{B}}T_{\text{bg}}}\right)-1}\right)\left(1-\exp\left(-\tau_{\nu}\right)\right)\;\;. \qquad (5.1)$$

We will hereafter consider the filling factor *f*, or the fraction of the beam filled by the source, to be unity and assume for $T_{\mathrm{bg}}$ the cosmic microwave background temperature of 2.7 K. The brightness temperature ratio between the main and rare isotopologue (bearing $^{12}$C and e.g. $^{13}$C, respectively) may be approximated as

$$\frac{T_{\mathrm{B}}^{12}}{T_{\mathrm{B}}^{13}}(\nu) \approx \frac{1 - \exp\left(-\tau_{\nu}^{12}\right)}{1 - \exp\left(-\tau_{\nu}^{13}\right)} \tag{5.2}$$

under the assumption that their frequencies are similar and their excitation (and background) temperatures match. The known isotopic ratio (e.g. $^{12}$C/$^{13}$C $\approx 77$, see Wilson & Rood 1994) can further simplify the expression:

$$\frac{T_{\mathrm{B}}^{12}}{T_{\mathrm{B}}^{13}}(\nu) \approx \frac{1 - \exp\left(-77\tau_{\nu}^{13}\right)}{1 - \exp\left(-\tau_{\nu}^{13}\right)} \tag{5.3}$$

Under the reasonable assumption that the rare isotopologue is optically thin ($\tau_{\nu}^{13} << 1$), one can use the Taylor expansion of the exponential function around zero to obtain

$$0 \approx \frac{1 - \exp\left(-77\tau_{\nu}^{13}\right)}{\tau_{\nu}^{13}} - \frac{T_{\mathrm{B}}^{12}}{T_{\mathrm{B}}^{13}}(\nu) \tag{5.4}$$

The two main-beam brightness temperatures are measured quantities, but without further simplifications under the assumption that $\tau_{\nu}^{12}$ (or $77\tau_{\nu}^{13}$) is large, Eqn. 5.4 has no analytical solution. We thus used the scipy.optimize.newton_krylov method from the SciPy library[1] (Virtanen et al. 2020; Baker et al. 2005; Knoll & Keyes 2004) in Python to find the roots, i.e. the $\tau_{\nu}^{13}$ that satisfies the equation. Multiplying this solution with the isotopic ratio yields the optical depth of the main isotopologue (hereafter shortened to $\tau_{\nu}$).

2. Calculate excitation temperature $T_{\mathrm{ex}}$:

With the known optical depth $\tau_{\nu}$, Eqn. 5.1 can be reorganized to express the excitation temperature $T_{\mathrm{ex}}$ as a function of the measured brightness temperature:

$$T_{\mathrm{ex}} = \frac{h\nu}{k_{\mathrm{B}}} \left[ \ln \left( 1 + \left( \frac{k_{\mathrm{B}} T_{\mathrm{B}}}{h\nu \left(1 - \exp\left(-\tau_{\nu}\right)\right)} + \frac{1}{\exp\left(\frac{h\nu}{k_{\mathrm{B}} T_{\mathrm{bg}}}\right) - 1} \right)^{-1} \right) \right]^{-1} \tag{5.5}$$

3. Calculate the column density in the lower *J* state:

The column density in the lower state may be calculated from molecular constants and the derived values for $\tau_{\nu}$ and $T_{\mathrm{ex}}$ (see e.g. Mangum & Shirley 2015; Rigby et al. 2019):

$$N(J_l) = \frac{8\pi}{c^3} \left( \frac{2J_l + 1}{2J_u + 1} \right) \frac{\nu^3}{A_{\mathrm{ul}}} \frac{1}{1 - \exp\left(\frac{-h\nu}{k_{\mathrm{B}} T_{\mathrm{ex}}}\right)} \int \tau_{\nu} \mathrm{d}v \tag{5.6}$$

4. Calculate the total column density:

With the knowledge of the column density of one *J* state, one may calculate the total column density through multiplication with the partition function $Q_{\mathrm{rot}}$ (see e.g. Rigby et al.

---

[1] `https://docs.scipy.org/doc/scipy/reference/generated/scipy.optimize.newton_krylov.html`

(2019), their equations 5 and 6; Mangum & Shirley (2015), their equations 51 and 52 for the approximation of $Q_{\rm rot}$):

$$
\begin{aligned}
N\,(\text{total}) \;&=\; N\,(J_l)\,\frac{Q_{\rm rot}}{2J_l+1}\exp\left(\frac{hB_0 J_l\,(J_l+1)}{k_{\rm B}T_{\rm ex}}\right)\\
&\approx\; N(J_l)\,\frac{\frac{k_{\rm B}T_{\rm ex}}{hB_0}+\frac{1}{3}}{2J_l+1}\exp\left(\frac{hB_0 J_l(J_l+1)}{k_{\rm B}T_{\rm ex}}\right)\,.
\end{aligned}
\tag{5.7}
$$

The rigid rotor rotation constant $B_0$ for each species was taken from the Cologne Database for Molecular Spectroscopy (CDMS)[2].

5. Sum over all velocity channels:

   At this point we calculated the total column density contained in every velocity channel of the data cube. The last step is to sum over the planes.

The calculations were performed with Python (step 1), in CLASS using own scripts (step 2 to 4), and in CLASS using build-in functionalities (step 5, 'MAP_SUM'). The used transitions and methods for each species are also summarized in Table 5.1. This procedure allowed us to determine column densities for species with bright enough emission from rare isotopologues, which in our data set meant CO, CS, $HCO^+$, HCN, and HNC. For other species, the rare isotopologues mainly show quite compact emission, if they are at all detected in maps. However, the hyperfine structure of transitions for certain species ($C_2H$, CN, and $N_2H^+$) facilitates an alternative calculation of $\tau_\nu$ and $T_{\rm ex}$. Provided with a data file describing the number of components, their respective velocity offset, and relative intensity (see Appendix C), the 'METHOD HFS' in CLASS performs fits to determine the opacity and excitation temperature responsible for the difference between observed and provided line properties. For species treated with this method, we only get one $\tau_\nu$ and one $T_{\rm ex}$ valid for all velocity channels. Steps 3 to 5 in the calculation of column densities are identical.

We mostly used the transitions contained in the PI230 data set, as the data quality is generally better than for the LASMA observations. For CN however, the PI230 data has a gap in its frequency coverage around the strongest transition, hindering a reliable fitting of hyperfine components. In this case we resorted to the CN transitions covered with LASMA, for which we used a main beam efficiency of $\eta_{\rm mb} = 0.63$ to correct the intensities and used the same template data cube for reprojection and smoothing to match the spatial resolution.

## 5.2   Approximating the $H_2$ column density in OMC-1

The $H_2$ column density derived from *Herschel* data and used in Chapter 3 does not cover the area around Orion KL and Orion South, as their high intensity emissions saturated the receiver. For the calculation of abundances however, it would be very useful to include these regions and see if abundances change in their high density and high temperature environments. Based on archival continuum observations from the LABOCA multi-channel bolometer array (Siringo et al. 2009) in the 870 $\mu$m (345 GHz) atmospheric window and temperature measurements taken from Friesen et al. (2017), we calculate an $H_2$ column density and gauge its accuracy by comparing it with the *Herschel* data. By restricting our calculation to pixels meeting certain criteria as described below, we effectively focus on the higher density parts of the filament ($N_{\rm H_2}^{Herschel} > 10^{22}$ cm$^{-2}$). The

---

[2]https://cdms.astro.uni-koeln.de/cdms/portal/

**Table 5.1:** Species and transitions used for abundance calculations in OMC-1.

| species | frequency[1] [MHz] | transition | method[2] | size[3] [pc$^2$] |
|---------|--------------------|------------|-----------|------------------|
| CO | 230538.000 | $2-1$ | isotope ratio | 0.32 |
| C$_2$H | 262004.260 | $3-2$ | HFS | 0.30 |
| CN | 340247.770 | $3-2$ | HFS | 0.25 |
| CS | 244935.644 | $5-4$ | isotope ratio | 0.09 |
| HCN | 265886.180 | $3-2$ | isotope ratio | 0.23 |
| HCO$^+$ | 267557.626 | $3-2$ | isotope ratio | 0.26 |
| HNC | 271981.142 | $3-2$ | isotope ratio | 0.12 |
| N$_2$H$^+$ | 279511.852 | $3-2$ | HFS | 0.21 |

**Notes.**
[1] For method HFS, the frequency refers to that of the main component.
[2] C$^{18}$O was used for CO, while the respective $^{13}$C isotopologue was used for all other species utilising the isotope ratio method.
[3] Refers to the respective area over which we could calculate the column density (and later abundance) for a species. It corresponds to the number of valid pixels times the pixel size.

comparison between the two density maps is then done with all pixels which have valid values in both maps (see also the later discussed Fig. 5.3).

The relation between dust emission and H$_2$ column density is described in e.g. Kauffmann et al. (2008). The measured flux per beam ($F_\nu^{\text{beam}}$) at wavelength $\lambda$ under the half power beam width $\theta_{\text{HPBW}}$ gives the H$_2$ column density ($N_{\text{H}_2}$), assuming a dust temperature ($T$), and dust mass opacity $\kappa_\nu$:

$$
\begin{aligned}
N_{\text{H}_2} = 2.02 \times 10^{20}\,\text{cm}^{-2} &\left[ \exp\left( 1.439 \left(\frac{\lambda}{\text{mm}}\right)^{-1} \left(\frac{T}{10\text{ K}}\right)^{-1} \right) - 1 \right] \\
&\left(\frac{\lambda}{\text{mm}}\right)^3 \left(\frac{\kappa_\nu}{0.01\text{ cm}^2\text{g}^{-1}}\right)^{-1} \left(\frac{F_\nu^{\text{beam}}}{\text{mJy beam}^{-1}}\right) \left(\frac{\theta_{\text{HPBW}}}{10\text{ arcsec}}\right)^{-2}
\end{aligned}
\tag{5.8}
$$

The first step to obtain the H$_2$ column densities is to reproject and smooth the LABOCA map using our template data cube from Chapter 3. This ensures that the map is on the same grid as our molecular column density maps, such that ratio maps are possible. The known or measured values are $\lambda = 870\ \mu$m, $\theta_{\text{HPBW}} = 32''$ (after smoothing, the native LABOCA resolution is $19''$), and $F_\nu^{\text{beam}}$. We assume $\kappa_\nu\ [\text{cm}^2\text{g}^{-1}] \approx 1.37$ (see e.g. Ossenkopf & Henning (1994) for dust with thin ice mantles). As no dust temperatures are available around KL and Orion South, we use the gas kinetic temperatures from ammonia observations[3] published in Friesen et al. (2017). For the high densities around the filament one may approximate $T_{\text{dust}} \approx T_{\text{kin}}$ (see also Section 3.3.1). However, the correlation plot of the two temperatures shown in Fig. 5.2 also highlights some deviations. More outlying data points can be seen around the dust temperature range from around 25 K to 35 K, where a larger fraction of pixels shows $T_{\text{dust}} < T_{\text{kin}}$ outside the highlighted $\pm 20\%$ tolerance. Towards

---

[3] Maps of gas kinetic temperature and associated uncertainties are publicly available at `https://dataverse.harvard.edu/dataverse/GAS_DR1`

even higher dust temperatures, the absolute differences seem to increase. However, there are fewer data points in the high temperature regime, making generalized statements difficult. An overall good correlation between $T_{\mathrm{dust}}$ and $T_{\mathrm{kin}}$ is still evident ($r$-value $= 0.78$), thus justifying the use of $T_{\mathrm{kin}}$ in our calculations. In order to maximise the quality of the resulting $H_2$ column density map, we use the following restrictions:

1. only pixels where $F_\nu^{\mathrm{beam}} > 1$ Jy/beam

2. only pixels where the uncertainty of the temperature calculation is low, $\Delta T_{\mathrm{kin}}/T_{\mathrm{kin}} < 0.1$, and $10\ \mathrm{K} < T_{\mathrm{kin}} < 150\ \mathrm{K}$

A first assessment of the agreement between *Herschel* and LABOCA derived $H_2$ column densities can be made with the correlation plot in the top panel of Fig. 5.3. The solid line shows a 1:1 relation (which would be the ideal case), while the shaded area indicates an agreement within a factor of two. While the overall correlation is high ($r$-value $= 0.85$ for the Pearson correlation coefficient), the LABOCA derived column densities seem to be systematically lower than those from *Herschel*. Such a discrepancy is covered by the uncertainties of our assumed dust properties, which can vary by a factor of a few (both opacity and underlying gas-to-dust ratio). Multiplying the LABOCA derived values by a factor of 2 (bottom panel of Fig. 5.3) puts all but a few data points within the shaded area. Hence we will use this adjusted conversion, which is further compared to the *Herschel* data for just OMC-1 in Fig. 5.4. Within OMC-1, the extreme ratio values are $\sim 0.16$ and $\sim 1.7$, while mean and median are $\sim 0.85$ and $\sim 0.82$, respectively. This means we slightly overestimate column densities compared to *Herschel*. When considering the used approximations and the limits of the ammonia temperature measurements for $T_{\mathrm{kin}}$ as a proxy for $T_{\mathrm{dust}}$, this agreement is still adequate for our purpose. As we are primarily interested in possible abundance variations within OMC-1, further (optimized) scaling of the derived column density will not offer more insights.

## 5.3   Resulting abundances

We calculated the molecular abundance $N\,[\mathrm{X}]\,/N\,[\mathrm{H}_2]$ for each of our eight considered species from the before determined molecular and $H_2$ column densities. The resulting maps are shown in Fig. 5.6. They differ in terms of valid pixels, as the brightness of the optically thin isotopologue was the limiting factor. For CS and HNC the emission was not bright enough outside the densest parts of the filament. Some complementing general statistics are given in Table 5.2, which lists the minimum, maximum, and mean values for OMC-1, the radical region (referred to as RR), and a second region (RR2). The introduction of this second region was motivated by the observation that CN and HNC have their respective global maximum abundance at almost the same position, while $C_2H$ has a local peak. The OMC-1 values were calculated considering all pixels in a given map, while those for the radical region and RR2 were calculated utilizing the pixels inside the highlighted boxes in Fig. 5.6. The perimeters of RR2 were selected such that it encompasses all three maxima and, as the CN and $C_2H$ enhancements are more extended, some of the surrounding area.

The uncertainty of abundances is determined by the uncertainty of the $H_2$ and respective molecular column density. The former is assumed to be around a factor of two (see the previous Section 5.2). For the latter, the influence of the measured brightness temperature $T_{\mathrm{B}}$ needs to be examined. As the main and optically thin isotopologue of all species are close in frequency, they were in large parts covered in the same frequency setups, or at least share several setups in our observations. This means that we are not that sensitive to absolute calibration uncertainties for our calculation

of $\tau_\nu$, which relies on intensity ratios. The calculation of $T_{ex}$ however uses a single brightness temperature $T_B$, for which we assume an uncertainty of around 30% (see also Section 3.2.2). Within reasonable values of $\tau_\nu$ and $T_B$, a 30% deviation of $T_B$ roughly translates to a 30% deviation of $T_{ex}$ as calculated with Eqn. 5.1. The resulting variance of the total column density (Eqn. 5.7) depends on the absolute $T_{ex}$ value and $\tau_\nu$, but lies well within a factor of two for the considered species and parameter ranges (see Fig. 5.5 with the example of HCN for both $T_{ex}$ and $N_{total}$). Assuming an uncertainty of a factor of two for both the molecular and $H_2$ column density results in an abundance uncertainty of around a factor of three. Any variation lower than this factor cannot be reliably verified by our data set.

Additional systematic errors concern the employed isotopic ratios. By using the ratios from Wilson & Rood (1994) for the local ISM, we e.g. assume that the ratios are not only suitable for OMC-1 specifically, but also constant over the mapped area. This may not necessarily be true due to selective photodissociation and fractionation. For the regions more directly exposed to the strong UV radiation from the Trapezium stars, the main isotopolgues may profit from self-shielding, while the rarer isotopologues could be dissociated more easily, thus decreasing the isotopic ratio. Fractionation on the other hand may increase the isotopic ratio through isotopic exchange reactions (see e.g. Milam et al. 2005). Depending on which species is used to determine e.g. the $^{12}C/^{13}C$ ratio (CO, CN, $H_2CO$, etc.), the value may differ as the chemical reaction rates causing fractionation are different for each molecule (Colzi et al. 2020).
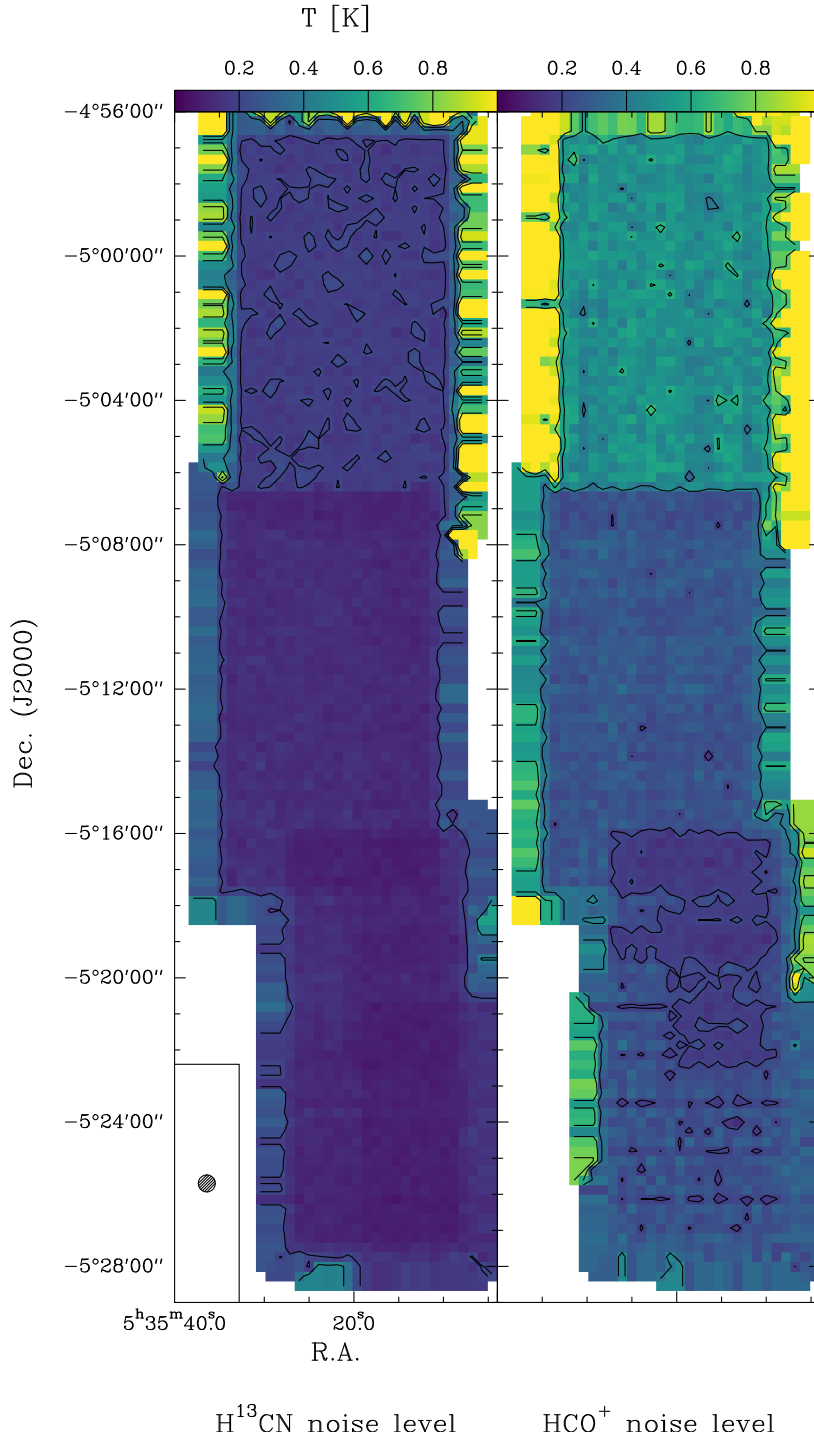
**Figure 5.1:** Exemplary noise maps of two molecules observed with the PI230 receiver, both on the same colour scale and with the same contour levels. The map edges are noisier in both cases, but one can also see differences within the maps. For H$^{13}$CN (*left*), OMC-3 is noisier than the rest of the map, but overall a fairly homogeneous noise level with $\sigma < 0.2$ K is achieved. In comparison, the HCO$^+$ map (*right*) is noisier as a whole, and also shows stronger variations within, with the northern part of OMC-1 having the lowest noise levels, and OMC-3 the highest.
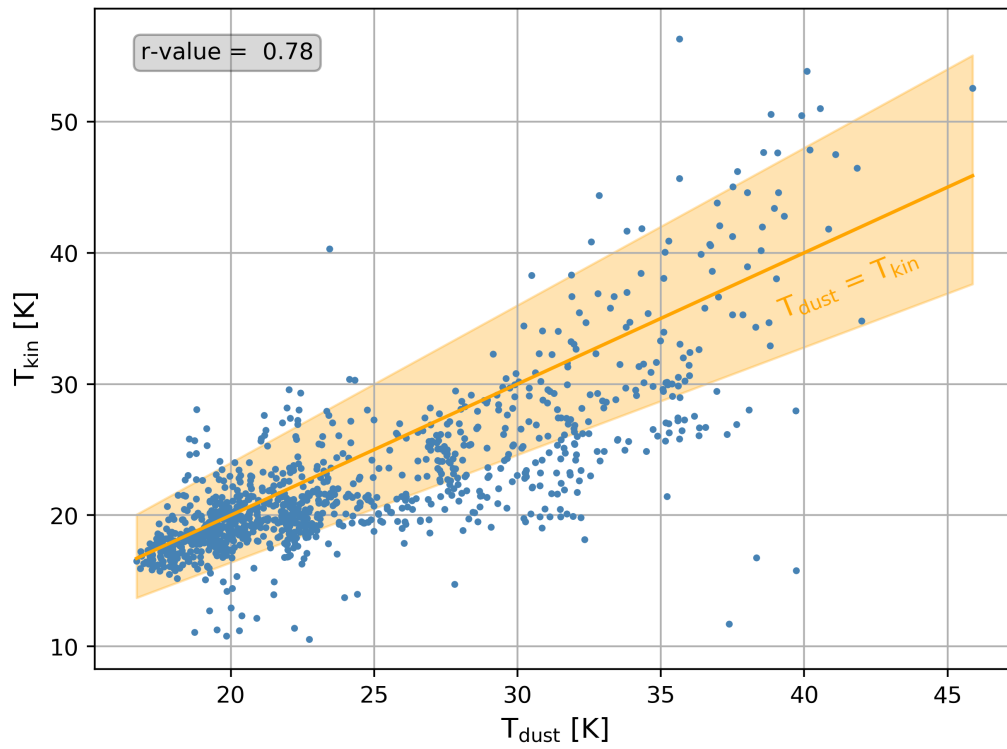
**Figure 5.2:** Correlation between kinetic gas temperature and dust temperature for pixels meeting the following conditions: $N\,[\mathrm{H_2}]^{Herschel} > 10^{22}$ cm$^{-2}$, $T_{\mathrm{kin}} > 10$ K, $\Delta T_{\mathrm{kin}}/T_{\mathrm{kin}} < 0.1$, and $F_{\nu}^{\mathrm{beam}} > 1$ Jy/beam. The shaded area highlights the $\pm 20\%$ interval around $T_{\mathrm{dust}} = T_{\mathrm{kin}}$.
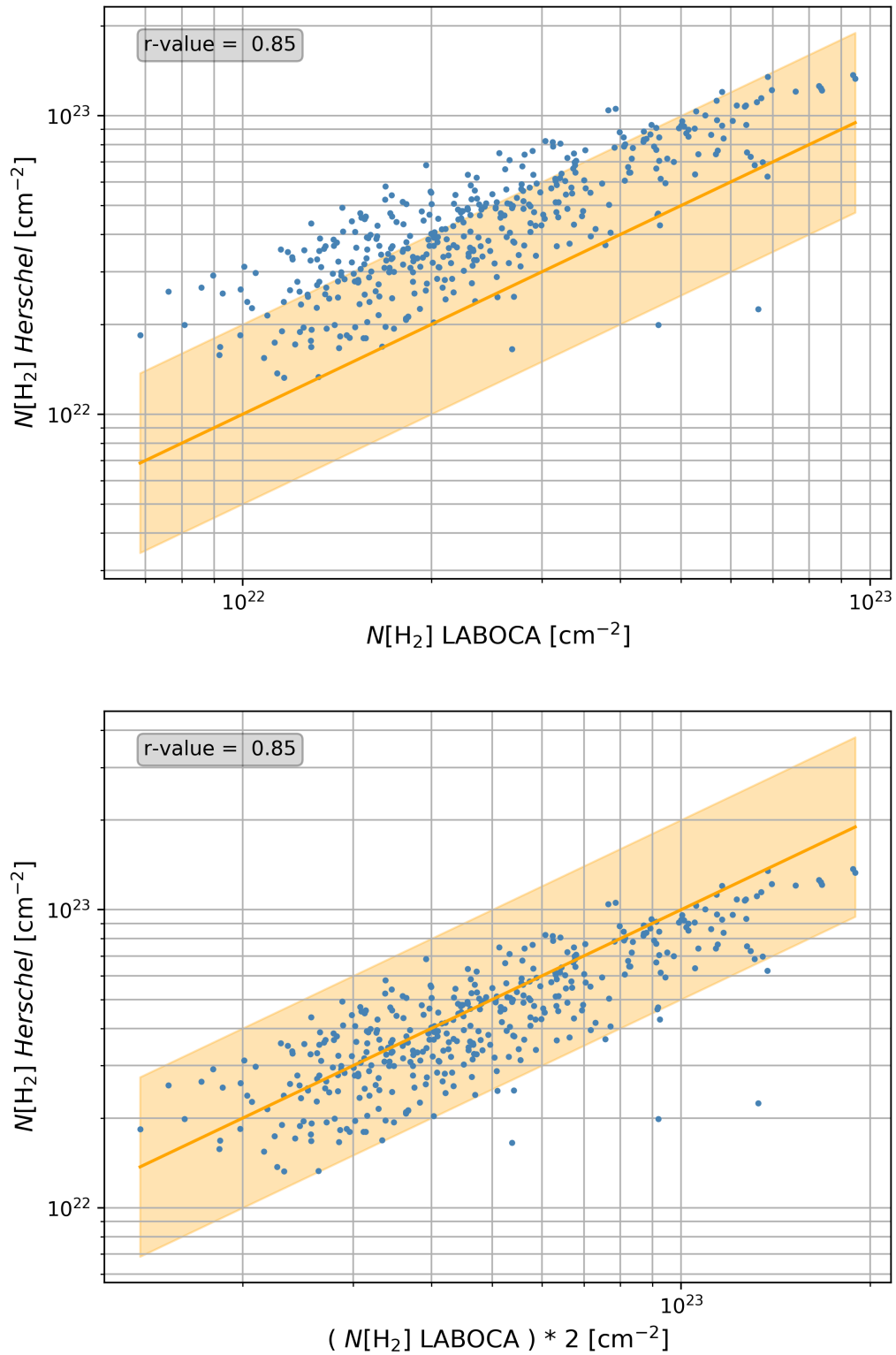
**Figure 5.3:** Correlation between *Herschel* and LABOCA derived $H_2$ column densities, using Eqn. 5.8 (*top*) and after additional application of a factor of two (*bottom*). The solid line shows a 1:1 relation, while the shaded area indicates an agreement within a factor of two.
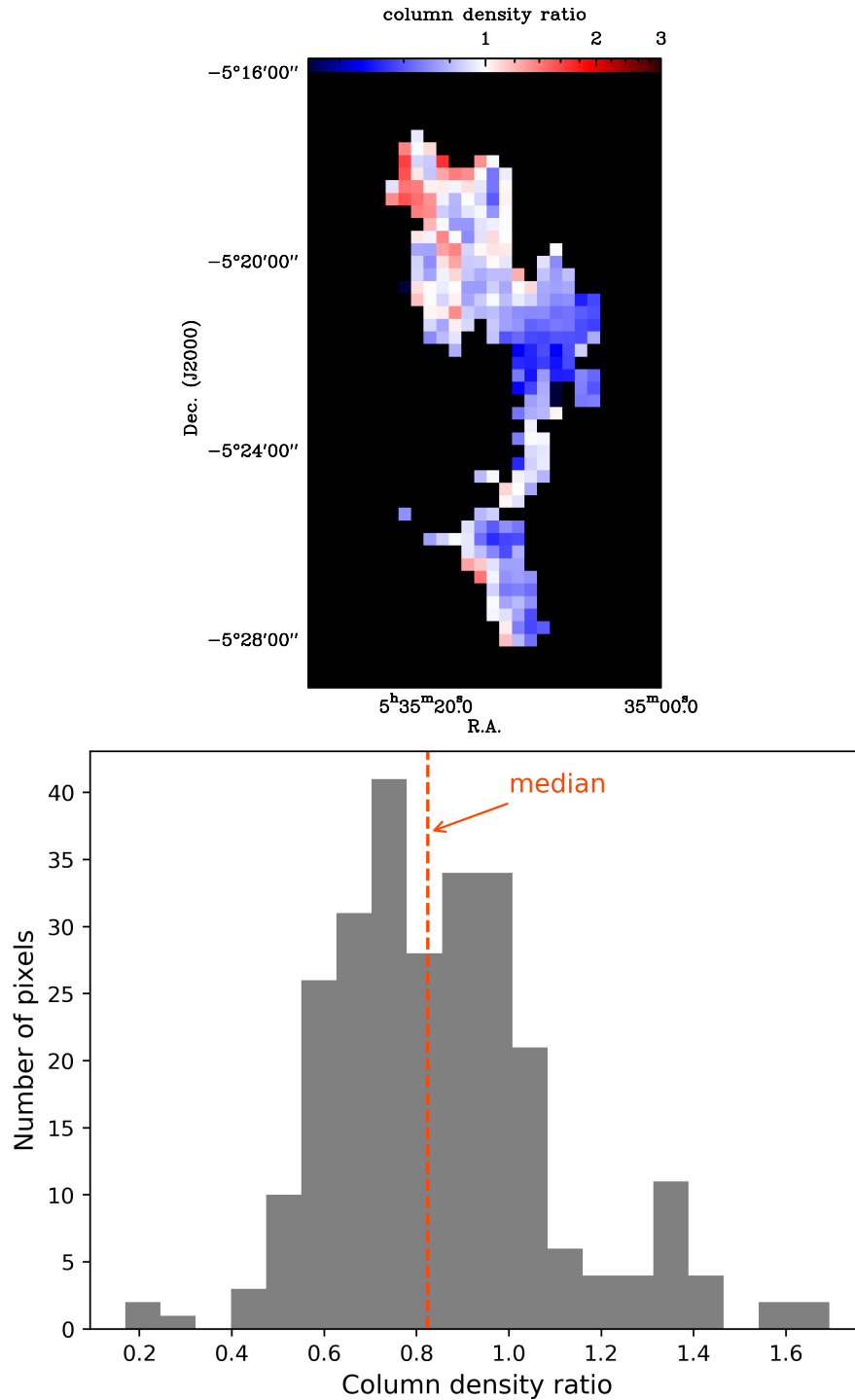
**Figure 5.4:** OMC-1 map (*top*) and histogram (*bottom*) of the *Herschel* and LABOCA derived $H_2$ column density ratio. The median is around 0.82, meaning the LABOCA values are slightly larger than those from *Herschel*. Considering the approximation $T_{\mathrm{dust}} \approx T_{\mathrm{kin}}$ and the fact that the used ammonia transitions in Friesen et al. (2017) may not optimally recover the whole temperature range, the agreement between column densities is satisfactory.
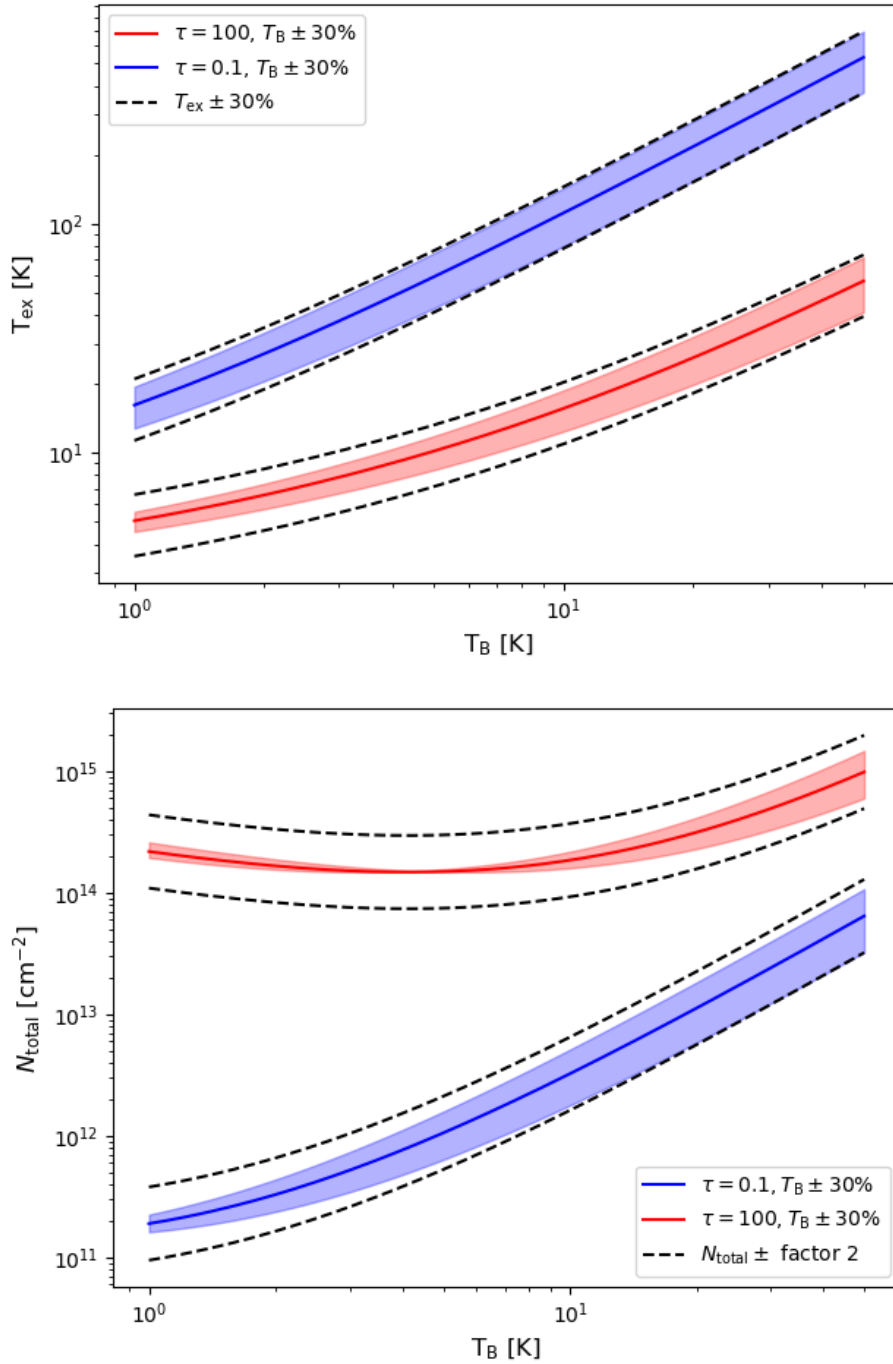
**Figure 5.5:** Uncertainty estimates for $T_{\text{ex}}$ (*top*) and $N_{\text{total}}$ (*bottom*) as a function of the measured temperature $T_{\text{B}}$, for which we assume a 30% error. The molecular constants for HCN are exemplarily chosen for the depicted calculations. We accounted for $1\,\text{K} \leq T_{\text{B}} \leq 50\,\text{K}$, as well as small ($\tau = 0.1$) and large opacities ($\tau = 100$).
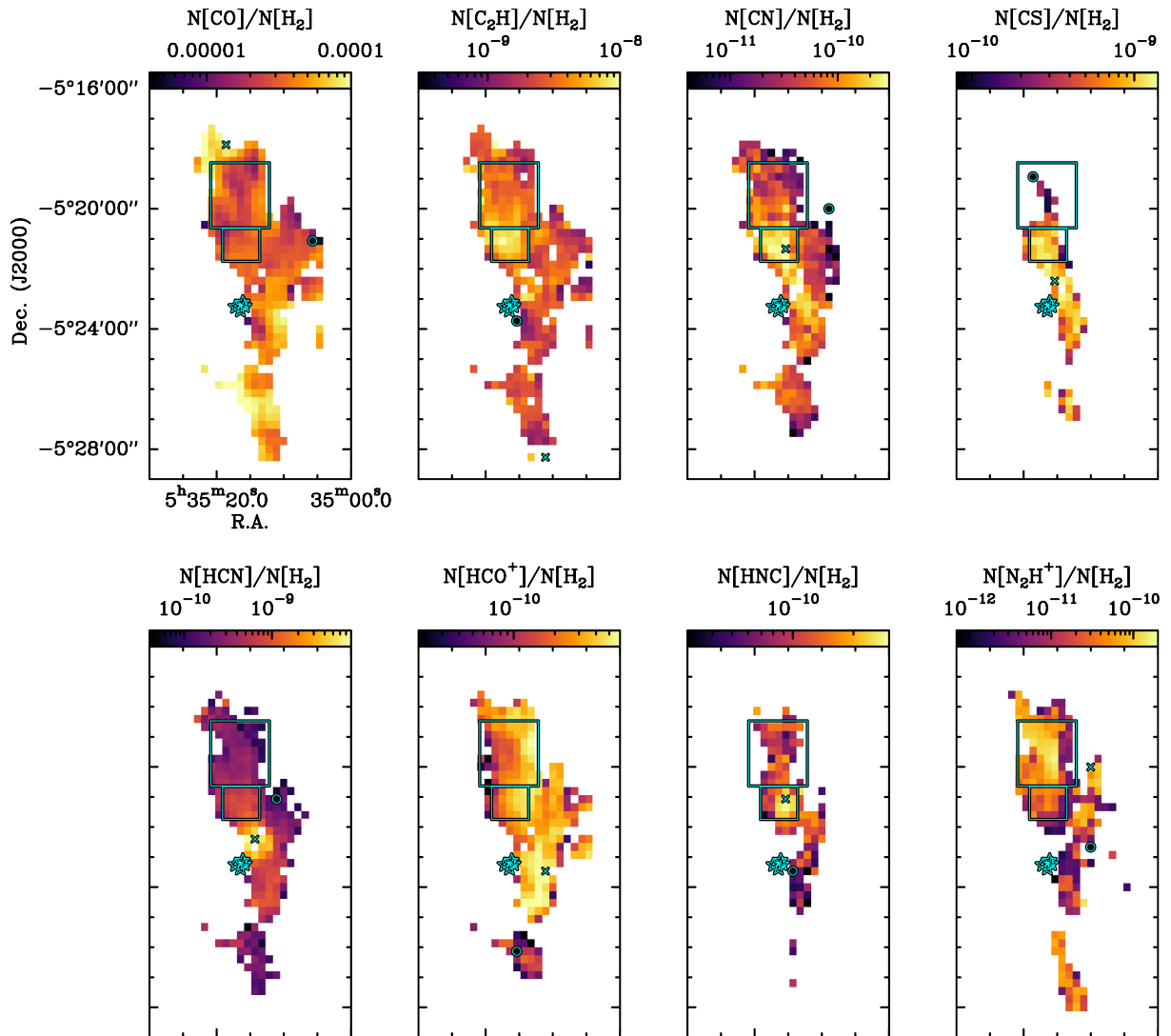
**Figure 5.6:** Molecular abundances in OMC-1. The positions of the Trapezium stars are marked with star symbols, while the pixels with minimum and maximum abundance are marked as '∘' and '×', respectively. The coloured boxes highlight the perimeters for the radical region (big box) and RR2 (smaller box), the latter chosen to encompass possible enhancements of $C_2H$, CN, and HNC.

**Table 5.2:** Molecular abundances $\frac{N[X]}{N[H_2]}$ in OMC-1 and two selected subregions, namely the historically discussed radical region (RR) and our selected area (RR2). For each species, the listed abundances were either calculated based on all valid pixels in the respective map (OMC-1), or for those pixels within the boundaries of the highlighted RR and RR2 subregions in Fig. 5.6.

| | OMC-1 min | OMC-1 max | OMC-1 mean | RR min | RR max | RR mean | RR2 min | RR2 max | RR2 mean |
|---|---|---|---|---|---|---|---|---|---|
| CO | $3.8 \times 10^{-6}$ | $1.5 \times 10^{-4}$ | $4.3 \times 10^{-5}$ | $1.3 \times 10^{-5}$ | $8.8 \times 10^{-5}$ | $3.3 \times 10^{-5}$ | $1.6 \times 10^{-5}$ | $4.1 \times 10^{-5}$ | $3.2 \times 10^{-5}$ |
| $C_2H$ | $3.1 \times 10^{-10}$ | $1.4 \times 10^{-8}$ | $3.2 \times 10^{-9}$ | $1.3 \times 10^{-9}$ | $8.6 \times 10^{-9}$ | $3.7 \times 10^{-9}$ | $2.8 \times 10^{-9}$ | $1.1 \times 10^{-8}$ | $6.3 \times 10^{-9}$ |
| CN | $3.2 \times 10^{-12}$ | $4.0 \times 10^{-10}$ | $7.8 \times 10^{-11}$ | $8.7 \times 10^{-12}$ | $2.2 \times 10^{-10}$ | $6.5 \times 10^{-11}$ | $4.9 \times 10^{-11}$ | $4.0 \times 10^{-10}$ | $2.1 \times 10^{-10}$ |
| CS | $7.9 \times 10^{-11}$ | $1.5 \times 10^{-9}$ | $7.2 \times 10^{-10}$ | $7.9 \times 10^{-11}$ | $7.2 \times 10^{-10}$ | $3.3 \times 10^{-10}$ | $1.4 \times 10^{-10}$ | $1.3 \times 10^{-9}$ | $9.0 \times 10^{-10}$ |
| HCN | $3.7 \times 10^{-11}$ | $8.1 \times 10^{-9}$ | $6.7 \times 10^{-10}$ | $7.0 \times 10^{-11}$ | $5.6 \times 10^{-10}$ | $2.7 \times 10^{-10}$ | $4.6 \times 10^{-10}$ | $1.4 \times 10^{-9}$ | $7.8 \times 10^{-10}$ |
| $HCO^+$ | $1.4 \times 10^{-11}$ | $6.7 \times 10^{-10}$ | $2.8 \times 10^{-10}$ | $2.0 \times 10^{-11}$ | $6.1 \times 10^{-10}$ | $2.6 \times 10^{-10}$ | $8.3 \times 10^{-11}$ | $4.9 \times 10^{-10}$ | $3.1 \times 10^{-10}$ |
| HNC | $2.4 \times 10^{-11}$ | $3.0 \times 10^{-10}$ | $1.1 \times 10^{-10}$ | $4.5 \times 10^{-11}$ | $1.9 \times 10^{-10}$ | $1.1 \times 10^{-10}$ | $3.6 \times 10^{-11}$ | $3.0 \times 10^{-10}$ | $1.7 \times 10^{-10}$ |
| $N_2H^+$ | $7.0 \times 10^{-13}$ | $2.1 \times 10^{-10}$ | $3.9 \times 10^{-11}$ | $3.3 \times 10^{-12}$ | $1.7 \times 10^{-10}$ | $6.0 \times 10^{-11}$ | $3.6 \times 10^{-12}$ | $5.2 \times 10^{-11}$ | $2.7 \times 10^{-11}$ |

For **CO**, C$^{18}$O was chosen as the optically thin isotopologue, as $^{13}$CO is likely optically thick itself. There is a factor of $\sim 39$ between the lowest and highest abundance, with enhancements seen towards the Orion Bar and in the northern part of the filament. Large parts of the filament, including the highlighted radical region, seem to have a fairly constant CO abundance however, which is underlined by the very similar median values for the different subregions.

**C$_2$H** shows stronger variations across the map (factor $\sim 45$), with the minimum close to the (projected) position of the Trapezium stars and the maximum in the very South of the mapped area. There is no enhancement in the radical region, but a local maximum south of it (included in the RR2 subregion). This local maximum seems to have counterparts in CN and HNC. OMC-1 and RR2 mean abundances differ by a factor $\sim 2$. Within our assumed uncertainty, it is unclear whether this enhancement is real, but it is noteworthy that the maximum lies close to those of CN and HNC.

**CN** has its global maximum abundance in RR2, where the mean value is $\sim 2.7$ times larger than for OMC-1 as a whole. The radical region shows no significant difference to OMC-1. The general range of values spans a factor of $\sim 125$, with the lowest values found at the eastern edge of the filament.

Due to the relative faintness of the $^{13}$CS transition, the **CS** abundance map is the one with the fewest valid pixels. Thus no meaningful conclusions can be drawn for the radical region, just the tentative assessment that the abundances seem to be lower than for the rest of the filament. The highest abundance is detected close to Orion KL, but there appear to be no strong variations in the direct environment.

The **HCN** abundance strongly peaks towards the direct environment of Orion KL, showing a fairly compact enhancement. The lowest and highest measured abundances differ by a factor of almost 220. The rest of the filament generally shows decreasing abundances with distance to the maximum. The mean abundance in the radical region is around half the mean OMC-1 value. However, as the maximum is so compact, the median values of the two regions are all but identical ($2.7 \times 10^{-10}$ vs. $3.2 \times 10^{-10}$).

In contrast to e.g. HCN, the **HCO$^+$** abundance shows no strong singular peak, but several rather extended enhancements. The Orion Bar seems to have generally lower abundances and includes the global minimum. A factor $\sim 48$ is found between the lowest and highest abundance, while the subregions display no significant deviations from the general OMC-1 mean value.

As for CS, the optically thin isotopologue of **HNC** is not well detected throughout larger parts of the map due to its low line intensity. Statistics are thus less robust. We see the global maximum in RR2, although it seems to be more compact than those of CN and C$_2$H. This may be the main reason why the mean abundance value of RR2 shows no significant deviation from OMC-1 as a whole. The maximum value itself is a factor $\sim 2.7$ larger.

**N$_2$H$^+$** shows the largest abundance variation across the map, with minimum and maximum value differing by a factor of $\sim 300$. Low values (and non-detections) are generally located close to the warmest parts of the filament, close to KL, Orion South, and the Trapezium stars. No strong deviation from the OMC-1 mean are found for the two subregions, but N$_2$H$^+$ does have a local maximum in the radical region. This local maximum value itself lies a factor $\sim 4.4$ above average.

Based on these results, we thus conclude that the radical region is not a distinct entity within OMC-1 characterised by a particular chemistry. Its abundances do not differ significantly from those of the surrounding material when looking at larger scales averaged over several pixels. For some species however, the overall variation of values over the mapped area spans two orders of magnitude. This bears the question whether abundances of spatially extended regions can be

meaningfully compared with pointed observations only.

### 5.3.1   Correlations

In addition to the assessment of the radical region, we also analysed the correlations between the calculated molecular abundances, and also selected parameters (e.g. $T_{kin}$), to quantify the differences and similarities found in the maps of Fig. 5.6. We determined the Pearson correlation coefficient (see also Section 3.4.2) for every pair of pixels with valid values in both maps[4]. As the maps differ in size, one has to exercise caution when comparing the correlations visualized in Fig. 5.7. This is particularly important for CS and HNC, as their fairly small abundance maps only probe a limited parameter space. Consequently, these two species will be largely excluded from a more extensive discussion. As each pixel has the same weight in our analyses, 'over represented' environments have the largest influence on the correlation coefficient.

**CO** shows no correlation with any other molecule. The slight positive correlation with $T_{kin}$ may be caused by increased sublimation of CO from grains into the gas phase at higher temperatures, while the slight negative correlation with $N_{H_2}$ could be an 'artifact' of the optically thin isotopologue $C^{18}O$ being more vulnerable to both selective photodissociation in the areas exposed to UV irradiation, and depletion. Overall, the CO abundances are more difficult to interpret, as the molecule is so readily excited and multiple components are present along each line-of-sight.

**$C_2H$** has the strongest correlation with CN, and weak to moderate correlations with CS and HNC. Interestingly, we do not recover the clear correlations of $C_2H$ with HCN or $HCO^+$, which have been found for the integrated intensities on large scales in the previous chapter (see Section 3.4.2.1). This may be related to optical depth effects: in the dense parts of the filament, where $\tau_\nu$ is large for e.g. HCN, the emission mainly originates from the outer layers, where likewise emission from UV sensitive species like $C_2H$ is enhanced. However, if the deeper cloud layers are accounted for (as with our abundance calculations), the correlation decreases.

**CN** behaves broadly like $C_2H$ (as qualitatively already suggested by their similar abundance maps), albeit with stronger correlations to HCN, as the species are chemically linked (see e.g. Boger & Sternberg 2005). The formation of CN through the photodissociation of HCN is also reflected in its correlation with $T_{kin}$, which is in turn strongly associated with the H II region in OMC-1. This setting may then cause some of the correlation seen between CN and the integrated $C^+$ intensity.

**HCN** shows the strongest correlation with $T_{kin}$. This may be explained through the neutral-neutral reaction $HNC + H \rightarrow HCN + H$ with a relatively low energy barrier (Hacar et al. 2020 and references therein), which changes the isomer ratio and is more effective at higher temperatures. A corresponding negative correlation between HNC and $T_{kin}$ is not recovered with our maps, as the HNC (or rather $HN^{13}C$) emission is not strong enough close to the H II region. As such, we are missing exactly those pixels for which we expect the strongest anti-correlation.

---

[4]The Pearson correlation coefficient only tests for *linear* correlations, which may not adequately represent the actual relation between the abundances of two species. Other coefficients, e.g. Spearman's rank correlation, assess how well the relationship can be described by e.g. a general monotonic function. However, as these functions have more degrees of freedom compared to the linear relation in the Pearson correlation coefficient, they require a larger sample size to give reliable results. We have more data points available here than in our correlation analyses from previous chapters, but not enough to be confident in any inferred Spearman rank coefficient. The respective documentation in the SciPy library (`https://docs.scipy.org/doc/scipy/reference/generated/scipy.stats.spearmanr.html`) suggests a sample size of around 500 to produce reasonable probability values. Depending on the species, we obtain between 58 (CS vs. HNC) and 293 (CO vs. $C_2H$) pixels (= samples) from the abundance maps (see Table A.4 for all sample sizes). We thus consider the Pearson correlation coefficient, as a qualitative indicator for existing correlations, to be sufficient for our purpose.

With the exception of N$_2$H$^+$, the **HCO$^+$** abundance shows no correlation with any of the examined species or parameters. The moderate negative correlation between N$_2$H$^+$ and HCO$^+$ may be an expression an important destruction path of N$_2$H$^+$, namely the reaction CO + N$_2$H$^+$ $\rightarrow$ N$_2$ + HCO$^+$ (Woon & Herbst 2009).

The expected negative correlation between CO and **N$_2$H$^+$** abundances, related to the production of HCO$^+$, is not clearly seen. As with HNC, N$_2$H$^+$ is not sufficiently bright in the warm parts where it is destroyed. To fully recover more of the anti-correlations, one would need deeper integrations in order to detect the reduced emission caused by the progressive destruction of species.
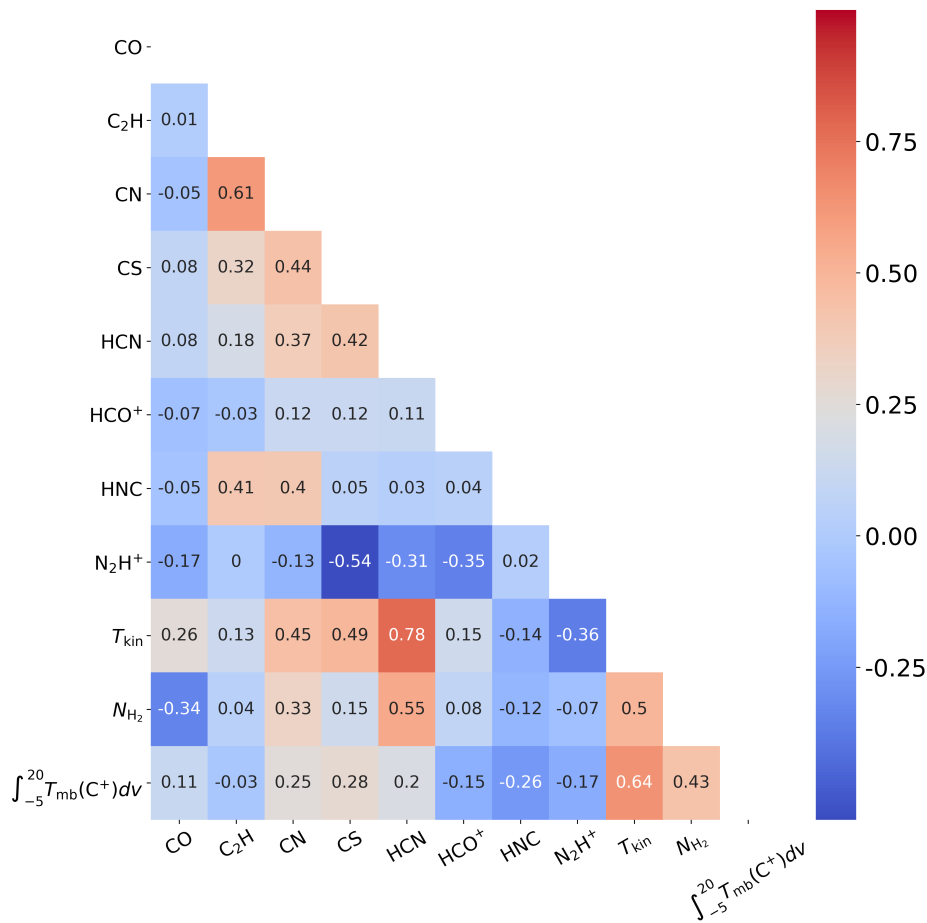


**Figure 5.7:** Pearson correlation coefficients between the molecular abundances from Fig. 5.6, and additional parameters, namely the gas kinetic temperature $T_{\mathrm{kin}}$ from Friesen et al. (2017), our calculated column density $N_{\mathrm{H_2}}$ from Section 5.2, and the integrated C$^+$ intensity from Pabst et al. (2019).

## 5.4 Discussion

Discussions on molecular abundances in the radical region have to date used single positions only, not maps (the exception being the analysis for CN in Greaves & White (1992)). As we saw in the previous section however, single positions might deviate more strongly from the OMC-1 mean, while averaging over a few pixels usually results in overall comparable values.

In order to make comparisons with other works more meaningful, we adjust our results as described below. The analysis in Ungerechts et al. (1997) is based on the most extensive and recent data set covering several molecules and is less sensitive to systematic errors introduced by the incorporation of ancillary data from other papers. We will thus mainly focus on the comparison with their results.

As Ungerechts et al. (1997) decided to list their abundances relative to CO, not $H_2$, we will convert our abundances for the comparison in Table 5.3 accordingly. Additionally, the authors only considered a single position, not an area, to which we will also adapt and list our values for that specific coordinate only. One aspect was however not accounted for in these conversions. Ungerechts et al. (1997) based their calculations on integrated intensity maps, while we based ours on a voxel approach. The resulting different treatment of velocity components along the line-of-sight is a source of variation between the two analyses. We find our abundances to be systematically lower in comparisons, but generally deviating little more than a factor of 10. An exception is the larger deviation of a factor $\sim 25$ found for CN. As their observations had a larger beam size ($\sim 50''$ vs. $\sim 32''$), these discrepancies are likely not caused by beam filling factors, as we would then expect their abundances – if at all – to be lower than ours. Their CO column density is also slightly larger than ours ($4.4 \times 10^{18}$ vs. $2.8 \times 10^{18}$), again favouring lower abundances. Their systematically higher abundances are likely caused by the assumed gas temperature, which they considered to be 28 K, as calculated from $CH_3CCH$ observations, in all cases. In contrast, we find temperatures between 4 K (CN) and 22 K ($N_2H^+$) in our calculation for the analysed position. The very low temperature of CN was also found by Greaves & White (1992), and the authors explained the strong CN $N = 1-0$ emission reported by Turner & Thaddeus (1977) as a result of the ensued large level population of $N = 1$ compared to $N = 2$ (for which $E_\mathrm{u} > T_\mathrm{ex}$). As Ungerechts et al. (1997) also observed the $N = 1 - 0$ transition, they might have also seen this overpopulation and, combined with their higher assumed $T_\mathrm{ex}$, arrived at higher column densities. However, the very low CN temperature may also be indicative of non-LTE conditions, or a clumpy medium on smaller scales which we do not resolve. In the latter case, our assumed filling factor $f = 1$ would be too large and the actual higher $T_\mathrm{ex}$ of the unresolved clumps 'spread out' and thus reduced over the beam.

With their six positions along the OMC-1 ridge, Ungerechts et al. (1997) notice a north-south gradient for their examined molecular ions ($HCO^+$ and $N_2H^+$), with values decreasing towards the South. Our abundance maps generally do not support that statement. As discussed above, $HCO^+$ has several local enhancements (albeit lower abundances towards the Bar), and $N_2H^+$ abundances increase with distance to Orion KL.

In conclusion, we generally find good agreement between the calculated abundances in Ungerechts et al. (1997) and our data set for most species. The more substantial deviations for CN can largely be explained by low excitation temperatures, and our systematically lower values may be generated by different temperature and opacity estimates. Additionally, our conservative approach of only considering channels above $5\,\sigma$ in our calculations means that our values may actually be lower limits. However, owed to the differences between a position and map based approach, our conclusions regarding abundance variations across OMC-1 differ. On even slightly larger scales, we find e.g. that abundances are overall similar for some species, while Ungerechts et al. (1997) see gradients. This highlights the challenges associated with the interpretation of single pointed observations.

**Table 5.3:** Comparing our molecular abundances with those from Ungerechts et al. (1997). In contrast to Table 5.2, our values now refer to those at a specific position ($\alpha_{2000} = 5^{\mathrm{h}}35^{\mathrm{m}}16.0^{\mathrm{s}}$, $\delta_{2000} = -5°19'14.0''$), and are written in the form $\frac{N[\mathrm{X}]}{N[\mathrm{CO}]}$, in accordance with the other authors' work.

|  | $C_2H$ | CN | HCN | $HCO^+$ | HNC | $N_2H^+$ |
|---|---|---|---|---|---|---|
| Ungerechts et al. (1997) | $4 \times 10^{-4}$ | $1 \times 10^{-4}$ | $1 \times 10^{-4}$ | $5 \times 10^{-5}$ | $4 \times 10^{-5}$ | $1 \times 10^{-5}$ |
| This work | $2 \times 10^{-4}$ | $4 \times 10^{-6}$ | $1 \times 10^{-5}$ | $8 \times 10^{-6}$ | $5 \times 10^{-6}$ | $7 \times 10^{-6}$ |

**Notes.** We also accounted for systematic errors introduced by different assumed isotopic ratios and adjusted our values accordingly. Ungerechts et al. (1997) used $^{16}\mathrm{O}/^{18}\mathrm{O} \approx 500$ and $^{12}\mathrm{C}/^{13}\mathrm{C} \approx 65$, instead of our used factors of 560 and 77 from Wilson & Rood (1994). CS was omitted in this comparison as our map has a blanked pixel at the examined position.

**Table 5.4:** Compact radio sources from Forbrich et al. (2016) in the RR2 subregion.

| source ID[1] | $\alpha_{\mathrm{J2000}}$ | $\delta_{2000}$ | peak[1] [mJy] | RSI | COUP[2] | $\log L_{\mathrm{t,c}}^2$ [erg s$^{-1}$] | VISION[3] | comment |
|---|---|---|---|---|---|---|---|---|
| 155 | 05:35:13.97369 | -05:21:23.2927 | $0.0297 \pm 0.0028$ | | 587 | 30.55 | 05351397-0521233 | |
| 168 | 05:35:14.21082 | -05:21:04.2842 | $0.0335 \pm 0.0029$ | | | | | |
| 176 | 05:35:14.31409 | -05:21:17.8338 | $0.0595 \pm 0.0028$ | | | | | |
| 182 | 05:35:14.40372 | -05:21:27.1653 | $0.0259 \pm 0.0028$ | $-0.23 \pm 0.40$ | | | | |
| 197 | 05:35:14.65775 | -05:20:42.2782 | $0.0378 \pm 0.0032$ | | 645 | 30.67 | 05351465-0520424 | |
| 238 | 05:35:15.45928 | -05:20:40.6911 | $0.1155 \pm 0.0031$ | | 703 | 30.25 | | Herbig Haro[4] |
| 242 | 05:35:15.60361 | -05:21:26.8917 | $0.2195 \pm 0.0028$ | $-0.17 \pm 0.08$ | 723 | 30.31 | | EG?[5] |
| 248 | 05:35:15.76824 | -05:21:13.2838 | $0.0472 \pm 0.0029$ | | | | | |
| 253 | 05:35:15.79898 | -05:21:13.9629 | $0.1258 \pm 0.0029$ | | | | | |
| 257 | 05:35:15.85064 | -05:21:10.1341 | $0.0380 \pm 0.0029$ | | | | | |
| 268 | 05:35:16.00286 | -05:21:09.8289 | $0.0976 \pm 0.0030$ | $-0.17 \pm 0.33$ | 762 | 30.57 | 05351600-0521099 | |
| 285 | 05:35:16.19646 | -05:21:32.3645 | $0.0497 \pm 0.0027$ | | 783 | 29.24 | 05351619-0521323 | |
| 315 | 05:35:16.65630 | -05:20:44.3434 | $0.0207 \pm 0.0032$ | | | | | |
| 343 | 05:35:17.21958 | -05:21:31.7147 | $0.9202 \pm 0.0029$ | $+0.26 \pm 0.09$ | 867 | 30.82 | 05351721-0521317 | |
| 357 | 05:35:17.50534 | -05:21:06.1892 | $0.0363 \pm 0.0030$ | | 896 | 30.40 | 05351750-0521062 | |
| 408 | 05:35:18.51886 | -05:21:28.3480 | $0.0167 \pm 0.0027$ | | | | | |
| 409 | 05:35:18.51914 | -05:20:42.7084 | $0.1089 \pm 0.0033$ | $+0.00 \pm 0.32$ | 976 | 30.36 | 05351852-0520428 | |
| 418 | 05:35:18.73430 | -05:21:28.0624 | $0.0429 \pm 0.0030$ | | | | | |
| 419 | 05:35:18.76103 | -05:21:27.6575 | $0.0406 \pm 0.0028$ | | | | | |
| 420 | 05:35:18.82192 | -05:21:26.6778 | $0.0339 \pm 0.0029$ | | | | | |
| 422 | 05:35:18.85762 | -05:21:41.1593 | $0.6760 \pm 0.0029$ | $+1.11 \pm 0.13$ | 997 | 30.86 | 05351885-0521412 | |

**Notes.**
[1] Source identifier and peak flux density from Forbrich et al. (2016).
[2] Source identifier and absorption corrected X-ray luminosity from the *Chandra* Orion Ultradeep Project (COUP, Getman et al. 2005b).
[3] Source identifier from the NIR Vienna survey in Orion (VISION, Meingast et al. 2016).
[4] Likely Herbig Haro outflow bow shock (Getman et al. 2005a; Grosso et al. 2006).
[5] Extragalactic origin possible as well (Getman et al. 2005a).

### 5.4.1 Association with compact radio sources and extremely high density gas

To ascertain if the tentative abundance enhancements of $C_2H$, CN, and HNC observed in RR2 might be related to nearby stars, we examined the (projected) positions of the Orion Nebula Cluster members. A suitable catalogue of compact radio sources is compiled in Forbrich et al. (2016). However, as no extinction is stated for the sources, we do not know their exact spatial locations on the line-of-sight, but most of the stellar population is likely located in front of the molecular cloud and is no longer embedded (see also Section 1.4.1). As a visual aid, Fig. 5.8 depicts the already shown abundance maps of $C_2H$, CN, and HNC in grey-scale, while the positions of compact radio sources are overplotted in colour. Some of these sources have known counterparts in other frequency regimes, namely near-infra red (NIR) and X-ray and are marked as such. We do not see an overdensity of sources, or a clustering of a specific source type, in the RR2 subregion. The present sources, listes in Table 5.4, are also not particularly strong in their respective frequency regimes compared to others in OMC-1. For 6 out of the 21 sources the radio spectral index (RSI) could be determined, but the errors are still quite large. This may be the reason that three sources have an RSI $< -0.1$ (indicative of synchrotron emission), while the other indices suggest a thermal origin. The radio source likely associated with a Herbig Haro outflow shock (identifier 703) is located at the very edge of our region and does not coincide with an abundance maximum.

Recently, extremely high gas densities have been detected through the $J = 7 - 6$ transition of $N_2H^+$ in OMC-1. Exceptional conditions like these could give rise to deviations from general abundances. However, the line was found to be enhanced in regions where $N_2H^+$ is illuminated by the nebula (warm and dense gas), and not in our discussed subregions (Hacar 2020, private communication). Should the tentatively seen abundance enhancements in our data be real, they are not obviously connected to either the ONC stars or local high density concentrations.

### 5.4.2 Comparison with modeled molecular abundances

Modeling molecular abundances is computationally expensive, such that compromises regarding e.g. the extent of chemical networks, inclusion of grain surface processes, or time-dependency of parameters are made. Additionally, actual sources vary in age, mass, geometry, metallicity, radiation field, stellar feedback, or galactocentric distance. As such, 'general' abundance values obtained from models not only have uncertainties associated with their degree of complexity, but the transferability to real observations is limited due to the large variations encountered between different molecular clouds and even regions within the same cloud. Molecular abundances can vary by several orders of magnitude at sub-parsec scale (Agúndez & Wakelam 2013). It is also important to keep an observations' spatial resolution in mind, as a clumpy distribution of a species may be 'diluted' on large scales where the structure is not resolved. In that case, one would not recover the modeled abundances, but obtain lower values.

Conscious of these limits, the state-of-the-art regarding the modeling of dark clouds is discussed and compared to observations of two sources in Agúndez & Wakelam (2013). This paper also forms the basis for the molecular abundances in the ISM reported in the KIDA data base[5] and the associated ISA (InterStellar Abundances) website[6]. The authors' chemical models are pseudo-time-dependent[7], consider $\sim 470$ species and $\sim 6100$ reactions[8], have no external UV radiation

---

[5] http://kida.astrophy.u-bordeaux.fr/

[6] http://isa.astrophy.u-bordeaux.fr/species.html

[7] With fixed temperature ($T = 10$ K) and density of H nuclei ($n_H = 2 \times 10^4$ cm$^{-3}$).

[8] Another source of uncertainty is the fact that not all reaction rates have been measured experimentally.
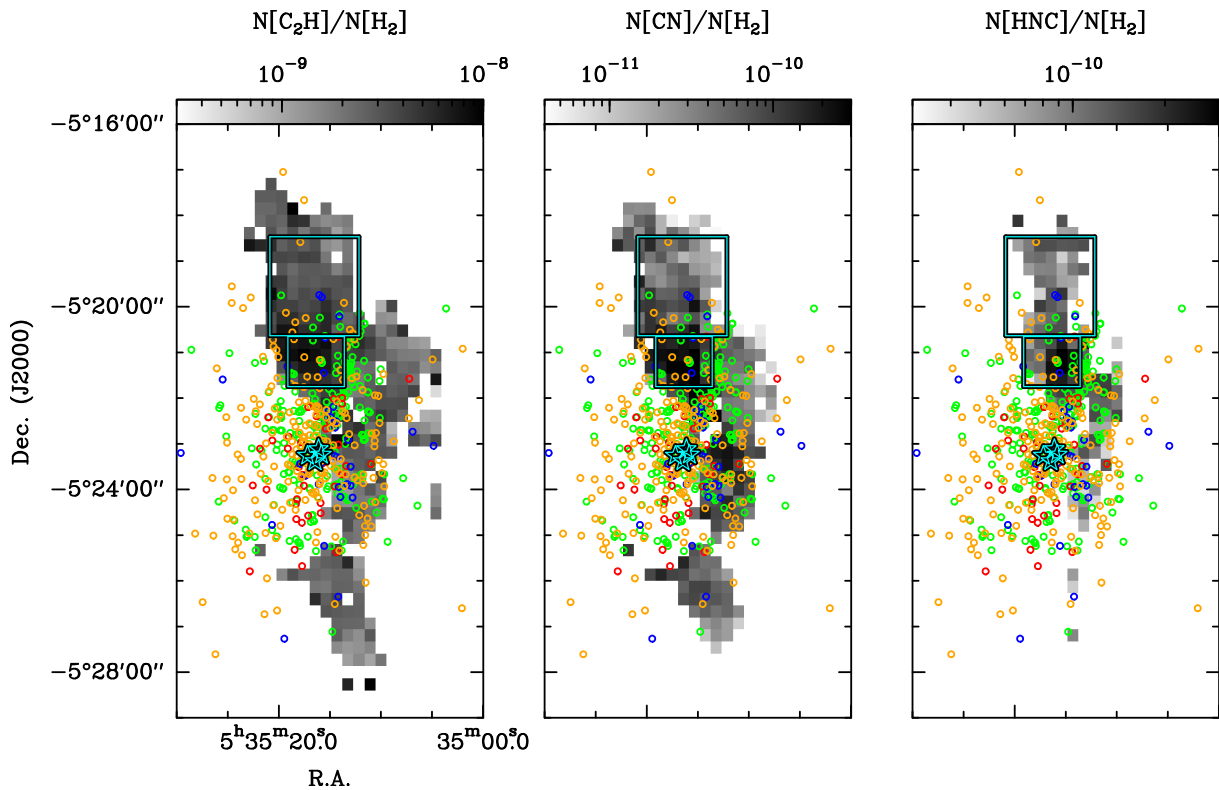
**Figure 5.8:** Abundance maps of C$_2$H, CN, and HNC overlaid with the positions of compact radio sources from Forbrich et al. (2016). The radical region, RR2, and the Trapezium stars are highlighted in cyan, and the compact radio sources marked with circles. The colours indicate if the radio source has a counterpart in the near-infra red (red) from Meingast et al. (2016), in X-ray (blue) from Getman et al. (2005b), in both frequency regimes (orange), or if it has no respective counterpart (green).

field ($A_\mathrm{v} = 30$), and account for gas phase processes only. The chemistry is thus mainly initiated through cosmic rays and driven by ion-neutral reactions.

The plots in Agúndez & Wakelam (2013) show the molecular abundances relative to H$_2$ as a function of time for each species and highlight the very different dynamics for each molecule, in which abundances change several orders of magnitude. We reproduce the authors' plots for the eight species considered in our analysis in Fig. 5.9 and added the range between minimum and maximum abundances found in OMC-1 from Table 5.2. We find some overlap between our abundances and those from the two sources discussed in the publication for most species. However, for HNC and HCO$^+$ there are more prominent deviations, both from the two other sources and the models. As HNC and HCO$^+$ are sensitive to temperature (as discussed in Section 5.3.1), the fixed $T = 10$ K for the models may be overall more problematic for these species, as is the exclusion of an external radiation field. Our comparatively low abundances for CN could also be more evidence for non-resolved substructures appearing diluted over our beam. Despite the shortcomings of the model parameters, which in some cases differ strongly from the conditions in OMC-1, our abundances seem to be reasonably reproduced. Agúndez & Wakelam (2013) note that the abundances for TMC-1 and L134N mostly refer to those at a specific position only (not maps). As such, their variances in the abundance plots are significantly smaller than those for OMC-1.

## 5.5  Summary

We obtained abundance maps for eight molecular species in OMC-1, aiming to clarify the nature of the radical region located in the northern part of the cloud. In contrast to previous works on the subject, we could build on our extensive data set to calculate the necessary opacities and excitation temperatures for all species individually, while our voxel based approach allowed us to account for different velocity components along each line-of-sight. Furthermore, our maps convey a more general impression of the degree of abundance variation across OMC-1, which pointed observations alone cannot give.

Apart from the radical region, an examination of a second region (RR2) was prompted by the observation that $C_2H$, CN, and HNC show a (local) abundance maximum at roughly the same position. However, averaged abundances for both regions and OMC-1 only vary within our uncertainties. Our analysis thus suggests that the radical region is not characterised by an exceptional chemistry, but rather conforms to the general conditions found within OMC-1 as a whole. We subsequently investigated the association of stellar ONC members with the abundances of $C_2H$, CN, and HNC. However, only the sources' projected positions, not their exact spatial positions, are known. We see no overdensities of sources or specific source types in the examined subregions. As we expect most stars to be located in front of the molecular cloud, their influence on the dense molecular material of the OMC-1 ridge is likely limited (naturally with the exception of the very luminous Trapezium stars).
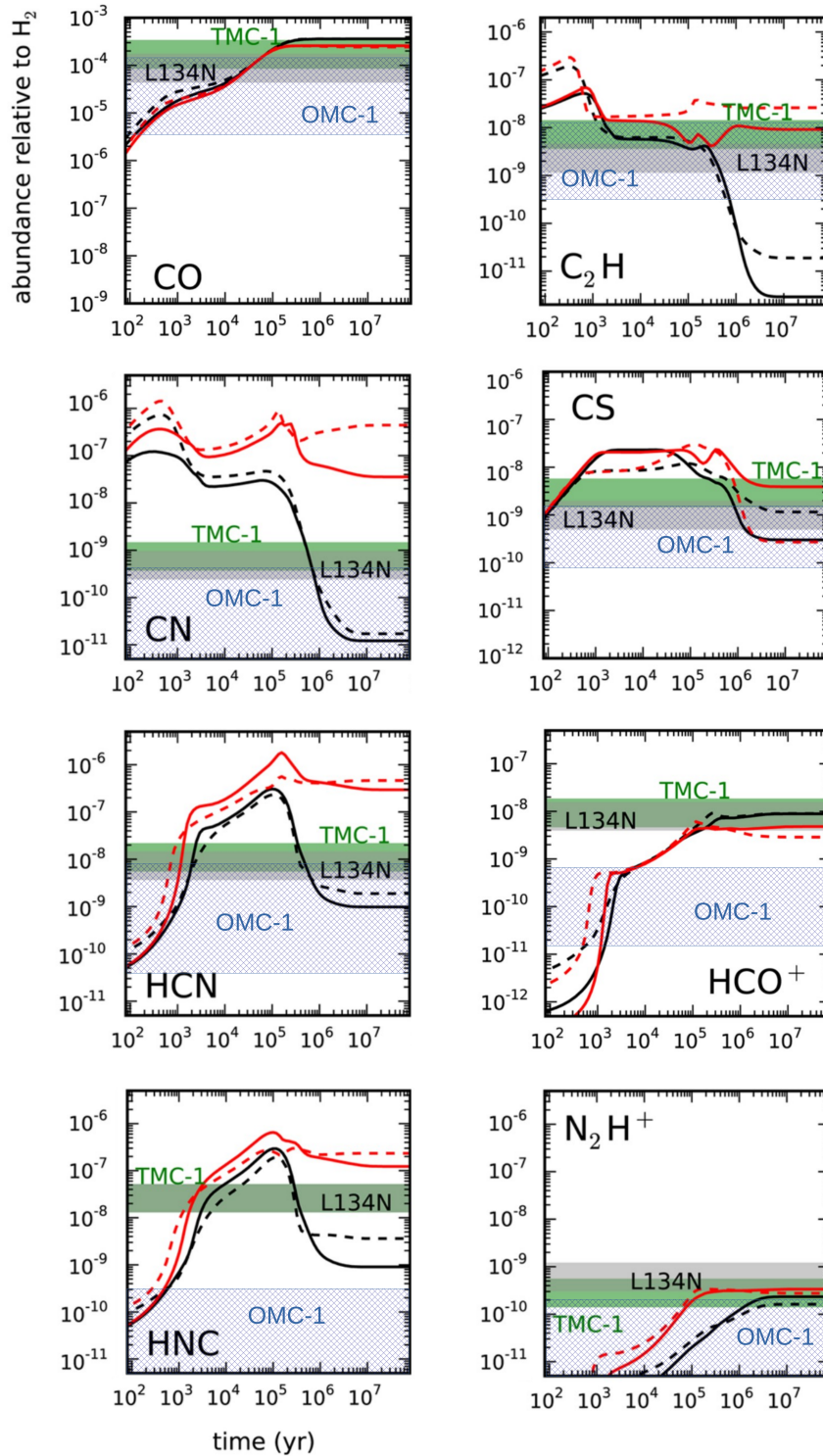
**Figure 5.9:** Models of molecular abundances as a function of time from Agúndez & Wakelam (2013) (adapted from their Figs. 2, 3, 4, and 5). The solid and dashed lines refer to chemical networks from different data bases and are further discussed in the original publication, as are the results for the two sources TMC-1 and L134N. For comparison, we added our values for OMC-1 from Table 5.2 as the blue hatched area.

# Conclusions and perspective

This thesis centers on an imaging line survey of Orion A and represents the first analysis of a spectroscopically unbiased data set of a large part of a molecular cloud in the 1.3 mm window. Obtaining this data set became possible with the new PI230 receiver on the APEX telescope, whose high sensitivity and large bandwidth make it a powerful tool for extensive mapping efforts. Chapter 2 reported on the receiver's commissioning phase and general performance.

In Chapter 3, we explored the emission of distinct cloud regions, which were selected to represent regimes of different column densities, temperatures, and UV irradiation. Examining the averaged spectra of these extended regions is essential, as these spectra retain the truly characteristic emission features, while local peculiarities are averaged out over large scales. By considering 29 molecular species (55 isotopologues in total), we not only include typically bright tracers of e.g. high density, but also fainter species, which facilitate a more detailed comparison of regions. Our results aim to help with the interpretation of more distant, unresolved sources, both in the Milky Way and extragalactic systems, by providing these 'template' regions that other observations may be compared to.

We found that the region around KL and Orion South, taking up less than 1% of the mapped area, is the source of $\sim 25\%$ of the total line luminosity. Such objects may thus contribute significantly to spectra averaged over larger regions, and some of their chemical signatures (e.g. significant contributions from $SO_2$, SiO, or complex organic molecules) remain detectable. In contrast, identifying the presence of dense and cold regions like OMC-2/3, with pre-stellar Class 0 and Class I objects, appears to be challenging close to very luminous star forming regions for non-resolved sources. Their signatures (e.g. high share of $N_2H^+$ emission, and low HCN/HNC ratio), are 'diluted' on larger scales due to their general lower line intensities. $N_2H^+$ was found to have the strongest correlation with column density, but no distinct correlation with typical high-density tracers like HCN, HNC or $HCO^+$. Electron excitation or radiative trapping are possible causes for the latters' bright emission lines, such that they do not exclusively trace dense gas and their interpretation in non-resolved sources may be difficult. We found that $\sim 50\%$ of the $HCO^+$ and HNC line luminosity originates from lower column density material, and $\sim 35\%$ for HCN. Typically used line ratios varied in reliability over large scales: while HCN/HNC increases with temperature (as theoretically expected), CN/HCN and CN/$HCO^+$ showed ambiguous results as tracers of UV irradiation.

In Chapter 4, we followed up on the rather unexpected detection of $CF^+$ in the averaged spectra of Chapter 3. We confirmed the molecule's presence through pointed observations of both $J = 2-1$ and $J = 3-2$ transitions at selected positions. Our analysis suggests an overall uniform distribution, in conflict with its proposed use as a reliable $C^+$ and PDR tracer. $CF^+$ emission may be a common occurrence in regions with a generally enhanced radiation field. However, more data on the $CF^+$ and $C^+$ relation might enable us to correct extragalactic $C^+$ observations for their atomic contribution, thus improving their star formation rate estimates. We consider the omission of photodissociation in previous calculations and models to be a significant factor for the relatively low emission of $CF^+$ observed in the Orion Bar. Nevertheless, more reaction rates will need to be experimentally

determined before a full treatment of the chemistry is possible.

Chapter 5 examined the abundance variation of eight species across OMC-1 with the aim to identify the nature of the 'radical region'. We found that the region is not characterised by a unique chemistry, but that its molecular abundances conform to those of OMC-1 as a whole within our uncertainties. By considering abundance maps, we could also correct previously reported abundance gradients seen with pointed observations. Additionally, the maps enabled us to better explore correlations between molecular abundances of different species and selected physical parameters, pointing to some of the underlying chemistry and mutual dependencies. We did not recover all of the correlations between species seen for the integrated intensities in Chapter 3, which we mostly attribute to opacity effects.

While Orion A offers a large range of environments, and its proximity allowed us to resolve it from parsec scale down to $\sim 60$ mpc ($\sim 1.2 \times 10^4$ AU), it is only a single object and cannot be representative of all molecular clouds. An important next step would thus be the application of our masks to comparable data sets of other sources observed with similar spatial resolution. This would enable us to gauge the variance between molecular clouds and how exactly parameters like age, metallicity, or galactocentric distance influence their emission profile. At the moment, no suitable data sets exist in the 1.3 mm window. In lower frequency regimes however, the ongoing LEGO project (Kauffmann et al. 2017) aims to develop a comprehensive picture of molecular emission lines in the 3 mm window throughout the Milky Way. Clouds selected to represent e.g. different densities, or galactic environment are observed with the EMIR receiver at the IRAM 30 m telescope. First results will soon be published for the W49 region (Barnes et al. 2020, accepted by MNRAS).

All three science projects of this thesis emphasise not only the advantage of the new unbiased imaging line surveys, but rather their future imperative. Without the full frequency coverage, we would not have detected the weak $CF^+$ line as a 'by-product' in our analysis of large scale emission. This molecule had never been a target for mapping efforts due to its low intensity. Furthermore, our maps of molecular abundances did not confirm gradients reported by other papers. Pointed observations alone may thus be too dependent on local conditions to be representative of their general surroundings.

The capability of imaging line surveys of resolved sources to trace back large scale emission features to smaller scale objects and regions will be necessary for the next generation of extragalactic observations, for which resolutions of parsec scale will be achieved.

# Acknowledgements

# Additional tables

**Table A.1:** All considered transitions for our fitting procedure. The comments are based on the spectrum of the high column density region. Notes concerning overlap between lines, especially with complex organic molecules, are thus likely not relevant on larger scales or for low column density/low temperature regions. Lines ignored due to e.g. locally too poor S/N are marked as such. In case of a strong overlap and one line being significantly stronger than the other (e.g. overlap with $HCO^+$), the area is contributed to the stronger line only. (*) Three CN transitions are strongly blended and part of this line falls into a gap in the frequency coverage. A Gauss fit is still possible, and we made sure that the fitted line has no peak intensity larger than the visible part of the line.

| Species | Isotopologue | Frequency [MHz] | Transition | $E_{up}$ [K] | $G_{up}$ | $A_{ij}$ [s$^{-1}$] | Comment |
|---|---|---|---|---|---|---|---|
| c-$C_3H_2$ | c-$C_3H_2$ | 204788.926 | $4_{2,2,0} - 3_{3,1,0}$ | 28.8 | 9 | 1.37e-04 | ignored, S/N not good |
| | | 216278.756 | $3_{3,0,0} - 2_{2,1,0}$ | 19.5 | 21 | 2.81e-04 | |
| | | 217822.148 | $6_{1,6,0} - 5_{0,5,0}$ | 38.6 | 39 | 5.93e-04 | |
| | | 217822.148 | $6_{0,6,0} - 5_{1,5,0}$ | 38.6 | 13 | 5.93e-04 | |
| | | 217940.046 | $5_{1,4,0} - 4_{2,3,0}$ | 35.4 | 33 | 4.43e-04 | |
| | | 218160.442 | $5_{2,4,0} - 4_{1,3,0}$ | 35.4 | 11 | 4.44e-04 | |
| | | 227169.127 | $4_{3,2,0} - 3_{2,1,0}$ | 29.1 | 27 | 3.42e-04 | |
| | | 249054.368 | $5_{2,3,0} - 4_{3,2,0}$ | 41.0 | 33 | 4.57e-04 | |
| | | 251314.337 | $7_{0,7,0} - 6_{1,6,0}$ | 50.7 | 45 | 9.35e-04 | |
| | | 251314.343 | $7_{1,7,0} - 6_{0,6,0}$ | 50.7 | 15 | 9.35e-04 | |
| | | 251508.691 | $6_{1,5,0} - 5_{2,4,0}$ | 47.5 | 13 | 7.42e-04 | |
| | | 251527.302 | $6_{2,5,0} - 5_{1,4,0}$ | 47.5 | 39 | 7.42e-04 | |
| | | 254987.640 | $5_{3,3,0} - 4_{2,2,0}$ | 41.1 | 11 | 5.17e-04 | ignored, S/N not good |
| | | 260479.746 | $5_{3,2,0} - 4_{4,1,0}$ | 44.7 | 33 | 1.77e-04 | ignored, blended with SiO |
| | | 265759.438 | $4_{4,1,0} - 3_{3,0,0}$ | 32.2 | 27 | 7.99e-04 | |
| CCH | CCH | 261978.120 | $3_{4,3} - 2_{3,3}$ | 25.1 | 7 | 1.96e-06 | |
| | | 262004.260 | $3_{4,4} - 2_{3,3}$ | 25.1 | 9 | 5.32e-05 | |
| | | 262006.482 | $3_{4,3} - 2_{3,2}$ | 25.1 | 7 | 5.12e-05 | |
| | | 262064.986 | $3_{3,3} - 2_{2,2}$ | 25.2 | 7 | 4.89e-05 | |
| | | 262067.469 | $3_{3,2} - 2_{2,1}$ | 25.2 | 5 | 4.47e-05 | |
| | | 262078.935 | $3_{3,2} - 2_{2,2}$ | 25.2 | 5 | 6.02e-06 | |
| | | 262208.614 | $3_{3,3} - 2_{3,3}$ | 25.2 | 7 | 3.96e-06 | |
| | | 262250.929 | $3_{3,2} - 2_{3,2}$ | 25.2 | 5 | 2.27e-06 | |
| | CCD | 216372.830 | $3_{4,5} - 2_{3,4}$ | 20.8 | 10 | 3e-05 | |
| | | 216373.320 | $3_{4,3} - 2_{3,2}$ | 20.8 | 6 | 2.67e-05 | |
| | | 216373.320 | $3_{4,4} - 2_{3,3}$ | 20.8 | 8 | 2.76e-05 | |
| | | 216428.320 | $3_{3,4} - 2_{2,3}$ | 20.8 | 8 | 2.78e-05 | |
| | | 216428.320 | $3_{3,3} - 2_{2,2}$ | 20.8 | 6 | 2.34e-05 | |
| | | 216428.760 | $3_{3,2} - 2_{2,1}$ | 20.8 | 4 | 2.1e-05 | |
| $CF^+$ | $CF^+$ | 205170.520 | $2_0 - 1_0$ | 14.8 | 5 | 4.62e-05 | may be blended with $CH_3CHO$ |
| $CH_3CCH$ | $CH_3CCH$ | 205018.080 | $12_4 - 11_4$ | 179.2 | 25 | 2.41e-05 | blended with $CH_3OCH_3$ |
| | | 205045.401 | $12_3 - 11_3$ | 128.8 | 50 | 2.54e-05 | |
| | | 205065.015 | $12_2 - 11_2$ | 92.8 | 25 | 2.63e-05 | |
| | | 205076.775 | $12_1 - 11_1$ | 71.2 | 25 | 2.69e-05 | |
| | | 205080.660 | $12_0 - 11_0$ | 64.0 | 25 | 2.71e-05 | |
| | | 222099.151 | $13_4 - 12_4$ | 189.8 | 27 | 3.13e-05 | |
| | | 222128.808 | $13_3 - 12_3$ | 139.4 | 54 | 3.27e-05 | |
| | | 222150.008 | $13_2 - 12_2$ | 103.4 | 27 | 3.37e-05 | |
| | | 222162.729 | $13_1 - 12_1$ | 81.8 | 27 | 3.44e-05 | |
| | | 222166.970 | $13_0 - 12_0$ | 74.6 | 27 | 3.46e-05 | |
| | | 239211.216 | $14_3 - 13_3$ | 150.9 | 58 | 4.13e-05 | |
| | | 239234.011 | $14_2 - 13_2$ | 114.9 | 29 | 4.24e-05 | |
| | | 239247.727 | $14_1 - 13_1$ | 93.3 | 29 | 4.31e-05 | |
| | | 239252.297 | $14_0 - 13_0$ | 86.1 | 29 | 4.33e-05 | |
| | | 256292.638 | $15_3 - 14_3$ | 163.2 | 62 | 5.12e-05 | |
| | | 256317.078 | $15_2 - 14_2$ | 127.2 | 31 | 5.24e-05 | |

| (Continuation) Species | Isotopologue | Frequency | Transition | $E_{up}$ | $G_{up}$ | $A_{ij}$ | Comment |
|---|---|---|---|---|---|---|---|
| | | 256331.746 | $11_3 - 10_3$ | 105.6 | 31 | 5.31e-05 | |
| | | 256336.636 | $15_0 - 14_0$ | 98.4 | 31 | 5.34e-05 | |
| | | 273373.006 | $16_3 - 15_3$ | 176.3 | 66 | 6.26e-05 | |
| | | 273399.067 | $16_2 - 15_2$ | 140.3 | 33 | 6.39e-05 | |
| | | 273414.707 | $16_1 - 15_1$ | 118.7 | 33 | 6.46e-05 | |
| | | 273419.921 | $16_0 - 15_0$ | 111.5 | 33 | 6.49e-05 | |
| $CH_3CN$ | $CH_3CN$ | 202215.371 | $11_6 - 10_6$ | 315.3 | 92 | 4.97e-04 | |
| | | 202258.154 | $11_5 - 10_5$ | 236.8 | 46 | 5.62e-04 | |
| | | 202293.183 | $11_4 - 10_4$ | 172.6 | 46 | 6.15e-04 | |
| | | 202320.443 | $11_3 - 10_3$ | 122.6 | 92 | 6.56e-04 | |
| | | 202339.921 | $11_2 - 10_2$ | 86.8 | 46 | 6.86e-04 | |
| | | 202351.612 | $11_1 - 10_1$ | 65.4 | 46 | 7.03e-04 | |
| | | 202355.509 | $11_0 - 10_0$ | 58.3 | 46 | 7.09e-04 | |
| | | 220594.423 | $12_6 - 11_6$ | 325.9 | 100 | 6.92e-04 | |
| | | 220641.084 | $12_5 - 11_5$ | 247.4 | 50 | 7.63e-04 | |
| | | 220679.287 | $12_4 - 11_4$ | 183.1 | 50 | 8.21e-04 | |
| | | 220709.016 | $12_3 - 11_3$ | 133.2 | 100 | 8.66e-04 | |
| | | 220730.261 | $12_2 - 11_2$ | 97.4 | 50 | 8.98e-04 | |
| | | 220743.011 | $12_1 - 11_1$ | 76.0 | 50 | 9.18e-04 | |
| | | 220747.261 | $12_0 - 11_0$ | 68.9 | 50 | 9.24e-04 | |
| | | 238972.389 | $13_6 - 12_6$ | 337.4 | 108 | 9.26e-04 | |
| | | 239022.924 | $13_5 - 12_5$ | 258.9 | 54 | 1e-03 | |
| | | 239064.299 | $13_4 - 12_4$ | 194.6 | 54 | 1.07e-03 | |
| | | 239096.497 | $13_3 - 12_3$ | 144.6 | 108 | 1.12e-03 | |
| | | 239119.504 | $13_2 - 12_2$ | 108.9 | 54 | 1.15e-03 | |
| | | 239133.313 | $13_1 - 12_1$ | 87.5 | 54 | 1.17e-03 | |
| | | 239137.916 | $13_0 - 12_0$ | 80.3 | 54 | 1.18e-03 | |
| | | 257349.179 | $14_6 - 13_6$ | 349.7 | 116 | 1.2e-03 | |
| | | 257403.584 | $14_5 - 13_5$ | 271.2 | 58 | 1.29e-03 | blended with $CH_3OH$ |
| | | 257448.128 | $14_4 - 13_4$ | 207.0 | 58 | 1.35e-03 | |
| | | 257482.791 | $14_3 - 13_3$ | 157.0 | 116 | 1.41e-03 | |
| | | 257507.561 | $14_2 - 13_2$ | 121.3 | 58 | 1.45e-03 | |
| | | 257522.427 | $14_1 - 13_1$ | 99.8 | 58 | 1.47e-03 | |
| | | 257527.383 | $14_0 - 13_0$ | 92.7 | 58 | 1.48e-03 | |
| | | 275724.702 | $15_6 - 14_6$ | 363.0 | 124 | 1.53e-03 | |
| | | 275782.974 | $15_5 - 14_5$ | 284.5 | 62 | 1.62e-03 | |
| | | 275830.683 | $15_4 - 14_4$ | 220.2 | 62 | 1.69e-03 | |
| | | 275867.810 | $15_3 - 14_3$ | 170.2 | 124 | 1.75e-03 | |
| | | 275894.340 | $15_2 - 14_2$ | 134.5 | 62 | 1.79e-03 | |
| | | 275910.263 | $15_1 - 14_1$ | 113.1 | 62 | 1.81e-03 | |
| | | 275915.571 | $15_0 - 14_0$ | 105.9 | 62 | 1.82e-03 | |
| $CH_3OH$ | $CH_3OH$ | 201071.847 | $8_{4,5,0} - 9_{3,6,0}$ | 163.9 | 68 | 9.12e-06 | |
| | | 201088.939 | $8_{4,4,0} - 9_{3,7,0}$ | 163.9 | 68 | 9.12e-06 | |
| | | 200820.674 | $15_{3,12,2} - 14_{4,11,2}$ | 341.2 | 124 | 1.27e-05 | |
| | | 201445.493 | $5_{2,3,0} - 6_{1,6,0}$ | 72.5 | 44 | 1.3e-05 | |
| | | 201996.513 | $18_{1,17,1} - 18_{0,18,1}$ | 417.9 | 148 | 2.92e-05 | |
| | | 205791.270 | $1_{1,1,0} - 2_{0,2,0}$ | 16.8 | 12 | 3.36e-05 | |
| | | 206001.302 | $12_{5,7,1} - 13_{4,9,1}$ | 317.1 | 100 | 1.04e-05 | |
| | | 209518.804 | $19_{1,18,1} - 19_{0,19,1}$ | 462.0 | 156 | 3.13e-05 | ignored, blended with $CH_3OCH_3$ |
| | | 213377.528 | $13_{6,8,1} - 14_{5,9,1}$ | 389.9 | 108 | 1.07e-05 | |
| | | 213427.061 | $1_{1,0,1} - 0_{0,0,1}$ | 23.4 | 12 | 3.37e-05 | |
| | | 215302.206 | $6_{1,6,3} - 7_{2,6,3}$ | 373.8 | 52 | 4.18e-05 | |
| | | 216945.521 | $5_{1,4,1} - 4_{2,3,1}$ | 55.9 | 44 | 1.21e-05 | |
| | | 217299.205 | $6_{1,5,3} - 7_{2,5,3}$ | 373.9 | 52 | 4.28e-05 | |
| | | 218440.063 | $4_{2,3,1} - 3_{1,2,1}$ | 45.5 | 36 | 4.69e-05 | |
| | | 220078.561 | $8_{0,8,1} - 7_{1,6,1}$ | 96.6 | 68 | 2.52e-05 | |
| | | 220401.317 | $10_{5,6,2} - 11_{4,8,2}$ | 251.6 | 84 | 1.12e-05 | ignored, blended with $^{13}CO$ |
| | | 227814.528 | $16_{1,16,0} - 15_{2,13,0}$ | 327.2 | 132 | 2.18e-05 | |
| | | 229589.056 | $15_{4,11,1} - 16_{3,14,1}$ | 374.4 | 124 | 2.08e-05 | |
| | | 229758.756 | $8_{1,8,2} - 7_{0,7,1}$ | 89.1 | 68 | 4.19e-05 | |
| | | 230027.047 | $3_{2,1,2} - 4_{1,4,2}$ | 39.8 | 28 | 1.49e-05 | |
| | | 231281.110 | $10_{2,9,0} - 9_{3,6,0}$ | 165.3 | 84 | 1.83e-05 | |
| | | 232418.521 | $10_{2,8,0} - 9_{3,7,0}$ | 165.4 | 84 | 1.87e-05 | |
| | | 232783.446 | $18_{3,16,0} - 17_{4,13,0}$ | 446.5 | 148 | 2.17e-05 | |
| | | 232945.797 | $10_{3,7,2} - 11_{2,9,2}$ | 190.4 | 84 | 2.13e-05 | |
| | | 233795.666 | $18_{3,15,0} - 17_{4,14,0}$ | 446.6 | 148 | 2.2e-05 | |
| | | 234683.370 | $4_{2,3,0} - 5_{1,4,0}$ | 60.9 | 36 | 1.87e-05 | |
| | | 234698.519 | $5_{4,2,2} - 6_{3,3,2}$ | 122.7 | 44 | 6.34e-06 | |
| | | 236936.089 | $14_{1,13,0} - 13_{2,12,0}$ | 260.2 | 116 | 3.11e-05 | |
| | | 239746.219 | $5_{1,5,0} - 4_{1,4,0}$ | 49.1 | 44 | 5.66e-05 | |
| | | 240241.490 | $5_{3,3,1} - 6_{2,5,1}$ | 82.5 | 44 | 1.44e-05 | |
| | | 240960.557 | $5_{1,5,3} - 4_{1,4,3}$ | 360.0 | 44 | 5.76e-05 | |
| | | 241159.199 | $5_{4,2,4} - 4_{4,1,4}$ | 398.1 | 44 | 2.15e-05 | |
| | | 241166.580 | $5_{3,2,4} - 4_{3,1,4}$ | 452.1 | 44 | 3.86e-05 | |
| | | 241179.886 | $5_{3,3,5} - 4_{3,2,5}$ | 357.4 | 44 | 3.83e-05 | |
| | | 241184.189 | $5_{4,1,5} - 4_{4,0,5}$ | 440.1 | 44 | 2.16e-05 | |
| | | 241187.428 | $5_{2,4,5} - 4_{2,3,5}$ | 399.3 | 44 | 5.07e-05 | |
| | | 241192.856 | $5_{2,4,3} - 4_{2,3,3}$ | 333.4 | 44 | 5.03e-05 | |
| | | 241196.430 | $5_{2,3,3} - 4_{2,2,3}$ | 333.4 | 44 | 5.03e-05 | |

| (Continuation) Species | Isotopologue | Frequency | Transition | $E_{up}$ | $G_{up}$ | $A_{ij}$ | Comment |
|---|---|---|---|---|---|---|---|
| | | 241198.285 | $5_{3,3,3} - 4_{3,2,3}$ | 430.8 | 44 | 3.83e-05 | |
| | | 241198.291 | $5_{3,2,3} - 4_{3,1,3}$ | 430.8 | 44 | 3.83e-05 | |
| | | 241203.706 | $5_{1,5,4} - 4_{1,4,4}$ | 326.2 | 44 | 5.75e-05 | |
| | | 241206.035 | $5_{0,5,4} - 4_{0,4,4}$ | 335.3 | 44 | 6e-05 | |
| | | 241210.764 | $5_{2,3,4} - 4_{2,2,4}$ | 434.6 | 44 | 5.04e-05 | |
| | | 241238.144 | $5_{1,4,5} - 4_{1,3,5}$ | 448.1 | 44 | 5.75e-05 | |
| | | 241267.862 | $5_{0,5,3} - 4_{0,4,3}$ | 458.4 | 44 | 6e-05 | |
| | | 241441.270 | $5_{1,4,3} - 4_{1,3,3}$ | 360.0 | 44 | 5.79e-05 | |
| | | 241700.159 | $5_{0,5,1} - 4_{0,4,1}$ | 47.9 | 44 | 6.04e-05 | |
| | | 241767.234 | $5_{1,5,2} - 4_{1,4,2}$ | 40.4 | 44 | 5.81e-05 | |
| | | 241791.352 | $5_{0,5,0} - 4_{0,4,0}$ | 34.8 | 44 | 6.05e-05 | |
| | | 241806.524 | $5_{4,2,0} - 4_{4,1,0}$ | 115.2 | 44 | 2.18e-05 | |
| | | 241806.525 | $5_{4,1,0} - 4_{4,0,0}$ | 115.2 | 44 | 2.18e-05 | |
| | | 241813.255 | $5_{4,2,2} - 4_{4,1,2}$ | 122.7 | 44 | 2.18e-05 | |
| | | 241829.629 | $5_{4,1,1} - 4_{4,0,1}$ | 130.8 | 44 | 2.19e-05 | |
| | | 241832.718 | $5_{3,3,0} - 4_{3,2,0}$ | 84.6 | 44 | 3.87e-05 | |
| | | 241833.106 | $5_{3,2,0} - 4_{3,1,0}$ | 84.6 | 44 | 3.87e-05 | |
| | | 241842.284 | $5_{2,4,0} - 4_{2,3,0}$ | 72.5 | 44 | 5.11e-05 | |
| | | 241843.604 | $5_{3,3,1} - 4_{3,2,1}$ | 82.5 | 44 | 3.88e-05 | |
| | | 241852.299 | $5_{3,2,2} - 4_{3,1,2}$ | 97.5 | 44 | 3.89e-05 | |
| | | 241879.025 | $5_{1,4,1} - 4_{1,3,1}$ | 55.9 | 44 | 5.96e-05 | |
| | | 241887.674 | $5_{2,3,0} - 4_{2,2,0}$ | 72.5 | 44 | 5.12e-05 | |
| | | 241904.147 | $5_{2,3,2} - 4_{2,2,2}$ | 60.7 | 44 | 5.09e-05 | |
| | | 241904.643 | $5_{2,4,1} - 4_{2,3,1}$ | 57.1 | 44 | 5.03e-05 | |
| | | 242446.084 | $14_{1,14,2} - 13_{2,11,2}$ | 248.9 | 116 | 2.29e-05 | |
| | | 243915.788 | $5_{1,4,0} - 4_{1,3,0}$ | 49.7 | 44 | 5.97e-05 | |
| | | 244337.983 | $9_{1,9,4} - 8_{0,8,4}$ | 395.6 | 76 | 4.06e-05 | ignored, S/N not good |
| | | 246873.301 | $19_{3,16,0} - 19_{2,17,0}$ | 490.7 | 156 | 8.27e-05 | |
| | | 247161.950 | $16_{2,15,1} - 15_{3,13,1}$ | 338.1 | 132 | 2.57e-05 | |
| | | 247228.587 | $4_{2,2,0} - 5_{1,5,0}$ | 60.9 | 36 | 2.12e-05 | |
| | | 247610.918 | $18_{3,15,0} - 18_{2,16,0}$ | 446.6 | 148 | 8.29e-05 | |
| | | 248282.424 | $17_{3,14,0} - 17_{2,15,0}$ | 404.8 | 140 | 8.3e-05 | |
| | | 248885.468 | $16_{3,13,0} - 16_{2,14,0}$ | 365.4 | 132 | 8.32e-05 | |
| | | 249192.836 | $16_{3,13,2} - 15_{4,12,2}$ | 378.3 | 132 | 2.54e-05 | |
| | | 249419.924 | $15_{3,12,0} - 15_{2,13,0}$ | 328.3 | 124 | 8.32e-05 | |
| | | 249443.301 | $7_{4,4,0} - 8_{3,5,0}$ | 145.3 | 60 | 1.48e-05 | |
| | | 249451.842 | $7_{4,3,0} - 8_{3,6,0}$ | 145.3 | 60 | 1.48e-05 | |
| | | 249887.467 | $14_{3,11,0} - 14_{2,12,0}$ | 293.5 | 116 | 8.32e-05 | |
| | | 250291.181 | $13_{3,10,0} - 13_{2,11,0}$ | 261.0 | 108 | 8.3e-05 | |
| | | 250506.853 | $11_{0,11,0} - 10_{1,10,0}$ | 153.1 | 92 | 8.46e-05 | |
| | | 250635.200 | $12_{3,9,0} - 12_{2,10,0}$ | 230.8 | 100 | 8.28e-05 | |
| | | 250924.398 | $11_{3,8,0} - 11_{2,9,0}$ | 203.0 | 92 | 8.24e-05 | |
| | | 251164.108 | $10_{3,7,0} - 10_{2,8,0}$ | 177.5 | 84 | 8.18e-05 | |
| | | 251359.888 | $9_{3,6,0} - 9_{2,7,0}$ | 154.2 | 76 | 8.09e-05 | |
| | | 251517.309 | $8_{3,5,0} - 8_{2,6,0}$ | 133.4 | 68 | 7.96e-05 | |
| | | 251641.787 | $7_{3,4,0} - 7_{2,5,0}$ | 114.8 | 60 | 7.76e-05 | |
| | | 251738.437 | $6_{3,3,0} - 6_{2,4,0}$ | 98.5 | 52 | 7.46e-05 | |
| | | 251811.956 | $5_{3,2,0} - 5_{2,3,0}$ | 84.6 | 44 | 6.97e-05 | |
| | | 251866.524 | $4_{3,1,0} - 4_{2,2,0}$ | 73.0 | 36 | 6.1e-05 | |
| | | 251890.886 | $5_{3,3,0} - 5_{2,4,0}$ | 84.6 | 44 | 6.97e-05 | |
| | | 251895.728 | $6_{3,4,0} - 6_{2,5,0}$ | 98.5 | 52 | 7.47e-05 | |
| | | 251900.452 | $4_{3,2,0} - 4_{2,3,0}$ | 73.0 | 36 | 6.1e-05 | |
| | | 251905.729 | $3_{3,0,0} - 3_{2,1,0}$ | 63.7 | 28 | 4.36e-05 | |
| | | 251917.065 | $3_{3,1,0} - 3_{2,2,0}$ | 63.7 | 28 | 4.36e-05 | |
| | | 251923.701 | $7_{3,5,0} - 7_{2,6,0}$ | 114.8 | 60 | 7.78e-05 | |
| | | 251984.837 | $8_{3,6,0} - 8_{2,7,0}$ | 133.4 | 68 | 7.98e-05 | |
| | | 252090.409 | $9_{3,7,0} - 9_{2,8,0}$ | 154.2 | 76 | 8.13e-05 | |
| | | 252252.849 | $10_{3,8,0} - 10_{2,9,0}$ | 177.5 | 84 | 8.25e-05 | |
| | | 252485.675 | $11_{3,9,0} - 11_{2,10,0}$ | 203.0 | 92 | 8.34e-05 | |
| | | 252803.388 | $12_{3,10,0} - 12_{2,11,0}$ | 230.8 | 100 | 8.42e-05 | |
| | | 253221.376 | $13_{3,11,0} - 13_{2,12,0}$ | 261.0 | 108 | 8.49e-05 | |
| | | 253755.809 | $14_{3,12,0} - 14_{2,13,0}$ | 293.5 | 116 | 8.56e-05 | |
| | | 254015.377 | $2_{0,2,1} - 1_{1,1,2}$ | 20.1 | 20 | 1.9e-05 | |
| | | 254419.419 | $11_{5,6,1} - 12_{4,8,1}$ | 289.2 | 92 | 1.79e-05 | |
| | | 254423.520 | $15_{3,13,0} - 15_{2,14,0}$ | 328.3 | 124 | 8.63e-05 | |
| | | 255241.888 | $16_{3,14,0} - 16_{2,15,0}$ | 365.4 | 132 | 8.71e-05 | |
| | | 256228.714 | $17_{3,15,0} - 17_{2,16,0}$ | 404.8 | 140 | 8.8e-05 | |
| | | 257402.086 | $18_{3,16,0} - 18_{2,17,0}$ | 446.5 | 148 | 8.9e-05 | ignored, blended with $CH_3CN$ |
| | | 258780.248 | $19_{3,17,0} - 19_{2,18,0}$ | 490.6 | 156 | 9.01e-05 | |
| | | 261704.409 | $12_{6,7,1} - 13_{5,8,1}$ | 359.8 | 100 | 1.78e-05 | |
| | | 261805.675 | $2_{1,1,1} - 1_{0,1,1}$ | 28.0 | 20 | 5.57e-05 | |
| | | 263793.875 | $5_{1,5,3} - 6_{2,5,3}$ | 360.0 | 44 | 8.22e-05 | ignored, blended with HCCCN |
| | | 265224.426 | $5_{1,4,3} - 6_{2,4,3}$ | 360.0 | 44 | 8.33e-05 | |
| | | 265289.562 | $6_{1,5,1} - 5_{2,4,1}$ | 69.8 | 52 | 2.58e-05 | |
| | | 266838.148 | $5_{2,4,1} - 4_{1,3,1}$ | 57.1 | 44 | 7.74e-05 | |
| | | 267403.471 | $9_{0,9,1} - 8_{1,7,1}$ | 117.5 | 76 | 4.67e-05 | |
| | | 267406.071 | $17_{1,17,0} - 16_{2,14,0}$ | 366.3 | 140 | 3.51e-05 | |
| | | 268743.954 | $9_{5,5,2} - 10_{4,7,2}$ | 228.4 | 76 | 1.76e-05 | |
| | | 278304.512 | $9_{1,9,2} - 8_{0,8,1}$ | 110.0 | 76 | 7.69e-05 | |
| | | 278342.261 | $2_{2,0,2} - 3_{1,3,2}$ | 32.9 | 20 | 1.65e-05 | |
| | | 278599.037 | $14_{4,10,1} - 15_{3,13,1}$ | 339.6 | 116 | 3.6e-05 | ignored, S/N not good |
| | | 279351.887 | $11_{2,10,0} - 10_{3,7,0}$ | 190.9 | 92 | 3.45e-05 | |
| | | 280679.621 | $19_{3,17,0} - 18_{4,14,0}$ | 490.6 | 156 | 3.87e-05 | ignored, S/N not good |

| (Continuation) Species | Isotopologue | Frequency | Transition | $E_{up}$ | $G_{up}$ | $A_{ij}$ | Comment |
|---|---|---|---|---|---|---|---|
| | | 281000.109 | $11_{2,9,0} - 10_{3,8,0}$ | 190.9 | 92 | 3.53e-05 | |
| CN | CN | 226287.418 | $2_{0,2,1} - 1_{0,2,1}$ | 16.3 | 2 | 1.03e-05 | |
| | | 226298.943 | $2_{0,2,1} - 1_{0,2,2}$ | 16.3 | 2 | 8.23e-06 | |
| | | 226303.037 | $2_{0,2,2} - 1_{0,2,1}$ | 16.3 | 4 | 4.17e-06 | |
| | | 226314.540 | $2_{0,2,2} - 1_{0,2,2}$ | 16.3 | 4 | 9.91e-06 | |
| | | 226332.499 | $2_{0,2,2} - 1_{0,2,3}$ | 16.3 | 4 | 4.56e-06 | |
| | | 226341.930 | $2_{0,2,3} - 1_{0,2,2}$ | 16.3 | 6 | 3.16e-06 | |
| | | 226359.871 | $2_{0,2,3} - 1_{0,2,3}$ | 16.3 | 6 | 1.61e-05 | |
| | | 226616.571 | $2_{0,2,1} - 1_{0,1,2}$ | 16.3 | 2 | 1.07e-05 | |
| | | 226632.190 | $2_{0,2,2} - 1_{0,1,2}$ | 16.3 | 4 | 4.26e-05 | |
| | | 226659.558 | $2_{0,2,3} - 1_{0,1,2}$ | 16.3 | 6 | 9.47e-05 | ignored, frequency gap |
| | | 226663.693 | $2_{0,2,1} - 1_{0,1,1}$ | 16.3 | 2 | 8.47e-05 | |
| | | 226679.311 | $2_{0,2,2} - 1_{0,1,1}$ | 16.3 | 4 | 5.27e-05 | |
| | | 226874.191 | $2_{0,3,3} - 1_{0,2,2}$ | 16.3 | 6 | 9.62e-05 | partially blanked (*) |
| | | 226874.781 | $2_{0,3,4} - 1_{0,2,3}$ | 16.3 | 8 | 1.14e-04 | partially blanked (*) |
| | | 226875.896 | $2_{0,3,2} - 1_{0,2,1}$ | 16.3 | 4 | 8.59e-05 | partially blanked (*) |
| | | 226887.420 | $2_{0,3,2} - 1_{0,2,2}$ | 16.3 | 4 | 2.73e-05 | |
| | | 226892.128 | $2_{0,3,3} - 1_{0,2,3}$ | 16.3 | 6 | 1.81e-05 | |
| | | 226905.357 | $2_{0,3,2} - 1_{0,2,3}$ | 16.3 | 4 | 1.13e-06 | ignored, S/N not good |
| | $^{13}$CN | 217467.150 | $2_{3,3,4} - 1_{2,2,3}$ | 15.7 | 9 | 1.01e-04 | |
| CO | CO | 230538.000 | $2 - 1$ | 16.6 | 5 | 6.91e-07 | |
| | $^{13}$CO | 220398.684 | $2 - 1$ | 15.9 | 5 | 6.08e-07 | |
| | C$^{18}$O | 219560.357 | $2 - 1$ | 15.8 | 5 | 6.01e-07 | |
| | C$^{17}$O | 224714.385 | $2 - 1$ | 16.2 | 5 | 6.43e-07 | |
| | $^{13}$C$^{18}$O | 209419.138 | $2_2 - 1_1$ | 15.1 | 4 | 4.36e-07 | |
| | | 209419.172 | $2_3 - 1_2$ | 15.1 | 6 | 5.23e-07 | |
| CS | CS | 244935.644 | $5 - 4$ | 35.3 | 11 | 3e-04 | |
| | $^{13}$CS | 231220.996 | $5 - 4$ | 33.3 | 11 | 2.52e-04 | |
| | | 277455.481 | $6 - 5$ | 46.6 | 13 | 4.42e-04 | |
| | C$^{34}$S | 241016.194 | $5 - 4$ | 34.7 | 11 | 2.86e-04 | |
| | C$^{33}$S | 242913.610 | $5_0 - 4_0$ | 35.0 | 44 | 2.91e-04 | |
| HCCCN | HCCCN | 209230.234 | $23 - 22$ | 120.5 | 141 | 7.24e-04 | |
| | | 218324.788 | $24 - 23$ | 131.0 | 147 | 8.23e-04 | |
| | | 227418.906 | $25 - 24$ | 141.9 | 153 | 9.31e-04 | |
| | | 236512.777 | $26 - 25$ | 153.2 | 159 | 1.05e-03 | |
| | | 245606.308 | $27 - 26$ | 165.0 | 165 | 1.17e-03 | |
| | | 254699.500 | $28 - 27$ | 177.3 | 171 | 1.31e-03 | |
| | | 263792.308 | $29 - 28$ | 189.9 | 177 | 1.46e-03 | blended with CH$_3$OH |
| | | 272884.734 | $30 - 29$ | 203.0 | 183 | 1.61e-03 | |
| HCN | HCN | 265886.180 | $3 - 2$ | 25.5 | 21 | 8.42e-04 | |
| | DCN | 217238.400 | $3_2 - 2_1$ | 20.9 | 5 | 3.83e-04 | |
| | | 217238.631 | $3_2 - 2_2$ | 20.9 | 5 | 7.08e-05 | |
| | | 217238.631 | $3_3 - 2_3$ | 20.9 | 7 | 5.06e-05 | |
| | | 217238.631 | $3_3 - 2_2$ | 20.9 | 7 | 4.05e-04 | |
| | | 217238.631 | $3_4 - 2_3$ | 20.9 | 9 | 4.55e-04 | |
| | H$^{13}$CN | 259011.821 | $3_2 - 2_2$ | 24.9 | 5 | 1.2e-04 | |
| | | 259011.821 | $3_3 - 2_3$ | 24.9 | 7 | 8.58e-05 | |
| | | 259011.821 | $3_2 - 2_1$ | 24.9 | 5 | 6.48e-04 | |
| | | 259011.821 | $3_3 - 2_2$ | 24.9 | 7 | 6.86e-04 | |
| | | 259011.821 | $3_4 - 2_3$ | 24.9 | 9 | 7.72e-04 | |
| | HC$^{15}$N | 258157.100 | $3 - 2$ | 24.8 | 7 | 7.65e-04 | |
| HCO | HCO | 260060.329 | $3_{0,3,4,4} - 2_{0,2,3,3}$ | 25.0 | 9 | 1.63e-04 | |
| | | 260082.192 | $3_{0,3,4,3} - 2_{0,2,3,2}$ | 25.0 | 7 | 1.61e-04 | |
| | | 260133.586 | $3_{0,3,3,3} - 2_{0,2,2,2}$ | 25.0 | 7 | 1.45e-04 | |
| | | 260155.769 | $3_{0,3,3,2} - 2_{0,2,2,1}$ | 25.0 | 5 | 1.37e-04 | |
| HCO$^+$ | HCO$^+$ | 267557.626 | $3 - 2$ | 25.7 | 7 | 1.45e-03 | blended with SO$_2$ and OCS |
| | DCO$^+$ | 216112.582 | $3 - 2$ | 20.7 | 7 | 7.66e-04 | |
| | H$^{13}$CO$^+$ | 260255.339 | $3 - 2$ | 25.0 | 7 | 1.34e-03 | |
| | HC$^{18}$O$^+$ | 255479.389 | $3 - 2$ | 24.5 | 7 | 1.27e-03 | |
| | HC$^{17}$O$^+$ | 261164.920 | $3 - 2$ | 25.1 | 42 | 1.35e-03 | |
| HCS$^+$ | HCS$^+$ | 213360.650 | $5 - 4$ | 30.7 | 11 | 1.97e-04 | |
| | | 256027.100 | $6 - 5$ | 43.0 | 13 | 3.46e-04 | |
| HDO | HDO | 225896.720 | $3_{1,2} - 2_{2,1}$ | 167.6 | 7 | 1.32e-05 | |

<div align="right"><strong>Continued on next page</strong></div>

| (Continuation) Species | Isotopologue | Frequency | Transition | $E_{up}$ | $G_{up}$ | $A_{ij}$ | Comment |
|---|---|---|---|---|---|---|---|
| | | 241561.550 | $2_{1,1} - 2_{1,2}$ | 95.2 | 5 | 1.19e-05 | |
| | | 266161.070 | $2_{2,0} - 3_{1,3}$ | 157.2 | 5 | 1.75e-05 | |
| $H_2CCO$ | $H_2CCO$ | 202014.311 | $10_{0,10} - 9_{0,9}$ | 53.3 | 21 | 9.24e-05 | ignored, S/N not good |
| | | 203940.225 | $10_{1,9} - 9_{1,8}$ | 66.9 | 63 | 9.41e-05 | |
| | | 220177.569 | $11_{1,11} - 10_{1,10}$ | 76.5 | 69 | 1.19e-04 | |
| | | 222197.635 | $11_{0,11} - 10_{0,10}$ | 64.0 | 23 | 1.24e-04 | |
| | | 224327.250 | $11_{1,10} - 10_{1,9}$ | 77.7 | 69 | 1.26e-04 | |
| | | 240185.794 | $12_{1,12} - 11_{1,11}$ | 88.0 | 75 | 1.55e-04 | |
| | | 242375.735 | $12_{0,12} - 11_{0,11}$ | 75.6 | 25 | 1.61e-04 | ignored, S/N not good |
| | | 244712.269 | $12_{1,11} - 11_{11,0}$ | 89.4 | 75 | 1.64e-04 | |
| | | 260191.982 | $13_{1,13} - 12_{1,12}$ | 100.5 | 81 | 1.98e-04 | |
| | | 262548.207 | $13_{0,13} - 12_{0,12}$ | 88.2 | 27 | 2.05e-04 | ignored, S/N not good |
| | | 265095.049 | $13_{1,12} - 12_{1,11}$ | 102.1 | 81 | 2.1e-04 | |
| $H_2CO$ | $H_2CO$ | 211211.468 | $3_{1,3} - 2_{1,2}$ | 32.1 | 21 | 2.27e-04 | |
| | | 216568.651 | $9_{1,8} - 9_{1,9}$ | 174.0 | 57 | 7.22e-06 | |
| | | 218222.192 | $3_{0,3} - 2_{0,2}$ | 21.0 | 7 | 2.82e-04 | |
| | | 218475.632 | $3_{2,2} - 2_{2,1}$ | 68.1 | 7 | 1.57e-04 | |
| | | 218760.066 | $3_{2,1} - 2_{2,0}$ | 68.1 | 7 | 1.58e-04 | |
| | | 225697.775 | $3_{1,2} - 2_{1,1}$ | 33.4 | 21 | 2.77e-04 | |
| | | 264270.140 | $10_{1,9} - 10_{1,10}$ | 209.9 | 63 | 1.08e-05 | |
| | | 281526.929 | $4_{1,4} - 3_{1,3}$ | 45.6 | 27 | 5.88e-04 | |
| | HDCO | 201341.350 | $3_{1,2} - 2_{1,1}$ | 27.3 | 7 | 1.96e-04 | |
| | | 246924.600 | $4_{1,4} - 3_{1,3}$ | 37.6 | 9 | 3.96e-04 | |
| | | 256585.430 | $4_{0,4} - 3_{0,3}$ | 30.8 | 9 | 4.74e-04 | |
| | | 257748.760 | $4_{2,3} - 3_{2,2}$ | 62.8 | 9 | 3.6e-04 | |
| | | 259034.910 | $4_{2,2} - 3_{2,1}$ | 62.9 | 9 | 3.66e-04 | |
| | | 268292.020 | $4_{1,3} - 3_{1,2}$ | 40.2 | 9 | 5.08e-04 | |
| | $H_2^{13}CO$ | 206131.626 | $3_{1,3} - 2_{1,2}$ | 31.6 | 21 | 2.11e-04 | |
| | | 212811.184 | $3_{0,3} - 2_{0,2}$ | 20.4 | 7 | 2.61e-04 | |
| | | 219908.525 | $3_{1,2} - 2_{1,1}$ | 32.9 | 21 | 2.56e-04 | |
| | | 274762.112 | $4_{1,4} - 3_{1,3}$ | 44.8 | 27 | 5.47e-04 | |
| $H_2CS$ | $H_2CS$ | 202923.515 | $6_{1,6} - 5_{1,5}$ | 47.3 | 39 | 1.18e-04 | |
| | | 205987.391 | $6_{0,6} - 5_{0,5}$ | 34.6 | 13 | 1.27e-04 | |
| | | 206053.584 | $6_{2,5} - 5_{2,4}$ | 87.3 | 13 | 1.13e-04 | |
| | | 206158.016 | $6_{2,4} - 5_{2,3}$ | 87.3 | 13 | 1.13e-04 | ignored, blended with SO |
| | | 209200.101 | $6_{1,5} - 5_{1,4}$ | 48.3 | 39 | 1.3e-04 | |
| | | 236726.770 | $7_{1,7} - 6_{1,6}$ | 58.6 | 45 | 1.91e-04 | |
| | | 240266.320 | $7_{0,7} - 6_{0,6}$ | 46.1 | 15 | 2.04e-04 | |
| | | 240381.750 | $7_{2,6} - 6_{2,5}$ | 98.9 | 15 | 1.88e-04 | |
| | | 240548.229 | $7_{2,5} - 6_{2,4}$ | 98.9 | 15 | 1.88e-04 | |
| | | 244047.840 | $7_{1,6} - 6_{1,5}$ | 60.0 | 45 | 2.1e-04 | |
| | | 270520.740 | $8_{1,8} - 7_{1,7}$ | 71.6 | 51 | 2.9e-04 | |
| | | 274520.870 | $8_{0,8} - 7_{0,7}$ | 59.3 | 17 | 3.07e-04 | |
| | | 274702.055 | $8_{2,7} - 7_{2,6}$ | 112.0 | 17 | 2.89e-04 | |
| | | 274952.473 | $8_{2,6} - 7_{2,5}$ | 112.1 | 17 | 2.9e-04 | |
| | | 278886.400 | $8_{1,7} - 7_{1,6}$ | 73.4 | 51 | 3.17e-04 | |
| | HDCS | 212648.339 | $7_{1,7} - 6_{1,6}$ | 49.8 | 15 | 1.39e-04 | |
| | | 216662.429 | $7_{0,7} - 6_{0,6}$ | 41.6 | 15 | 1.5e-04 | |
| | $H_2C^{34}S$ | 202492.418 | $6_{0,6} - 5_{0,5}$ | 34.0 | 13 | 1.21e-04 | |
| $H_2S$ | $H_2S$ | 216710.435 | $2_{2,0} - 2_{1,1}$ | 84.0 | 5 | 4.83e-05 | |
| HNC | HNC | 271981.142 | $3 - 2$ | 26.1 | 7 | 9.34e-04 | |
| | DNC | 228910.489 | $3 - 2$ | 22.0 | 7 | 5.57e-04 | |
| | $HN^{13}C$ | 261263.310 | $3 - 2$ | 25.1 | 7 | 6.48e-04 | |
| HNCO | HNCO | 218981.009 | $10_{1,10} - 9_{1,9}$ | 101.1 | 21 | 1.42e-04 | |
| | | 219798.274 | $10_{0,10} - 9_{0,9}$ | 58.0 | 21 | 1.47e-04 | |
| | | 220584.751 | $10_{1,9} - 9_{1,8}$ | 101.5 | 21 | 1.45e-04 | |
| | | 240875.727 | $11_{1,11} - 10_{1,10}$ | 112.6 | 23 | 1.9e-04 | |
| | | 241774.032 | $11_{0,11} - 10_{0,10}$ | 69.6 | 23 | 1.96e-04 | |
| | | 242639.704 | $11_{1,10} - 10_{1,9}$ | 113.1 | 23 | 1.95e-04 | |
| | | 262769.477 | $12_{1,12} - 11_{1,11}$ | 125.3 | 25 | 2.48e-04 | |
| | | 263748.625 | $12_{0,12} - 11_{0,11}$ | 82.3 | 25 | 2.56e-04 | |
| | | 264693.655 | $12_{1,11} - 11_{1,10}$ | 125.9 | 25 | 2.54e-04 | |
| $N_2H^+$ | $N_2H^+$ | 279511.701 | $3 - 2$ | 26.8 | 63 | 1.26e-03 | |
| | $N_2D^+$ | 231321.665 | $3 - 2$ | 22.2 | 21 | 7.14e-04 | |
| NO | NO | 250436.848 | $3_{1,3,4} - 2_{-1,2,3}$ | 19.2 | 8 | 1.84e-06 | |
| | | 250440.659 | $3_{1,3,3} - 2_{-1,2,2}$ | 19.2 | 6 | 1.55e-06 | |

| (Continuation) Species | Isotopologue | Frequency | Transition | $E_{up}$ | $G_{up}$ | $A_{ij}$ | Comment |
|---|---|---|---|---|---|---|---|
| | | 250448.530 | $3_{1,3,2} - 2_{-1,2,1}$ | 19.2 | 4 | 1.38e-06 | |
| | | 250796.436 | $3_{-1,3,4} - 2_{1,2,3}$ | 19.3 | 8 | 1.85e-06 | |
| | | 250815.594 | $3_{-1,3,3} - 2_{1,2,2}$ | 19.3 | 6 | 1.55e-06 | |
| | | 250816.954 | $3_{-1,3,2} - 2_{1,2,1}$ | 19.3 | 4 | 1.39e-06 | |
| NS | NS | 207436.246 | $5_{1,-1,6} - 4_{1,1,5}$ | 27.6 | 12 | 1.51e-04 | |
| | | 207436.246 | $5_{1,-1,5} - 4_{1,1,4}$ | 27.6 | 10 | 1.44e-04 | |
| | | 207438.692 | $5_{1,-1,4} - 4_{1,1,3}$ | 27.6 | 8 | 1.42e-04 | |
| | | 207834.866 | $5_{1,1,6} - 4_{1,-1,5}$ | 27.7 | 12 | 1.52e-04 | |
| | | 207838.365 | $5_{1,1,5} - 4_{1,-1,4}$ | 27.7 | 10 | 1.45e-04 | |
| | | 207838.365 | $5_{1,1,4} - 4_{1,-1,3}$ | 27.7 | 8 | 1.43e-04 | |
| | | 253570.476 | $6_{1,1,7} - 5_{1,-1,6}$ | 39.8 | 14 | 2.83e-04 | |
| | | 253570.476 | $6_{1,1,6} - 5_{1,-1,5}$ | 39.8 | 12 | 2.73e-04 | |
| | | 253572.148 | $6_{1,1,5} - 5_{1,-1,4}$ | 39.8 | 10 | 2.71e-04 | |
| | | 253968.393 | $6_{1,-1,7} - 5_{1,1,6}$ | 39.9 | 14 | 2.84e-04 | |
| | | 253970.581 | $6_{1,-1,6} - 5_{1,1,5}$ | 39.9 | 12 | 2.75e-04 | |
| | | 253970.581 | $6_{1,-1,5} - 5_{1,1,4}$ | 39.9 | 10 | 2.73e-04 | |
| OCS | OCS | 206745.161 | $17 - 16$ | 89.3 | 35 | 2.55e-05 | |
| | | 218903.356 | $18 - 17$ | 99.8 | 37 | 3.04e-05 | |
| | | 231060.983 | $19 - 18$ | 110.9 | 39 | 3.58e-05 | |
| | | 243218.040 | $20 - 19$ | 122.6 | 41 | 4.18e-05 | |
| | | 255374.461 | $21 - 20$ | 134.8 | 43 | 4.84e-05 | |
| | | 267530.239 | $22 - 21$ | 147.7 | 45 | 5.57e-05 | ignored, blended with HCO$^+$ |
| | | 279685.318 | $23 - 22$ | 161.1 | 47 | 6.37e-05 | |
| SiO | SiO | 217104.980 | $5 - 4$ | 31.3 | 11 | 5.21e-04 | |
| | | 260518.020 | $6 - 5$ | 43.8 | 13 | 9.15e-04 | blended with c-C$_3$H$_2$ |
| | $^{29}$SiO | 214385.036 | $5 - 4$ | 30.9 | 11 | 5e-04 | |
| | | 257254.227 | $6 - 5$ | 43.2 | 13 | 8.78e-04 | |
| | $^{30}$SiO | 211852.797 | $5 - 4$ | 30.5 | 11 | 4.83e-04 | |
| | | 254215.845 | $6 - 5$ | 42.7 | 13 | 8.47e-04 | |
| SO | SO | 206176.005 | $5_4 - 4_3$ | 38.6 | 9 | 1.03e-04 | blended with H$_2$CS |
| | | 214357.039 | $8_7 - 7_7$ | 81.2 | 15 | 3.42e-06 | |
| | | 215220.653 | $5_5 - 4_4$ | 44.1 | 11 | 1.22e-04 | |
| | | 219949.442 | $5_6 - 4_5$ | 35.0 | 13 | 1.36e-04 | |
| | | 236452.325 | $2_1 - 1_2$ | 15.8 | 3 | 1.45e-06 | ignored, S/N not good |
| | | 246404.687 | $3_2 - 2_3$ | 21.1 | 5 | 1.03e-06 | ignored, S/N not good |
| | | 251825.770 | $6_5 - 5_4$ | 50.7 | 11 | 1.96e-04 | |
| | | 254573.500 | $9_8 - 8_8$ | 99.7 | 17 | 4.32e-06 | |
| | | 258255.813 | $6_6 - 5_5$ | 56.5 | 13 | 2.16e-04 | |
| | | 261843.684 | $6_7 - 5_6$ | 47.6 | 15 | 2.33e-04 | |
| | $^{34}$SO | 201846.573 | $5_4 - 4_3$ | 38.1 | 9 | 9.66e-05 | |
| | | 211013.673 | $5_5 - 4_4$ | 43.5 | 11 | 1.15e-04 | ignored, frequency gap |
| | | 215839.436 | $5_6 - 4_5$ | 34.4 | 13 | 1.29e-04 | |
| | | 246663.638 | $6_5 - 5_4$ | 49.9 | 11 | 1.84e-04 | |
| | | 253208.020 | $6_6 - 5_5$ | 55.7 | 13 | 2.04e-04 | |
| | | 256877.456 | $6_7 - 5_6$ | 46.7 | 15 | 2.2e-04 | |
| SO$^+$ | SO$^+$ | 208590.016 | $5_{1,5} - 4_{-1,4}$ | 26.7 | 10 | 4.7e-05 | blended with CH$_3$OCH$_3$ |
| | | 208965.420 | $5_{-1,5} - 4_{1,4}$ | 26.8 | 10 | 4.72e-05 | blended with C$_2$H$_3$CN |
| | | 254977.935 | $6_{-1,6} - 5_{1,5}$ | 38.9 | 12 | 8.77e-05 | blended with C$_2$H$_5$CN |
| | | 255353.237 | $6_{1,6} - 5_{-1,5}$ | 39.0 | 12 | 8.81e-05 | |
| SO$_2$ | SO$_2$ | 200809.180 | $16_{1,15} - 16_{0,16}$ | 130.7 | 33 | 4.7e-05 | |
| | | 203391.550 | $12_{0,12} - 11_{1,11}$ | 70.1 | 25 | 8.8e-05 | |
| | | 204246.760 | $18_{3,15} - 18_{2,16}$ | 180.6 | 37 | 9.27e-05 | |
| | | 204384.300 | $7_{4,4} - 8_{3,5}$ | 65.5 | 15 | 1.11e-05 | |
| | | 205300.570 | $11_{2,10} - 11_{1,11}$ | 70.2 | 23 | 5.32e-05 | |
| | | 208700.320 | $3_{2,2} - 2_{1,1}$ | 15.3 | 7 | 6.72e-05 | |
| | | 209936.050 | $12_{5,7} - 13_{4,10}$ | 133.0 | 25 | 1.59e-05 | |
| | | 213068.400 | $26_{3,23} - 26_{2,24}$ | 350.8 | 53 | 1.16e-04 | |
| | | 214689.380 | $16_{3,13} - 16_{2,14}$ | 147.8 | 33 | 9.9e-05 | |
| | | 214728.330 | $17_{6,12} - 18_{5,13}$ | 229.0 | 35 | 1.89e-05 | |
| | | 216643.300 | $22_{2,20} - 22_{1,21}$ | 248.4 | 45 | 9.27e-05 | |
| | | 221965.210 | $11_{1,11} - 10_{0,10}$ | 60.4 | 23 | 1.14e-04 | |
| | | 223883.569 | $6_{4,2} - 7_{3,5}$ | 58.6 | 13 | 1.16e-05 | |
| | | 224264.811 | $20_{2,18} - 19_{3,17}$ | 207.8 | 41 | 3.94e-05 | |
| | | 225153.702 | $13_{2,12} - 13_{1,13}$ | 93.0 | 27 | 6.52e-05 | |
| | | 226300.027 | $14_{3,11} - 14_{2,12}$ | 119.0 | 29 | 1.07e-04 | |
| | | 229347.628 | $11_{5,7} - 12_{4,8}$ | 122.0 | 23 | 1.91e-05 | |
| | | 234421.586 | $16_{6,10} - 17_{5,13}$ | 213.3 | 33 | 2.35e-05 | |
| | | 235151.720 | $4_{2,2} - 3_{1,3}$ | 19.0 | 9 | 7.69e-05 | |
| | | 236216.685 | $16_{1,15} - 15_{2,14}$ | 130.7 | 33 | 7.5e-05 | |
| | | 237068.870 | $12_{3,9} - 12_{2,10}$ | 94.0 | 25 | 1.14e-04 | |

Continued on next page

| (Continuation) Species | Isotopologue | Frequency | Transition | $E_{up}$ | $G_{up}$ | $A_{ij}$ | Comment |
|---|---|---|---|---|---|---|---|
| | | 240942.791 | $18_{1,17} - 18_{0,18}$ | 163.1 | 37 | 7.02e-05 | |
| | | 241615.798 | $5_{2,4} - 4_{1,3}$ | 23.6 | 11 | 8.45e-05 | |
| | | 243087.647 | $5_{4,2} - 6_{3,3}$ | 53.1 | 11 | 1.03e-05 | |
| | | 244254.218 | $14_{0,14} - 13_{1,13}$ | 93.9 | 29 | 1.64e-04 | |
| | | 245563.423 | $10_{3,7} - 10_{2,8}$ | 72.7 | 21 | 1.19e-04 | |
| | | 248057.401 | $15_{2,14} - 15_{1,15}$ | 119.3 | 31 | 8.06e-05 | |
| | | 248830.824 | $10_{5,5} - 11_{4,8}$ | 111.9 | 21 | 2.19e-05 | |
| | | 251199.675 | $13_{1,13} - 12_{0,12}$ | 82.2 | 27 | 1.76e-04 | |
| | | 251210.586 | $8_{3,5} - 8_{2,6}$ | 55.2 | 17 | 1.2e-04 | |
| | | 253956.567 | $15_{6,10} - 16_{5,11}$ | 198.6 | 31 | 2.82e-05 | ignored, possibly artifact |
| | | 254280.536 | $6_{3,3} - 6_{2,4}$ | 41.4 | 13 | 1.14e-04 | |
| | | 254283.319 | $24_{2,22} - 24_{1,23}$ | 292.7 | 49 | 1.33e-04 | |
| | | 255553.303 | $4_{3,1} - 4_{2,2}$ | 31.3 | 9 | 9.28e-05 | |
| | | 255958.044 | $3_{3,1} - 3_{2,2}$ | 27.6 | 7 | 6.63e-05 | |
| | | 256246.946 | $5_{3,3} - 5_{2,4}$ | 35.9 | 11 | 1.07e-04 | |
| | | 257099.966 | $7_{3,5} - 7_{2,6}$ | 47.8 | 15 | 1.22e-04 | |
| | | 258942.199 | $9_{3,7} - 9_{2,8}$ | 63.5 | 19 | 1.32e-04 | |
| | | 262256.905 | $11_{3,9} - 11_{2,10}$ | 82.8 | 23 | 1.41e-04 | |
| | | 267537.450 | $13_{3,11} - 13_{2,12}$ | 105.8 | 27 | 1.51e-04 | ignored, blended with $HCO^+$ |
| | | 268168.334 | $9_{5,5} - 10_{4,6}$ | 102.7 | 19 | 2.39e-05 | |
| | | 271529.015 | $7_{2,6} - 6_{1,5}$ | 35.5 | 15 | 1.11e-04 | |
| | | 273462.668 | $14_{6,8} - 15_{5,11}$ | 184.8 | 29 | 3.3e-05 | |
| | | 273752.961 | $17_{2,16} - 17_{1,17}$ | 149.2 | 35 | 9.97e-05 | |
| | | 275240.182 | $15_{3,13} - 15_{2,14}$ | 132.5 | 31 | 1.64e-04 | |
| | | 280807.280 | $26_{4,22} - 26_{3,23}$ | 364.3 | 53 | 2.33e-04 | |

**Table A.2:** Uncertainties for the averaged total intensities $\Delta \int T_{\mathrm{mb}}dv$ [K km s$^{-1}$] from Table 3.4.

| species | all averaged | high column density | high column density without KL and Orion South | high column density, low temperature | high column density, high temperature, without KL and Orion South | low column density | low temperature | low column density, low temperature | low column density, high temperature | high temperature without KL and Orion South | H II | radical region | dense PDR |
|---|---|---|---|---|---|---|---|---|---|---|---|---|---|
| CO | 0.01 | 0.03 | 0.12 | 0.06 | 0.03 | 0.60 | 0.01 | 0.01 | 7.13 | 0.64 | 0.01 | 0.01 | 0.03 |
| $^{13}$CO | 0.01 | 0.01 | <0.01 | 0.01 | 0.01 | <0.01 | 0.02 | 0.11 | <0.01 | 0.02 | 0.01 | 0.01 | <0.01 |
| C$^{18}$O | 0.08 | <0.01 | 0.01 | 0.03 | 0.04 | 0.02 | 0.28 | 0.02 | 0.07 | 0.01 | 0.05 | 0.03 | 0.25 |
| C$^{17}$O | 0.14 | 0.11 | 0.15 | 0.01 | 0.35 | 0.15 | 0.03 | 0.02 | 0.02 | 0.03 | 0.76 | 0.35 | 0.29 |
| $^{13}$C$^{18}$O | - | 0.02 | 0.01 | 0.02 | 0.01 | - | 0.02 | - | - | - | - | 0.02 | - |
| c-C$_3$H$_2$ | 0.03 | 0.36 | 0.21 | 0.04 | 0.27 | - | - | - | 0.03 | 0.07 | 0.07 | 0.19 | 0.26 |
| C$_2$H | 0.11 | 0.24 | 0.18 | 0.11 | 0.39 | 0.09 | 0.05 | 0.05 | 0.14 | 0.08 | 0.05 | 0.15 | 0.11 |
| C$_2$D | - | 0.05 | 0.05 | 0.04 | 0.05 | - | - | - | - | - | - | 0.06 | - |
| CF$^+$ | 0.01 | 0.02 | 0.02 | - | 0.02 | 0.02 | 0.01 | - | - | - | - | - | - |
| CH$_3$CCH | 0.02 | 0.39 | 0.25 | 0.07 | 0.37 | - | - | - | - | 0.03 | 0.26 | 0.29 | - |
| CH$_3$CN | - | 0.93 | 0.08 | - | 0.08 | - | - | - | - | 1.27 | 0.10 | - | - |
| CH$_3$OH | 0.28 | 3.38 | 0.49 | 0.25 | 14.13 | 0.05 | 0.03 | 0.03 | 0.05 | 0.08 | 1.61 | 6.32 | 0.05 |
| CN | 0.41 | 0.62 | 0.48 | 0.20 | 0.33 | 0.48 | 0.13 | 0.09 | 0.11 | 0.44 | 0.31 | 0.91 | 0.40 |
| $^{13}$CN | - | 0.02 | 0.02 | - | 0.09 | - | - | - | - | - | - | 0.03 | - |
| CS | 0.31 | 0.03 | 0.43 | 0.04 | 0.05 | 0.07 | 0.03 | 0.02 | 0.02 | 0.25 | 0.37 | 0.02 | 0.27 |
| $^{13}$CS | 0.02 | 0.25 | 0.10 | - | 0.20 | - | - | - | - | - | 0.07 | 0.04 | 0.06 |
| C$^{34}$S | 0.02 | 0.10 | 0.10 | - | <0.01 | - | - | - | 0.02 | 0.02 | 0.03 | 0.02 | 0.26 |
| C$^{33}$S | - | 0.10 | 0.02 | - | 0.09 | - | - | - | - | - | 0.03 | 0.02 | 0.03 |
| HC$_3$N | - | 0.75 | 0.19 | - | 0.32 | - | - | - | - | - | 0.32 | 0.07 | 0.03 |
| HCN | 0.08 | 0.01 | 0.01 | 0.18 | <0.01 | 0.02 | 0.07 | 0.07 | 0.03 | 0.07 | 0.13 | 0.01 | <0.01 |
| DCN | 0.11 | 0.06 | 0.08 | 0.02 | 0.08 | - | - | - | - | 0.06 | 0.04 | 0.02 | 0.04 |
| H$^{13}$CN | 0.02 | 0.14 | 0.06 | 0.02 | 0.07 | - | - | - | 0.01 | 0.05 | 0.05 | 0.16 | 0.03 |
| HC$^{15}$N | - | 0.36 | 0.05 | - | 0.05 | - | - | - | - | - | 0.03 | 0.02 | - |
| HCO | - | 0.01 | 0.01 | - | 0.04 | - | - | - | - | - | - | 0.02 | 0.04 |
| HCO$^+$ | 0.18 | 0.03 | 0.01 | 0.09 | 0.03 | 0.34 | 0.04 | 0.30 | 0.03 | 0.09 | 0.32 | 0.07 | 0.58 |
| DCO$^+$ | 0.01 | 0.04 | 0.04 | 0.02 | 0.07 | 0.01 | 0.01 | 0.01 | - | - | - | 0.02 | - |
| H$^{13}$CO$^+$ | 0.03 | 0.03 | 0.02 | 0.02 | 0.09 | 0.01 | 0.01 | 0.01 | 0.01 | 0.08 | 0.16 | <0.01 | 0.03 |
| HC$^{18}$O$^+$ | - | 0.02 | 0.02 | - | 0.02 | - | - | - | - | - | 0.02 | 0.02 | - |
| HC$^{17}$O$^+$ | - | - | - | - | - | - | - | - | - | - | - | - | - |
| HCS$^+$ | 0.01 | 0.11 | 0.11 | - | 0.14 | - | - | - | - | 0.02 | 0.05 | 0.03 | - |
| HDO | - | 0.03 | - | - | - | - | - | - | - | - | - | - | - |
| H$_2$CCO | - | 0.06 | - | - | - | - | - | - | - | - | - | 0.03 | - |
| H$_2$CO | 0.64 | 0.97 | 1.41 | 0.47 | 1.06 | 0.35 | 0.33 | 0.24 | 0.14 | 0.42 | 0.59 | 0.16 | 1.13 |
| HDCO | - | 0.11 | 0.02 | 0.02 | 0.10 | - | - | - | - | - | 0.02 | 0.06 | - |
| H$_2^{13}$CO | - | 0.10 | 0.02 | 0.02 | 0.08 | - | - | - | - | - | 0.05 | 0.02 | - |
| H$_2$CS | 0.08 | 0.85 | 0.76 | - | 1.09 | - | - | - | 0.03 | 0.12 | 0.42 | 0.27 | 0.02 |
| HDCS | - | - | - | - | 0.03 | - | - | - | - | - | - | 0.04 | - |
| H$_2$C$^{34}$S | - | - | - | - | - | - | - | - | - | - | - | - | - |
| H$_2$S | - | 0.15 | - | - | 0.04 | - | - | - | - | - | - | - | - |
| HNC | 0.02 | 0.06 | <0.01 | 0.03 | 0.02 | 0.08 | 0.08 | 0.02 | 0.02 | 0.09 | 0.03 | 0.03 | 0.03 |
| DNC | 0.01 | 0.10 | 0.02 | 0.02 | 0.07 | - | 0.01 | - | - | - | - | 0.02 | - |
| HN$^{13}$C | - | 0.09 | 0.13 | 0.02 | 0.08 | - | 0.01 | - | - | - | 0.02 | 0.02 | - |
| HNCO | - | 0.11 | - | - | 0.03 | - | - | - | - | - | - | - | - |
| N$_2$H$^+$ | 0.11 | 0.29 | 0.32 | 0.11 | 0.14 | 0.06 | 0.08 | 0.08 | 0.03 | 0.01 | 0.20 | 0.16 | - |
| N$_2$D$^+$ | - | 0.01 | 0.01 | 0.03 | - | - | - | - | - | - | - | - | - |
| NO | 0.01 | 0.05 | 0.05 | 0.05 | 0.08 | 0.01 | 0.03 | 0.03 | - | - | 0.05 | - | - |
| NS | - | 0.19 | 0.18 | - | 0.18 | - | - | - | - | - | - | 0.13 | - |
| OCS | - | 0.35 | - | - | - | - | - | - | - | - | 0.10 | - | - |
| SiO | 0.08 | 0.35 | 0.30 | - | 0.26 | - | - | - | - | - | 0.54 | - | - |
| $^{29}$SiO | - | 0.06 | - | - | - | - | - | - | - | - | - | - | - |
| $^{30}$SiO | - | - | - | - | - | - | - | - | - | - | - | - | - |
| SO | 0.30 | 1.04 | 0.84 | 0.17 | 1.00 | 0.14 | 0.07 | 0.05 | 0.09 | 0.18 | 1.20 | 0.14 | 0.18 |
| $^{34}$SO | - | 0.81 | - | - | 0.06 | - | - | - | - | - | 0.04 | 0.01 | - |
| SO$^+$ | - | - | - | - | 0.05 | - | - | - | - | - | - | 0.02 | 0.04 |
| SO$_2$ | 0.07 | 4.28 | 0.16 | - | 0.38 | - | - | - | - | - | 1.48 | - | - |

**Notes.** Errors refer to those of the Gaussian line fits and do not account for the calibration uncertainties discussed in Section 3.2.2. Errors add up for species with many transitions and are usually larger in cases of strong overlap between lines. However, they are in general of the order of $3 - 6\%$.

**Table A.3:** Overlap between regions. To be read from left to right, e.g. $\sim 39\%$ of the 'high column density' region overlap with the 'low temperature' region. Conversely, $\sim 9\%$ of the 'low temperature' region overlap with the 'high column density' region.

| | high column density | high column density without KL and Orion South | high column density, low temperature | high column density, high temperature, without KL and Orion South | low column density | low temperature | low column density, low temperature | low column density, high temperature | high temperature without KL and Orion South | H II | radical region | dense PDR |
|---|---|---|---|---|---|---|---|---|---|---|---|---|
| high column density | - | 0.924 | 0.393 | 0.494 | - | 0.393 | - | - | 0.494 | 0.085 | 0.159 | - |
| high column density without KL and Orion South | 1.000 | - | 0.426 | 0.535 | - | 0.426 | - | - | 0.535 | 0.063 | 0.172 | - |
| high column density, low temperature | 1.000 | 1.000 | - | - | - | 1.000 | - | - | - | - | - | - |
| high column density, high temperature, without KL and Orion South | 1.000 | 1.000 | - | - | - | - | - | - | 1.000 | 0.086 | 0.321 | - |
| low column density | - | - | - | - | - | 0.498 | 0.498 | 0.502 | 0.502 | 0.024 | 0.008 | 0.025 |
| low temperature | 0.090 | 0.090 | 0.090 | - | 0.910 | - | 0.910 | - | - | - | - | - |
| low column density, low temperature | - | - | - | - | 1.000 | 1.000 | - | - | - | - | - | - |
| low column density, high temperature | - | - | - | - | 1.000 | - | - | - | 1.000 | 0.047 | 0.015 | 0.050 |
| high temperature without KL and Orion South | 0.109 | 0.109 | - | 0.109 | 0.891 | - | - | 0.891 | - | 0.051 | 0.049 | 0.045 |
| H II | 0.311 | 0.211 | - | 0.156 | 0.689 | - | - | 0.689 | 0.844 | - | - | 0.256 |
| radical region | 0.722 | 0.722 | - | 0.722 | 0.278 | - | - | 0.278 | 1.000 | - | - | - |
| dense PDR | - | - | - | - | 1.000 | - | - | 1.000 | 1.000 | 0.348 | - | - |

**Notes.** The majority of these overlaps is discussed in this paper, as they correspond to regions themselves (e.g. the overlap between the 'high column density' and 'low temperature' regions is identical to the region 'high column density, low temperature'). The exception to this are the three regions that are not based on column density or temperature thresholds, namely 'H II', 'radical region' and 'dense PDR'.

**Table A.4:** Sample sizes for determining the Pearson correlation coefficient between the molecular abundances in Section 5.3.1.

|         | CO  | $C_2H$ | CN  | CS  | HCN | $HCO^+$ | HNC | $N_2H^+$ | $C^{+}$ [*] |
|---------|-----|--------|-----|-----|-----|---------|-----|----------|-----|
| CO      | -   | -      | -   | -   | -   | -       | -   | -        | -   |
| $C_2H$  | 293 | -      | -   | -   | -   | -       | -   | -        | -   |
| CN      | 244 | 235    | -   | -   | -   | -       | -   | -        | -   |
| CS      | 84  | 81     | 81  | -   | -   | -       | -   | -        | -   |
| HCN     | 223 | 215    | 213 | 83  | -   | -       | -   | -        | -   |
| $HCO^+$ | 252 | 244    | 215 | 84  | 200 | -       | -   | -        | -   |
| HNC     | 115 | 110    | 113 | 58  | 113 | 114     | -   | -        | -   |
| $N_2H^+$| 203 | 193    | 174 | 70  | 168 | 183     | 112 | -        | -   |
| $C^{+}$ [*] | 311 | 293 | 244 | 84  | 223 | 252     | 115 | 203      | -   |

**Notes.** The sample size equals the number of pixels overlapping in the respective abundance maps of species. [*] We do not have the abundance available for $C^+$, but use the [-5, 20] km s$^{-1}$ integrated line intensity instead.

# Additional figures
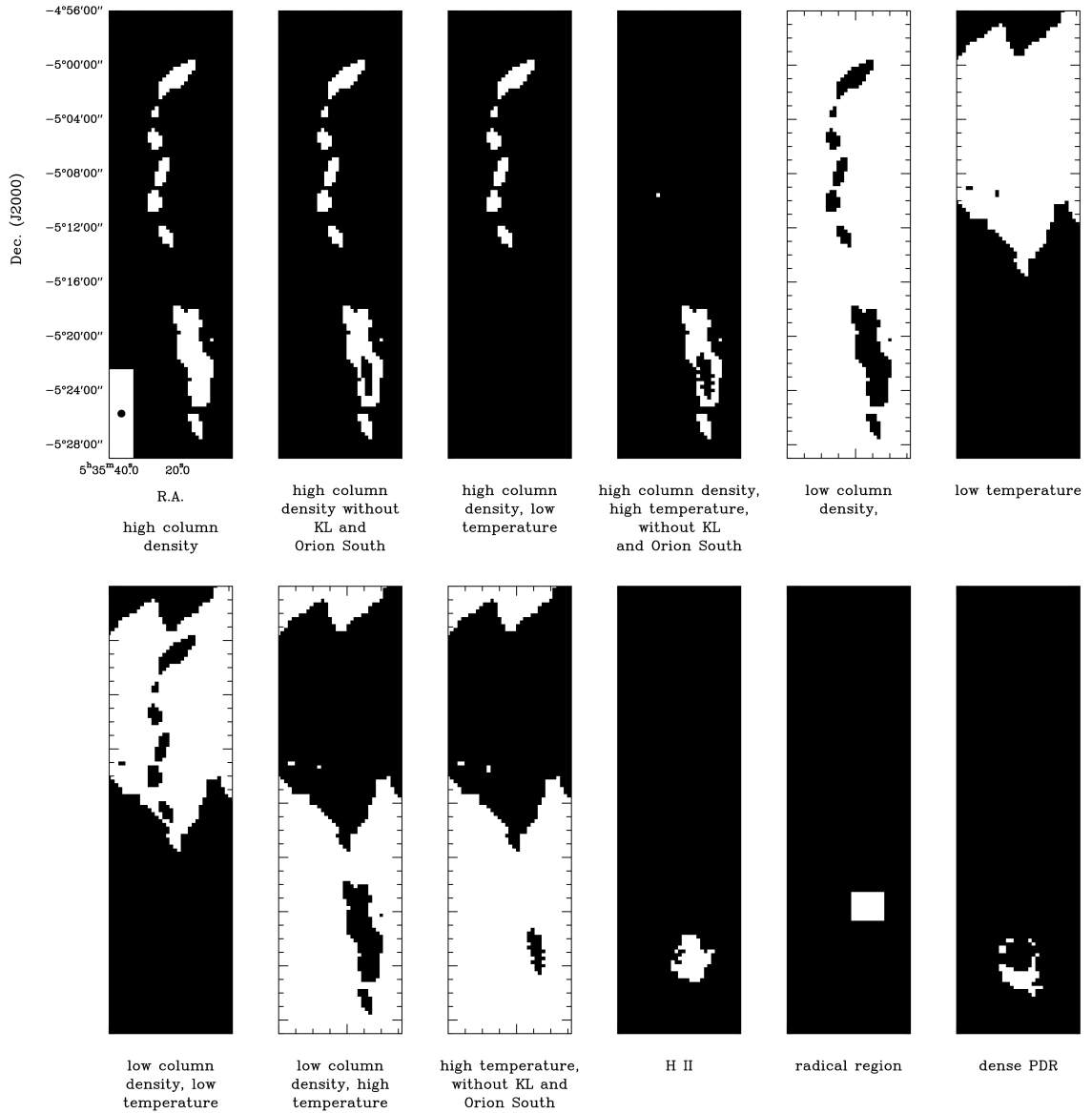


**Figure B.1:** Masks obtained with parameters as described in Table 3.3. The images are intended as a visual aid and give an impression on the spatial extension of the considered regions. White pixel are part of the region, black pixels are not.
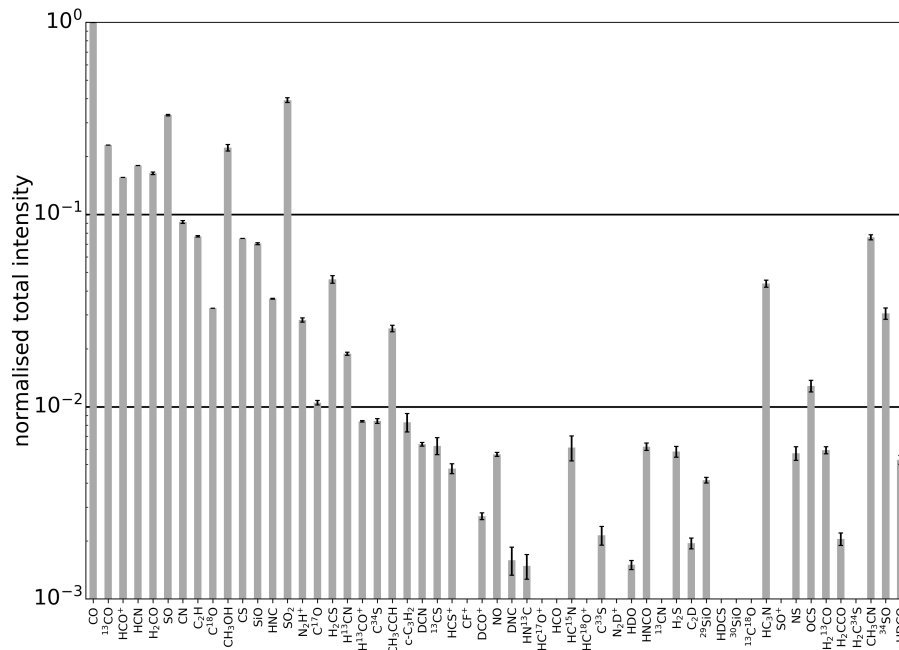
**(a)** high column density
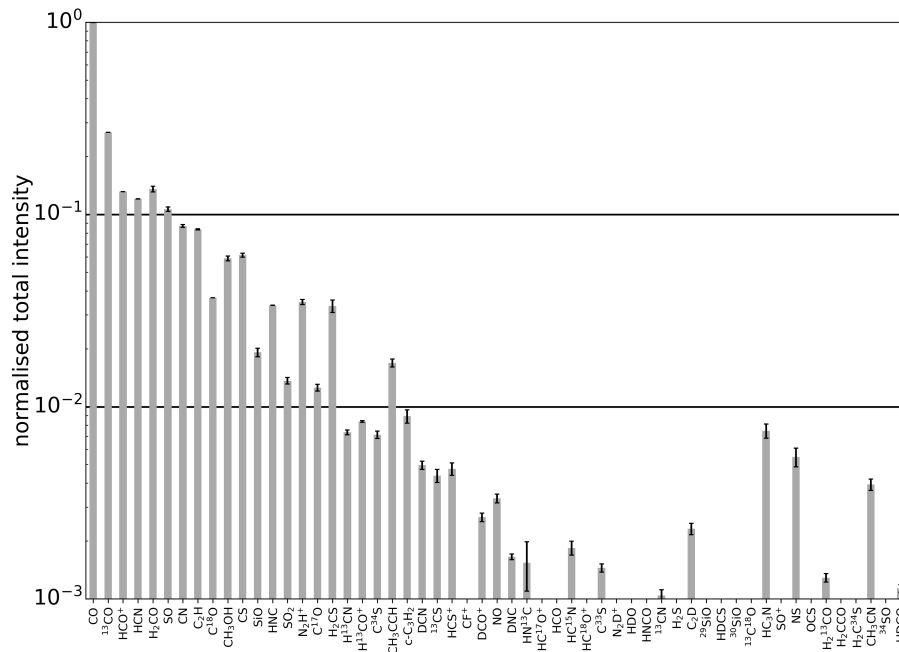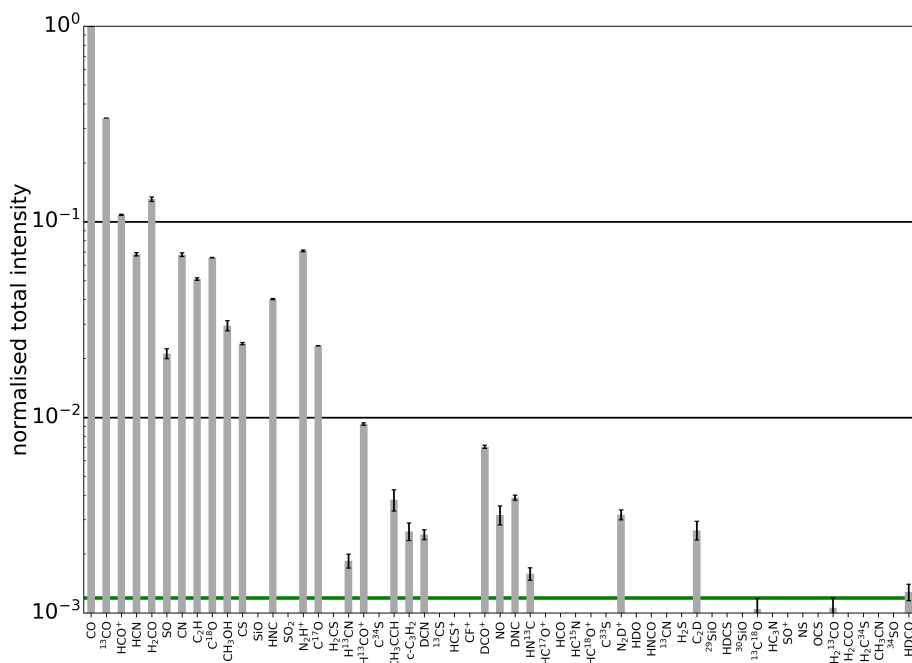


**(b)** high column density, without KL and Orion South

**(c)** high column density, low temperature



**(d)** high column density, high temperature, without KL and Orion South

(e) low column density



(f) low temperature

**(g)** low column density, low temperature



**(h)** low column density, high temperature
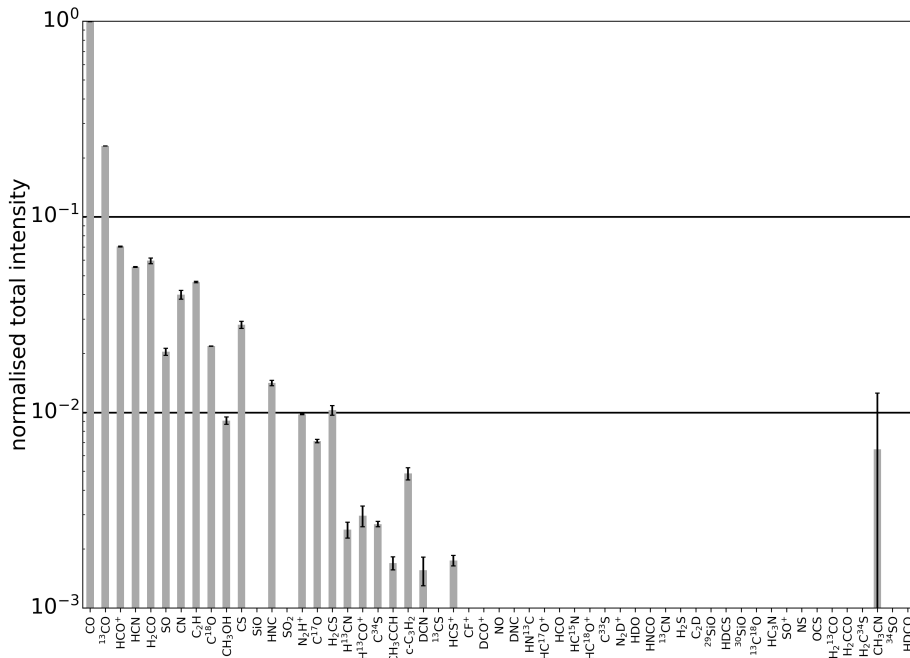
(i) high temperature, without KL and Orion South
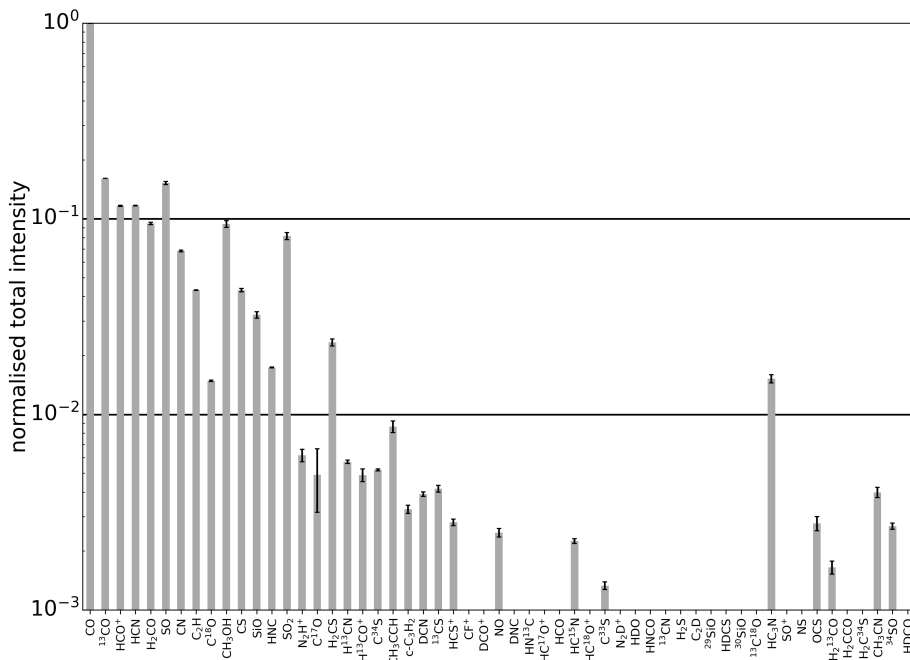


(j) H II
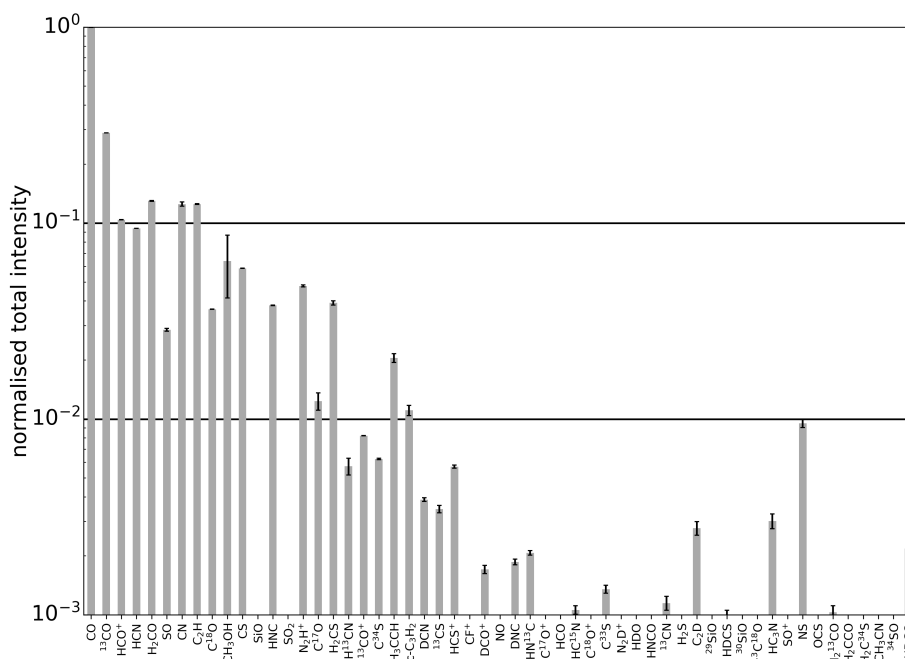
**(k)** radical region
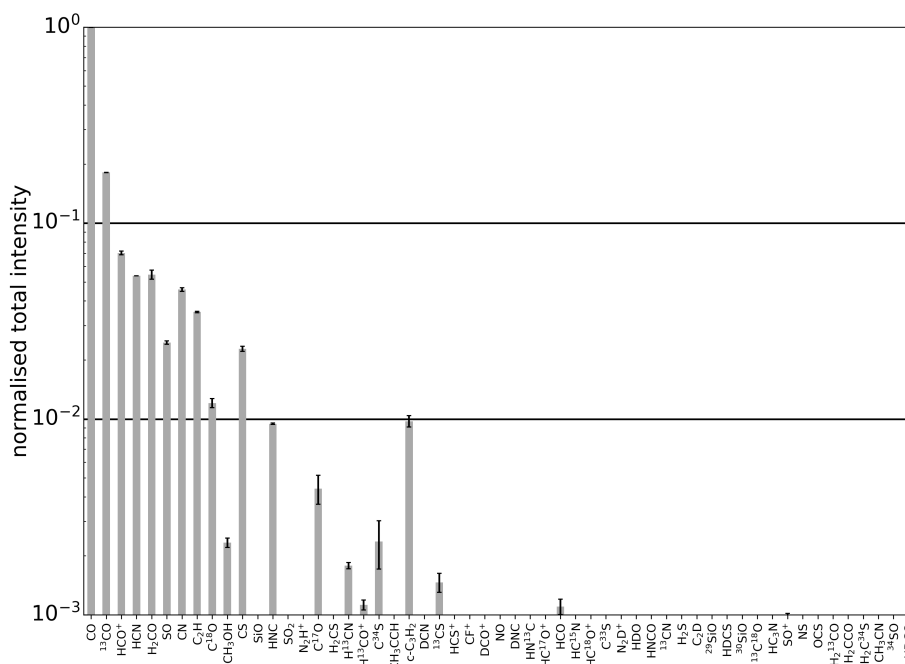


**(l)** dense PDR

**Figure B.2:** Total intensities of all considered species for the regions described in Table 3.3, normalised by the respective total CO intensity. Due to the noise level of the region and its total CO intensity, a normalised total intensity of 0.1% is not detectable for region (c). Therefore, a green line approximating the detection limit for a $5\sigma$ feature (assuming the median line width of the region and $\sigma_{\mathrm{median}}$) is added in this case. Detections below that limit indicate that the local noise is below $\sigma_{\mathrm{median}}$. Error bars refer to the fit uncertainties.

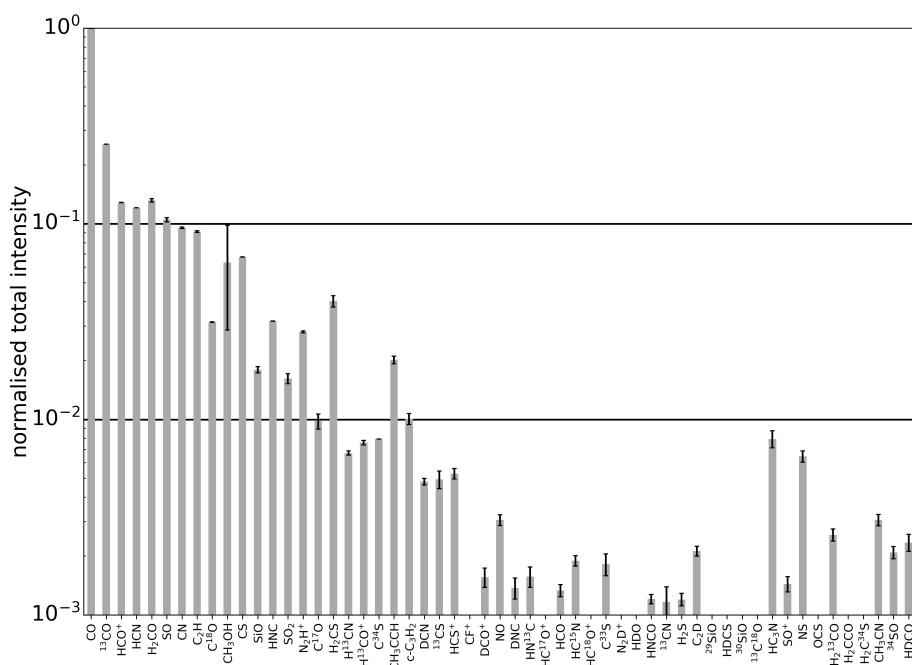Percentage of the total intensity emitted by the different species
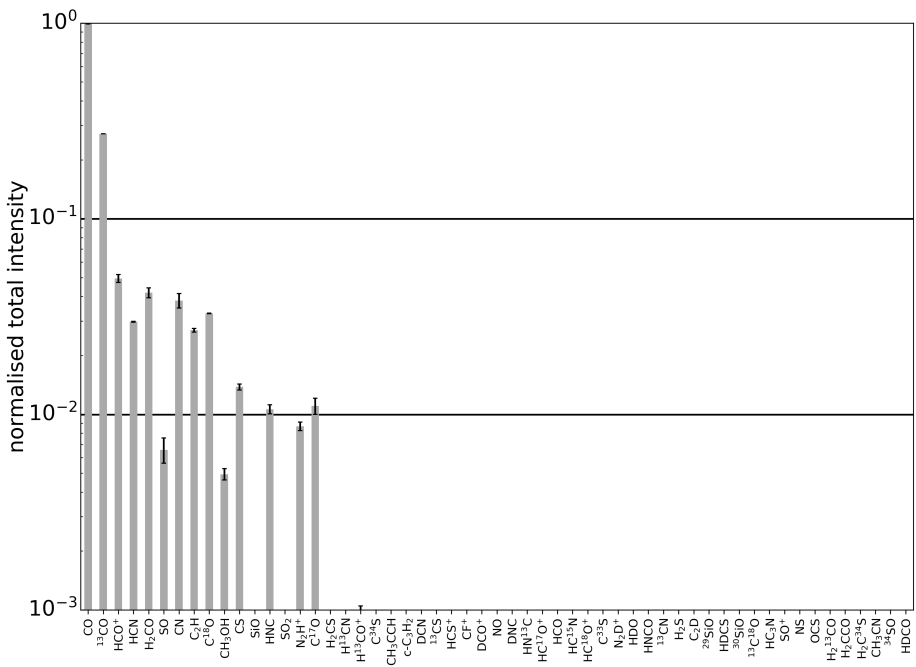
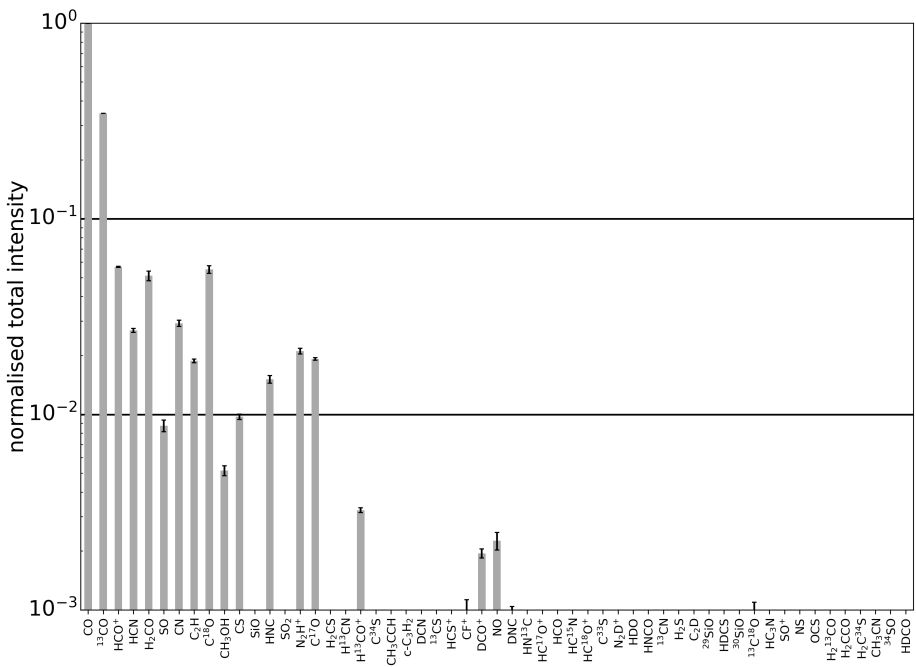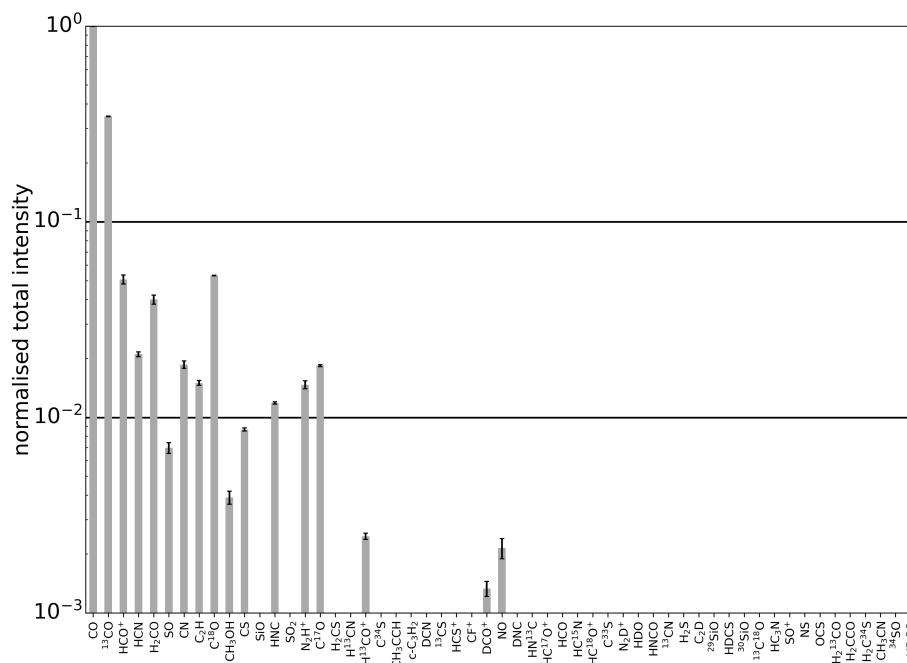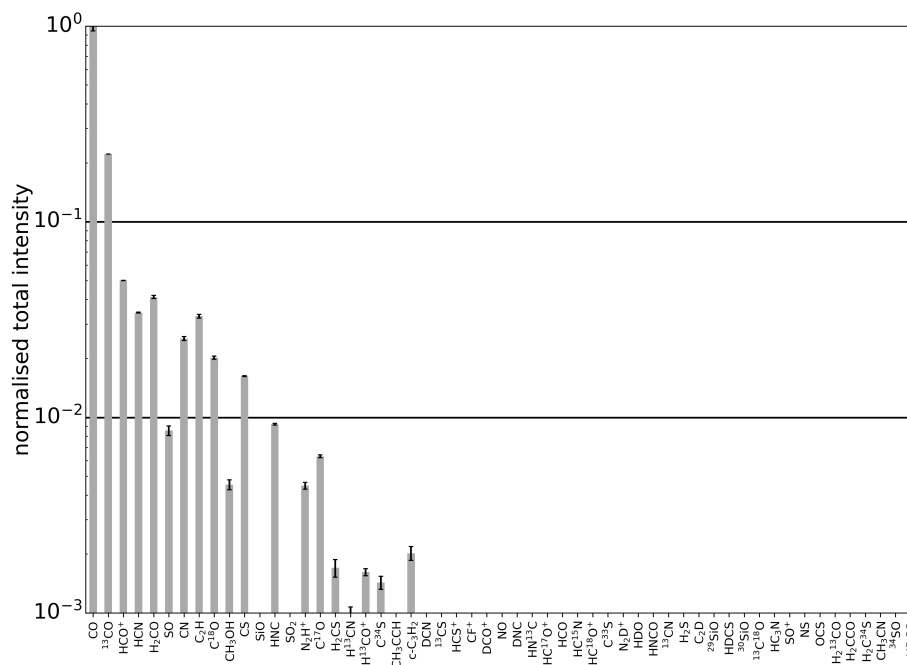| Species | all averaged | high column density | high column density without KL and Orion South | high column density, low temperature | high column density, high temperature, without KL and Orion South | low column density | low temperature | low column density, low temperature | low column density, high temperature | high temperature, without KL and Orion South | H II | radical region | dense PDR | KL and Orion South* |
|---|---|---|---|---|---|---|---|---|---|---|---|---|---|---|
| CO | 55 | 29 | 43 | 48 | 42 | 64 | 60 | 62 | 67 | 61 | 47 | 44 | 65 | 16 |
| $^{13}CO$ | 14 | 6.7 | 12 | 16 | 11 | 18 | 21 | 21 | 15 | 14 | 7.5 | 13 | 12 | 2.2 |
| $C^{18}O$ | 1.8 | 0.9 | 1.6 | 3.1 | 1.3 | 2.1 | 3.3 | 3.3 | 1.4 | 1.3 | 0.7 | 1.6 | 0.8 | 0.4 |
| $C^{17}O$ | 0.6 | 0.3 | 0.5 | 1.1 | 0.4 | 0.7 | 1.1 | 1.1 | 0.4 | 0.4 | 0.2 | 0.5 | 0.3 | 0.1 |
| $^{13}C^{18}O$ | | | | 0.1 | | | 0.1 | | | | | | | |
| $c$-$C_3H_2$ | 0.1 | 0.2 | 0.4 | 0.1 | 0.4 | | | | 0.1 | 0.3 | 0.2 | 0.5 | 0.6 | 0.1 |
| $C_2H$ | 2.2 | 2.2 | 3.6 | 2.4 | 3.9 | 1.7 | 1.1 | 0.9 | 2.2 | 2.8 | 2 | 5.5 | 2.3 | 1 |
| $C_2D$ | | 0.1 | 0.1 | 0.1 | 0.1 | | | | | | | 0.1 | | |
| $CF^+$ | | | | | | 0.1 | 0.1 | | | | | | | |
| $CH_3CCH$ | 0.1 | 0.7 | 0.7 | 0.2 | 0.9 | | | | | 0.1 | 0.4 | 0.9 | | 0.8 |
| $CH_3CN$ | | 2.2 | 0.2 | | 0.1 | | | | | | 0.4 | 0.2 | | 4.1 |
| $CH_3OH$ | 1.5 | 6.5 | 2.5 | 1.4 | 2.7 | 0.3 | 0.3 | 0.2 | 0.3 | 0.6 | 4.4 | 5.5 | 0.2 | 10 |
| $CN$ | 2.9 | 2.6 | 3.7 | 3.3 | 4.1 | 2.5 | 1.7 | 1.2 | 1.7 | 2.4 | 3.2 | 5.5 | 3 | 1.6 |
| $^{13}CN$ | | | | | | | | | | | | 0.1 | | |
| $CS$ | 1.5 | 2.2 | 2.6 | 1.1 | 2.9 | 0.9 | 0.6 | 0.5 | 1.1 | 1.7 | 2 | 2.6 | 1.5 | 1.7 |
| $^{13}CS$ | 0.1 | 0.2 | 0.2 | | 0.2 | | | | | | 0.2 | 0.2 | 0.1 | 0.2 |
| $C^{34}S$ | 0.2 | 0.2 | 0.3 | | 0.3 | | | | 0.1 | 0.2 | 0.2 | 0.3 | 0.2 | 0.2 |
| $C^{33}S$ | | 0.1 | 0.1 | | 0.1 | | | | | | 0.1 | 0.1 | | 0.1 |
| $HC_3N$ | | 1.3 | 0.3 | | 0.3 | | | | | | 0.7 | 0.1 | | 2.1 |
| $HCN$ | 3.9 | 5.2 | 5.2 | 3.3 | 5.1 | 1.9 | 1.6 | 1.3 | 2.3 | 3.4 | 5.5 | 4.1 | 3.5 | 5.3 |
| $DCN$ | 0.1 | 0.2 | 0.2 | 0.1 | 0.2 | | | | | 0.1 | 0.2 | 0.2 | 0.1 | 0.2 |
| $H^{13}CN$ | 0.2 | 0.5 | 0.3 | 0.1 | 0.3 | | | | 0.1 | 0.2 | 0.3 | 0.3 | 0.1 | 0.8 |
| $HC^{15}N$ | | 0.2 | 0.1 | | 0.1 | | | | | | 0.1 | | | 0.3 |
| $HCO$ | | | | | 0.1 | | | | | | | | 0.1 | |
| $HCO^+$ | 4.2 | 4.5 | 5.6 | 5.2 | 5.5 | 3.2 | 3.4 | 3.1 | 3.4 | 4.3 | 5.4 | 4.5 | 4.6 | 3.5 |
| $DCO^+$ | | 0.1 | 0.1 | 0.3 | 0.1 | | 0.1 | 0.1 | | | | 0.1 | | |
| $H^{13}CO^+$ | 0.2 | 0.2 | 0.4 | 0.4 | 0.3 | 0.1 | 0.2 | 0.2 | 0.1 | 0.2 | 0.2 | 0.4 | 0.1 | 0.1 |
| $HC^{18}O^+$ | | | | | | | | | | | | | | |
| $HC^{17}O^+$ | | | | | | | | | | | | | | |
| $HCS^+$ | | 0.1 | 0.2 | | 0.2 | | | | | 0.1 | 0.1 | 0.2 | | 0.1 |
| $HDO$ | | | | | | | | | | | | | | 0.1 |
| $H_2CCO$ | | 0.1 | | | | | | | | | | | | 0.1 |
| $H_2CO$ | 3.8 | 4.8 | 5.8 | 6.3 | 5.6 | 2.7 | 3.1 | 2.5 | 2.8 | 3.6 | 4.4 | 5.7 | 3.6 | 3.8 |
| $HDCO$ | | 0.2 | | 0.1 | 0.1 | | | | | | | 0.1 | | 0.3 |
| $H_2^{13}CO$ | | 0.2 | 0.1 | 0.1 | 0.1 | | | | | | 0.1 | | | 0.3 |
| $H_2CS$ | 0.5 | 1.3 | 1.4 | | 1.7 | | | | 0.1 | 0.6 | 1.1 | 1.7 | | 1.2 |
| $HDCS$ | | | | | | | | | | | | | | |
| $H_2C^{34}S$ | | | | | | | | | | | | | | |
| $H_2S$ | | 0.2 | | | 0.1 | | | | | | | | | 0.3 |
| $HNC$ | 0.9 | 1.1 | 1.4 | 1.9 | 1.4 | 0.7 | 0.9 | 0.7 | 0.6 | 0.9 | 0.8 | 1.7 | 0.6 | 0.7 |
| $DNC$ | | | 0.1 | 0.2 | 0.1 | | 0.1 | | | | | 0.1 | | |
| $HN^{13}C$ | | | 0.1 | 0.1 | 0.1 | | | | | | | 0.1 | | |
| $HNCO$ | | 0.2 | | | 0.1 | | | | | | | | | 0.3 |
| $N_2H^+$ | 0.8 | 0.8 | 1.5 | 3.4 | 1.2 | 0.6 | 1.3 | 0.9 | 0.3 | 0.6 | 0.3 | 2.1 | | 0.2 |
| $N_2D^+$ | | | | 0.2 | | | | | | | | | | |
| $NO$ | | 0.2 | 0.1 | 0.2 | 0.1 | | 0.1 | 0.1 | | | 0.1 | | | 0.2 |
| $NS$ | | 0.2 | 0.2 | | 0.3 | | | | | | | 0.4 | | 0.1 |
| $OCS$ | | 0.4 | | | | | | | | | 0.1 | | | 0.7 |
| $SiO$ | 0.9 | 2 | 0.8 | | 0.8 | | | | | | 1.5 | | | 3.2 |
| $^{29}SiO$ | | 0.1 | | | | | | | | | | | | 0.2 |
| $^{30}SiO$ | | | | | | | | | | | | | | |
| $SO$ | 3.7 | 9.5 | 4.6 | 1 | 4.5 | 0.4 | 0.5 | 0.4 | 0.6 | 1.2 | 7.1 | 1.2 | 1.6 | 14 |
| $^{34}SO$ | | 0.9 | | | 0.1 | | | | | | 0.1 | | | 1.7 |
| $SO^+$ | | | | | 0.1 | | | | | | | | 0.1 | |
| $SO_2$ | 0.8 | 11 | 0.6 | | 0.7 | | | | | | 3.8 | | | 22 |

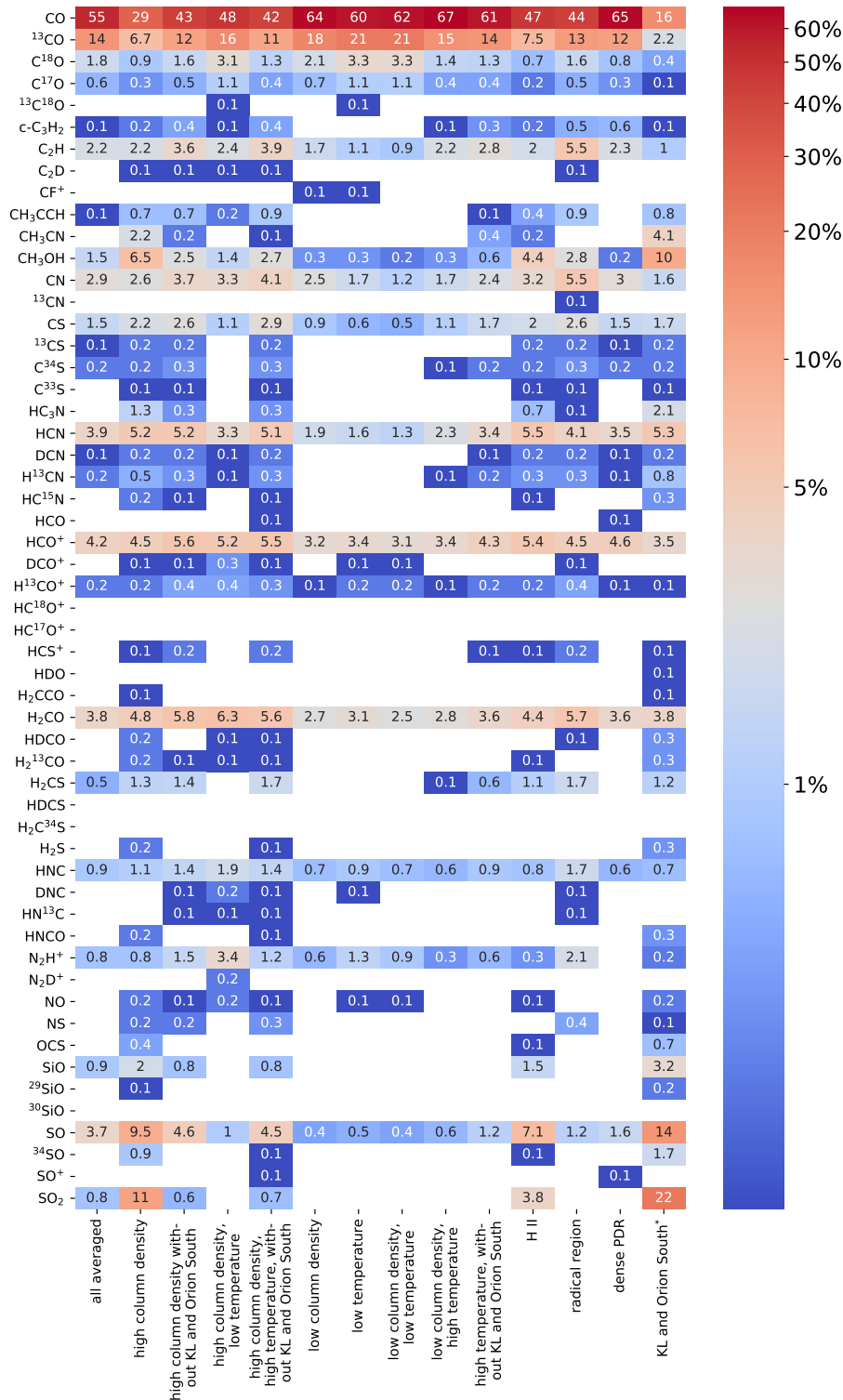Colour bar scale: 60%, 50%, 40%, 30%, 20%, 10%, 5%, 1%

**Figure B.3:** Share of each species to the total intensity of each region. For each species (rows), the colour bar offers a visual aid to quickly identify regions with lower or higher values. For each region (columns), the colour bar helps to assess the influence of different species. Shares under 0.1% are blank. [*] The values for 'KL and Orion South' are approximated as discussed in Section 3.4.1.
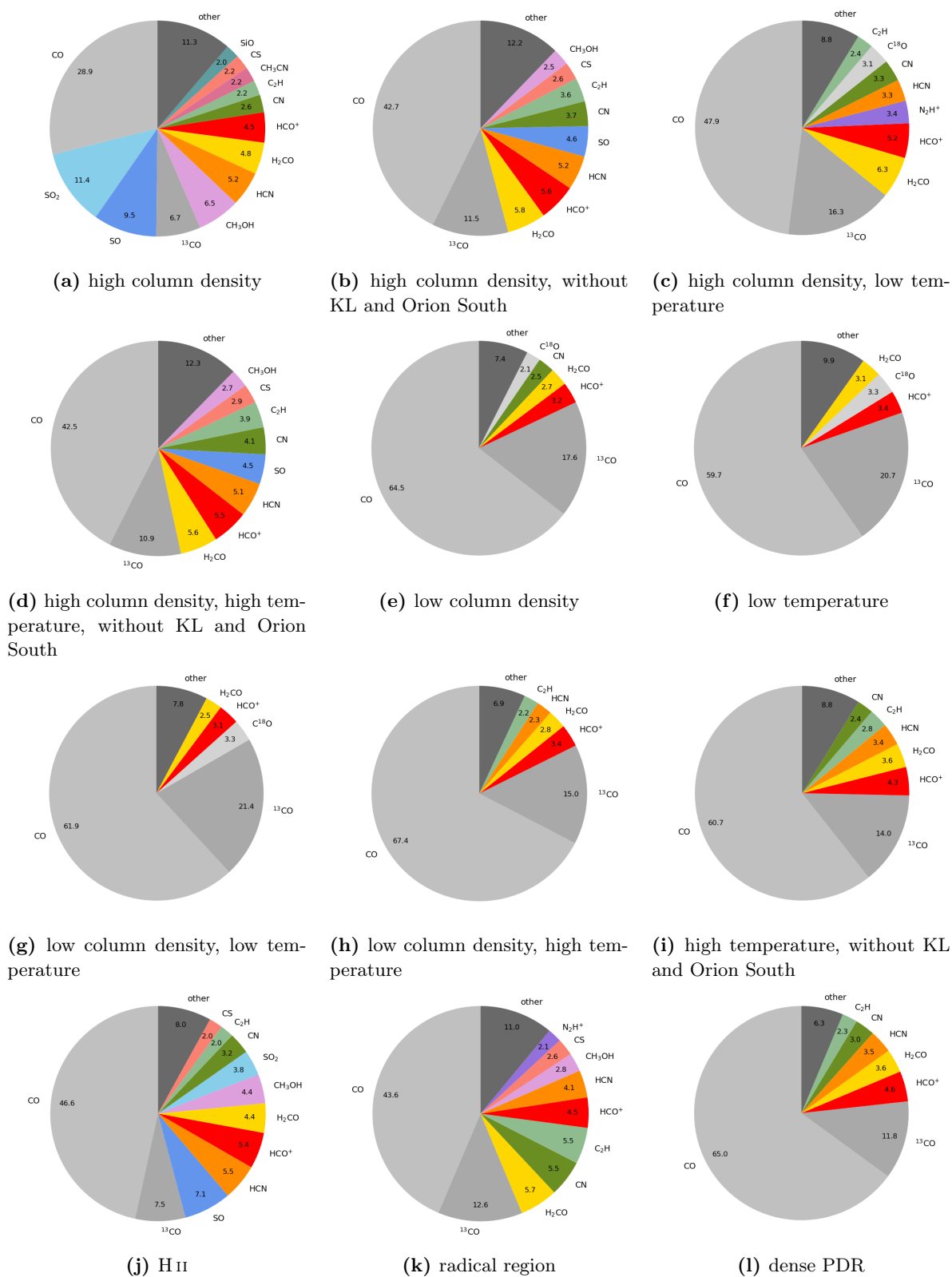
**(a)** high column density

**(b)** high column density, without KL and Orion South

**(c)** high column density, low temperature

**(d)** high column density, high temperature, without KL and Orion South

**(e)** low column density

**(f)** low temperature

**(g)** low column density, low temperature

**(h)** low column density, high temperature

**(i)** high temperature, without KL and Orion South

**(j)** H II

**(k)** radical region

**(l)** dense PDR

**Figure B.4:** Pie charts depicting the share of the total intensity emitted by different species for all regions from Table 3.3 (see Fig. 3.5 for the plot of the averaged data). Shares under 2% are summed under 'other'.
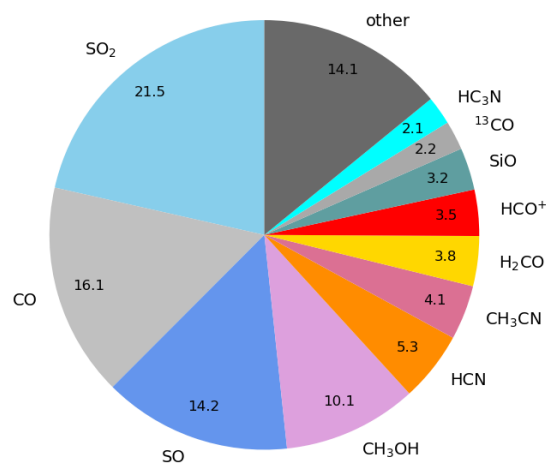
**Figure B.5:** Approximated emission profile from the region around KL and Orion South.
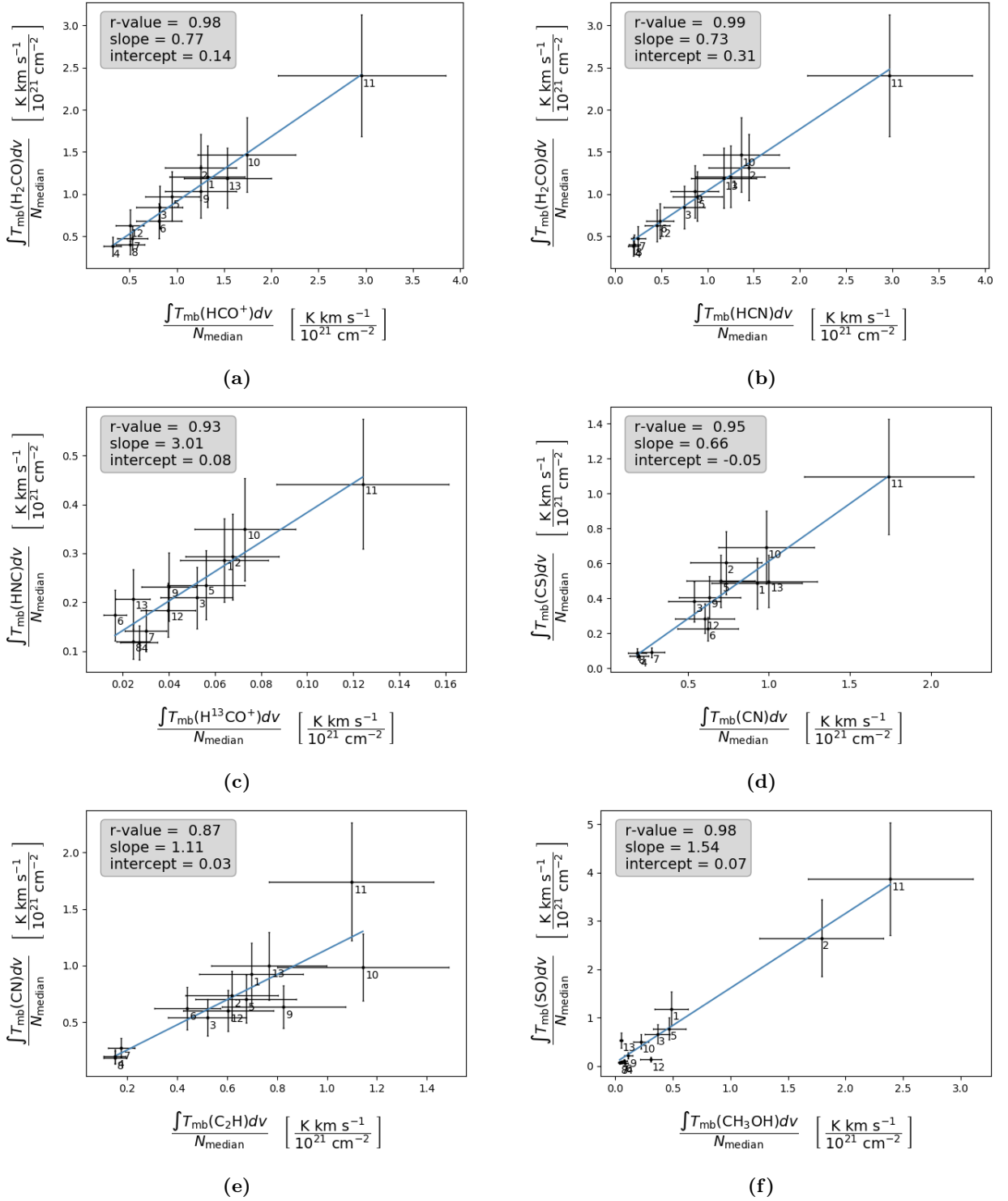
**Figure B.6:** Examples of correlation plots between species. The numbers refer to the region identifiers listed in Table 3.3. Due to the small number of samples, the r-value should be viewed with caution; it only gives an indication of possible correlation. The error bars indicate the assumed 30% uncertainty.
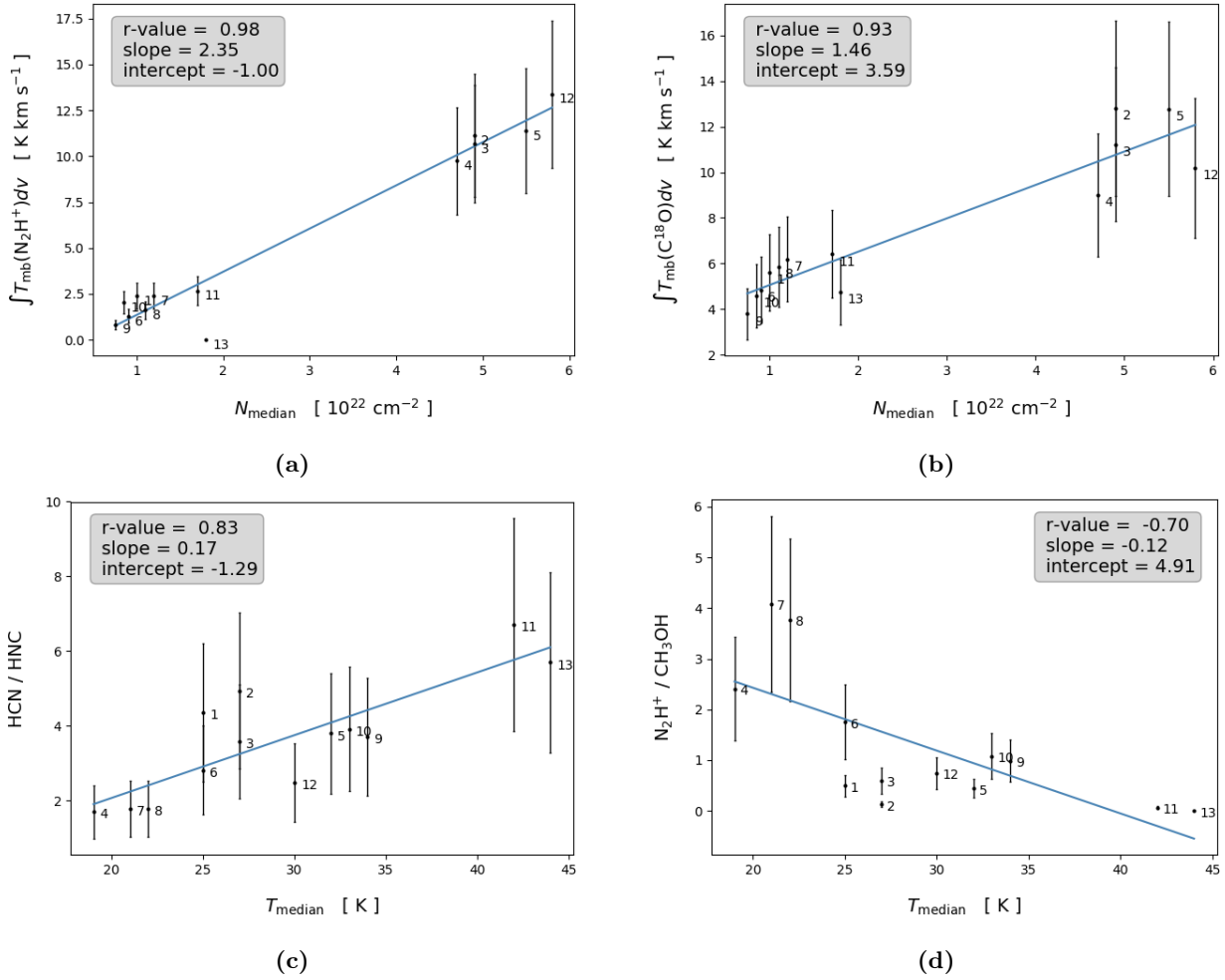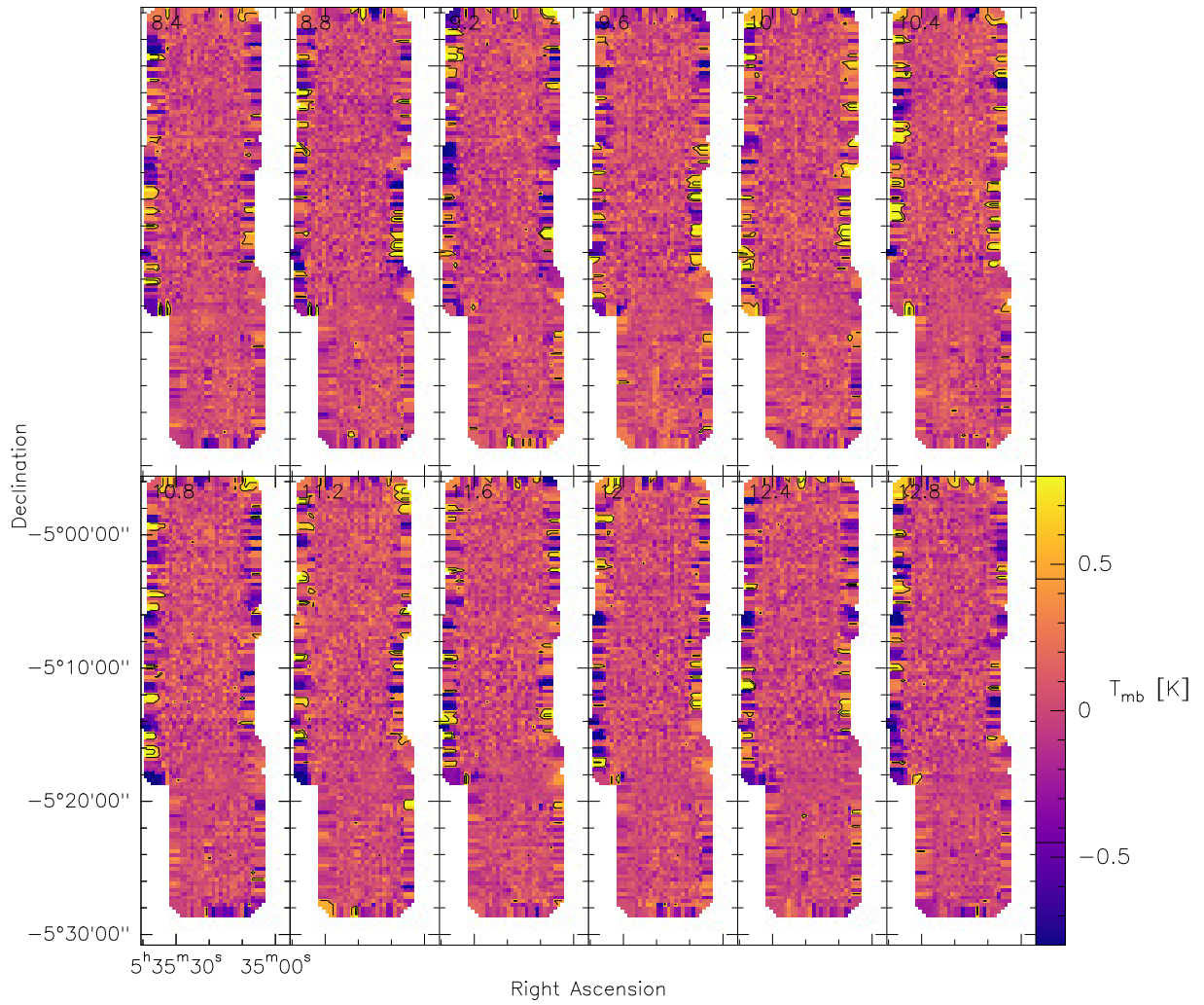
**Figure B.7:** Examples of correlation plots between species and physical parameters. The numbers refer to the region identifiers listed in Table 3.3. Due to the small number of samples, the r-value should be viewed with caution; it only gives an indication of possible correlation. The error bars indicate the assumed 30% uncertainty.

**Figure B.8:** CF$^+$ $J = 2 - 1$ channel maps from 8.4 to 12.8 km s$^{-1}$, with the contour marking the $3\sigma$ rms noise level. The line is too weak to be mapped, which excludes the explanation of strong point sources being responsible for the CF$^+$ detections in the averaged spectra of Chapter 3.

# Additional files

The relative velocities and line intensities for the hyperfine fits with CLASS for $C_2H$, CN, and $N_2H^+$ (see Section 5.1) have been calculated from the reported frequencies, Einstein A coefficients, and statistical weights in the CDMS[1] and JPL[2] data bases. The CLASS routine 'METHOD HFS' requires the number of components in the first line of the file, while the following lines contain the relative velocity and intensity for each component. The velocity and intensity $(A_{ul}^i g_{ul}^i)$ for each component $i$ have been normalised to that of the strongest component.

**$C_2H$ HFS**

```
11
194.42073059082      9.2251464957371E-04
29.931526184082      0.028654968366027
0                    1
-2.5405120849609     0.7485379576683
-69.524154663086     0.71491229534149
-72.368812561035     0.46679192781448
-85.500755310059     0.062865495681763
-233.99546813965     0.057894736528397
-249.9899597168      2.4749373551458E-03
-266.44961547852     5.9064324013889E-03
-282.44412231445     0.023705096915364
```

---

[1] https://cdms.astro.uni-koeln.de/cdms/portal/
[2] http://spec.jpl.nasa.gov/

**CN HFS**

19
706.25                      0.02197353169322
694.59490966797             4.2024264112115E-03
692.22528076172             4.294375423342E-03
680.57019042969             0.030924305319786
665.25048828125             4.347104113549E-03
659.96020507813             4.5279306359589E-03
644.64050292969             0.04920394346118
225.27700805664             3.7722445558757E-03
211.3349609375              0.090074084699154
201.19528198242             0.089825555682182
190.66987609863             0.74507504701614
187.25323486328             0.2797047495842
187.25323486328             0.46956962347031
0                           0.73519068956375
0                           1
-0.68883621692657           0.53358030319214
-12.371499061584            0.065042912960052
-15.209504127502            0.064878366887569
-27.663663864136            1.3464795192704E-03

**N$_2$H$^+$ HFS**

28
| | |
|---|---|
| 2.5155463218689 | 5.707070697099E-03 |
| 2.1801402568817 | 0.055916305631399 |
| 2.1130590438843 | 0.09480519592762 |
| 2.1130590438843 | 0.040656562894583 |
| 1.7105715274811 | 7.8571429476142E-03 |
| 0.7714341878891 | 0.088023081421852 |
| 0.53664988279343 | 0.27417027950287 |
| 0.50310927629471 | 0.12727272510529 |
| 0.46956863999367 | 0.041233766824007 |
| 0.43602803349495 | 0.080303028225899 |
| 0.36894679069519 | 0.54040402173996 |
| 0.23478431999683 | 6.2121213413775E-03 |
| 0.16770309209824 | 0.50505048036575 |
| 0.067081235349178 | 0.34920635819435 |
| 0.033540617674589 | 0.71428567171097 |
| 0.033540617674589 | 0.57575750350952 |
| 0.033540617674589 | 0.77922075986862 |
| 0 | 0.10714285075665 |
| 0 | 1 |
| -0.30186554789543 | 0.042568542063236 |
| -0.50310927629471 | 0.058585859835148 |
| -2.1801402568817 | 0.012337661348283 |
| -2.2807619571686 | 0.012626263312995 |
| -2.5490870475769 | 0.065656565129757 |
| -2.6832494735718 | 0.080808073282242 |
| -2.7503306865692 | 0.020173158496618 |
| -2.9515743255615 | 0.010404041036963 |
| -3.0857367515564 | 0.010562770999968 |

# Bibliography

Abel, N. P., Ferland, G. J., O'Dell, C. R., & Troland , T. H. 2016, ApJ, 819, 136 (Cited on page 79.)

Agúndez, M. & Wakelam, V. 2013, Chemical Reviews, 113, 8710 (Cited on pages 109, 110 and 112.)

Aladro, R., Martín, S., Martín-Pintado, J., et al. 2011, A&A, 535, A84 (Cited on page 58.)

André, P., Men'shchikov, A., Bontemps, S., et al. 2010, A&A, 518, L102 (Cited on page 11.)

Bachiller, R. & Pérez Gutiérrez, M. 1997, ApJ, 487, L93 (Cited on page 53.)

Baker, A. H., Jessup, E. R., & Manteuffel, T. 2005, SIAM Journal on Matrix Analysis and Applications, 26, 962 (Cited on page 91.)

Ballesteros-Paredes, J., André, P., Hennebelle, P., et al. 2020, Space Sci. Rev., 216, 76 (Cited on page 10.)

Bally, J. 2008, Overview of the Orion Complex, Vol. 4 (ASP Monograph Publications), 459 (Cited on page 17.)

Bally, J., Langer, W. D., Stark, A. A., & Wilson, R. W. 1987, ApJ, 312, L45 (Cited on page 17.)

Becklin, E. E. & Neugebauer, G. 1967, ApJ, 147, 799 (Cited on page 17.)

Berné, O., Marcelino, N., & Cernicharo, J. 2014, ApJ, 795, 13 (Cited on pages 17 and 57.)

Blake, G. A., Sutton, E. C., Masson, C. R., & Phillips, T. G. 1987, ApJ, 315, 621 (Cited on pages 36 and 89.)

Blitz, L. & Williams, J. P. 1999, in NATO Advanced Science Institutes (ASI) Series C, Vol. 540, NATO Advanced Science Institutes (ASI) Series C, ed. C. J. Lada & N. D. Kylafis, 3 (Cited on pages 10 and 11.)

Boger, G. I. & Sternberg, A. 2005, ApJ, 632, 302 (Cited on page 104.)

Bolatto, A. D., Wolfire, M., & Leroy, A. K. 2013, ARA&A, 51, 207 (Cited on page 15.)

Brinkmann, N., Wyrowski, F., Kauffmann, J., et al. 2020, A&A, 636, A39 (Cited on page 35.)

Bron, E., Daudon, C., Pety, J., et al. 2018, A&A, 610, A12 (Cited on pages 36, 53 and 57.)

Carpenter, J. M. 2000, AJ, 120, 3139 (Cited on page 21.)

Chevance, M., Kruijssen, J. M. D., Hygate, A. P. S., et al. 2020, MNRAS, 493, 2872 (Cited on page 10.)

Chini, R., Reipurth, B., Ward-Thompson, D., et al. 1997, ApJ, 474, L135 (Cited on pages 21, 35, 64, 67 and 79.)

Colzi, L., Sipilä, O., Roueff, E., Caselli, P., & Fontani, F. 2020, arXiv e-prints, arXiv:2006.03362 (Cited on page 95.)

Combes, F. 1991, ARA&A, 29, 195 (Cited on page 10.)

Cuadrado, S., Salas, P., Goicoechea, J. R., et al. 2019, A&A, 625, L3 (Cited on page 83.)

Dagdigian, P. J., Kłos, J., Wolfire, M., & Neufeld, D. A. 2019, ApJ, 872, 203 (Cited on pages 62 and 63.)

Denis-Alpizar, O., Guzmán, V. V., & Inostroza, N. 2018, MNRAS, 479, 753 (Cited on pages 62 and 63.)

Denis-Alpizar, O. & Rubayo-Soneira, J. 2019, MNRAS, 486, 1255 (Cited on page 79.)

Dent, W. R. F., Matthews, H. E., & Ward-Thompson, D. 1998, MNRAS, 301, 1049 (Cited on page 13.)

Dobbs, C. L., Burkert, A., & Pringle, J. E. 2011, MNRAS, 413, 2935 (Cited on page 10.)

Draine, B. T. 1978, ApJS, 36, 595 (Cited on page 7.)

Draine, B. T. 2011, Physics of the Interstellar and Intergalactic Medium (Princeton University Press) (Cited on pages 15 and 16.)

Endres, C. P., Schlemmer, S., Schilke, P., Stutzki, J., & Müller, H. S. P. 2016, Journal of Molecular Spectroscopy, 327, 95 (Cited on pages 29 and 38.)

Esplugues, G. B., Tercero, B., Cernicharo, J., et al. 2013, A&A, 556, A143 (Cited on page 36.)

Evans, Neal J., I. 1999, ARA&A, 37, 311 (Cited on pages 10 and 15.)

Fechtenbaum, S., Bontemps, S., Schneider, N., et al. 2015, A&A, 574, L4 (Cited on pages 66 and 78.)

Forbrich, J., Rivilla, V. M., Menten, K. M., et al. 2016, ApJ, 822, 93 (Cited on pages 108, 109 and 110.)

Foster, J. B., Jackson, J. M., Barnes, P. J., et al. 2011, ApJS, 197, 25 (Cited on page 40.)

Foster, J. B., Rathborne, J. M., Sanhueza, P., et al. 2013, PASA, 30, e038 (Cited on page 40.)

Friesen, R. K., Pineda, J. E., co-PIs, et al. 2017, ApJ, 843, 63 (Cited on pages 40, 92, 93, 99 and 105.)

Furlan, E., Fischer, W. J., Ali, B., et al. 2016, ApJS, 224, 5 (Cited on pages 21, 64 and 67.)

Galli, D., Walmsley, M., & Gonçalves, J. 2002, A&A, 394, 275 (Cited on pages 13 and 40.)

Gerin, M., Neufeld, D. A., & Goicoechea, J. R. 2016, ARA&A, 54, 181 (Cited on page 62.)

Getman, K. V., Feigelson, E. D., Grosso, N., et al. 2005a, ApJS, 160, 353 (Cited on page 108.)

Getman, K. V., Flaccomio, E., Broos, P. S., et al. 2005b, ApJS, 160, 319 (Cited on pages 108 and 110.)

Girichidis, P., Offner, S. S. R., Kritsuk, A. G., et al. 2020, Space Sci. Rev., 216, 68 (Cited on page 10.)

Goldsmith, P. F. 2001, ApJ, 557, 736 (Cited on page 36.)

Goldsmith, P. F. & Kauffmann, J. 2017, ApJ, 841, 25 (Cited on pages 58 and 85.)

Gómez, L., RodrÍguez, L. F., Loinard, L., et al. 2005, ApJ, 635, 1166 (Cited on page 20.)

Graninger, D. M., Herbst, E., Öberg, K. I., & Vasyunin, A. I. 2014, ApJ, 787, 74 (Cited on page 54.)

Gratier, P., Bron, E., Gerin, M., et al. 2017, A&A, 599, A100 (Cited on pages 36, 53, 54 and 57.)

Greaves, J. S. & White, G. J. 1992, MNRAS, 259, 457 (Cited on pages 41, 45, 89, 105 and 106.)

Grosso, N., Feigelson, E. D., Getman, K. V., et al. 2006, A&A, 448, L29 (Cited on page 108.)

Güsten, R., Nyman, L. Å., Schilke, P., et al. 2006, A&A, 454, L13 (Cited on pages 23 and 36.)

Guzmán, A. E., Sanhueza, P., Contreras, Y., et al. 2015, ApJ, 815, 130 (Cited on pages 40, 43 and 65.)

Guzmán, V., Pety, J., Gratier, P., et al. 2012a, A&A, 543, L1 (Cited on pages 61, 62 and 83.)

Guzmán, V., Roueff, E., Gauss, J., et al. 2012b, A&A, 548, A94 (Cited on pages 64 and 79.)

Habart, E., Abergel, A., Walmsley, C. M., Teyssier, D., & Pety, J. 2005, A&A, 437, 177 (Cited on page 85.)

Hacar, A., Bosman, A. D., & van Dishoeck, E. F. 2020, A&A, 635, A4 (Cited on page 104.)

Harada, N., Sakamoto, K., Martín, S., et al. 2018, ApJ, 855, 49 (Cited on page 59.)

Hartmann, L. 2001, AJ, 121, 1030 (Cited on page 10.)

Heiner, J. S., Vázquez-Semadeni, E., & Ballesteros-Paredes, J. 2015, MNRAS, 452, 1353 (Cited on page 14.)

Herbst, E. & Klemperer, W. 1973, ApJ, 185, 505 (Cited on page 8.)

Hillenbrand, L. A. & Hartmann, L. W. 1998, ApJ, 492, 540 (Cited on page 21.)

Hollenbach, D. J. & Tielens, A. G. G. M. 1999, Reviews of Modern Physics, 71, 173 (Cited on page 4.)

Jackson, J. M., Rathborne, J. M., Foster, J. B., et al. 2013, PASA, 30, e057 (Cited on page 40.)

Jiménez-Donaire, M. J., Bigiel, F., Leroy, A. K., et al. 2017, MNRAS, 466, 49 (Cited on page 59.)

Jiménez-Donaire, M. J., Bigiel, F., Leroy, A. K., et al. 2019, ApJ, 880, 127 (Cited on page 59.)

Johnstone, D. & Bally, J. 1999, ApJ, 510, L49 (Cited on pages 17, 21 and 35.)

Johnstone, D., Boonman, A. M. S., & van Dishoeck, E. F. 2003, A&A, 412, 157 (Cited on page 36.)

Jones, E., Oliphant, T., Peterson, P., et al. 2001-2019, SciPy: Open source scientific tools for Python (Cited on page 52.)

Kauffmann, J., Bertoldi, F., Bourke, T. L., Evans, N. J., I., & Lee, C. W. 2008, A&A, 487, 993 (Cited on pages 5 and 93.)

Kauffmann, J., Goldsmith, P. F., Melnick, G., et al. 2017, A&A, 605, L5 (Cited on pages 36, 57 and 114.)

Kavak, Ü., van der Tak, F. F. S., Tielens, A. G. G. M., & Shipman, R. F. 2019, A&A, 631, A117 (Cited on page 79.)

Klein, B., Hochgürtel, S., Krämer, I., et al. 2012, A&A, 542, L3 (Cited on page 23.)

Kleinmann, D. E. & Low, F. J. 1967, ApJ, 149, L1 (Cited on page 17.)

Klessen, R. S. & Glover, S. C. O. 2016, Saas-Fee Advanced Course, 43, 85 (Cited on page 4.)

Knoll, D. & Keyes, D. 2004, Journal of Computational Physics, 193, 357 (Cited on page 91.)

Kounkel, M. 2017, PhD thesis, University of Michigan (Cited on page 35.)

Kwan, J. & Scoville, N. 1976, ApJ, 210, L39 (Cited on page 20.)

Lada, C. J. & Lada, E. A. 2003, ARA&A, 41, 57 (Cited on page 11.)

Lequeux, J. 2005, The Interstellar Medium (Springer) (Cited on page 11.)

Leurini, S., Rolffs, R., Thorwirth, S., et al. 2006, A&A, 454, L47 (Cited on page 83.)

Lis, D. C., Serabyn, E., Keene, J., et al. 1998, ApJ, 509, 299 (Cited on pages 21 and 35.)

Liszt, H. S. & Pety, J. 2016, ApJ, 823, 124 (Cited on page 58.)

Liszt, H. S., Pety, J., Gerin, M., & Lucas, R. 2014, A&A, 564, A64 (Cited on page 62.)

Mangum, J. G. & Shirley, Y. L. 2015, PASP, 127, 266 (Cited on pages 90, 91 and 92.)

Maret, S., Hily-Blant, P., Pety, J., Bardeau, S., & Reynier, E. 2011, A&A, 526, A47 (Cited on pages 29 and 38.)

Masson, C. R., Berge, G. L., Claussen, M. J., et al. 1984, ApJ, 283, L37 (Cited on page 35.)

McCarthy, M. C., Gottlieb, C. A., Gupta, H., & Thaddeus, P. 2006, ApJ, 652, L141 (Cited on page 6.)

McKee, C. F. & Holliman, John H., I. 1999, ApJ, 522, 313 (Cited on page 10.)

McKee, C. F. & Ostriker, E. C. 2007, ARA&A, 45, 565 (Cited on page 10.)

Megeath, S. T., Gutermuth, R., Muzerolle, J., et al. 2016, AJ, 151, 5 (Cited on page 11.)

Meier, D. S. & Turner, J. L. 2005, ApJ, 618, 259 (Cited on page 59.)

Meingast, S., Alves, J., Mardones, D., et al. 2016, A&A, 587, A153 (Cited on pages 108 and 110.)

Menten, K. M., Reid, M. J., Forbrich, J., & Brunthaler, A. 2007, A&A, 474, 515 (Cited on pages 17 and 35.)

Milam, S. N., Savage, C., Brewster, M. A., Ziurys, L. M., & Wyckoff, S. 2005, ApJ, 634, 1126 (Cited on page 95.)

Miville-Deschênes, M.-A., Murray, N., & Lee, E. J. 2017, ApJ, 834, 57 (Cited on page 11.)

Molinari, S., Bally, J., Noriega-Crespo, A., et al. 2011, ApJ, 735, L33 (Cited on page 10.)

Muller, S., Kawaguchi, K., Black, J. H., & Amano, T. 2016, A&A, 589, L5 (Cited on page 62.)

Nagy, Z., van der Tak, F. F. S., Fuller, G. A., & Plume, R. 2015, A&A, 577, A127 (Cited on pages 53 and 85.)

Nagy, Z., Van der Tak, F. F. S., Ossenkopf, V., et al. 2013, A&A, 550, A96 (Cited on page 62.)

Neufeld, D. A., Schilke, P., Menten, K. M., et al. 2006, A&A, 454, L37 (Cited on pages 62 and 64.)

Neufeld, D. A. & Wolfire, M. G. 2009, ApJ, 706, 1594 (Cited on pages 63, 83 and 84.)

Neufeld, D. A. & Wolfire, M. G. 2016, ApJ, 826, 183 (Cited on page 83.)

Neufeld, D. A., Wolfire, M. G., & Schilke, P. 2005, ApJ, 628, 260 (Cited on page 62.)

Novotny, O., Mitchell, J. B. A., LeGarrec, J. L., et al. 2005, Journal of Physics B Atomic Molecular Physics, 38, 1471 (Cited on pages 62 and 85.)

Öberg, K. I., Bottinelli, S., Jørgensen, J. K., & van Dishoeck, E. F. 2010, ApJ, 716, 825 (Cited on page 7.)

O'Dell, C. R., Muench, A., Smith, N., & Zapata, L. 2008, Star Formation in the Orion Nebula II: Gas, Dust, Proplyds and Outflows (ASP Monograph Publications), 544 (Cited on pages 17, 20 and 35.)

Ossenkopf, V. & Henning, T. 1994, A&A, 291, 943 (Cited on page 93.)

Pabst, C., Higgins, R., Goicoechea, J. R., et al. 2019, Nature, 565, 618 (Cited on pages 20, 40, 58, 63, 65 and 105.)

Pagani, L., Bergin, E., Goldsmith, P. F., et al. 2019, A&A, 624, L5 (Cited on page 20.)

Patience, J., Zavala, R. T., Prato, L., et al. 2008, ApJ, 674, L97 (Cited on page 17.)

Peterson, D. E. & Megeath, S. T. 2008, The Orion Molecular Cloud 2/3 and NGC 1977 Regions (ASP Monograph Publications), 590 (Cited on pages 21 and 35.)

Peterson, D. E., Megeath, S. T., Luhman, K. L., et al. 2008, ApJ, 685, 313 (Cited on page 35.)

Pety, J., Guzmán, V. V., Orkisz, J. H., et al. 2017, A&A, 599, A98 (Cited on pages 17, 36, 53, 54, 57 and 58.)

Pickett, H. M., Poynter, R. L., Cohen, E. A., et al. 1998, JQSRT, 60, 883 (Cited on pages 29 and 38.)

Pineda, J. L., Langer, W. D., Velusamy, T., & Goldsmith, P. F. 2013, A&A, 554, A103 (Cited on page 61.)

Pokhrel, R., Myers, P. C., Dunham, M. M., et al. 2018, ApJ, 853, 5 (Cited on pages 11 and 12.)

Rigby, A. J., Moore, T. J. T., Eden, D. J., et al. 2019, A&A, 632, A58 (Cited on page 91.)

Roman-Duval, J., Heyer, M., Brunt, C. M., et al. 2016, ApJ, 818, 144 (Cited on page 10.)

Sakai, N., Ceccarelli, C., Bottinelli, S., Sakai, T., & Yamamoto, S. 2012, ApJ, 754, 70 (Cited on page 53.)

Salas, P., Oonk, J. B. R., Emig, K. L., et al. 2019, A&A, 626, A70 (Cited on page 79.)

Schilke, P., Groesbeck, T. D., Blake, G. A., Phillips, & T. G. 1997, ApJS, 108, 301 (Cited on page 48.)

Schöier, F. L., van der Tak, F. F. S., van Dishoeck, E. F., & Black, J. H. 2005, A&A, 432, 369 (Cited on page 79.)

Scoville, N. Z. & Wilson, C. D. 2004, in Astronomical Society of the Pacific Conference Series, Vol. 322, The Formation and Evolution of Massive Young Star Clusters, ed. H. J. G. L. M. Lamers, L. J. Smith, & A. Nota, 245 (Cited on page 10.)

Shematovich, V. I. 2012, Solar System Research, 46, 391 (Cited on pages 8 and 9.)

Shirley, Y. L. 2015, PASP, 127, 299 (Cited on pages 15 and 58.)

Siringo, G., Kreysa, E., Kovács, A., et al. 2009, A&A, 497, 945 (Cited on page 92.)

Smith, I. W. M., Herbst, E., & Chang, Q. 2004, MNRAS, 350, 323 (Cited on page 9.)

Sota, A., Maíz Apellániz, J., Walborn, N. R., et al. 2011, ApJS, 193, 24 (Cited on page 17.)

Stacey, G. J., Hailey-Dunsheath, S., Ferkinhoff, C., et al. 2010, ApJ, 724, 957 (Cited on page 61.)

Stahler, S. W. & Palla, F. 2005, The Formation of Stars (Wiley-VCH) (Cited on pages 11 and 17.)

Sutton, E. C., Blake, G. A., Masson, C. R., & Phillips, T. G. 1985, ApJS, 58, 341 (Cited on page 36.)

Tahani, K., Plume, R., Bergin, E. A., et al. 2016, ApJ, 832, 12 (Cited on page 17.)

Tang, X. D., Henkel, C., Menten, K. M., et al. 2018, A&A, 609, A16 (Cited on page 40.)

Tercero, B., Cernicharo, J., Pardo, J. R., & Goicoechea, J. R. 2010, A&A, 517, A96 (Cited on page 36.)

Tercero, B., Vincent, L., Cernicharo, J., Viti, S., & Marcelino, N. 2011, A&A, 528, A26 (Cited on page 36.)

Tielens, A. G. G. M. 2005, The Physics and Chemistry of the Interstellar Medium (Cambridge University Press) (Cited on pages 4, 6, 7, 8, 9, 10, 13, 14, 20 and 21.)

Tielens, A. G. G. M. & Hollenbach, D. 1985, ApJ, 291, 747 (Cited on page 83.)

Tielens, A. G. G. M., Meixner, M. M., van der Werf, P. P., et al. 1993, Science, 262, 86 (Cited on page 83.)

Tizniti, M., Le Picard, S. D., Lique, F., et al. 2014, Nature Chemistry, 6, 141 (Cited on page 62.)

Tucker, K. D. & Kutner, M. L. 1978, ApJ, 222, 859 (Cited on page 89.)

Turner, B. E. & Gammon, R. H. 1975, ApJ, 198, 71 (Cited on page 89.)

Turner, B. E. & Thaddeus, P. 1977, ApJ, 211, 755 (Cited on pages 40, 89 and 106.)

Ungerechts, H., Bergin, E. A., Goldsmith, P. F., et al. 1997, ApJ, 482, 245 (Cited on pages 36, 58, 89, 106 and 107.)

van Dishoeck, E. F. 2014, Faraday Discussions, 168, 9 (Cited on pages 3, 4, 5, 6, 7, 8, 9 and 12.)

Vidali, G., Pirronello, V., Li, L., et al. 2007, Journal of Physical Chemistry A, 111, 12611 (Cited on page 9.)

Virtanen, P., Gommers, R., Oliphant, T. E., et al. 2020, Nature Methods, 17, 261 (Cited on page 91.)

Visser, R., van Dishoeck, E. F., & Black, J. H. 2009, A&A, 503, 323 (Cited on page 8.)

Wakelam, V., Caselli, P., Ceccarelli, C., Herbst, E., & Castets, A. 2004, A&A, 422, 159 (Cited on page 53.)

Wakelam, V., Herbst, E., Loison, J. C., et al. 2012, ApJS, 199, 21 (Cited on page 63.)

Watanabe, Y., Nishimura, Y., Harada, N., et al. 2017, ApJ, 845, 116 (Cited on page 58.)

Wiesenfeld, L. & Goldsmith, P. F. 2014, ApJ, 780, 183 (Cited on page 61.)

Wilson, T. L. & Rood, R. 1994, ARA&A, 32, 191 (Cited on pages 91, 95 and 107.)

Wirström, E. S., Geppert, W. D., Hjalmarson, Å., et al. 2011, A&A, 533, A24 (Cited on page 9.)

Wiseman, J. J. & Ho, P. T. P. 1998, ApJ, 502, 676 (Cited on page 35.)

Woon, D. E. & Herbst, E. 2009, Astrophysical Journal Supplement Series, 185, 273 (Cited on page 105.)

Wyrowski, F., Schilke, P., Hofner, P., & Walmsley, C. M. 1997, ApJ, 487, L171 (Cited on pages 40 and 45.)

Yamamoto, S. 2017, Introduction to Astrochemistry: Chemical Evolution from Interstellar Clouds to Star and Planet Formation (Springer) (Cited on pages 4 and 6.)

Yu, K. C., Bally, J., & Devine, D. 1997, ApJ, 485, L45 (Cited on page 35.)